



HAL
open science

Étude de nano-aimants préformés : des particules individuelles aux assemblées

Florent Tournus

► **To cite this version:**

Florent Tournus. Étude de nano-aimants préformés : des particules individuelles aux assemblées. Science des matériaux [cond-mat.mtrl-sci]. Université Claude Bernard Lyon 1, 2017. tel-02323292

HAL Id: tel-02323292

<https://hal.science/tel-02323292>

Submitted on 21 Oct 2019

HAL is a multi-disciplinary open access archive for the deposit and dissemination of scientific research documents, whether they are published or not. The documents may come from teaching and research institutions in France or abroad, or from public or private research centers.

L'archive ouverte pluridisciplinaire **HAL**, est destinée au dépôt et à la diffusion de documents scientifiques de niveau recherche, publiés ou non, émanant des établissements d'enseignement et de recherche français ou étrangers, des laboratoires publics ou privés.

Florent TOURNUS

**« Étude de nano-aimants préformés :
des particules individuelles aux assemblées »**

Habilitation à Diriger des Recherches
délivrée par l'**Université Claude Bernard Lyon 1**

Soutenue le **15 mai 2017** devant le jury constitué de :

Emmanuel COTTANCIN

Dominique GIVORD (absent)

Yves HUTTEL

Annick LOISEAU

Frédéric PETROFF

Vincent REPAIN

HABILITATION À DIRIGER DES RECHERCHES

Florent TOURNUS

**« Étude de nano-aimants préformés :
des particules individuelles aux assemblées »**

Table des matières

Introduction.....	p. 3
Chapitre 1 : Dépôt aléatoire de nanoparticules, diffusion et organisation d'agrégats sur des surfaces.....	p. 7
Chapitre 2 : Modélisation et analyse de courbes de magnétométrie, pour une caractérisation précise des propriétés magnétiques de nanoparticules.....	p. 39
Chapitre 3 : Nanoparticules bimétalliques, propriétés structurales, magnétiques et réactivité.....	p. 81
Chapitre 4 : Études en cours, nouveaux développements et perspectives.....	p. 113
Annexe.....	p. 127

Introduction

À bientôt 40 ans, et après un peu plus de dix années de recherches à l'Institut Lumière Matière (ILM, issu de la fusion en 2013 du LPMCN, laboratoire dans lequel j'ai été recruté en 2005, avec le LASIM et le LPCML), il m'a paru opportun de faire un bilan sur mes activités et sur les perspectives scientifiques envisagées pour les années à venir. L'« habilitation à diriger des recherches » (HDR), ultime diplôme délivré par l'université française, vient formaliser l'autorisation de diriger (et non plus simplement « encadrer ») des étudiants préparant leur doctorat. Au-delà de cet aspect administratif, l'obtention de l'HDR est une étape importante dans le déroulement d'une carrière de chercheur. Soutenir son HDR est aussi l'occasion, face à un jury de pairs, d'obtenir une reconnaissance concernant le bien-fondé et la cohérence de mes travaux antérieurs, ainsi qu'une marque de confiance quant à ma capacité à mener des projets originaux, de manière indépendante et pertinente¹. Il est donc important pour moi, au-delà de la possibilité de diriger des thèses, de recevoir cette reconnaissance et cette confiance, afin d'être ensuite dans les meilleures conditions pour avancer dans ma vie de chercheur (collaborations, projets, concours...).

Membre de l'équipe « Nanostructures magnétiques », mes activités de recherche actuelles s'articulent autour de la synthèse physique et l'étude des propriétés de nanoparticules, mais aussi de la modélisation et l'analyse de mesures magnétiques, la caractérisation structurale de nanoparticules par microscopie électronique en transmission et l'étude du comportement d'agrégats sur des surfaces. Ces activités de recherche, essentiellement fondamentales, s'inscrivent dans la problématique générale de la compréhension des effets de réduction de taille et du lien entre structure (à l'échelle atomique, mais aussi au niveau de l'organisation des nanoparticules) et propriétés physiques. Cette compréhension me semble nécessaire pour pleinement mettre à profit les spécificités des nano-objets dans d'éventuelles applications. Depuis peu je m'intéresse également à la combinaison de propriétés plasmoniques et magnétiques au sein de nano-systèmes hybrides.

Précisons rapidement mon parcours (dans ce manuscrit, je ne reviendrai pas sur mes résultats obtenus dans le cadre de ma thèse ou de mes post-doctorats, un CV détaillé est également inclus à la fin de ce document) qui m'a amené à être recruté comme Chargé de Recherches (CR) au CNRS. Mon travail de thèse a porté sur l'« Étude du dopage de matériaux covalents cages nanostructurés ». Les matériaux cages sont intéressants, entre autres, parce qu'ils offrent différentes possibilités de dopage : en plus du dopage par substitution, on peut avoir un dopage endoèdre ou exoèdre selon la localisation du dopant à l'intérieur ou l'extérieur de la cage. J'ai étudié expérimentalement (notamment par spectroscopie Raman, absorption X et diffraction X) et théoriquement (simulations *ab initio* dans le formalisme de la théorie de la fonctionnelle de la densité) le cas de plusieurs matériaux nanostructurés à base de cages covalentes : le C₆₀ et les clathrates de silicium. Nous avons montré comment le dopage peut permettre d'obtenir des structures exotiques (avec de nouvelles liaisons chimiques) et de modifier ainsi les propriétés électroniques, structurales etc. d'un matériau, pouvant donner naissance à des matériaux nouveaux. Après cette thèse mêlant expériences et simulations numériques, j'ai effectué une

¹ L'arrêté du 23 novembre 1988 (modifié en 1992, 1995 et 2002) indique « *L'habilitation à diriger des recherches sanctionne la reconnaissance du haut niveau scientifique du candidat, du caractère original de sa démarche dans un domaine de la science, de son aptitude à maîtriser une stratégie de recherche dans un domaine scientifique ou technologique suffisamment large et de sa capacité à encadrer de jeunes chercheurs.* »

année de post-doc à Louvain-la-Neuve pour étudier des systèmes à base de nanotubes de carbone par calculs *ab initio* (DFT). J'ai ensuite passé une année de post-doc au CEA Grenoble pour un travail exclusivement expérimental sur l'étude de nanoparticules comme catalyseurs pour la croissance de nanotubes et nanofils. À cette occasion, j'ai été formé à la microscopie électronique et je me suis familiarisé avec le magnétisme des nanoparticules, ouvrant ainsi la voie à mon travail de recherche en tant que CR CNRS dans le groupe « Nanostructures Magnétiques ».

Depuis 2005, mes recherches sont centrées sur la synthèse physique et l'étude des propriétés de nanoparticules métalliques (et bimétalliques). Il est important de noter qu'expérimentalement mes travaux se sont beaucoup appuyés sur un générateur d'agrégat assez unique, basé sur une technique de vaporisation laser, disponible au PLYRA (Plateforme Lyonnaise de Recherche sur les Agrégats) et en particulier sur le dispositif de dernière génération équipé d'un sélecteur de masse, que nous avons commencé à utiliser au moment de mon arrivée comme CR au laboratoire. Cet aspect expérimental, avec la possibilité de disposer d'échantillons de nanoparticules « modèles », a fortement guidé mes activités de recherche. Celle-ci peuvent être regroupées selon trois thématiques scientifiques principales, qui feront chacune l'objet d'un chapitre de ce manuscrit :

- Dépôt aléatoire de nanoparticules, diffusion et organisation d'agrégats sur des surfaces
- Modélisation et analyse de courbes de magnétométrie, pour une caractérisation précise des propriétés magnétiques de nanoparticules
- Nanoparticules bimétalliques, propriétés structurales, magnétiques et réactivité

Ces trois pans de mon travail de recherche se complètent et s'alimentent mutuellement. Par exemple, pour des nanoparticules qui se révèlent prometteuses d'un point de vue des propriétés magnétiques (comme le FePt) on pourra chercher dans un deuxième temps à les organiser en réseau, ou encore la maîtrise de la distribution spatiale des particules dans un échantillon autorise ensuite à déduire de manière fiable les propriétés de nano-aimants à partir de mesures sur des assemblées. Une modélisation fine des mesures magnétiques permet également d'aller plus loin, et de manière plus fiable, dans l'interprétation des courbes de magnétométrie expérimentales. Certaines recherches s'inscrivant dans ces deux premiers axes (deux premiers chapitres de ce manuscrit) peuvent ainsi être vues comme la mise au point d'outils, garantissant par la suite une rigueur dans l'analyse de mesures sur des échantillons de nanoparticules. Mais cela ne se réduit pas à cet aspect utilitaire puisque combiner ces différents aspects permet d'apporter de nouvelles informations, de tester des théories physiques, de mettre à jour certaines propriétés (sur la diffusion de particules, leur anisotropie magnétique etc.)... J'espère que ce manuscrit, en donnant une vue d'ensemble sur les résultats obtenus depuis une dizaine d'années, permettra d'illustrer ce point qui me tient à cœur et qui a guidé ma démarche durant ces années de recherche.

Ce document n'a pas vocation à présenter de manière exhaustive un sujet ou une thématique scientifique précise. Il ne s'agit pas d'une « deuxième thèse », mais davantage d'un rapport d'étape dans mon parcours de chercheur. Par conséquent, ce manuscrit ne rappellera pas les techniques utilisées (dépôt d'agrégats, microscopie électronique, mesures sur synchrotron etc.), il ne présentera pas non plus de façon détaillée l'état de l'art sur les différents sujets abordés, et ne prétendra pas donner une vue d'ensemble comme le ferait par exemple un livre ou un article de revue (pour cela, voir par exemple [Andreazza2015], article de revue co-écrit récemment sur les nanoalliages de type CoPt). En revanche, il donnera une idée globale de mon approche de la recherche, de mes intérêts et motivations, et des résultats que j'ai pu obtenir. Dans les trois chapitres qui suivent, j'ai ainsi fait le choix de résumer brièvement les principaux résultats scientifiques (résultats publiés, sachant que

comme on le sait, une part non négligeable de l'activité de recherche ne transparait pas dans les publications...) et d'illustrer plus précisément certains travaux en incluant directement les articles correspondants (trois par chapitre).

Le quatrième chapitre fera quant à lui le point sur mes activités très récentes (résultats non publiés) et les recherches en cours, ainsi que sur les perspectives variées proposées pour les prochaines années, à plus ou moins long terme. L'idée est de m'ouvrir à de nouvelles thématiques, toujours en lien avec les nanosystèmes et en continuant de mettre à profit mon expertise, mais dépassant le cadre des nanoparticules synthétisées par la technique LECBD (Low Energy Cluster Beam Deposition) maîtrisée à Lyon depuis de nombreuses années.

Enfin, pour clore ce document une annexe présente la liste de mes articles publiés, ainsi que mon CV, avec mon parcours, ma production scientifique, suivi de quelques éléments sur mon implication dans des activités d'encadrement, d'enseignement, d'animation de la recherche, ainsi que les diverses activités annexes et responsabilités au sein du laboratoire et du CNRS.

Chapitre 1 : Dépôt aléatoire de nanoparticules, diffusion et organisation d'agrégats sur des surfaces

Cette thématique englobe différents axes de recherche suivis depuis mon recrutement au laboratoire. Dans un souci de maîtrise des échantillons de nanoparticules obtenus par dépôt d'agrégats, je me suis penché sur la question des distances inter-particules ainsi que la formation de dimères (clairement visibles lorsqu'on effectue un histogramme de taille sur des dépôts de nanoparticules triées en taille), ceci dans le cas d'un dépôt aléatoire. En ce qui concerne les distances inter-particule, et notamment la distance au premier voisin, on peut facilement établir des expressions analytiques [Tournus2011e] qui s'avèrent fort utiles d'une part pour vérifier expérimentalement que le modèle de dépôt aléatoire est valide (cf. Fig. 1), et d'autre part pour prévoir les distances que l'on obtiendra dans le cas d'un échantillon préparé avec une certaine densité de particules (et bien sûr, réciproquement, déterminer les conditions expérimentales à utiliser pour avoir une distance 1^{er} voisin moyenne d'une certaine valeur). On rappelle que la connaissance et la maîtrise des distances entre particules voisines est essentielle pour des études de magnétisme où l'on souhaite généralement minimiser les interactions (en particulier dipolaires) entre les particules, de façon à pouvoir déduire des propriétés intrinsèques à partir de mesures magnétiques d'ensemble.

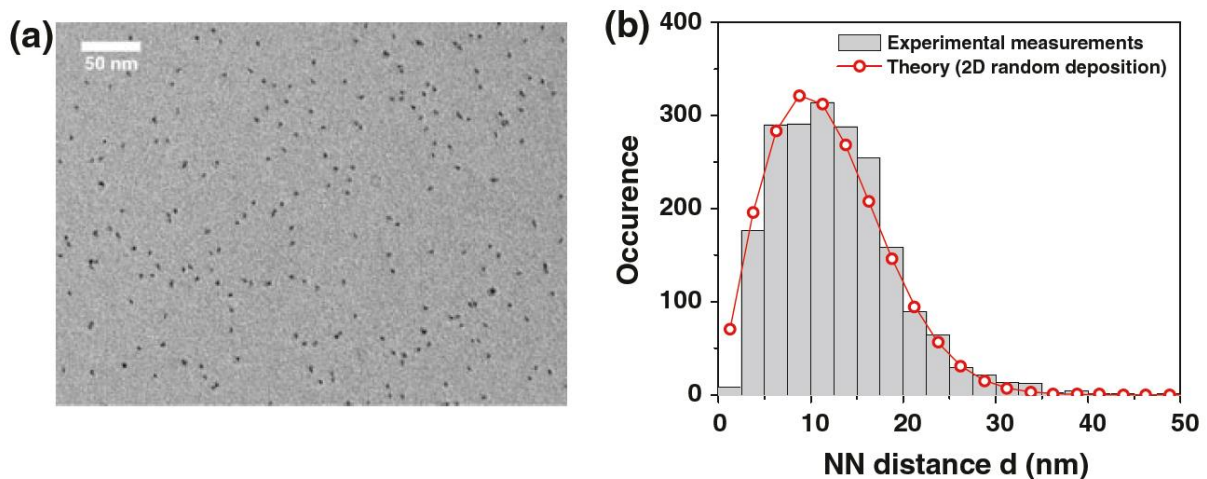


Fig. 1 : a) Image MET typique d'un dépôt de nanoparticules (ici, du Co de diamètre moyen 4,3 nm) avec une densité surfacique de 1800 particules/ μm^2 . b) Distribution de distances au premier voisin (Nearest Neighbor : NN) déduite des observations MET (histogramme) comparée à la distribution théorique attendue pour un dépôt aléatoire de cette densité. Figure tirée de [Tournus2011e].

Puisque nous synthétisons différents types d'échantillons, sous forme de couches 2D, de films 3D de particules noyées dans une matrice ou encore de multicouches (couches 2D d'agrégats séparés par un « spacer » d'épaisseur t), j'ai comparé les distances au 1^{er} voisin dans ces différents cas [Tournus2011e]. J'ai ainsi pu établir une expression approchée très simple pour la distance 1^{er} voisin moyenne dans le cas des échantillons multicouches (cf. Fig. 2). Les courbes présentées sur la Fig. 2 permettent par exemple de voir que des couches avec une distance moyenne d_{2D} dans le plan de 10 nm (correspondant à une densité de 2500 particules/ μm^2), séparées par une épaisseur de 5 nm de matrice, résultent en réalité en une distance 1^{er} voisin moyenne d'environ 7 nm.

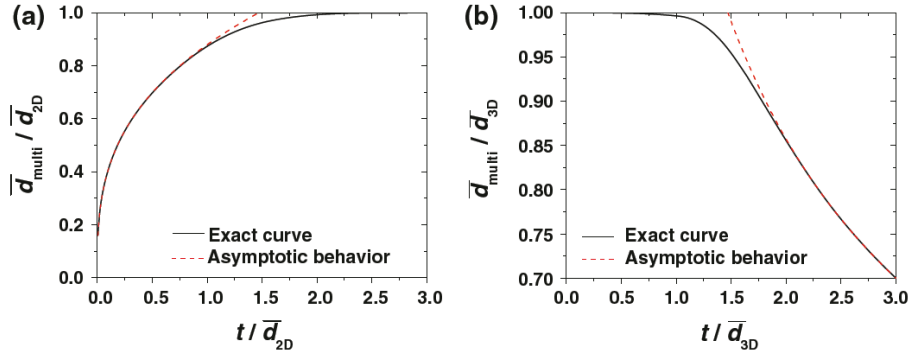


Fig. 2 : a) Évolution du rapport entre les distances 1^{er} voisin moyennes de l'échantillon multicouche (d_{multi}) et dans une seule couche (d_{2D}) en fonction de l'épaisseur t de la couche de séparation. L'expression asymptotique (loi de puissance avec un exposant 1/3) est tout à fait satisfaisante. b) Évolution du rapport entre les distances 1^{er} voisin moyennes de l'échantillon multicouche (d_{multi}) et dans un échantillon 3D de même concentration volumique (d_{3D}) en fonction de l'épaisseur t de la couche de séparation, comparée à l'expression asymptotique (loi de puissance avec un exposant -1/2). Figure tirée de [Tournus2011e].

Comme on peut s'en douter, pour un dépôt aléatoire il existe une certaine probabilité qu'un agrégat arrive sur la surface avec une distance au 1^{er} voisin tellement faible qu'en réalité les deux particules vont entrer en contact. Ceci entraîne un phénomène de formation de dimères (et trimères... plus généralement de multimères), qui est directement détectable sur les histogrammes de taille obtenus par observations MET de couches 2D d'agrégats triés en taille : en plus d'un pic principal correspondant à la taille des particules incidentes, on distingue un 2^e pic (parfois même un 3^e) correspondant aux dimères et dont l'amplitude dépend de la taille des particules incidentes et de la densité surfacique. Étant donnée l'importance que peuvent avoir les multimères sur les propriétés magnétiques (cf. Fig. 3 et chap. 2) il était important de bien maîtriser la formation de ces derniers. Un travail de modélisation a donc été mené permettant de rationaliser cet aspect pour nos échantillons de nanoparticules. Là encore, une comparaison à la théorie permet de vérifier l'aspect aléatoire des dépôts, une déviation par rapport aux proportions de multimères attendues peut ainsi être la signature d'un phénomène de diffusion des agrégats sur la surface. La publication « *Multimer formation for two-dimensional random nanoparticle deposition* » [Tournus2011d], insérée ci-dessous, détaille ce travail de recherche.

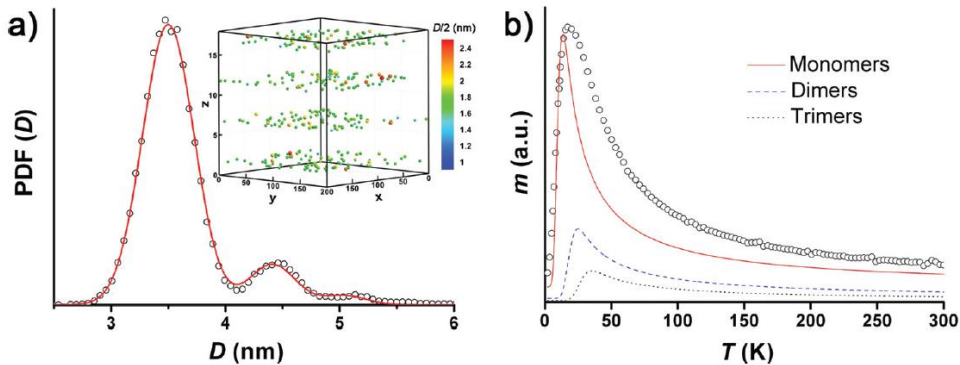


Fig. 3 : a) Distribution de taille de particules de Co triées en taille (échantillon multicouches) déduite de simulations numériques de dépôt aléatoire suivi de coalescence (points) comparée au résultat des ajustements des mesures magnétiques (ligne). b) Contribution des monomères, dimères et trimères correspondant à l'ajustement théorique de la courbe de susceptibilité ZFC mesurée (points) : l'ensemble des contributions doit être considéré pour bien rendre compte des observations expérimentales, même si les monomères restent largement majoritaires. Figure tirée de [Tournus2011].

Multimer formation for two-dimensional random nanoparticle deposition

Florent Tournus*

LPMCN, UMR 5586 CNRS and Université de Lyon, Université Lyon 1, F-69622 Villeurbanne, France

(Received 10 May 2011; published 25 July 2011)

Efforts are currently under way to produce nanoparticle samples with a size dispersion as low as possible, using deposition of preformed clusters on a substrate. However, even for diluted cluster films, contact or coalescence between neighboring clusters cannot be totally avoided due to the random nature of the deposition process. Consequently, the incident particle-size distribution will necessarily be degraded, with the statistical formation of multimers (dimers, trimers, or more generally n mers). In this article, we consider diluted assemblies of nanoparticles (with a narrow size distribution) randomly deposited on a surface and develop theoretical tools to assess the various multimer proportions. We establish simple and reliable analytical approximations of the probability for a cluster to form an n mer and the subsequent multimer proportion. These results can be applied in the analysis of experimental samples: They constitute a convenient tool for experimentalists in the design of their nanoparticle sample and the interpretation of experimental measurements.

DOI: 10.1103/PhysRevE.84.011612

PACS number(s): 68.43.Hn, 68.55.-a, 81.15.Aa, 02.50.-r

I. INTRODUCTION

The preparation of nanoparticle samples by deposition of preformed particles has proven to be a powerful technique [1–11]. In particular, it allows independent control of the cluster concentration and size, thereby offering the possibility of producing diluted samples of nanoparticles. In order to reliably and accurately infer the intrinsic nanoparticle properties from a macroscopic assembly, and thus decipher potential size effects, two conditions need to be met: Clusters must have a narrow size distribution (important information can be hidden or accompanied by large uncertainties for systems with a broad size distribution) and particles must remain far enough from each other to avoid any interaction.

For this purpose, efforts are currently under way to produce nanoparticle samples with a size dispersion as low as possible, using deposition of preformed clusters on a substrate. Nevertheless, even for diluted cluster films, because of the random deposition process, contact or coalescence between neighboring clusters cannot be totally avoided [12,13]. Consequently, the incident particle-size distribution will necessarily be degraded, with the statistical formation of multimers: dimers, trimers, or more generally n mers, which are particles formed on the surface by the partial coalescence of n clusters in contact. It is then crucial to take into account this proportion of larger particles in order to correctly interpret experimental measurements. For instance, it has been shown how multimers can have a strong impact on magnetic measurements, even if they constitute only a small proportion of the total particles [12]. Moreover, a good knowledge of the characteristics of such random nanoparticle samples is very useful: It allows *a priori* control of the final sample characteristics, it can help in the interpretation of experimental measurements [8,12], and it can provide a way to check the random nature of a sample, for instance, to detect particle diffusion.

Random particle deposition is usually modeled as a random sequential adsorption (RSA) process with hard (i.e., nonpenetrating) particles. A lot of theoretical studies have

been performed in this framework [14–23], with the (more complicated) case of high packing fraction being extensively discussed. Moreover, recent developments have been reported, going beyond the usual simplifying assumptions of monosized particles [24] or infinite samples [25]. While this model may be adapted to a variety of cases, it is not suited to cluster deposition on a substrate because it excludes the formation of dimers (and more generally multimers), which are effectively met in such samples.

In this paper, we consider diluted assemblies of nanoparticles (with a narrow size distribution) randomly deposited on a surface [two-dimensional (2D) samples] and develop theoretical tools to assess the various multimer proportions. First, we express the probability for a cluster to remain a monomer or to form a dimer. Then, more generally, we show how the probability for a cluster to form a multimer can be written as a power series of a dimensionless parameter. This allows us to establish analytical approximations, up to tetramers. We also derive Taylor expansions for the multimer proportions and compare the theoretical results to numerical simulations. Then, we express the proportions as a function of the monomer proportion and discuss the link between the incident and apparent particle density. Finally, we show how these results can be applied in the analysis of experimental samples.

II. DEPOSITED CLUSTERS AND PARTICLE DISTRIBUTION ON A SURFACE

In the case under examination, it is essential to make a clear distinction between the individual incident particles (i.e., those that are landing on the substrate), which we refer to as *clusters*, and the particles that can be observed on the sample, in its final configuration: These *particles* may be monomers or multimers (dimers, trimers, etc.), that is, they may be constituted of a single *cluster* or several *clusters*. In the following, we use the term n mer for a particle which is a multimer made of n clusters.

The number of particles N in a sample is different (always smaller) from the number of deposited clusters. With N_{tot} incident clusters, we find on the surface N_1 monomers, N_2 dimers, N_3 trimers, and so on, so that the total number

*florent.tournus@univ-lyon1.fr

of particles is $N = \sum_{k=1}^{\infty} N_k \neq N_{\text{tot}}$. In the same way, a distinction needs to be made between the *probability* for a cluster to form an n mer and the observed *proportion* of n mers among the particles. We can write the probability P_n for a cluster to form an n mer and the proportion of n mer x_n as¹

$$P_n = nN_n/N_{\text{tot}} \quad \text{and} \quad x_n = N_n/N. \quad (1)$$

From these equations, the probabilities P_k can be used to relate N to N_{tot} and x_n to P_n :

$$N = N_{\text{tot}} \sum_{k=1}^{\infty} P_k/k \quad \text{and} \quad x_n = \frac{P_n/n}{\sum_{k=1}^{\infty} P_k/k}. \quad (2)$$

This means that all the probabilities P_k must, in principle, be known if we want to compute N from N_{tot} or the respective proportions x_n of each multimer. Let us emphasize that on one hand, the quantity which is experimentally controlled when synthesizing a sample is N_{tot} (and not N), while on the other hand, only N and the proportions x_n are accessible by a direct characterization [typically by transmission electron microscopy (TEM)] of the sample once its synthesis is over.

Since, for the diluted samples we are interested in, P_k decreases with k and eventually vanishes for large k , the sum in the expressions above may be truncated. This is discussed in the following. From a theoretical point of view, it is easier to express the probabilities P_n , which we then use to determine the proportions x_n and the ratio N/N_{tot} . Note that this ratio is equal to the one between the apparent particle density ρ and the incident cluster density σ , which are simply $\rho = N/S_{\text{tot}}$ and $\sigma = N_{\text{tot}}/S_{\text{tot}}$, where S_{tot} is the sample area.

III. PROBABILITY TO REMAIN A MONOMER AND TO FORM A DIMER

A cluster remains a monomer if and only if its nearest neighbor (NN) distance, edge to edge, is positive. Therefore, by introducing the probability density function $F(r)$ of the edge-to-edge NN distance, the probability P_1 for a cluster to remain a monomer is

$$P_1 = \int_0^{\infty} F(r) dr. \quad (3)$$

Unfortunately, in the realistic case of a sample made by random deposition of clusters having a nonzero size dispersion, although the statistical distribution of center-to-center NN distance $\mathcal{F}(r)$ is well known, $F(r)$ usually cannot be analytically expressed [13]. Nevertheless, one may use the approximation $F(r) \simeq \mathcal{F}(r + \bar{D})$ to determine P_1 , with \bar{D} being the mean cluster diameter. The conditions required for this approximation to be valid have been previously discussed [13]. They impose a maximum cluster density σ for a given relative size dispersion. For instance, in the case of a relative diameter dispersion of around 10%, which can be met experimentally [6,11,12,26], it reads $\sigma \ll 3/\bar{D}^2$. Since we only consider diluted samples, in the following we neglect the

cluster diameter dispersion and consider that each cluster has a diameter D . However, it should be kept in mind that the results derived here will be acceptable only for sufficiently small cluster densities (the larger the size dispersion, the smaller the density has to be).

Using the known NN distance distribution for a random 2D particle sample, $\mathcal{F}(r) = 2\pi\sigma r \exp(-\sigma\pi r^2)$, one then obtain

$$P_1 = \exp(-\sigma\pi D^2). \quad (4)$$

This simple expression can be derived directly by stating that in order to remain a monomer, a cluster must have no other cluster in a disk of radius D around its center. Indeed, because the cluster deposition is supposed to be a random Poisson process, the probability to have k clusters in a surface S is

$$p_k(S) = \frac{(\sigma S)^k e^{-\sigma S}}{k!}. \quad (5)$$

This allows us to write the above expression for P_1 , where the area $S = \pi D^2$ is the *capture area* of a cluster.

In a similar way, one may try to express the probability P_2 of forming a dimer using Eq. (5). In order to form a dimer, a cluster must have another cluster in its capture area. The probability of such an event occurring is $p_1(S) = \sigma S \exp(-\sigma S)$. However, this does not represent exactly the probability for a cluster to form a dimer since this neighbor could have another cluster close enough to be in contact: This would correspond to a trimer (or even a larger multimer). To really form a dimer, the first neighbor must have no other neighbor in its own capture area. This condition implies that

$$P_2 = p_1(S)p_0(\Sigma), \quad (6)$$

where Σ is equal to S minus the common surface shared by the capture areas of the two clusters forming the dimer [see Fig. 1(a)]. Note that here, and in the following, we do not take into account the coalescence that can occur between the clusters, leading to a change in the particle diameter and a center-of-mass shift. Σ depends on the separation r between the two clusters: The average value $\bar{p}_0(\Sigma)$ of $p_0[\Sigma(r)]$ must then be determined in order to express P_2 , which can also be written as the average of $P_2(r) = p_1(S)p_0[\Sigma(r)]$.

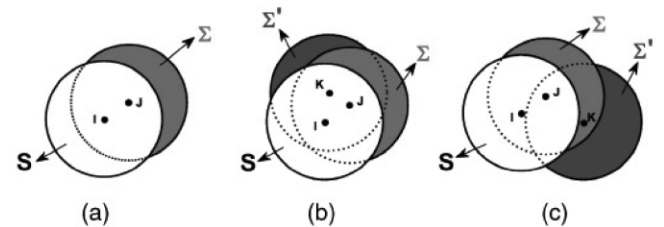


FIG. 1. (Color online) Representation of the capture area of neighboring clusters for a dimer (a) and a trimer [(b) and (c)]. Σ represents the surface of the capture area centered around J , which is not already included in the capture area S of cluster I . Σ' represents the surface of the cluster K capture area, which does not overlap S or Σ .

¹The average number of clusters forming an n mer is indeed $N_{\text{tot}} P_n$, so that we have $N_n = N_{\text{tot}} P_n/n$ since n clusters are required to form an n mer.

IV. PROBABILITIES FOR A CLUSTER TO FORM A MULTIMER AS POWER SERIES

In the next section, we continue the calculation started above, in order to establish an analytical approximation for P_2 . At this point, we simply write that $\Sigma(r) = a(r)S$. It can be seen immediately from the above formulas that the probabilities P_1 and P_2 only depend on the dimensionless parameter σS . More generally, one can note that the situation is not affected by a scale modification: Multiplying the lengths by a factor α does not change the probabilities P_n or the proportions x_n while σ will be divided by α^2 and S multiplied by α^2 . Of course, one can choose any quantity constructed from σS as the control variable: For instance, we may use the coverage ratio $\tau = \sigma\pi R^2$. In the following, we express the quantities of interest as functions of the dimensionless parameter $\epsilon = \sigma\pi D^2$.

Taylor expansions (power series of ϵ) can then be used as good approximations for P_n (and x_n), as long as ϵ is small enough (i.e., the sample is diluted enough). Note also that the condition that ϵ remains small already needed to be fulfilled in order for the cluster size dispersion to be negligible. We can establish that the leading term (first nonzero power of ϵ) for the probability P_n is ϵ^{n-1} , which can be stated using a mathematical notation as

$$P_n = O(\epsilon^{n-1}). \quad (7)$$

From the expression of P_1 seen earlier, we have $P_1 = \exp(-\epsilon)$, which can be written exactly as a power series:

$$P_1 = \sum_{k=0}^{\infty} \frac{(-\epsilon)^k}{k!} = 1 - \epsilon + \frac{\epsilon^2}{2} + \dots, \quad (8)$$

with ϵ^0 (i.e., 1) as the leading term. For the probability of dimer formation, we have

$$P_2(r) = \epsilon e^{-[1+a(r)]\epsilon}, \quad (9)$$

which clearly shows that the leading term will be ϵ (since the exponential term can be written as $1 - \epsilon[1 + a(r)] + \dots$). This is true for any value of r , and hence we have the same conclusion for the average probability P_2 . In the same way, we can write the probability for a cluster to form a trimer, which involves two distinct terms according to the two possibilities of forming a trimer [see Figs. 1(b) and 1(c)]:

$$P_3 = p_2(S)p_0(\Sigma)p_0(\Sigma') + p_1(S)p_1(\Sigma)p_0(\Sigma'), \quad (10)$$

meaning that a cluster I can either have exactly two other clusters, J and K , in its capture area, with those clusters having no other neighbors; or I can have a single cluster J in its capture area S , J having itself a neighbor K (with no other neighbors) in the remaining part (Σ) of its capture area. By introducing the vector \mathbf{r} between I and J and \mathbf{r}' between J and K , we can write that $\Sigma(r) = a(r)S$ and $\Sigma'(\mathbf{r}, \mathbf{r}') = b(\mathbf{r}, \mathbf{r}')S$. As for P_2 , the average probability P_3 must be calculated by integration over all the possible values of \mathbf{r} and \mathbf{r}' . The two terms of $P_3(\mathbf{r}, \mathbf{r}')$ read, respectively,

$$\frac{\epsilon^2}{2} e^{-\epsilon[1+a(r)+b(\mathbf{r}, \mathbf{r}')]} \quad \text{and} \quad a(r)\epsilon^2 e^{-\epsilon[1+a(r)+b(\mathbf{r}, \mathbf{r}')]} \quad (11)$$

Thus, the leading term of $P_3(\mathbf{r}, \mathbf{r}')$ is in any case of the order of ϵ^2 , which demonstrates that $P_3 = O(\epsilon^2)$. One could go on with the same type of reasoning for larger n mers in order to verify the above statement.

One can also see that since the sum $\sum_{k=1}^{\infty} P_k/k$ has 1 as a leading term, the ratio N/N_{tot} or ρ/σ is of the order of 1. Moreover, x_n is of the same order as P_n . Instead of using the dimensionless parameter ϵ , one may use $\eta = \rho\pi D^2$ for the expansion into power series: Because $\rho/\sigma = O(1)$, the series has the same leading order when expressed as a function of ϵ or η . Then, we can write

$$x_n = O(\eta^{n-1}). \quad (12)$$

Note that in the definition of η , while the apparent particle density ρ is involved, the diameter D is the median diameter of the incident clusters (i.e., of the monomers).

These considerations on the leading terms of the different multimer proportions have a very tangible impact on the characteristics of diluted nanoparticle films. They indeed present a ‘‘hierarchy’’ in the multimer populations: The ratios x_2/x_1 , x_3/x_2 , x_4/x_3 and more generally x_n/x_{n-1} are all of the same order (of the order of ϵ or η). This shows that x_n becomes rapidly negligible for increasing n , as long as we are dealing with diluted samples (small ϵ value). To fix the ideas, for instance, if the dimer proportion in a sample is around 10%, then the trimer proportion will be of the order of 1% and that of tetramers will be of the order of 0.1%.

V. ANALYTICAL APPROXIMATIONS UP TO TETRAMERS

From what has been seen before, the first term of a power series in ϵ will be of the order of ϵ^3 for tetramers (4mers) and ϵ^4 for pentamers (5mers). It means that using power series approximations up to the ϵ^3 term is equivalent to neglecting particles larger than tetramers and simply considering that they have zero probability of formation. In the following, we make this approximation and derive analytical approximations of P_1 , P_2 , P_3 , and P_4 up to the third order in ϵ . This can be done immediately for P_1 , where we can expand $\exp(-\epsilon)$ to find

$$P_1 \simeq 1 - \epsilon + \frac{1}{2}\epsilon^2 - \frac{1}{6}\epsilon^3. \quad (13)$$

For P_2 , we can write $P_2 = \int_0^D P_2(r)f(r)dr$ where $f(r)dr$ is the probability that, knowing that clusters I and J form a dimer, the IJ distance lies between r and $r + dr$. This corresponds to

$$P_2 = \int_0^D \epsilon \left\{ 1 - \epsilon[1 + a(r)] + \frac{\epsilon^2}{2}[1 + a(r)] + o(\epsilon^2) \right\} f(r)dr. \quad (14)$$

By introducing two constants α_2 and α_3 , this can be written as

$$P_2 = \epsilon + \alpha_2\epsilon^2 + \alpha_3\epsilon^3 + o(\epsilon^3). \quad (15)$$

We can easily establish that $f(r) = 2r/D^2$ and

$$a(r) = 1 - \frac{2\alpha}{\pi} + \frac{\sin(2\alpha)}{\pi} \quad \text{with} \quad \alpha = \arccos\left(\frac{r}{2D}\right). \quad (16)$$

We then have $\alpha_2 = -\int_0^D [1 + a(r)]f(r)dr$, which can be exactly calculated. We find

$$\alpha_2 = -1 - \frac{3\sqrt{3}}{4\pi} \simeq -1.413. \quad (17)$$

We can also write

$$\alpha_3 = 2 \int_{\pi/3}^{\pi/2} \left[2 - \frac{2\alpha}{\pi} + \frac{\sin(2\alpha)}{\pi} \right]^2 \sin(2\alpha) d\alpha, \quad (18)$$

which can also be calculated exactly:

$$\alpha_3 = \frac{-5}{12\pi^2} + \frac{\sqrt{3}}{\pi} + \frac{1}{2} \simeq 1.009. \quad (19)$$

In the end, we have computed the *exact* values of the power series coefficients for P_2 , which can be approximated by

$$P_2 \simeq \epsilon - 1.413 \epsilon^2 + 1.009 \epsilon^3. \quad (20)$$

In the same way, by introducing two coefficients β_2 and β_3 , we can write

$$P_3 = \beta_2 \epsilon^2 + \beta_3 \epsilon^3. \quad (21)$$

The condition $\sum_{k=1}^{\infty} P_k = 1$ implies that for the ϵ^2 coefficient we have $1/2 + \alpha_2 + \beta_2 = 0$, and consequently $\beta_2 = -\frac{1}{2} - \alpha_2$. This allows us to determine the exact value of β_2 :

$$\beta_2 = \frac{1}{2} + \frac{3\sqrt{3}}{4\pi} \simeq 0.913. \quad (22)$$

Note that the same result can be obtained by direct integration of the relation $\beta_2 = \int_0^D [\frac{1}{2} + a(r)]f(r)dr$. On the other hand, the integral expression of the β_3 coefficient is quite complicated and prevents us from finding its exact value. Nevertheless, a precise numerical evaluation is still possible by using the known expression $b(\mathbf{r}, \mathbf{r}')$. We find $\beta_3 \simeq -1.648$, so that we can approximately express P_3 by

$$P_3 \simeq 0.913 \epsilon^2 - 1.648 \epsilon^3. \quad (23)$$

Finally, the probability $P_4 = \gamma \epsilon^3$ can be deduced from the normalization condition $\sum_{k=1}^{\infty} P_k = 1$, which corresponds to $-1/6 + \alpha_3 + \beta_3 + \gamma = 0$. We then can write the approximation:

$$P_4 \simeq 0.806 \epsilon^3. \quad (24)$$

The set of equations (13), (20), (23), and (24) can be used to analytically determine the probability that a cluster forms an *n*mer, up to tetramers. These approximations, in the form of a Taylor series, are more and more accurate when $\epsilon \rightarrow 0$. Of course, for a given ϵ value, the quality of the approximation degrades as n increases: The relative contribution of the neglected terms of the power series (ϵ^4 and higher terms) is indeed growing with n . In particular, it should be noted that when the probability of forming a tetramer reaches a significant value (1% for instance), the condition $\epsilon \ll 1$ is no longer fulfilled and the ϵ^4 term, which is the first to be neglected in the P_4 expansion, is in fact not negligible as compared to the ϵ^3 term! The range of validity of the analytical expressions we have established is discussed in the next section.

VI. MULTIMER PROPORTIONS AND COMPARISON TO NUMERICAL SIMULATIONS

In Fig. 2, we compare the approximate expressions up to third order in ϵ to the results of numerical simulations [27], for P_1 , P_2 , and P_3 . As mentioned above, the range of validity is wider when going from trimers to dimers and monomers. Anyway, the underlying theoretical framework may not really be applicable for ϵ values higher than ~ 0.5 , except for samples with a very good monodispersity of incident clusters.

In order to express the particle proportions x_n , we have to relate ϵ to the other useful dimensionless parameter $\eta = \rho \pi D^2$. Note that the difference between ϵ and η lies in the use of the *apparent* (or final) particle density instead of the *incident* (or initial) cluster density. This makes η easy to determine experimentally by TEM observations. We can write, using what we have established earlier,

$$\frac{\eta}{\epsilon} = \frac{\rho}{\sigma} = \sum_{k=1}^{\infty} \frac{P_k}{k} \simeq 1 - 0.5 \epsilon + 0.098 \epsilon^2 - 0.01 \epsilon^3. \quad (25)$$

This gives the following Taylor expansion for the inverse ratio,

$$\frac{\epsilon}{\eta} = \frac{\sigma}{\rho} \simeq 1 + 0.5 \epsilon + 0.152 \epsilon^2 + 0.037 \epsilon^3, \quad (26)$$

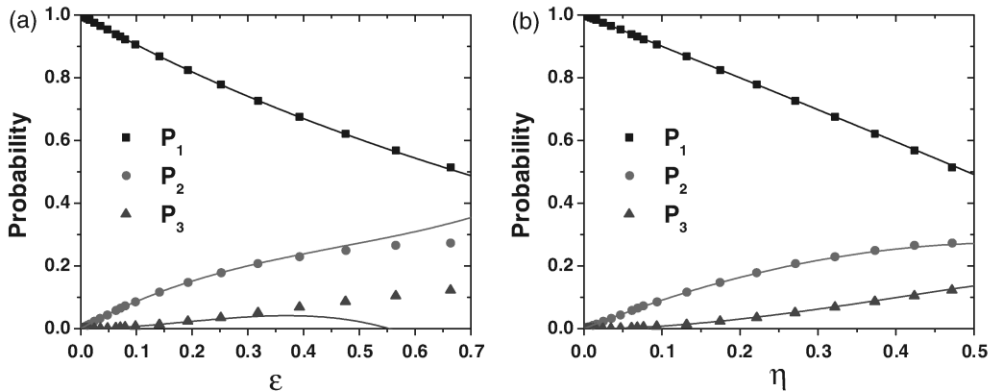


FIG. 2. (Color online) Probabilities P_1 , P_2 , and P_3 for a cluster to respectively remain a monomer or form a dimer or a trimer, as a function of the dimensionless parameter ϵ (a) or η (b). Solid lines correspond to the analytical approximations (Taylor expansions), while the points are the results of numerical simulations.

which leads, by recursion, to

$$\frac{\epsilon}{\eta} \simeq 1 + 0.5 \eta + 0.402 \eta^2 + 0.39 \eta^3. \quad (27)$$

This expression allows us to express the P_n probabilities as a function of η :

$$P_1 \simeq 1 - \eta - 0.069 \eta^3, \quad (28)$$

$$P_2 \simeq \eta - 0.913 \eta^2 - 0.002 \eta^3, \quad (29)$$

$$P_3 \simeq 0.913 \eta^2 - 0.735 \eta^3, \quad (30)$$

$$P_4 \simeq 0.806 \eta^3. \quad (31)$$

From the relation $x_n = (P_n/n)(\epsilon/\eta)$, we then obtain

$$x_1 \simeq 1 - 0.5 \eta - 0.098 \eta^2 - 0.081 \eta^3, \quad (32)$$

$$x_2 \simeq 0.5 \eta - 0.206 \eta^2 - 0.028 \eta^3, \quad (33)$$

$$x_3 \simeq 0.304 \eta^2 - 0.093 \eta^3, \quad (34)$$

$$x_4 \simeq 0.201 \eta^3. \quad (35)$$

The same equation can be used to express the proportions x_n as a function of ϵ . We find

$$x_1 \simeq 1 - 0.5 \epsilon + 0.152 \epsilon^2 - 0.032 \epsilon^3, \quad (36)$$

$$x_2 \simeq 0.5 \epsilon - 0.457 \epsilon^2 + 0.227 \epsilon^3, \quad (37)$$

$$x_3 \simeq 0.304 \epsilon^2 - 0.397 \epsilon^3, \quad (38)$$

$$x_4 \simeq 0.201 \epsilon^3. \quad (39)$$

These power expansions, as a function of ϵ or η , are compared to the results of numerical simulations in Fig. 2 for the probabilities P_n and in Fig. 3 for the multimer proportions x_n . In these figures, we do not show the tetramer formation probability or proportion since, as explained earlier, it is always very small (less than 2%) and the power expansions turn out to be rapidly unreliable (for ϵ or η greater than 0.3 or 0.2). As expected (see discussion above), it can be seen in the figures that the accuracy of the analytical approximations is much better for monomers and dimers than for trimers. It also appears that the Taylor expansions in the η power series are closer to the results of numerical simulations than those in the ϵ power

series. The overall excellent agreement between the analytical and numerical results (up to $\eta \simeq 0.5$) demonstrates how the power expansions derived earlier can be useful for an efficient analysis of experimental samples.

VII. ANOTHER USEFUL DIMENSIONLESS PARAMETER

Another dimensionless parameter which is easily accessible from TEM experiments is the proportion of monomers x_1 . It may even be easier to determine accurately x_1 than η , which involves the particle density (problems with image borders) and the cluster (monomer) diameter (uncertainty due to image analysis). By introducing the parameter $y = 1 - x_1$, which verifies $y \ll 1$ in the case under consideration, we can expand the multimer proportions in the y power series. We first establish, from the $x_1(\eta)$ expression, that $\eta/y \simeq 2(1 - 0.196 \eta - 0.124 \eta^2)$. This then leads to $\eta/y \simeq 2(1 - 0.392 y - 0.342 y^2)$, which enables us to write

$$x_1 = 1 - y, \quad (40)$$

$$x_2 \simeq y - 1.216 y^2 + 0.08 y^3, \quad (41)$$

$$x_3 \simeq 1.216 y^2 - 1.696 y^3, \quad (42)$$

$$x_4 \simeq 1.616 y^3. \quad (43)$$

We compare in Fig. 4 these Taylor expansions to the results of numerical simulations. The agreement is very satisfactory for the dimer and trimer proportions, down to around 80% of monomers ($y \simeq 0.2$). Within this range, even the tetramer proportion is quite well reproduced. However, the Taylor expansions, although they guarantee a correct limit for $y \rightarrow 0$, do not represent the best polynomial fits of the simulation data points. Therefore, by keeping a third-degree polynomial function, we can find expressions for x_2 , x_3 , and x_4 that precisely fit the numerical results up to $y = 0.3$ (i.e., samples with a proportion of monomers as low as 70%). These best-fit expressions are (see Fig. 4)

$$x_2 \simeq y - 1.216 y^2 + 0.469 y^3, \quad (44)$$

$$x_3 \simeq 0.007 y + 1.055 y^2 - 1.198 y^3, \quad (45)$$

$$x_4 \simeq -0.013 y + 0.266 y^2 + 0.038 y^3. \quad (46)$$

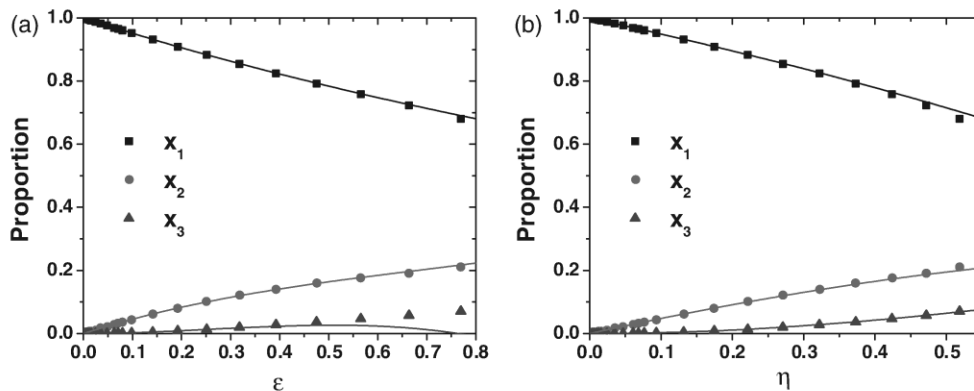


FIG. 3. (Color online) Proportions x_1 , x_2 , and x_3 of monomers, dimers, and trimers, as a function of the dimensionless parameter ϵ (a) or η (b). Solid lines correspond to the analytical approximations (Taylor expansions), while the points are the results of numerical simulations.

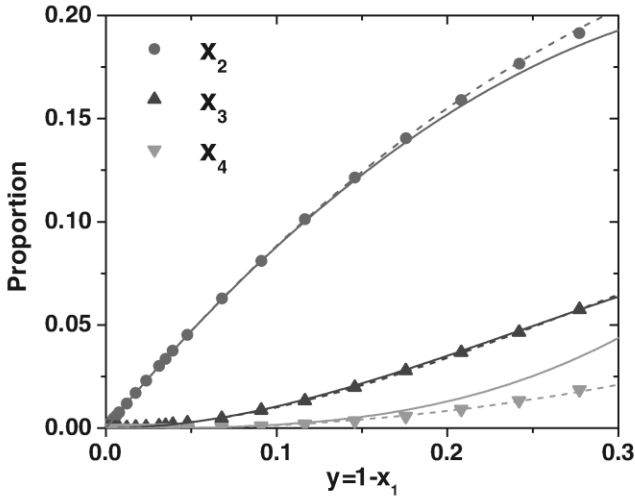


FIG. 4. (Color online) Proportions x_2 , x_3 , and x_4 of dimers, trimers, and tetramers, as a function of the dimensionless parameter $y = 1 - x_1$. Solid lines correspond to the analytical approximations (Taylor expansions), while the points are the results of numerical simulations. Best polynomial fits are shown as dashed lines.

VIII. RATIO BETWEEN THE INCIDENT AND APPARENT PARTICLE DENSITY

From the various relations we have established, the apparent particle density ρ can be linked in different way to the incident cluster density σ . We can write

$$\frac{\rho}{\sigma} \simeq 1 - 0.5\epsilon + 0.098\epsilon^2 - 0.01\epsilon^3, \quad (47)$$

which is in very good agreement with numerical simulations [see Fig. 5(a)]. It can be noticed that the first two terms of this Taylor expansion are identical to those of the monomer proportion x_1 , so that we can use the relation

$$\rho \simeq \sigma x_1 \quad (48)$$

as a quite efficient and extremely simple “rule of thumb” approximation (see Fig. 5). We can also derive other expansions for the inverse ratio:

$$\frac{\sigma}{\rho} \simeq 1 + 0.5\eta + 0.402\eta^2 + 0.390\eta^3, \quad (49)$$

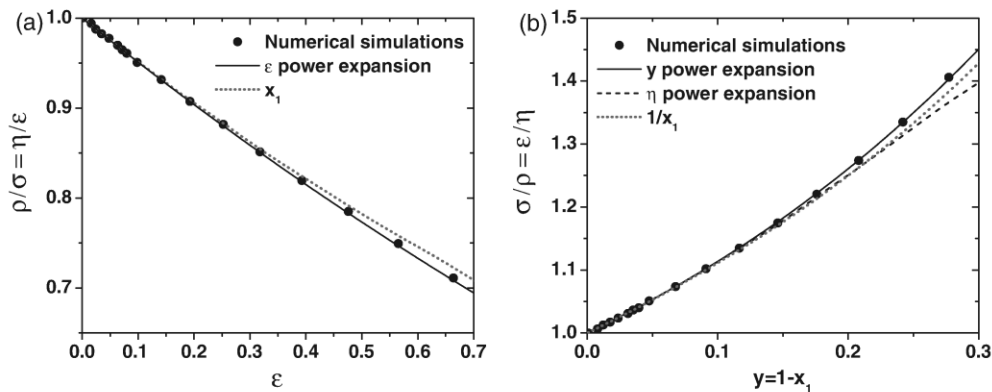


FIG. 5. (Color online) Evolution of (a) the ρ/σ ratio and (b) the σ/ρ ratio. Points correspond to the results of numerical simulations, while lines correspond to different analytical approximations.

$$\frac{\sigma}{\rho} \simeq 1 + y + 1.216y^2 + 1.517y^3. \quad (50)$$

As shown in Fig. 5(b), those approximations are satisfactory on a large range, the most accurate one being the y power expansion, which remains valid even for samples having a monomer proportion as low as 70%. These analytical expressions can be used to infer the incident cluster density from the observed final particle density of a sample, or conversely, to predict the particle density from the known deposited cluster density.

IX. ANALYZING EXPERIMENTAL SAMPLES

The various analytical approximations we have established in the present article clearly constitute a useful tool to predict the structural characteristics of a nanoparticle sample and to choose the right synthesis parameters for its design.

On the other hand, analysis on a given sample can determine if the particles have been deposited following a random deposition scheme. One way to do so is to (i) measure the particle density ρ , the experimental monomer proportion x_{exp} , and the median diameter of monomers \bar{D} ; (ii) determine the value of $\eta_{\text{exp}} = \rho\pi\bar{D}^2$ and calculate the expected monomer proportion x_{th} from the theoretical Taylor expansion; and (iii) compare the proportions x_{exp} and x_{th} (using a statistical test) to see if they are significantly different or not. Note that the “randomness” test is here focused on the monomer proportion, which should correspond to what is expected from the particle density and cluster size. For samples with a significant proportion of trimers, it is also possible to check the agreement between theory and experimentally observed proportions, independent from the particle size and density. Indeed, let us emphasize that in the framework of a random cluster deposition all multimer proportions can be expressed as a function of the monomer proportion only.

This last point is of special interest because it is possible that the monomer proportion differs from the expected value (knowing the particle density and cluster size) while the multimer proportions are consistent with random deposition (and a given x_1): This can happen in the case of a limited diffusion of clusters on the surface, which would result in an extended capture area, larger than $\pi\bar{D}^2$. In such a case,

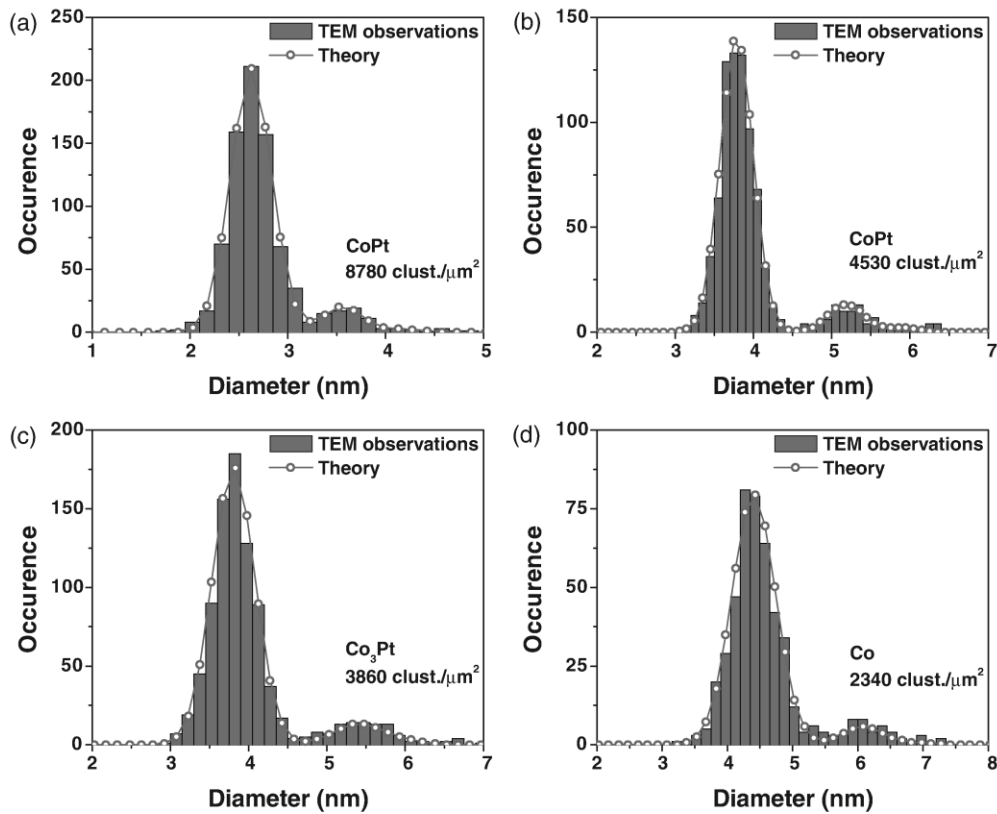


FIG. 6. (Color online) Experimental and theoretical size histograms for various samples of mass-selected nanoparticles deposited on amorphous carbon. The cluster nature and incident density are indicated on each graphic.

an equivalent *capture radius* may be inferred from x_{exp} [through the determination of η_{exp} such that $x_1(\eta_{\text{exp}}) = x_{\text{exp}}$] and subsequently compared to the cluster diameter. This approach could give valuable information on cluster diffusion on a surface. Nevertheless, the diffusion of particles on the substrate can also lead to morphologies differing strongly from those expected for a random deposition process [28], so that it is impossible to simply analyze the particle-size distribution in terms of extended capture radius. This is expected to happen when there are non-negligible interactions between the particles on the surface.

Finally, let us examine a few nanoparticle samples in order to illustrate the applicability of the presented theoretical framework. The samples have been prepared by mass-selected low-energy cluster beam deposition [6,9,26], where preformed clusters are deposited under ultra-high vacuum (UHV) conditions on a substrate (the amorphous carbon film of a TEM grid here), with an easily controlled size (Gaussian shape, with a relative size dispersion around 7%) and a fully adjustable incident cluster density. This density is usually kept low enough so that the particles remain well separated, thus ensuring that the physical properties (magnetic properties, for instance) are the signature of the individual particles. In Fig. 6, the experimental particle-size histograms are shown for various samples (different nature of the clusters, different size, and different cluster density), as obtained from TEM image analysis (the measured projected area of each cluster is converted to an equivalent diameter through the usual

spherical approximation). The theoretical multimer proportions (monomers, dimers, and trimers), calculated from the apparent particle density and monomer diameter [Eqs. (32)–(34)], are compared to the experimental measurements in Fig. 6. Let us emphasize that the population of each class of size (discrete data points that depend on the histogram binning) has been determined from the theoretical size distribution (continuous function): This is in no way a fit, just a direct comparison between the size histogram expected from theory, assuming a completely random deposition, and the experimental histogram. The density indicated in each graphics is the incident cluster density inferred from the final particle density. As can be seen, the analytical approximations derived in the present study are in excellent agreement with the experimental results for a variety of samples (that always remain diluted). This is consistent with a random cluster deposition scheme and indicates that, as expected, the particle diffusion is negligible on an amorphous carbon surface. Although this may seem trivial, note that Fig. 6(a) corresponds to a sample which has been annealed at $\simeq 750$ K for 2 h: It was not obvious at all that such a procedure would not degrade the particle random disposition and size distribution.

X. CONCLUSION

We have considered diluted assemblies of nanoparticles randomly deposited on a surface (2D samples). Even with a low cluster density, there exists a probability that two or more

clusters are close enough to form a dimer or more generally a multimer (or n mer), that is, a particle made of several incident clusters having coalesced (potentially partially). Therefore, a fraction of the particles in a sample does not correspond to the deposited nanoparticle size. Since these largest multimer particles can contribute in a non-negligible way to the overall properties of a sample, it is important to have a theoretical tool to assess the various multimer proportions.

Within a well-defined framework (low-density samples of nanoparticles having a narrow size distribution), we have mathematically expressed the probability for a cluster to form an n mer and the subsequent multimer proportion. Using the dimensionless parameter ϵ (or η), which appears to control entirely the structure of the nanoparticle sample, we have discussed the order of magnitude of each multimer proportion. From a Taylor expansion, in power series of either ϵ or η , we

have established simple analytical approximations that allow a reliable sample characterization. Expressions involving the monomer proportion as the control parameter have also been established, together with relations between the incident and the final particle density.

The applicability of the analysis developed in the present article has been demonstrated on a few samples of mass-selected nanoparticles. We think that the simple analytical results we have established can constitute a convenient tool for experimentalists in the design of their nanoparticle sample and the analysis of experimental measurements.

ACKNOWLEDGMENT

The author acknowledges A. Tamion for fruitful discussions.

-
- [1] J. Bansmann, S. H. Baker, C. Binns, J. A. Blackman, J.-P. Bucher, J. Dorantes-Dávila, V. Dupuis, L. Favre, D. Kechrakos, A. Kleibert, K.-H. Meiwes-Broer, G. M. Pastor, A. Perez, O. Toulemonde, K. N. Trohidou, J. Tuaille, and Y. Xie, *Surf. Sci. Rep.* **56**, 189 (2005).
- [2] C. Binns, K. N. Trohidou, J. Bansmann, S. H. Baker, J. A. Blackman, J.-P. Bucher, D. Kechrakos, A. Kleibert, S. Louch, K.-H. Meiwes-Broer, G. M. Pastor, A. Perez, and Y. Xie, *J. Phys. D: Appl. Phys.* **38**, R357 (2005).
- [3] A. N. Dobrynin, D. N. Ievlev, C. Hendrich, K. Temst, P. Lievens, U. Hörmann, J. Verbeeck, G. Van Tendeloo, and A. Vantomme, *Phys. Rev. B* **73**, 245416 (2006).
- [4] A. Kleibert, J. Passig, K.-H. Meiwes-Broer, M. Getzlaff, and J. Bansmann, *J. Appl. Phys.* **101**, 114318 (2007).
- [5] K. Wegner, P. Piseri, H. Vahedi Tafreshi, and P. Milani, *J. Phys. D: Appl. Phys.* **39**, R439 (2006).
- [6] D. Tainoff, L. Bardotti, F. Tournus, G. Guiraud, O. Boisron, and P. Mélinon, *J. Phys. Chem. C* **112**, 6842 (2008).
- [7] F. Tournus, A. Tamion, N. Blanc, A. Hannour, L. Bardotti, B. Prével, P. Ohresser, E. Bonet, T. Epicier, and V. Dupuis, *Phys. Rev. B* **77**, 144411 (2008).
- [8] K. Fauth, G. E. Ballentine, C. Praetorius, A. Kleibert, N. Wilken, A. Voitkans, and K.-H. Meiwes-Broer, *Phys. Status Solidi B* **247**, 1170 (2010).
- [9] A. Perez, P. Mélinon, V. Dupuis, L. Bardotti, B. Masenelli, F. Tournus, B. Prével, J. Tuaille-Combes, E. Bernstein, A. Tamion, N. Blanc, D. Tainoff, O. Boisron, G. Guiraud, M. Broyer, M. Pellarin, N. Del Fatti, F. Vallée, E. Cottancin, J. Lermé, J. L. Vialle, C. Bonnet, P. Maioli, A. Crut, C. Clavier, J. L. Rousset, and F. Morfin, *Int. J. Nanotech.* **7**, 523 (2010).
- [10] A. Tamion, C. Raufast, M. Hillenkamp, E. Bonet, J. Jouanguy, B. Canut, E. Bernstein, O. Boisron, W. Wernsdorfer, and V. Dupuis, *Phys. Rev. B* **81**, 144403 (2010).
- [11] F. Tournus, N. Blanc, A. Tamion, M. Hillenkamp, and V. Dupuis, *Phys. Rev. B* **81**, 220405(R) (2010).
- [12] F. Tournus, A. Tamion, N. Blanc, A. Hillion, and V. Dupuis, *J. Appl. Phys.* **109**, 07B502 (2011).
- [13] F. Tournus, *J. Nanopart. Res.* (in press).
- [14] E. L. Hinrichsen, J. Feder, and T. Jøssang, *J. Stat. Phys.* **44**, 793 (1986).
- [15] P. Schaaf and J. Talbot, *J. Chem. Phys.* **91**, 4401 (1989).
- [16] P. Schaaf and J. Talbot, *Phys. Rev. Lett.* **62**, 175 (1989).
- [17] S. Torquato, B. Lu, and J. Rubinstein, *Phys. Rev. A* **41**, 2059 (1990).
- [18] J. W. Evans, *Rev. Mod. Phys.* **65**, 1281 (1993).
- [19] S. Torquato, *Phys. Rev. E* **51**, 3170 (1995).
- [20] S. Torquato, *Phys. Rev. Lett.* **74**, 2156 (1995).
- [21] J. W. Leggoe and J. B. Riggs, *Mater. Sci. Eng. A* **426**, 289 (2006).
- [22] M. D. Rintoul, S. Torquato, and G. Tarjus, *Phys. Rev. E* **53**, 450 (1996).
- [23] A. Tewari and A. M. Gokhale, *Mater. Sci. Eng. A* **385**, 332 (2004).
- [24] A. Tewari and A. M. Gokhale, *Mater. Sci. Eng. A* **396**, 22 (2005).
- [25] A. Tewari and A. M. Gokhale, *Acta Mater.* **54**, 1957 (2006).
- [26] R. Alayan, L. Arnaud, A. Bourgey, M. Broyer, E. Cottancin, J. R. Huntzinger, J. Lermé, J. L. Vialle, M. Pellarin, and G. Guiraud, *Rev. Sci. Instrum.* **75**, 2461 (2004).
- [27] A simple homemade FORTRAN code is used, where the position of each incident cluster is randomly chosen in a 2D square box. Particles are assumed to be disks of the same diameter D . The proportion of multimers is then determined from the computed interparticle distances that allow to identify particles in contact with each other. No coalescence is taken into account, as in the model used to derive analytical expressions. Different ϵ values are considered by varying the cluster diameter D while keeping the cell side equal to $1 \mu\text{m}$ and the number of incident clusters equal to 5000. Moreover, the results are deduced from 100 successive numerical experiments. These conditions have been chosen to ensure good convergence.
- [28] P. Jensen, *Rev. Mod. Phys.* **71**, 1695 (1999).

Ces diverses considérations théoriques ont permis de valider, une fois pour toutes, l'aspect aléatoire du dépôt d'agrégats et sont aussi d'un intérêt appliqué direct puisqu'elles ont été intégrées dans une « boîte à outil » permettant de bien contrôler les paramètres géométriques importants lors de la fabrication d'un échantillon de nanoparticules.

Le modèle de dépôt aléatoire, vérifié pour des agrégats déposés sur carbone amorphe, n'est parfois pas du tout vérifié si les particules diffusent sur la surface. Des comportements très intéressants ont ainsi été observés sur graphite HOPG (et sont bien connus grâce aux travaux de mon collègue L. Bardotti). Le platine, qui avait été choisi comme système « test » pour des premières études avec le dispositif de tri en masse des agrégats, se comporte de manière tout à fait particulière. En effet, lorsque des agrégats triés en masse sont déposés sur un substrat de HOPG où ils peuvent facilement diffuser, on observe la formation d'amas présentant un ordre hexagonal assez prononcé, où les agrégats voisins ne se touchent pas. Ce résultat surprenant, qui avait été observé par l'équipe de M. Pellarin (ex-LASIM), dans des conditions de vide secondaire, est inchangé lorsque le dépôt se fait en ultra-vide sur un substrat bien préparé.

Afin de bien comprendre l'effet des différents paramètres (la charge, le flux, le substrat, les conditions de vide) sur la morphologie des dépôts, nous avons mené une étude plus systématique des dépôts d'agrégats de platine dans différentes conditions. Le platine pouvant être un cas pathologique, nous avons également déposé des agrégats d'or triés en masse, dont la morphologie des dépôts est bien connue dans le cas d'agrégats neutres non triés, afin de voir l'effet de la nature de l'élément [Tainoff2008]. La morphologie des dépôts obtenus avec des agrégats d'or est complètement différente de celle observée dans le cas du platine : les agrégats diffusent sur le substrat et coalescent pour former des amas ramifiés. À l'aide d'un dépôt successif d'or puis de platine, tous les deux triés en masse, et déposés dans les mêmes conditions, nous avons pu montrer que le platine avait bel et bien un comportement particulier (cf. Figure 4). Celui-ci se manifeste également dans le cas d'agrégats de platine neutres, non triés en taille.

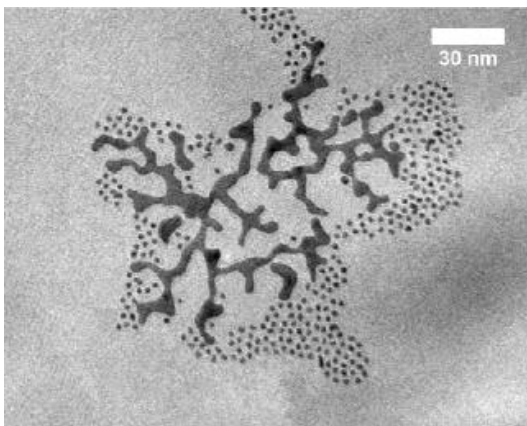


Fig. 4 : Morphologie observée par MET pour un dépôt successif d'agrégats d'or et de platine triés en taille. Les agrégats d'or ont partiellement coalescé pour former des amas ramifiés tandis que les agrégats de platine ne se touchent pas et s'auto-organisent. Figure tirée de [Tainoff2008].

La comparaison entre le cas de l'or et du platine a ensuite été poussée plus loin, en étudiant l'effet de la pression dans l'enceinte lors du dépôt d'agrégats ainsi que l'effet de la taille des particules déposées [Bardotti2011]. Nous sommes alors arrivés à la conclusion claire qu'il s'agissait d'un effet de surface (dépendance en pression et en taille) et certainement d'une réactivité particulière du Pt vis-à-vis de CO présent sous forme de traces lors du dépôt (même sous UHV). Cette étude est détaillée dans la publication « **Mass-selected clusters deposited on graphite: Spontaneous organization controlled by cluster surface reaction** » reproduite ci-dessous [Bardotti2011].

Mass-selected clusters deposited on graphite: Spontaneous organization controlled by cluster surface reaction

L. Bardotti,^{1,2,*} F. Tournus,^{1,2} P. Mélinon,^{1,2} M. Pellarin,^{1,3} and M. Broyer^{1,3}

¹Université de Lyon, F-69000, France

²Laboratoire PMCN, CNRS UMR 5586, Université Lyon 1, F-69622 Villeurbanne Cedex, France

³LASIM, CNRS UMR 5579, Université Lyon 1, F-69622 Villeurbanne Cedex, France

(Received 26 March 2010; revised manuscript received 6 December 2010; published 24 January 2011)

The formation of thin films by deposition of size-selected platinum and gold clusters on graphite surfaces is analyzed. By precise adjustments of the environment of the clusters, their size, and their nature, the cluster reactivity is evidenced as a parameter to control thin-film morphologies. Thus, by adjusting the kinetics of species adsorption (likely CO) on the cluster surface, one can avoid coalescence between neighboring clusters on the substrate and induce a local spontaneous organization of size-selected clusters.

DOI: 10.1103/PhysRevB.83.035425

PACS number(s): 61.46.-w, 36.40.-c, 81.16.Rf, 81.16.Dn

I. INTRODUCTION

Nanoparticle-based thin films are extremely promising for future applications in the fields of magnetism, catalysis, electronics, etc.¹⁻³ Since the properties of these films are closely related to their morphologies (i.e., size, shape, structure, and density of the supported particles), extensive studies have been performed in past decades to get a better understanding of thin-film formation and more specifically of the behavior of nanoparticles on surfaces.⁴ The main objective of most of these studies was to extract the relevant experimental parameters and their impact in order to control the final morphologies of thin films, however they are synthesized (i.e., atomic or cluster deposition). In the specific case of preformed cluster deposition, the ability of clusters to diffuse on various substrates has been evidenced and quantified,⁵ and the impact of this diffusion on the resulting thin-film morphologies has been analyzed.⁶

These studies have pointed out that the nucleation and growth processes occurring during the soft landing of clusters on surfaces are usually quite similar to those taking place during atomic deposition (note, however, a large difference corresponding to the fact that, contrary to atoms, two incoming clusters can coalesce on the surface).⁷ Thus, in most cases, incident clusters can be viewed as “superatoms” (i.e., their internal structure can be neglected), and consequently most of the theoretical approaches (kinetic rate equations⁸ or Monte Carlo simulations) developed for molecular-beam deposition have been successfully extrapolated for cluster deposition.⁹

It is now well established that a submonolayer deposition of clusters on a surface leads to islands of clusters, the density of which (N_{isl}) mainly originates from the competition between two time scales: the time needed for a cluster to diffuse on the surface (related to the deposition temperature and the substrate nature) and the time between two successive arrivals of clusters on the surface (related directly to the incident flux). As a consequence, for a given system (nanoparticles and substrate) the incident cluster flux and/or the substrate temperature have proven to be powerful parameters for precise control of the thin-film morphology (i.e., density of isolated clusters or islands of clusters and shape of these islands).¹⁰ Up to now, these results have even been used to organize nanoparticles on specific surfaces (i.e., reconstructed, vicinal, or artificially

structured surfaces) by physical methods (molecular-beam deposition or cluster deposition).¹¹⁻¹⁴

In another field of research, the catalytic properties of supported nanoparticles have been the subject of extensive investigations. As a matter of fact, a vast number of technological applications involving catalytic and electrocatalytic processes utilize metal nanoparticles dispersed on appropriate supports. In this domain, one of the most striking examples is the high reactivity of oxide-supported Au nanoparticles in CO oxidation, while extended Au surfaces exhibit relative inertness for this reaction.¹⁵⁻¹⁷ Another example is reported by Meier *et al.*¹⁸ They observed that the reactivity of a single Pd nanoparticle is increased by two orders of magnitude while its size changes from 200 to 6 nm. The reason for such a nanoscale approach is that with a given amount of materials a practical catalyst should provide a surface area as large as possible. However, as the size of a catalyst becomes smaller, its catalytic behavior normally alters. Despite considerable theoretical and experimental interest, it is still not fully understood how the size of a metal particle influences its reactivity. However, a general consensus on the particle's size effect would be that variation in specific activity comes from two factors: geometrical and electronic.^{19,20} Specifically, as the size of a catalytic crystallite varies, the structural factor is affected by changes in the coordination numbers of atoms and relative population of facets.²¹ In addition, the electronic factor involves modification of the work function or surface dipole of a metal catalyst surface, depending upon particle size.^{22,23}

However, in spite of a huge amount of research activity in both domains (nucleation and growth and nanoparticle reactivity), the resulting knowledge has up to now rarely been associated in a unique study (note, however, the work of Bréchnac *et al.*,²⁴ Layson and Thiel,²⁵ and Alayan *et al.*²⁶ related to the oxidation effect of indium or silver clusters on the coalescence processes). The main goal of the present work is to determine whether by adjusting the nature, the size, and the environment of the nanoparticles (and thus the kinetics of the cluster-surface reaction) one can control the resulting thin-film morphologies. In this paper we will first show that the behaviors of gold and platinum clusters on graphite are completely different and that the most relevant way to understand the resulting morphologies is to take into

account the cluster reactivity. Then, by adjusting the size and the environment of the clusters during deposition, we will show that cluster reactivity appears as a parameter to tune the morphologies of nanoparticle-based thin films and can even lead to a local spontaneous organization of clusters on surfaces, as was already suspected in previous experimental studies.^{26,27}

We emphasize that since the objective here is not to quantify the diffusion of clusters on the surface, we will not focus on the arrangement of islands of clusters on the surface (island density considerations, for instance) but rather on their specific internal morphologies.

II. EXPERIMENTAL PROCEDURE

For the purpose of this study, a laser cluster source that allows the synthesis and deposition of clusters without fragmentation upon the surface with tunable size and chemical nature in various environments is particularly well adapted.²⁸ Clusters are then produced in a laser vaporization–gas condensation source.²⁹ Briefly, a plasma created by the impact of a Nd:YAG (yttrium aluminum garnet) laser beam focused on a metallic rod is thermalized by injection of a continuous flow of helium at low pressure (typically 30 mbar), inducing cluster growth. Clusters are subsequently stabilized and cooled down in a supersonic expansion taking place at the exit nozzle of the source. A low-energy cluster beam is then obtained, with clusters of different sizes, mostly neutral but also ionized, allowing the growth of thin cluster films on a substrate. Moreover, the low kinetic energy of clusters (typically 0.1 eV/atom) gained during supersonic expansion ensures the absence of fragmentation upon impact on the substrate (see Ref. 30 for more details). In order to lower the spread of the cluster size distribution, a mass-selection device (electrostatic quadrupole deviator), fully described elsewhere,³¹ has been used here. With this size selection, the relative cluster size dispersion is lower than 10% and is adjustable with the voltage applied on the deviator. The flux of the selected ionized clusters (F) is then measured by a picoamperemeter connected to a Faraday cup. In the following, all experiments are performed at room temperature (RT) and in different pressure conditions (varying from $P_{\text{dep}} = 10^{-5}$ to 4×10^{-10} Torr). Note that samples are observed with transmission electron microscopy (TEM) after exposure to air. However, we have checked with

in situ ultrahigh-vacuum (UHV) scanning tunneling microscope observations that transfer to air has no impact on sample morphologies, which are, in addition, extremely stable for months. Due to their extremely different reactivities, gold and platinum clusters have been chosen as reference clusters in this study.

III. EXPERIMENTAL RESULTS

A. Pure platinum and gold clusters deposited in UHV

In previous studies, we have evidenced that gold and platinum incident clusters (with diameter $d_m = 2.2$ nm) have drastically different behaviors when deposited in UHV on highly oriented pyrolytic graphite (HOPG) surfaces.^{26,32} More specifically, in the case of gold clusters [Fig. 1(a)], ramified islands resulting from an aggregation with partial coalescence of incident clusters are formed on the surface. As already mentioned in the Introduction, such morphologies are completely predicted by Monte Carlo simulation, and the island morphologies where arms result from the coalescence of about 20 to 100 incident clusters can be understood according to the melting temperature of the gold clusters.³³ In the platinum cluster case [Fig. 1(b)], films are composed of “bunches” of clusters, which reveals the ability of clusters to diffuse on this surface. More surprising are the island morphologies. As a matter of fact, looking carefully at a typical individual island [Fig. 1(b)], one can observe that it is composed of an aggregation of 2.2-nm incident clusters without contact, and, even more surprising, a local spontaneous order between nanoparticles can be detected. Analyses performed mainly with TEM have evidenced, in this case, that the mean characteristic distance between the centers of mass of two adjacent clusters is $\bar{d}_{\text{center}} = 3.4$ nm. Note that the distance distribution between the edges of neighboring clusters is then centered on $\bar{d}_{\text{edge}} = 1.2$ nm. Complementary studies have revealed that this spontaneous hexagonal order without contact is related neither to the charge of the incoming clusters nor to the local surface specificities (arrays of point defects and moiré of HOPG).³² It should rather originate from a local surface deformation or from cluster surface effects. Moreover, recent grazing-incidence small-angle x-ray scattering (GISAXS) experiments have been performed at the European Synchrotron Radiation Facility (ESRF) (Collaboration Research Group D2AM BM2 beamline). As can be seen in Fig. 1(c), a lateral correlation peak is

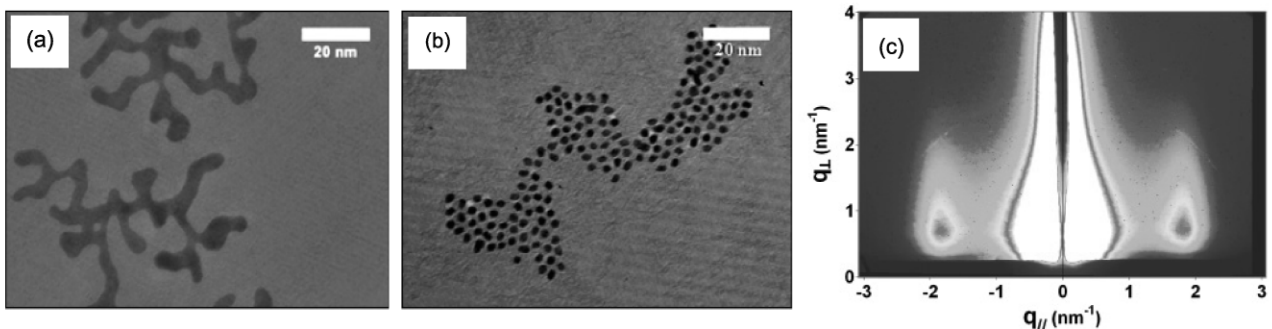


FIG. 1. (Color online) TEM images of size-selected clusters ($d_m = 2.2$ nm) deposited on graphite: gold clusters (a) and platinum clusters (b). (c) GISAXS measurements in the case of platinum clusters. In both cases $P_{\text{dep}} = 4 \times 10^{-10}$ Torr.

observed at $q_{\parallel} = 1.8 \text{ nm}^{-1}$; this evidences the existence of a mean characteristic distance between noncontacting clusters (\bar{d}_{center}). We find a value of $\bar{d}_{\text{center}} = 3.5 \text{ nm}$, which confirms TEM measurements and shows that this local order expands all over the surface. However, these studies have been performed on a single cluster size (i.e., $d_m = 2.2 \text{ nm}$) and are not able to identify clearly either the mechanism leading to this spontaneous organization or the characteristic relevant distance (i.e., \bar{d}_{edge} or \bar{d}_{center}).

Dealing with this last point, depending on the properties of the element, a transition from spherical to strongly ramified shapes when the particle size increases has been recently observed during the cluster formation in the laser vaporization source.³⁴ In the specific case of platinum, it has been shown that such a transition from compact to ramified clusters appears beyond a critical diameter (d_{critical}) of about 2.5 nm. For large clusters, these particular shapes, far from spherical ones, offer the opportunity to extract the relevant distance characterizing the mechanism in our study. Indeed, the shape distribution will result in a broadening of either the d_{center} or d_{edge} distribution, depending on which type of distance is imposed by the physical mechanism: for instance, if there exists a preferred d_{edge} distance, the d_{center} dispersion will be larger than that for d_{edge} . Thus, we have deposited platinum clusters of larger size (i.e., $d_m = 3.2$ and 5.1 nm in the spherical approximation) on graphite and extracted in each case from image analysis the distance distributions between center of mass (d_{center}) and edges (d_{edge}).

In Fig. 2, one can see that for 4.3-nm deposited clusters a local organization is observed. In this case, the first-neighbor interparticle distance distributions and particularly their dispersion clearly show that the characteristic distance is d_{edge} rather than d_{center} . Note that $\bar{d}_{\text{edge}} \simeq 1.2 \text{ nm}$ obtained for 4.3-nm clusters is the same as for all platinum cases investigated (i.e., 2.2 and 5.1 nm). Coming back now to the physical origin of this self-organization without contact between clusters on graphite, among those proposed earlier, a cluster surface effect (intimately related to reactivity) appears the most probable, but a local deformation of the substrate at the particle periphery could still not be excluded.

B. Environmental effect

In the case of a cluster surface effect (i.e., a surface molecular coating), one can expect that the environment of the clusters during diffusion could be a way to control their self-organization. To verify this statement, size-selected clusters (gold and platinum) have been deposited in different environments (i.e., different deposition base pressures P_{dep}).

Figure 3 reveals that, as expected for a cluster surface effect, the number of contact events between gold clusters depends strongly on the base pressure in the deposition chamber. Thus, in the case of UHV deposition, all the clusters are trapped by islands during the growth process, and after contact a partial coalescence takes place (leading to large ramified islands composed of a single particle), while in the case of higher base pressure, the situation evolves slowly toward an absence of contact between particles composing the island and then toward a lower degree of n -mers (i.e., particles resulting from contact with or without coalescence of n incident clusters).

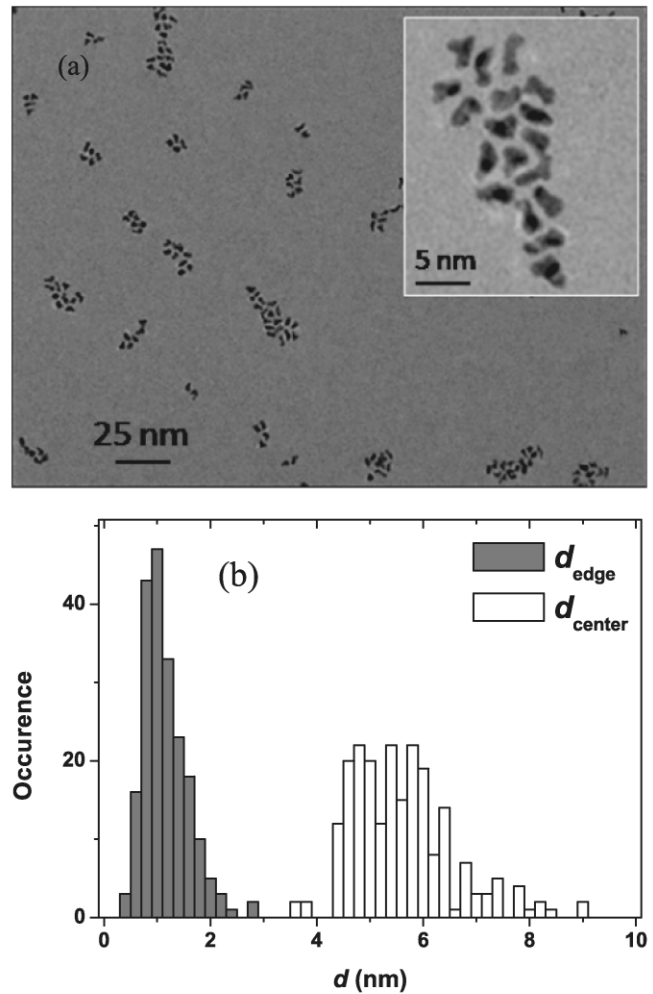


FIG. 2. (a) Typical island morphologies, observed by TEM, resulting from the deposition of size-selected platinum clusters of $d_m = 4.3 \text{ nm}$ with $P_{\text{dep}} = 4 \times 10^{-10} \text{ Torr}$. (b) Corresponding nearest-neighbor distance distributions.

In contrast to the platinum case, where the mean value of n is $\bar{n} = 1$ for all P_{dep} investigated here (Fig. 4), for gold, the mean size of the supported particles does not correspond to the incident cluster size ($\bar{n} > 1$). This shows that, even with the lowest P_{dep} used here, some coalescence events always occur between gold clusters ($\bar{n} \simeq 3$). This last statement explains the poor cluster organization observed in the case of gold even if \bar{d}_{edge} is exactly the same as in the platinum case (i.e., $\bar{d}_{\text{edge}} \simeq 1.2 \text{ nm}$). A higher pressure will certainly lead to morphologies and a degree of organization comparable to those in the platinum case (work is in progress on this point). On the other hand, according to the higher reactivity of platinum compared to gold (especially to CO), a pressure far below 10^{-10} Torr is certainly required to allow a complete contact between supported Pt clusters composing islands and thus to get morphologies similar to those for gold [Fig. 3(a)]. We emphasize first that these results confirm a mechanism based on a cluster surface reaction, so we discard the idea of a local graphite deformation and second that \bar{d}_{edge} is “universal,” whatever the P_{dep} , size, shape, and even nature of the clusters.

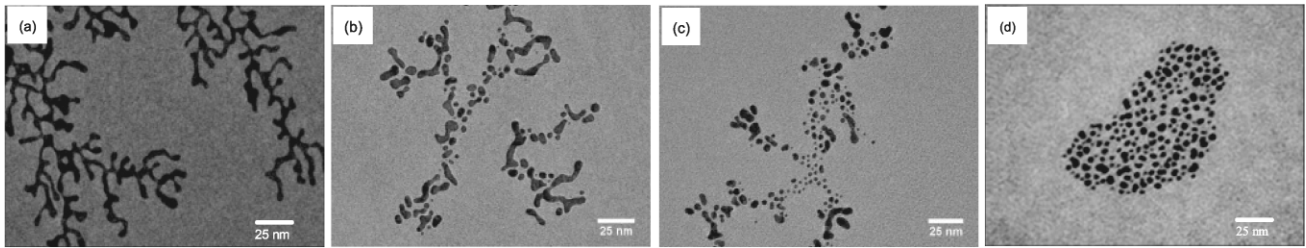


FIG. 3. Effect of the pressure (P_{dep}) during the deposition of the size-selected gold clusters (2 nm in diameter) on island morphologies. (a) $P_{\text{dep}} = 4 \times 10^{-10}$ Torr; (b) $P_{\text{dep}} = 2 \times 10^{-9}$ Torr; (c) $P_{\text{dep}} = 10^{-7}$ Torr; (d) $P_{\text{dep}} = 10^{-6}$ Torr. Note that since the self-organization of platinum clusters is already observed in UHV, in contrast to the gold case, gold clusters have been chosen here for illustration in order to get the largest effect possible.

Since in our experimental device the time of free cluster flight³¹ (approximately 3×10^{-3} s with a cluster velocity around 600 ms^{-1} and a traveling distance $\simeq 2$ m) is comparable to the time of residence of the incident clusters on the surface before nucleation and/or capture (typically 10^{-4} s),⁹ one could envisage that the surface reaction occurs before deposition. However, the pressure modifications in the above experiments have been performed exclusively in the deposition chamber (without modification in other parts of the experimental setup). Moreover, time-of-flight spectrometry measurements do not reveal any impurities on the clusters. As a consequence, one can conclude that surface adsorption only occurs on the substrate rather than during the free flight between the cluster production and their deposition. This information confirms the fundamental role of the metal or support in the cluster reactivity.³⁵

C. Cluster size effect

Pronounced size effects in the reactivity behavior of nanoparticles have been evidenced in the literature. They are usually attributed to changes in the atom coordination number in different geometric structures and/or changes in the electronic structure as a function of the cluster size.¹⁶ As a consequence, in our systems where island morphologies are suspected to be driven by surface reactions, the incident

cluster size should be another tool (with P_{dep}) to control cluster organization on the surface. In order to check this point, thin films of platinum and gold clusters of different sizes (i.e., 2.2, 4.3, and 5.1 nm) have been produced. To get rid of the environment effect, the following discussion will use a fixed P_{dep} for a given element. However, according to the different behaviors of gold and platinum, P_{dep} has been chosen in each case to provide the most pronounced effect (i.e., $P_{\text{dep}} = 4 \times 10^{-10}$ Torr for platinum, and $P_{\text{dep}} = 10^{-7}$ Torr for gold).

In the case of gold, Figs. 5(d)–5(f) and 6 reveal that \bar{n} increases with the incident cluster size and that, for $d_m = 5.1$ nm, the resulting islands, still ramified, are then composed of a large single particle ($\bar{n} \gg 1$). Note that in this latest case the resulting island morphology is extremely similar to the one obtained for smaller particles but deposited under higher vacuum [Fig. 3(a)]. In the platinum case [Figs. 5(a)–5(c)], for the largest cluster case, even if \bar{d}_{edge} remains constant (i.e., $\bar{d}_{\text{edge}} \simeq 1.2$ nm), no more organization of the cluster is visible, and the size of the incoming cluster is no longer preserved on the surface (Fig. 6). This observation suggests that the number of n -mer formation events strongly depends on the incident cluster size. As a consequence, one can imagine that for even larger cluster sizes, morphologies close to those of gold could be obtained.

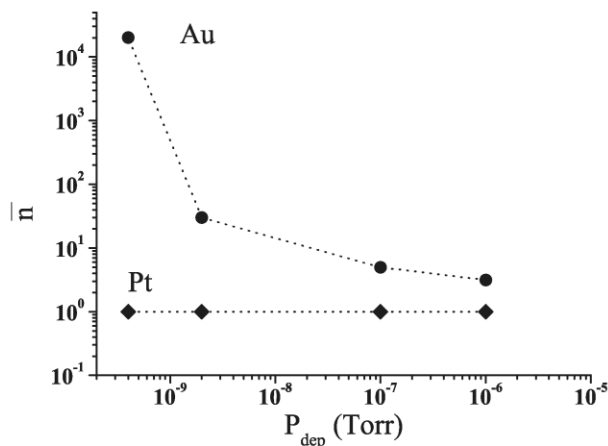


FIG. 4. Evolution of the mean n -mer size \bar{n} with the deposition pressure for 2.2-nm clusters of gold (circles) and platinum (diamonds). Dashed lines are only guides for eyes.

IV. DISCUSSION

Above a critical size (d_c) and for a fixed pressure, a contact can occur between clusters, leading to n -mer formation and thus to a progressive loss of the incident cluster size ($\bar{n} \neq 1$). The same results are obtained for a fixed size but below a critical pressure (P_c). These two parameters thus have antagonistic effects. The mean value \bar{n} (from 1 to infinity) will then depend on the degree to which experimental parameters are far from critical ones. These statements are valid for both gold and platinum clusters, but in different ranges of size and pressure, which we attribute to the extremely different reactivities of gold and platinum. As a consequence, an adsorption of species on the surface of diffusing clusters that can prevent their contact (i.e., n -mer formation) and thus their coalescence appears the most probable phenomenon to explain all our observations.

Unfortunately, the characteristic identification of such species is extremely delicate to implement. Note that, even

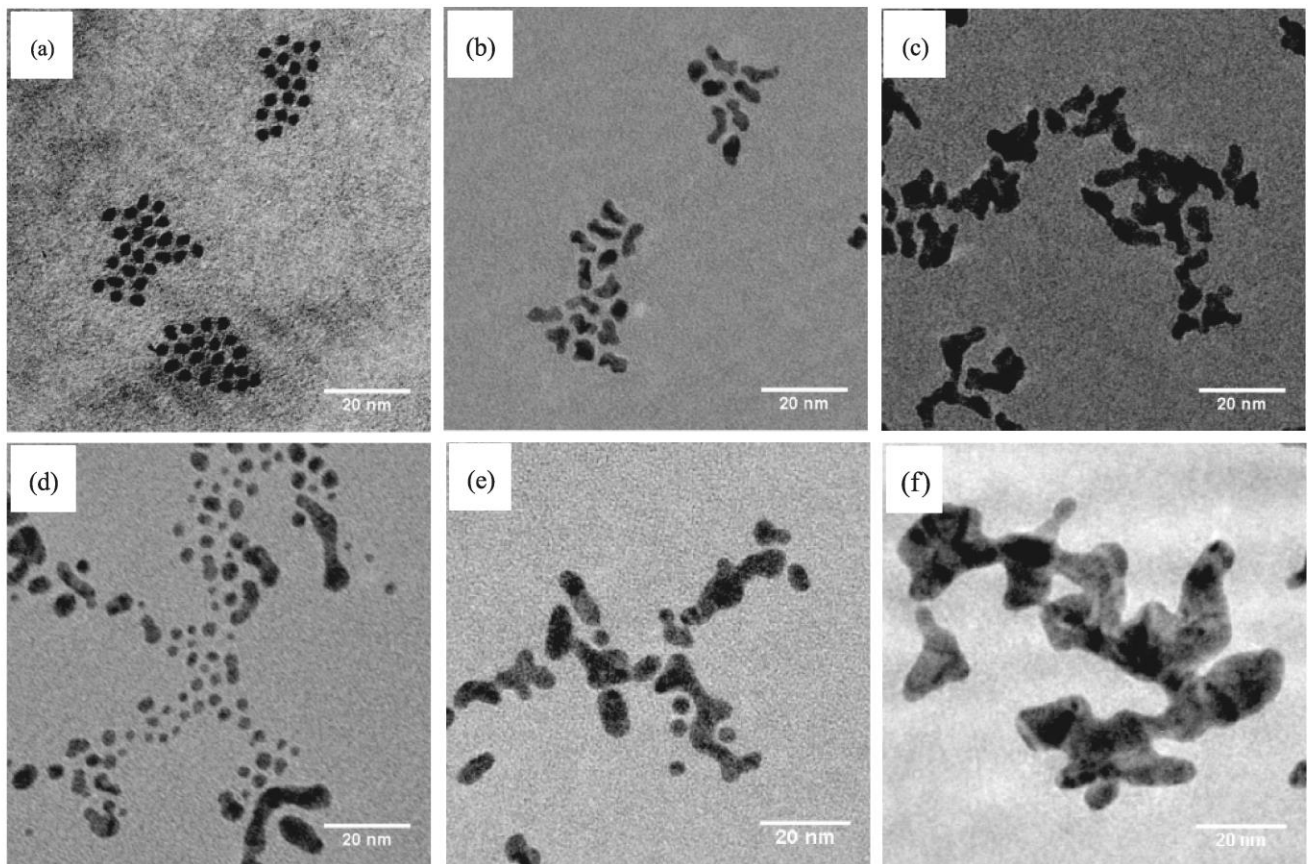


FIG. 5. Typical TEM morphologies of thin films obtained by deposition of platinum clusters, with $P_{\text{dep}} = 4 \times 10^{-10}$ Torr: (a) $d_m = 2.2$ nm; (b) $d_m = 4.3$ nm; (c) $d_m = 5.1$ nm; and gold clusters, with $P_{\text{dep}} = 10^{-7}$ Torr: (d) $d_m = 2.2$ nm; (e) $d_m = 4.3$ nm; and (f) $d_m = 5.1$ nm.

in high-resolution mode, such species have not been detected by TEM observations. This does not exclude their presence but confirms their small weight. However, according to the well-known extreme reactivity of platinum surfaces to carbon monoxide [the reaction of a Pt atom with CO leads to a significant stabilization of 2.52 eV without energy barrier on Pt(111) surfaces],³⁶ CO adsorption on a platinum cluster surface appears the most likely effect here. Additionally, Longwitz *et al.* have shown that the adsorption of CO is not limited by a pressure offset and can take place for CO partial pressure lower than 10^{-9} Torr.³⁷ This can explain the absence of contact between particles even in UHV conditions. Still dealing with a CO surface adsorption, we emphasize that in a Pt-CO system, the CO molecule stands perpendicular to the surface, with $d_{\text{Pt-C}} = 0.175$ nm and $d_{\text{C-O}} = 0.115$ nm for a $1\Sigma^+$ ground state.³⁸ Consequently, the “thickness” of an adsorbed CO layer (0.29 nm) is significantly lower than the half separation between clusters observed in our case ($d_{\text{edge}}/2 = 0.6$ nm), and the adsorption of CO multilayers on a Pt surface is impossible.^{37,39} However, the steric repulsion between the oxygen atoms of two CO molecules facing each other has to be taken into account: in the case of a free linear CO dimer it is around 0.35 nm.⁴⁰ As shown schematically in Fig. 7, a 1.2-nm interparticle distance would correspond to a 0.62-nm separation between the oxygen atoms. This indicates that a basic steric repulsion between clusters cannot explain our experimental observations. Since in this system the σ donation

is larger than the π back donation and induces a total charge of CO,⁴¹ such a charge transfer can be involved in the repulsion between neighboring clusters and might explain the greater O-O separation than that expected from a pure steric repulsion. Note that a similar reasoning must be valid for the case of gold clusters.

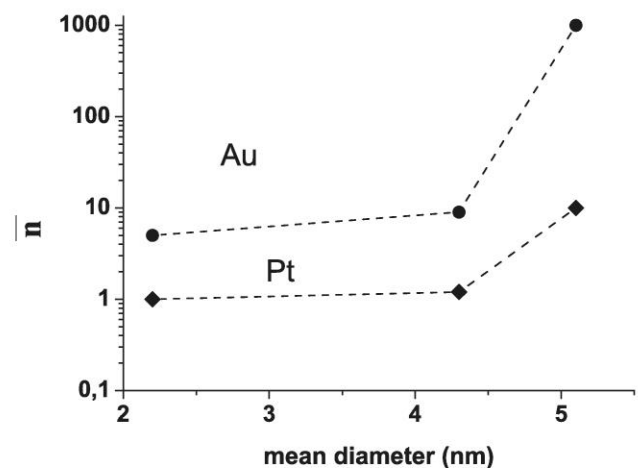


FIG. 6. Evolution of the mean n -mer size \bar{n} with the incident cluster size for gold (circles) and platinum (diamonds). Dashed lines are only guides for eyes.

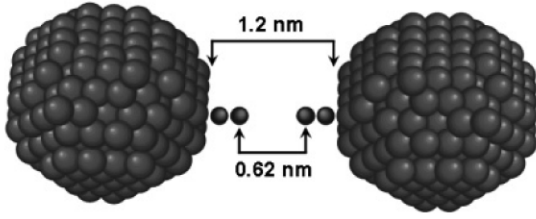


FIG. 7. (Color online) Schematic illustration of two neighboring Pt clusters, showing the experimentally observed mean edge-to-edge distance ($\simeq 1.2$ nm) and the corresponding O-O separation for two adsorbed CO molecules facing each other.

Even if we still do not know precisely the nature of the species adsorbed on the cluster, a possible mechanism can be given concerning the behavior of clusters on the surface. Up to now, most of the thin-film morphologies obtained by cluster deposition have been explained by the competition between several time scales:

(i) τ_{dep} : the time between two successive arrivals of clusters on the surface, which is related to the experimental cluster flux (F) by $\tau_{\text{dep}} \simeq 1/F$;

(ii) τ_{diff} : the time for the clusters to diffuse by one diameter (d), which is related to the diffusion coefficient of the clusters (D) and thus to the deposition temperature (T_{dep}) and the cluster size by $\tau_{\text{diff}} \simeq d^2/D$; and

(iii) τ_{col} : the time of coalescence between two contacting clusters, which is related to the cluster-cluster interaction and thus to the nature and the size of the cluster.

Note that other characteristic time scales, more specific to atomic deposition, can be neglected here: the time of atomic diffusion along island edges and the time of residence of atoms on the surface before evaporation.

More precisely, the final film is usually composed of a density of islands on the surface (N_{isl}) resulting from nucleation and growth processes. The characteristic distance between islands ($\ell_{\text{isl}} = N_{\text{isl}}^{-1/2}$) corresponds roughly to the mean free path of the diffusing cluster on the surface before nucleation and growth. Kinetic rate equations as well as simulations have evidenced that

$$\ell_{\text{isl}} \simeq \sqrt{D\tau_{\text{isl}}} \sim \left(\frac{D}{F}\right)^{\chi/2}, \quad (1)$$

and consequently,

$$\tau_{\text{isl}} \simeq \frac{\tau_{\text{dep}}^{\chi}}{\tau_{\text{diff}}^{\chi-1}}, \quad (2)$$

where τ_{isl} corresponds to the time of residence of an incident cluster on the surface before it meets another cluster or is captured by an already formed island, and χ is a parameter that depends on the atomic processes involved in the film growth (diffusion of monomers, n -mers, etc.).

Dealing now with the island morphology (compact versus ramified), it will depend on the ratio between the time between two successive arrivals of clusters on an island edge and the time needed for the coalescence process (complete or partial) between neighboring clusters. Thus, depending on the relative magnitude of these time scales, one can get different island densities and different island morphologies. Whereas an

analysis including these time scales is usually adequate to describe classical morphologies (islands composed of contacting particles or even isolated particles), it needs to be refined in the present case where islands are composed by aggregation of noncontacting particles. Thus, an additional time scale needs to be included: the time required for a cluster surface to be completely passivated by adsorption of molecules (τ_{pass}). Note that we will consider in the following that the passivation of the cluster will prevent the contact between particles and thus their coalescence. This time depends obviously on the nature of the clusters, on P_{dep} , and *a priori* on their size. In this case, the resulting island morphology will depend on the ratio between τ_{pass} and τ_{isl} . As a matter of fact, two extreme cases appear: If $\tau_{\text{pass}} \ll \tau_{\text{isl}}$, then all diffusing clusters are coated before nucleation processes, and islands are composed of size-selected noncontacting particles. Conversely, if $\tau_{\text{pass}} \gg \tau_{\text{isl}}$, then diffusing clusters remain “naked” until they meet another particle on the surface; thus contact between particles takes place, and depending on the magnitude of τ_{col} , one can get a ramified or a compact island. Let us analyze our experimental results in the framework of this schematic model.

In the case of fixed flux and deposition pressure and a variable size of incident clusters (Sec. III C), gold will be chosen for convenience in the following discussion because of extensive studies already performed on gold clusters on graphite.⁴² Gold cluster diffusion was found by Luedtke and Landman⁴³ to proceed via the stick-slip mechanism. Thus, from simple geometric arguments, it might be argued that their rate of diffusion should scale as $N^{2/3}$, where N is the number of atoms in the cluster, as has been observed by Deltour *et al.*⁴⁴ for Lennard-Jones clusters:

$$D_N \simeq D_1 N^{2/3}. \quad (3)$$

Then, combining Eqs. (1) and (3), one can find

$$\tau_{\text{isl}} \sim D_1 N^{\frac{2(\chi-1)}{3}}. \quad (4)$$

Since $0 < \chi < 1$ ($\chi \simeq 0.4$ here; see Jensen⁹), τ_{isl} increases with the cluster size. If we assume that τ_{pass} is size independent, this evolution will favor the formation of islands composed of noncontacting clusters for larger incident cluster size. However, this is in disagreement with our experimental observations (Sec. III C) and reveals the extreme importance of the size effect on the reactivity of these systems. Indeed, for fixed P_{dep} , our observations suggest, in agreement with previous studies, a very large decrease of τ_{pass} with incident cluster size.^{16,17} As a consequence, for a given deposition pressure, a critical size (d_c) of incident cluster for n -mer formation appears (for $P_{\text{dep}} = 4 \times 10^{-10}$ Torr, $d_c < 2$ nm for gold and $d_c > 4$ nm for platinum).

V. CONCLUSION

In conclusion, we have studied the morphologies of nanoparticle islands grown by deposition of size-selected Au and Pt clusters on HOPG. We have shown that the contact or absence of contact between neighboring particles is controlled by the base pressure and the cluster size. In the case of noncontacting particles, the edge-to-edge distance is always found to be around 1.2 nm. According to these observations, we attribute this original behavior to a reaction occurring on the

clusters' surfaces: above a critical pressure or a critical size the kinetics of this reaction is rapid enough to passivate the clusters before they meet some neighbors, implying the existence of a gap between particles on the surface. The striking contrast between the critical values of these two parameters reflects the extreme difference in reactivity between Pt and Au nanoparticles.

In addition to the usual parameters (particle flux and temperature, which determine the density of islands), the kinetic control of this surface reaction appears as a way to change the morphologies of nanoparticle-based thin films on graphite: it offers the extra opportunity to change the inner structure of cluster islands. We emphasize that avoiding particle coalescence allows for keeping the individuality of the incident size-selected clusters, while surface diffusion remains possible; these are the key ingredients for self-organization. The Pt clusters' self-organization, which has been evidenced before,^{26,27,32} can then be traced back to such a surface reaction and not to a substrate-mediated interparticle interaction. The substrate must, however, play a crucial role, through a modification of the cluster reactivity, since the surface reaction only occurs after cluster deposition (clusters in the beam are found to be free of any adsorbate, according to time-of-flight spectrometry).

Furthermore, we could certainly take advantage of the absence of contact between neighboring particles to drive a high-quality organization of clusters (better than the Poissonian limit) by deposition on template substrates with a regular array of "nucleation sites" (moiré of graphene epitaxially grown on metal, vicinal surfaces, etc.). In addition, Monte Carlo simulations of thin-film growth incorporating such a "passivation" by a surface reaction would help us to get a deeper understanding of the cluster islands' detailed geometry and to estimate a relevant value of τ_{pass} . Finally, mixing Au and Pt by synthesizing alloy nanoparticles of variable composition, which is an ongoing work, can present another way to tailor the reactivity and thus the morphologies obtained by cluster deposition.

ACKNOWLEDGMENTS

We are indebted to O. Boisron, C. Albin, G. Suteau (LPMCN), and C. Clavier (LASIM) for technical assistance on the cluster source and to A. Ramos, H. Tolentino (Institut Néel, Grenoble, France), J. P. Simon (Laboratoire de Cristallographie, Grenoble, France), and D. Babonneau (LMP, Poitiers, France) for support on GISAXS experiments (ESRF Grenoble, France, CRG D2AM BM2 beamline) and data analysis.

*laurent.bardotti@univ-lyon1.fr

¹A. O. Orlov, I. Amlani, G. H. Bernstein, C. S. Lent, and G. L. Snider, *Science* **277**, 928 (1997).

²S. Sun, C. B. Murray, D. Weller, L. Folsk, and A. Moser, *Science* **287**, 1989 (2000).

³R. P. Andres, T. Bein, M. Dorogi, S. Feng, J. I. Henderson, C. P. Kubiak, W. Mahoney, R. G. Osifchin, and R. Reifenberger, *Science* **272**, 1313 (1996).

⁴J. M. Wen, S. L. Chang, J. W. Burnett, J. W. Evans, and P. A. Thiel, *Phys. Rev. Lett.* **73**, 2591 (1994).

⁵L. Bardotti, P. Jensen, A. Hoareau, M. Treilleux, and B. Cabaud, *Phys. Rev. Lett.* **74**, 4694 (1995).

⁶C. Binns, *Surf. Sci. Rep.* **44**, 1 (2001).

⁷H. Brune, *Surf. Sci. Rep.* **31**, 125 (1998).

⁸S. Stoyonov and D. Kashiev, in *Current Topics in Material Science*, edited by E. Kaldis (North-Holland, Amsterdam, 1981).

⁹P. Jensen, *Rev. Mod. Phys.* **71**, 5 (1999).

¹⁰J. Villain, A. Pimpinelli, L. H. Tang, and D. E. Wolf, *J. Phys. I (France)* **2**, 2107 (1992).

¹¹H. Brune, M. Giovannini, K. Bromann, and K. Kern, *Nature (London)* **394**, 451 (1998).

¹²F. Leroy, J. Eymery, P. Gentile, and F. Fournel, *Appl. Phys. Lett.* **80**, 3078 (2002).

¹³V. Repain, G. Baudot, H. Ellmer, and S. Rousset, *Europhys. Lett.* **58**, 730 (2002).

¹⁴A. Hannour, L. Bardotti, B. Prével, E. Bernstein, P. Mélinon, A. Perez, J. Gierak, E. Bourhis, and D. Maily, *Surf. Sci.* **594**, 1 (2005).

¹⁵M. Haruta and S. Tsubota, *Catalysis and Electrocatalysis at Nanoparticle Surfaces* (Marcel Dekker, New York, 2003).

¹⁶U. Heiz, A. Sanchez, S. Abbet, and W. D. Schneider, *Eur. Phys. J. D* **9**, 35 (1999).

¹⁷Y. Chen, P. Crawford, and P. Hu, *Catal. Lett.* **119**, 21 (2007).

¹⁸J. Meier, K. A. Friedrich, and U. Stimming, *Faraday Discuss.* **121**, 365 (2002).

¹⁹N. M. Markovic, T. J. Schmidt, V. Stamenkovic, and P. N. Ross, *Fuel Cells* **2**, 105 (2001).

²⁰K. J. J. Mayrhofer, B. B. Blizanac, M. Arenz, V. R. Stamenkovic, P. N. Ross, and N. M. Markovic, *J. Phys. Chem. B* **109**, 14433 (2005).

²¹R. E. Benfield, *J. Chem. Soc., Faraday Trans.* **88**, 1107 (1992).

²²B. C. Han, C. R. Miranda, and G. Ceder, *Phys. Rev. B* **77**, 075410 (2008).

²³B. Hammer and J. K. Norskov, *Adv. Catal.* **45**, 71 (2000).

²⁴C. Bréchnignac, P. Cahuzac, F. Carlier, C. Colliex, J. Leroux, A. Masson, B. Yoon, and U. Landman, *Phys. Rev. Lett.* **88**, 196103 (2002).

²⁵A. R. Layson and P. A. Thiel, *Surf. Sci.* **472**, L151 (2001).

²⁶R. Alayan, L. Arnaud, M. Broyer, E. Cottancin, J. Lermé, S. Marhaba, J.-L. Vialle, and M. Pellarin, *Phys. Rev. B* **76**, 075424 (2007).

²⁷B. Rellinghaus, S. Stappert, M. Acet, and E. Wassermann, *Mat. Res. Soc.* **707**, 239 (2002).

²⁸A. Perez *et al.*, *Int. J. Nanotechnol.* **7**, 523 (2010).

²⁹P. Milani and W. A. deHeer, *Rev. Sci. Instrum.* **61**, 1835 (1990).

³⁰P. Mélinon, V. Paillard, V. Dupuis, A. Perez, P. Jensen, A. Hoareau, J. P. Perez, J. Tuaille, M. Broyer, J.-L. Vialle, M. Pellarin, B. Baguenard, and J. Lermé, *Int. J. Mod. Phys. B* **9**, 339 (1995).

³¹R. Alayan, L. Arnaud, A. Bourgey, M. Broyer, E. Cottancin, J. R. Huntzinger, J. Lermé, J.-L. Vialle, M. Pellarin, and G. Guiraud, *Rev. Sci. Instrum.* **75**, 2461 (2004).

³²D. Tainoff, L. Bardotti, F. Tournus, G. Guiraud, O. Boisron, and P. Mélinon, *J. Phys. Chem. C* **112**, 6842 (2008).

³³L. Bardotti, B. Prével, M. Treilleux, P. Mélinon, and A. Perez, *Appl. Surf. Sci.* **164**, 52 (2000).

- ³⁴R. Alayan, L. Arnaud, M. Broyer, E. Cottancin, J. Lermé, J.-L. Vialle, and M. Pellarin, *Phys. Rev. B* **73**, 125444 (2006).
- ³⁵Y. Zhou, T. Holme, J. Berry, T. R. Ohno, D. Ginley, and R. O'Hayre, *J. Phys. Chem. C* **114**, 506 (2010).
- ³⁶S. Roszak and K. Balasubramanian, *Chem. Phys. Lett.* **212**, 150 (1993).
- ³⁷S. R. Longwitz, J. Schnadt, E. Kruse Vestergaard, R. T. Vang, E. Lægsgaard, I. Stensgaard, H. Brune, and F. Besenbacher, *J. Phys. Chem. B* **108**, 14497 (2004).
- ³⁸J. Kua and W. A. Goddard, *J. Phys. Chem. B* **102**, 9481 (1998).
- ³⁹A. V. Myshlyavtsev and P. V. Stishenko, *Appl. Surf. Sci.* **276**, 5376 (2010).
- ⁴⁰L. M. Nxumalo, E. K. Ngidi, and T. A. Ford, *J. Mol. Struct.* **786**, 168 (2006).
- ⁴¹H. Nakatsuji, H. Morita, H. Nakai, Y. Murata, and K. Fukutani, *J. Chem. Phys.* **104**, 714 (1996).
- ⁴²L. J. Lewis, P. Jensen, N. Combe, and J.-L. Barrat, *Phys. Rev. B* **61**, 16084 (2000).
- ⁴³W. D. Luedtke and U. Landman, *Phys. Rev. Lett.* **82**, 3835 (1999).
- ⁴⁴P. Deltour, J.-L. Barrat, and P. Jensen, *Phys. Rev. Lett.* **78**, 4597 (1997).

Pour aller plus loin dans la compréhension des mécanismes mis en jeu, nous avons également étudié le cas d'agrégats d'alliages bimétalliques contenant différentes proportions de Pt, ce qui nous a permis de faire le lien entre la présence de platine et l'absence de contact entre particules voisines sur le substrat de graphite [Tournus2011c, Bardotti2012, Bardotti2014]. Il apparaît alors très intéressant d'étendre les possibilités d'auto-organisation à des particules bi-métalliques (AuPt, CoPt, FePt) d'intérêt catalytique ou magnétique (cf. Figures 5 et 6). L'absence de contact provient d'un effet de réactivité de surface dont on peut rendre compte qualitativement à l'aide d'un temps de passivation de la surface des agrégats incidents (l'hypothèse privilégiée étant par des molécules de CO) [Bardotti2011, Bardotti2011a].

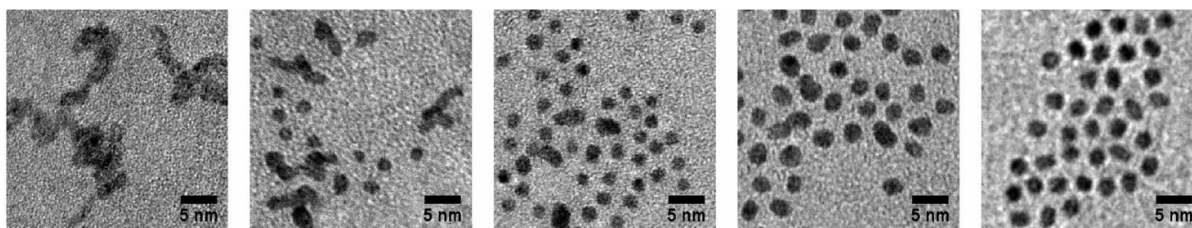


Fig. 5 : Morphologies typiques observées par MET pour des dépôts d'agrégats Co_xPt_{1-x} sur HOPG, avec de gauche à droite $x=1$, $x=0,75$, $x=0,5$, $x=0,25$ et $x=0$. Figure tirée de [Bardotti2014].

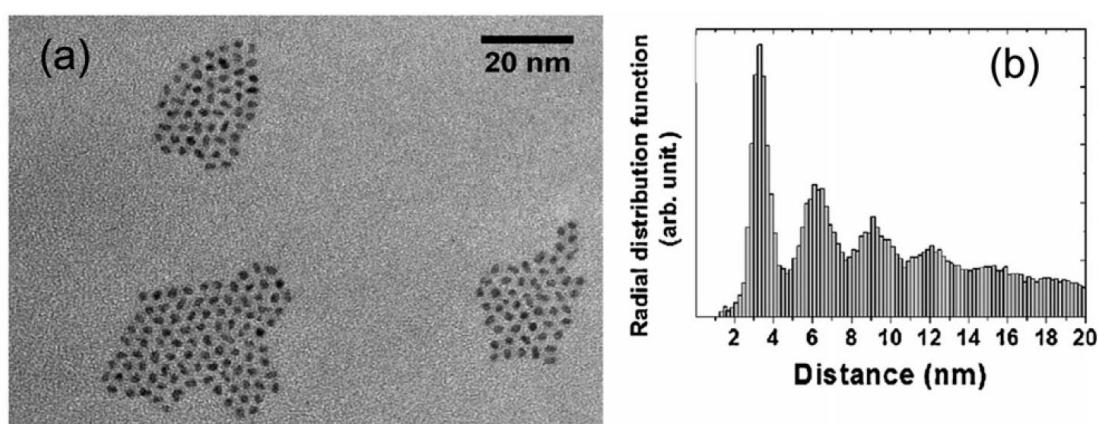


Fig. 6 : a) Morphologie typique observée par MET pour un dépôt d'agrégats FePt triés en taille (2,2 nm de diamètre) sur HOPG à température ambiante. b) Distribution radiale de paires correspondant à cet échantillon de FePt/HOPG : les pics reflétant un ordre local hexagonal sont clairement visibles. Figure tirée de [Bardotti2014].

Nous avons par ailleurs étudié le comportement d'agrégats déposés (toujours dans des conditions d'UHV) sur des nanotubes de carbone [Bardotti2014a, Delagrangé2014]. L'analyse des morphologies obtenues a permis de mettre en évidence la diffusion de « gros » agrégats de FePt (quelques nanomètres de diamètre) sur la surface des nanotubes (cf. Figure 7). La comparaison avec les cas du carbone amorphe et du graphite révèle une faible interaction agrégat/nanotube ainsi qu'un effet de la géométrie courbe des tubes sur le processus de diffusion. De plus, la forte sensibilité aux défauts et l'interaction agrégat-agrégat spécifique entraînant une organisation locale des particules de FePt ouvrent des perspectives intéressantes (cf. Figure 7). Ce système d'agrégats préformés déposés sur des nanotubes représente une opportunité assez unique pour l'étude de la transition entre un comportement 2D et 1D pour la diffusion/agrégation de particules. Des modélisations Monte Carlo cinétique

(collaboration avec O. Pierre-Louis, équipe « Modélisation de la Matière Condensée et des Interfaces » de l'ILM) ont été effectuées pour explorer cette transition [Delagrangé2014]. Celles-ci montrent que la densité d'amas augmente lorsque le diamètre des tubes diminue, s'approchant progressivement d'un comportement 1D (cf. Figure 8), en accord avec les observations expérimentales. Les effets de confinement disparaissent quand le périmètre des tubes est légèrement plus grand que la distance caractéristique entre amas de particules.

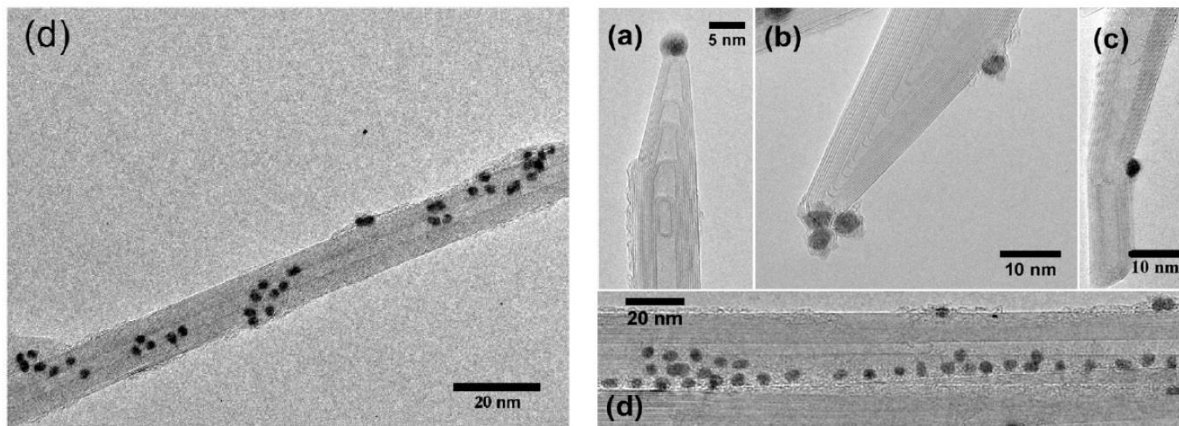
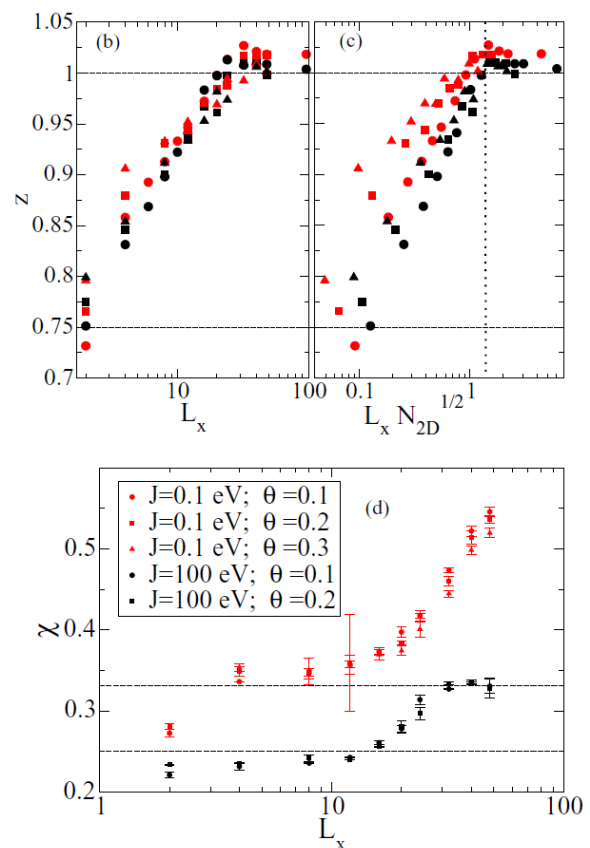


Fig. 7 : Gauche : amas de particules de FePt sur nanotube de carbone (multi-parois, synthétisés par CVD), mettant en évidence la diffusion des agrégats sur les tubes. Droite : quelques exemples illustrant la sensibilité des particules de FePt aux défauts présents sur les tubes (changements de courbure, sillons entre deux tubes...). Figure adaptée de [Bardotti2014a].

Fig. 8 : Résultats de simulations numériques montrant l'évolution des exposants z et χ en fonction du confinement des particules diffusant sur les nanotubes (L_x correspond au diamètre réduit des tubes, et $N_{2D}^{1/2}$ à la distance typique entre amas). La densité d'amas varie en fonction du taux de couverture θ à la puissance $1-z$ et du flux de particules incidentes à la puissance $-\chi$. Les limites correspondant aux cas 2D et 1D sont indiquées en pointillés : on a $z=1$ (la densité d'amas ne dépend donc pas de la quantité de particules déposées) et $\chi=1/3$ pour le cas 2D, tandis qu'on a $z=3/4$ et $\chi=1/4$ pour le cas 1D. Différentes valeurs de taux de couverture ont été considérées, ainsi que différentes énergies de collage des agrégats sur les amas (autorisant ou non le détachement et/ou la diffusion en bord d'amas). Figure tirée de [Delagrangé2014].



Enfin, nous avons étudié le comportement d'agrégats de Pt, Fe et FePt déposés sur du graphène épitaxié sur une surface d'Ir(111). Cette étude s'inscrivait dans le cadre de l'ANR NMGEM (« Nanomagnétisme sur Graphène Epitaxié sur Métaux », de 2011 à 2014) coordonnée par J. Coraux (Institut Néel). L'idée était de tirer parti du réseau hexagonal de moiré présent sur cette surface (périodicité de 2,5 nm) pour essayer d'organiser des nano-objets, d'intérêt magnétique. Cette approche était en effet déjà fructueuse avec le dépôt de certains types d'atomes permettant d'obtenir des réseaux de plots très bien ordonnés. Nous avons voulu l'étendre au cas de particules préformées, permettant de contrôler indépendamment la taille, la densité surfacique et la composition des nanoparticules. En combinant des mesures STM et de diffraction X *in situ* (grâce à la mise au point d'un système de transfert ultravide entre l'ESRF et l'iLM), nous avons mis en évidence la sensibilité des particules de Pt (de diamètre environ 1,5 nm) au moiré présent sur cette surface. En particulier, des mesures de GISAXS ont révélé des pics d'ordre permettant de quantifier la proportion de particules situées sur des sites spécifiques du moiré et d'étudier la stabilité en température de l'organisation obtenue [Linan2015]. Les résultats expérimentaux récents, extrêmement intéressants (en particulier dans le cas des particules de FePt), donneront lieu à d'autres publications et cette thématique se poursuit activement (étude des effets de taille, de température de dépôt et de recuit, des propriétés magnétiques etc.). Pour détailler ce travail, la publication « **Moiré induced organization of size-selected Pt clusters soft landed on epitaxial graphene** » [Linan2015] est reproduite ci-dessous.

SCIENTIFIC REPORTS



OPEN

Moiré induced organization of size-selected Pt clusters soft landed on epitaxial graphene

Received: 23 October 2014

Accepted: 24 April 2015

Published: 17 August 2015

Sébastien Linas^{1,†}, Fabien Jean², Tao Zhou³, Clément Albin¹, Gilles Renaud³, Laurent Bardotti¹ & Florent Tournus¹

Two-dimensional hexagonal arrays of Pt nanoparticles (1.5 nm diameter) have been obtained by deposition of preformed and size selected Pt nanoparticles on graphene. This original self-organization is induced, at room temperature, by the 2D periodic undulation (the moiré pattern) of graphene epitaxially grown on the Ir(111) surface. By means of complementary techniques (scanning tunneling microscopy, grazing incidence X ray scattering), the Pt clusters shapes and organization are characterized and the structural evolution during annealing is investigated. The soft-landed clusters remain quasi-spherical and a large proportion appears to be pinned on specific moiré sites. The quantitative determination of the proportion of organized clusters reveals that the obtained hexagonal array of the almost spherical nanoparticles is stable up to 650 K, which is an indication of a strong cluster-surface interaction.

Supported metallic clusters have attracted a lot of interest in the last decades due to the dependence of their physical and chemical properties on their sizes and local environments^{1–6}. Thus, a regular array of mono-dispersed clusters, providing a similar environment to each nanoparticle (NP), can highly facilitate their study or their use for optical⁷, magnetic^{8,9} or catalytic^{10–13} applications. Nanoparticles of typical lateral size and height of 1 to 2 nm are particularly relevant for the catalysis as they have been found to display much enhanced catalytic activity for this specific size^{12,14}. One way to produce such arrays is the deposition or growth of NPs on templates in the form of patterned substrates. Among all possible templates, extensive studies have been performed on graphene epitaxially grown on several transition metals (g/metal)^{15,16}. As a matter of fact, moirés are often present. They arise from the lattice mismatch between the graphene and the metal surface¹⁷, and correspond to a regular 2D spatial variation of the corrugation and the electron density in graphene. Such a moiré super-lattice extends over the whole surface with a lattice unit cell parameter of a few nanometers (typically 2–3 nm). Additionally the properties of the graphene layer can be tuned by selecting the metal surface. For instance, in the case of Ru(0001)^{18,19}, graphene is strongly chemisorbed to the substrate whereas graphene is quasi freestanding when grown on Ir(111)^{20–23}. As a consequence, by combining the exceptional properties of graphene with the possibility to produce perfect moiré super lattices on transition metals^{24–26}, this system appears as an ideal template for the fabrication of two-dimensional NP arrays. It has therefore been recently used to organize, by atomic vapor deposition (AVD), Ru²⁷, Pt^{28–30} and Co³¹ clusters on graphene in epitaxy on Ru(0001) (g/Ru(0001)) as well as Ir^{32,33}, Pt^{33,34}, W³³ and Re³³ clusters on graphene in epitaxy on Ir(111) (g/Ir(111)). Nevertheless, the perfection of the cluster lattice strongly depends on the metal supporting the graphene film. Of the above mentioned, g/Ir(111) induces cluster arrays, the exceptional order and

¹Institut Lumière Matière (ILM), Université de Lyon, UMR5306 Université Lyon 1-CNRS, 69622 Villeurbanne, France. ²Institut Néel, CNRS and Université Joseph Fourier, BP166, F-38042 Grenoble Cedex 9, France. ³Univ. Grenoble Alpes, INAC-SP2M, F-38000 Grenoble, France, CEA, INAC-SP2M, F-38000 Grenoble, France. [†]Current Address: Laboratoire des Multimatériaux et Interfaces (LMI), UMR 5615, Université Lyon 1-CNRS, 43 bd du 11 Novembre 1918, 69622 Villeurbanne, France. Correspondence and requests for materials should be addressed to F.T. (email: florent.tournus@univ-lyon1.fr)

narrow size distribution of which makes them particularly attracting³⁴. In the specific case of platinum clusters on g/Ir(111), three growth regimes have been found. First, a nucleation regime (up to 0.1 monolayer (ML) coverage) is characterized by a steep increase of the cluster density and by the presence of predominantly one atomic layer high clusters. For higher coverage (up to 0.75 ML), the cluster density becomes almost independent from the coverage and the cluster size increases while almost all clusters evolve toward a height of two monolayers. For even higher coverages, the sintering taking place between neighboring clusters induces a progressive loss of organization³³. Finally, since Pt clusters have a rather flat shape; the largest average size of ordered clusters is limited to 65 atoms³⁵. Due to these specific growth regimes, the main limitations of platinum clusters produced by atomic deposition on g/Ir(111), regarding the catalytic applications for instance, are their small height of 1 to 2 MLs and the impossibility to tune independently cluster coverage and sizes.

The deposition of preformed spherical size-selected clusters appears as an original alternative technique to overcome these limitations^{36,37}. A recent study, combining scanning tunneling microscopy (STM) observations and first principles calculations concluded to the possibility of moiré induced organization of extremely small Pd_{n(n<20)} clusters on g/Ru(0001)³⁶. If the organization of small NPs is expected in a way similar to the organization of clusters formed by physical evaporation, the organization of much larger NPs on templates such as g/Ru(0001) or g/Ir(111) is expected to be more difficult, because of the much smaller ratio between interfacial NP atoms and bulk or surface ones. In the present work, we report on the investigation of a diluted two dimensional (2D) array of preformed and size selected Pt clusters (c.a. 80 atoms and 1.5 nm mean diameter) that are soft-landed at room temperature (RT) on g/Ir(111) by means of three complementary techniques: STM, grazing incidence X-ray diffraction (GIXD) and grazing incidence small-angle X-ray scattering (GISAXS). The morphological and structural evolutions of this system are also investigated during annealings above RT. An efficient and original method to quantify the organization order of the cluster super-lattice at a macroscopic scale is proposed.

Results and Discussion

Typical STM images of size-selected Pt clusters deposited on g/Ir(111) are shown in Fig. 1a,b for two incident NP densities. They reveal isolated particles with a density corresponding to the incident one, evidencing the absence of coalescence and confirming the absence of fragmentation of the supported clusters. Moreover, neither cluster aggregation nor specific step decoration is detected, indicating that clusters do not diffuse over distances larger than a few nanometers. Note that, this low diffusion is in complete contrast with the case of Pt clusters deposited on graphite, where NPs diffuse rapidly and gather to form “island” of NPs³⁸. This limited diffusion of platinum NPs on g/Ir(111) suggests their pinning on the surface. Such a pinning could result from adsorbed species on the g/Ir(111) surface (e.g. carbonaceous material^{37,39}), defects of the graphene lattice^{20,40} or anchoring of the NPs on specific sites of the moiré pattern. Nevertheless, immobilization of NPs by adsorbed species has not been observed in the case of Pt clusters deposited on graphite⁴¹. Such a contamination is unlikely here since all samples were kept under ultrahigh vacuum (UHV) and is additionally confirmed by STM atomic resolution observations⁴². Concerning the trapping of clusters by natural defects, according to the extremely high quality of graphene grown on Ir(111)²⁴, a pure heterogeneous growth on defects appears unlikely. On the contrary, according to the moiré specific site density (1.85×10^5 sites. μm^{-2} , assuming one pinning site per moiré unit cell), the observed supported cluster density rather favor their pinning on the moiré pattern. The NP height histogram measured by STM is shown in Fig. 1c. The average NPs height ($\langle H \rangle = 1.5$ nm with a relative dispersion of $\frac{\sigma_H}{H} \sim 14\%$, σ_H being the standard deviation of H) is close to the diameter of the incident clusters (chosen by the experimental parameters), suggesting that the supported NPs conserve their 3D shape when going from the free to the supported state (note that in this range of size, the incident platinum clusters are expected to have a quasi-spherical shape corresponding to multiply-twinned structures^{43–45}, but their internal structure may be different once deposited). This last result is drastically different from those obtained previously by AVD where, as mentioned before, supported clusters are rather flat (typically 1 to 3 monolayers high)³⁵. For the low surface coverage the moiré of g/Ir(111) as well as the clusters are clearly visible in STM images as in the AVD studies. Unfortunately the convolution between the tip and the clusters, enhanced by the 3D morphology of the supported NPs, prevents the precise determination by STM of their structural relationship with the surface and their location on the moiré lattice. To get more information on this last point, the nearest neighbor distance d_{NN} (center to center) of Pt clusters is shown in Fig. 1d for a medium density. The d_{NN} histogram can be fitted by two Gaussian functions centered on $d_1 = 2.4$ nm and $d_2 = 2.4 \times \sqrt{3}$ nm. This shows that, despite the randomness of the cluster deposition process⁴⁶, the final locations of at least some Pt clusters on g/Ir(111) are not randomly distributed. Additionally the mean d_{NN} distance is clearly compatible with the pinning of the Pt NPs on specific sites of the g/Ir(111) moiré. However, we emphasize at this point that this analysis cannot exclude the presence of some randomly distributed clusters. Such a feature could explain the absence of a clear cluster organization on the STM images for this surface coverage.

Furthermore, STM does not provide precise information on several characteristics of this system, e.g. the epitaxial relationship of the NPs with the substrate, their precise shape or the correlation length of the NPs organization. GIXD and GISAXS studies were then conducted to answer these questions.

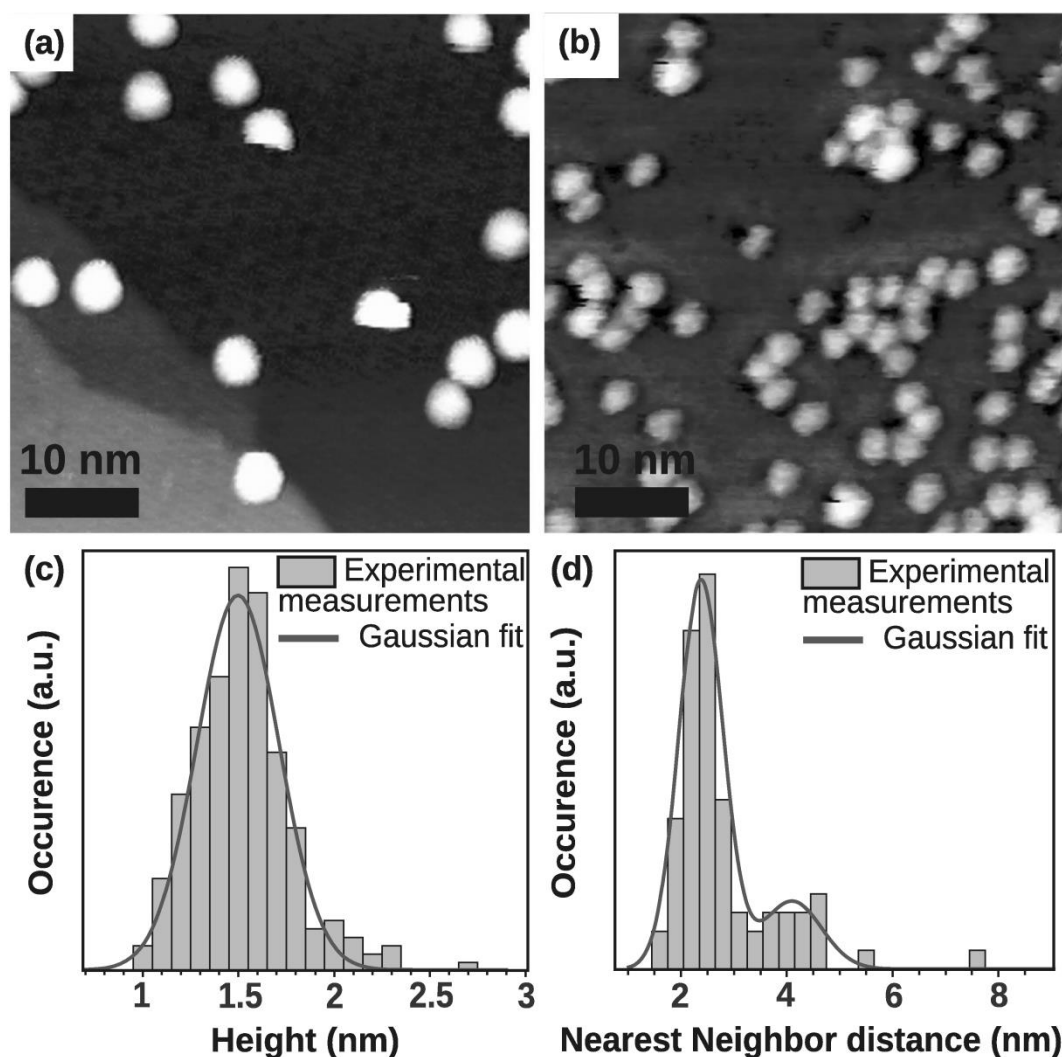


Figure 1. (a,b) Typical STM topographs of size-selected (1.5 nm in diameter) platinum clusters supported on g/Ir(111). The coverage of the NPs corresponds to a low (a) and medium (b) density. (c) Height distribution of the Pt clusters measured by STM, fitted by a Gaussian function. (d) Nearest neighbor distance (center to center) distribution of Pt clusters deposited on g/Ir(111) with a medium density. The distribution is fitted by two Gaussian functions.

In-plane scans of the scattered X-ray intensity were recorded along the h direction in the vicinity of the (200) rod of Ir (Fig. 2a) for g/Ir(111) before and after NP deposition. The (200) rod of Ir is centered at $h = 2$, the (200) Bragg peak of graphene at $h \approx 2.23$ and two moiré peaks can be observed around $h \approx 1.9$ and $h \approx 2.1^{26}$. The unit cell parameter of the moiré can be deduced from the relative positions of the (110) Bragg peaks of Ir and graphene (not shown), according to: $a_{\text{moiré}} = (a_{\text{Ir}}^{-1} - a_{\text{Graphene}}^{-1})^{-1} = 2.48$ nm. This result is in complete agreement with previous studies^{26,32} and with the present STM observations. The deposition of NPs induces three main effects at RT on the in-plane scans (Fig. 2a), (i) a broadening of the Ir rod, (ii) a decrease of the graphene Bragg peak around $h \approx 2.23$ and (iii) the raise of the moiré peak around $h \approx 1.9$ (see inset of Fig. 2a).

Concerning the striking broadening of the Ir rod, because the nearest neighbor distances of Pt (2.77 Å) is very close to that of Ir (2.72 Å), NPs in epitaxy on the Ir(111) surface are expected to yield diffraction peaks in the vicinity of the Ir peaks and rods. These peaks of epitaxial NPs would be very broad if the NPs were randomly distributed on the surface. On the other hand, if the particles are organized on the moiré, the diffraction peaks at the moiré, Ir and graphene rod positions will have a lower width than expected just from the particle size. If the NPs are not in epitaxy but adopt many orientations, the scattered intensity is distributed over a portion of sphere and thus the intensity measured in a single radial scan such as that of Fig. 2a should be negligible. Measurable intensity from the NPs along such scans is expected only if a significant fraction of the NPs are in epitaxy with the substrate. Consequently,

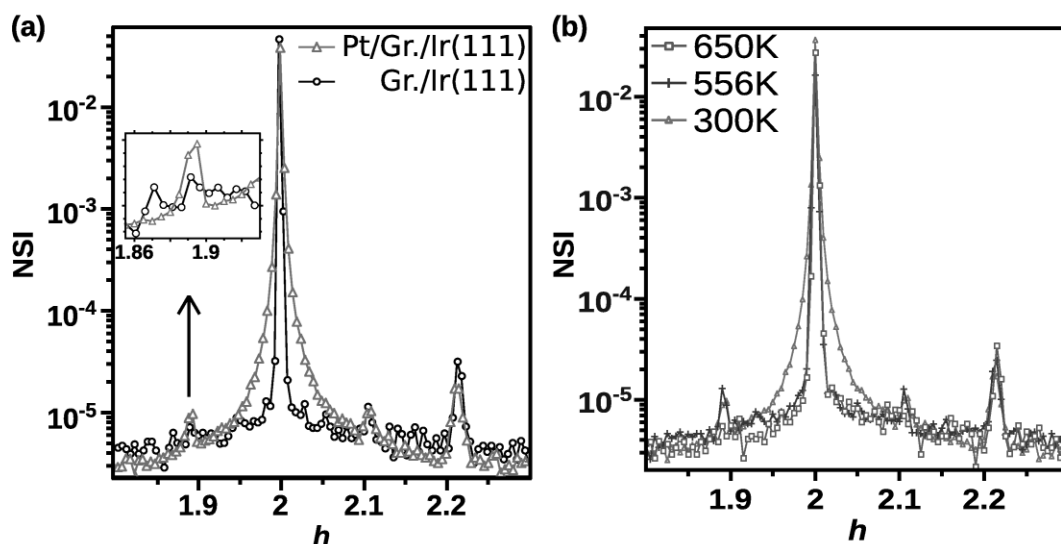


Figure 2. In-plane scans along the h direction in the neighborhood of the (200) Ir rod. The temperatures are (a) RT and (b) RT to 650 K. The samples were (a), bare g/Ir(111) (black circles) and g/Ir(111) covered with a medium density of Pt clusters (red triangle) and (b) g/Ir(111) covered with a medium density of Pt clusters. In (a), the inset shows a zoom of the scan in linear scale.

the much wider peak appearing around the (200) rod upon NP deposition shows that some NPs are in epitaxy with Ir(111).

The decrease of the graphene Bragg peak ($h \approx 2.23$) can be understood as an effect of the Pt deposition inducing inhomogeneous distortions of the graphene. Such distortions can also induce a peak broadening, but this is hardly detected because of the low signal compared to the background.

The last observation is the increase of the moiré peak intensity, which implies that some NPs are pinned on a specific site of the moiré cell.

Hence, a qualitative analysis by GIXD indicates that a significant fraction of the NPs are in epitaxy with the Ir(111) substrate; and at least part of them are perfectly anchored to a specific moiré site; the rest possibly being in different places (*i.e.* with no coherence from one unit cell to the other). We then define Θ as the proportion of clusters pinned on the moiré.

The indications of the organization and epitaxy of the clusters given by GIXD have been followed during an annealing of the samples. In Fig. 2b, the vicinity of the (200) rod of Ir is reported for the same sample before and after annealing. After annealing at 460 K, the width of the (200) rod of Ir is reduced to the value found for the bare g/Ir(111). The intensity of the moiré peak around $h \approx 1.9$ decreases and reaches the background level at $T = 650$ K.

At this point, two preliminary conclusions can be drawn. Between RT and 460 K the clusters that were in epitaxy but are not positioned on specific sites have lost their epitaxial relationship with Ir(111). The decrease of the moiré peak with temperature above 560 K (see Fig. 2c) suggests either a loss of epitaxy or a decrease of Θ or a combination of these two features.

To obtain more quantitative information on the cluster shape and organization, the scattered intensity has been measured near the origin of the reciprocal space using the GISAXS technique⁴⁷.

The scattered intensity at small angles [$I(\mathbf{q})$, where \mathbf{q} is the scattering wave vector] contains information about the shape of the NPs and the spatial organization of the particles⁴⁸. In a GISAXS pattern, a correlation peak appears in addition to the form factor if the clusters are spatially organized. In Fig. 3a (left panel) a map of the reciprocal space for $2\theta < 100$ mrad and at $\alpha_f = \alpha_c = 7$ mrad is shown for g/Ir(111) covered by Pt NPs. This map is a result of collecting GISAXS patterns at different azimuths and for which the intensity at the Yoneda peak⁴⁹ ($\alpha_f = \alpha_c = 7$ mrad) has been extracted. One can see in Fig. 3b that a correlation peak is only visible in GISAXS patterns measured when the incident beam is aligned with the [100] (left panel) and [110] (center panel) Ir crystallographic orientations. As was shown for Co clusters organized on the 2D-patterned Au(111)⁵⁰ and Au(677)⁵¹ surfaces, this in-plane reciprocal space map demonstrates the presence of a two-dimensional order of the Pt NPs. The corresponding unit cell of this 2D array is hexagonal with two sides aligned along the Ir[100] and the Ir[010] directions and a lattice parameter of $d_{Pt\ array} = 2.485$ nm. The sharpness and the dependence of the correlation peak with crystallographic orientation show that the organization of the clusters is not only due to a favored first neighbor distances as is in the case of Pt NPs deposited on graphite⁴¹, but clearly reflect the pinning of the clusters on specific sites. We can conclude from these results that some of the Pt NPs are pinned on the hexagonal moiré of g/Ir(111).

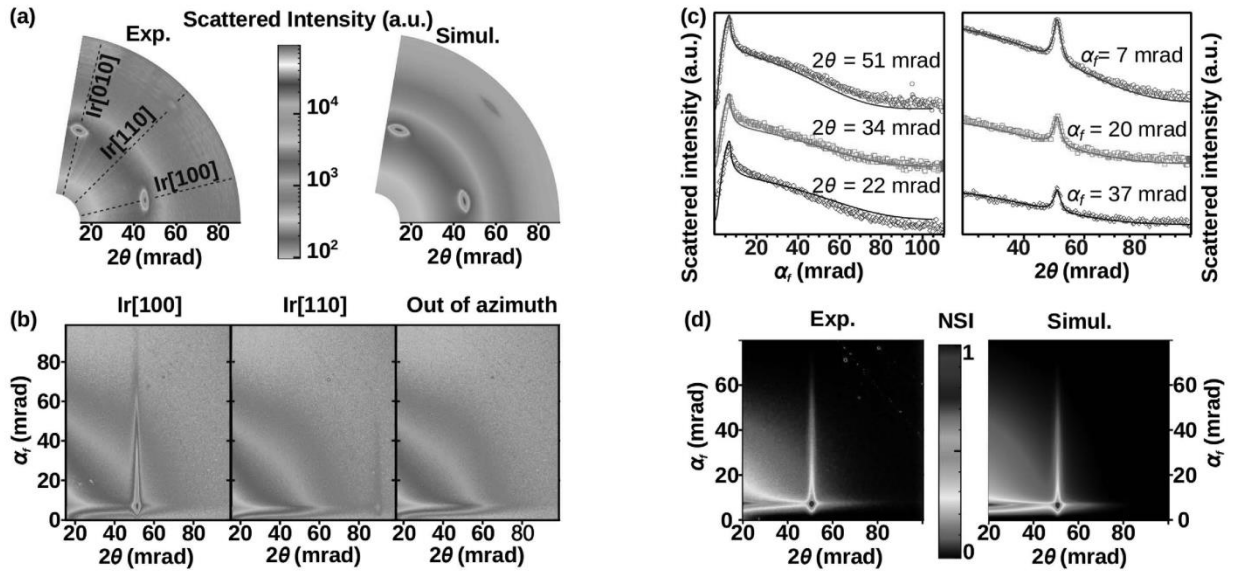


Figure 3. (a) Map of the reciprocal space at RT at $\alpha_f = \alpha_c = 7$ mrad (left) and the corresponding simulation (right). (b) GISAXS patterns at RT, with the incident beam along the Ir[100] (left), Ir[110] (center) directions and out of azimuth (right). (c) Perpendicular (left) and parallel (right) line cuts of the 2D GISAXS pattern shown in (d), the continuous lines correspond to the best fits and the symbols (circles, squares and diamonds) correspond to the experimental data points. The curves have been shifted for clarity. (d) 2D experimental GISAXS pattern at RT with the incident beam along the Ir[100] direction (left) and the corresponding simulation (right). (a,b) correspond to a sample of Pt clusters deposited on g/Ir(111) with a high density (in order to have a better visibility of the correlation peak in the direction Ir[110]), while (c,d) correspond to a medium cluster density.

Additional characteristics of the 2D array of Pt clusters can be extracted by fitting the GISAXS patterns, using the IsGISAXS⁴⁸ software. $I(\mathbf{q})$ is assumed to be the incoherent sum (since non-organized particles lie at random locations, their phases cancel on average and the summation can be made incoherently) of the intensity scattered by NPs lying at random locations (I_R) and that scattered by the NPs anchored on the graphene moiré (I_L):

$$I(\mathbf{q}) = \Theta I_L(\mathbf{q}) + (1 - \Theta) I_R(\mathbf{q}) \quad (1)$$

The usual⁴⁹ approximation to simulate the GISAXS intensity of an assembly of nanoparticles is the local mono-disperse approximation (LMA) which assumes that all NPs locally have the same size; the size variation arising only over long distances. However, in the present case, we have a random deposition of NPs having a pre-defined size distribution and the 2D super-lattice is randomly occupied by preformed cluster, which may slightly vary in size from site to site. The experimental system studied in this work is thus a model system for the decoupling approximation⁵² (DA) in which the size of each NP is independent of its neighborhood. In this framework, the scattered intensity is the sum of two terms^{48,49}:

$$I_m(\mathbf{q}) = \left\{ \langle |\mathcal{F}(\mathbf{q})|^2 \rangle_D - |\langle \mathcal{F}(\mathbf{q}) \rangle_D|^2 \right\} + |\langle \mathcal{F}(\mathbf{q}) \rangle_D|^2 S_m(\mathbf{q}); \quad m = L, R \quad (2)$$

where \mathcal{F} is an effective form factor⁴⁸ calculated within the distorted-wave Born approximation and $\langle \dots \rangle_D$ denotes averaging over the size distribution. $S(\mathbf{q})$ is the total interference function which describes the statistical distribution of the Pt clusters on the surface and thus their lateral correlations.

In order to extract quantitative parameters from GISAXS measurements, parallel and perpendicular line cuts, obtained from a GISAXS pattern (see Fig. 3c,d) are fitted using the following procedure. First, the cluster morphological parameters ($\langle D \rangle$, $\langle H \rangle$, σ_D) are determined from an out of azimuth direction assuming that the NPs are truncated spheres. Then, this set of parameters is used to fit the correlation peak around the Ir[100] direction. This gives access to the characteristic length (C.L.) of the exponentially decaying correlation of the 2D Pt cluster array. Note that $S_L(\mathbf{q})$ is considered to correspond to a perfect 2D hexagonal lattice (reflecting the moiré pattern), with a lattice parameter adjusted to reproduce the peak positions in the GISAXS map (*i.e.* $d_{Pt \text{ array}} = 2.485$ nm). Finally, Θ can be determined from the correlation peak intensity, with respect to the flat background signal from the uncorrelated particles. For this purpose, a line cut from an off-azimuth GISAXS pattern (*i.e.* where $S_L(\mathbf{q})$ is simply equal to 1) is subtracted to the corresponding line cut along the Ir[100] direction. The resulting curve is then proportional to the $S_L(\mathbf{q})$ difference and only the correlation peak remains. The proportion

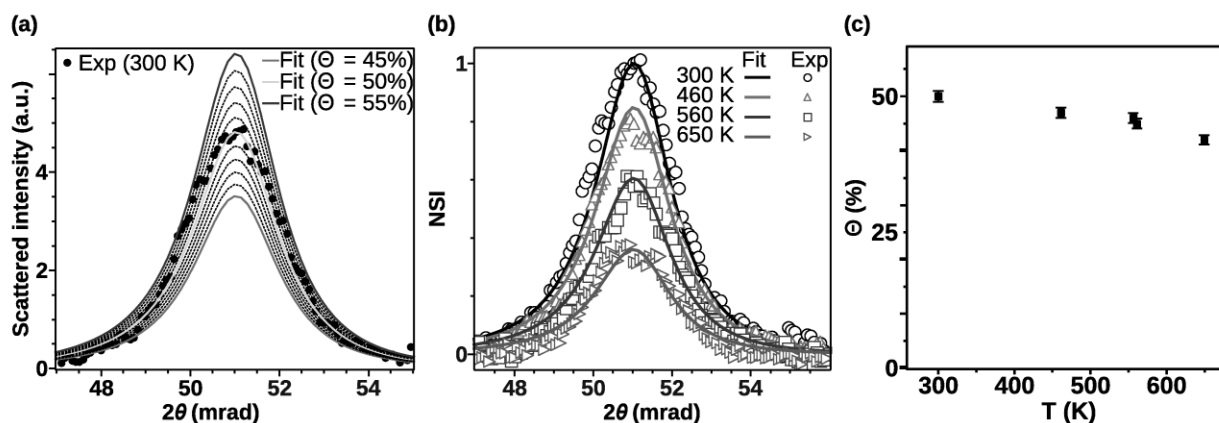


Figure 4. (a) Fit of the RT experimental GISAXS correlation peak (black dots) with various fraction Θ of Pt clusters lying on the moiré lattice. Difference of 2D GISAXS pattern line cuts ($\alpha_f = \alpha_c \approx 7$ mrad) with the incident beam 10° off azimuth and in the Ir[100] direction. The intermediates values of Θ are represented in dashed black lines, with an increment of 1%. (b) Best fits of experimental GISAXS correlation peaks at various temperatures. (c) Plot of Θ versus the annealing temperature. Pt NPs have been deposited on g/Ir(111) with a medium density.

of organized Pt clusters is thus deduced from a set of simulations at different Θ values (Fig. 4a). In the end, as shown in Fig. 3, an excellent agreement between the experimental data and the simulations is found, not only for representative line cuts but also for the entire GISAXS patterns and azimuthal map (Fig. 3).

The morphological parameters found for the best fit of the GISAXS data are $\langle D \rangle = 1.51$ nm, $\langle H \rangle = 1.25$ nm and a Gaussian dispersion of standard deviation $\frac{\sigma_D}{\langle D \rangle} = 12\%$. The shape of the NPs derived from GISAXS is almost spherical ($\frac{H}{D} \approx 0.83$) with a small wetting of the substrate. Note that this height is compatible with the STM results (the slight difference might arise from the GISAXS truncated sphere model of the NPs, which dismisses the true atomic arrangement and in particular the faceting). The size of the graphene domains (*ca.* 62 nm), calculated from the GIXD graphene peaks²⁶, is close to the correlation length (C.L. ≈ 92 nm), deduced from the GISAXS correlation peak. This suggests that the cluster hexagonal organization is limited by the size of the graphene domains. The proportion of clusters pinned on the moiré is found to be $\Theta = 50 \pm 2\%$ for a medium density of clusters. Note that, for the sample covered with a high density of clusters (see Figure S1 in the supporting information) the results are very similar ($\Theta = 50\%$). We deduce that half of the preformed Pt clusters deposited on g/Ir(111) self-organize as an incomplete (*i.e.* with vacancies) 2D lattice of clusters, the rest being off lattice. Let us emphasize that the occupation ratio of the moiré sites are 8 and 27% for the samples covered with a medium and a high densities of NPs respectively.

As the temperature increases (RT to 650 K) the intensity of the correlation peak clearly decreases (Fig. 4b): Θ is found to decrease (Fig. 4c) from 50 to 42% without change in cluster shape and size. It can be noticed that the 2D array is relatively stable upon high temperature annealing since at 650 K only 16% of the clusters previously pinned by the moiré have left the super-lattice. Between $T = 556$ and 560 K the value of Θ determined by GISAXS barely evolves while the moiré peak in GIXD (Fig. 2c) drastically decreases: this can be interpreted as a loss of epitaxy with the Ir(111) surface, although the clusters are still anchored at specific moiré site. This emphasizes the strength of the GISAXS technique which is sensitive to all NPs whether they are in epitaxy or not.

For temperatures higher than 650 K, the shape of the clusters is modified (see Figure S2 in supporting information). These morphological modifications are probably due to the coalescence or sintering of NPs, or possibly to intercalation of Pt below the graphene. Anyway the system is no more a diluted 2D array of size selected clusters and the modification is irreversible as confirmed by measurements after cooling down to RT.

The stability of the cluster arrays with temperature indicates a strong bonding of the NPs to the substrate. However the decrease of Θ suggests that the clusters leaving the specific moiré sites are trapped elsewhere. Two explanations can be drawn to account for the out of lattice clusters: (i) in some areas of the sample the clusters are fully organized whereas on other areas clusters are not pinned on the moiré specific sites. This could be the results of a non-complete coverage of Ir(111) by graphene, or trapping of the clusters by wrinkles that form in g/Ir(111)⁵³. However, the homogeneity observed from STM images of various areas seems to refute this hypothesis. (ii) The cluster adsorption energy landscape could present one principal potential well, able to attract clusters in an area corresponding to *ca.* half the super-lattice unit cell, while there exists many smaller potentials wells distributed over the rest of the unit cell. A theoretical study should help understanding the kinetics and thermodynamics of NP trapping

on g/Ir(111). This could eventually give clues to enhance the ratio of organized clusters, for instance by increasing the temperature during the deposition process.

Conclusions

In summary, we have shown that about half of the incident Pt clusters soft-landed at RT organize on a 2D array templated by the moiré of g/Ir(111). The striking agreement between experimental and simulated GISAXS patterns enables a first quantitative characterization, on a macroscopic length-scale, of the organization of quasi-spherical Pt nanoparticles. From GIXD measurements, we have found that some of the NPs are in epitaxy with the Ir(111) substrate. Additionally, a moderate annealing (at 460 K) suppresses the epitaxial relationship, while the particle shape and size remain unchanged. Besides, as deduced from the GISAXS correlation peak, the organization shows minor variations up to 650 K. This demonstrates that the obtained 2D arrays of NPs are stable against quite high temperature annealing: 84% of the clusters that were organized at RT are still anchored on specific moiré sites at 650 K. Our findings provide a first step in the investigation of self-organized 2D arrays of preformed clusters deposited on a graphene surface. The preparation of well-defined Pt nanoparticles samples can then be promising for catalytic applications. Furthermore, our original approach could also be extended to bi-metallic and/or magnetic materials which cannot be organized on graphene by atomic deposition. Indeed, the clusters obtained by AVD are the result of a nucleation and growth process occurring on the surface. On the moiré of g/Ir(111), cluster super-lattices can then be formed for high cohesive energy metals, as Ir, Pt or W, whereas lower cohesive energy materials, such as Au, Fe or Ni³³, do not organize. The mass-selected low energy cluster beam deposition (MS-LECBD) technique, where preformed clusters having a 3D morphology are soft-landed on a surface, could overcome this limitation.

Methods

Preparation of g/Ir(111). The substrates preparation was performed in the UHV chamber (base vacuum 5×10^{-11} mbar)⁵⁴ of the BM32 beamline of the European Synchrotron Radiation Facility⁵⁵ (Grenoble, France). Two different Ir single crystals, cut and polished on a (111) surface termination within 0.1° were used (one was provided by Surface Preparation Laboratory and the other by Mateck). They were cleaned by cycling high temperature annealing periods (1473 K) and ion bombardment (1.3 kV/10 μ A Ar⁺ for 30 min at RT), with a final annealing in oxygen (5×10^{-7} mbar for 10 min at 1300 K). The graphene was prepared following a well-established method, consisting of a temperature programmed growth step (adsorption of ethylene at RT followed by a flash annealing at 1473 K) and a chemical vapor deposition step (annealing at 1273 K under an ethylene partial pressure of 10^{-7} mbar)^{24,25}.

The g/Ir(111) substrates were then transferred in a homemade UHV transfer device (10^{-8} to 10^{-9} mbar) from the BM32 beamline to the nearby cluster deposition chamber (PLYRA facility⁵⁶). The transfer typically lasted a few hours.

Clusters synthesis. Pt clusters have been synthesized by the mass-selected MS-LECBD technique described elsewhere^{37,57}. Briefly, the NPs have been first produced by a laser vaporization source and subsequently mass-selected using a quadrupolar electrostatic deviator⁵⁷. In the present experiment, the deviator was set to produce incident clusters with a diameter of *ca.* $D = 1.5$ nm³⁷. The clusters were then soft landed at RT on a g/Ir(111) under UHV (10^{-11} to 10^{-10} mbar). The kinetic energy of the incident clusters is around 0.4 eV/atom, ensuring that there will neither be cluster fragmentation on the surface nor surface defect creation. The incident flux of NPs (cations) has been determined using a Faraday cup connected to a pico-amperemeter. With this technique, the density and size of the clusters are set independently. In this work low (10^4 NPs μ m⁻²), medium (3×10^4 NPs μ m⁻²) and high (10^5 NPs μ m⁻²) densities of incident clusters were deposited (relative uncertainties of 8%). The deposition chamber is connected to an Omicron UHV STM allowing *in situ* STM observation of the samples at RT. After NPs deposition, the samples were transferred back under UHV to the synchrotron facility in Grenoble (France).

GIXD and GISAXS measurements with synchrotron light were performed in an UHV chamber (5×10^{-11} mbar) coupled with a Z-axis diffractometer at the ESRF BM32 beamline^{54,55}. The monochromatic photon beam had an energy of 11 keV, a focus size of 300×300 (H \times V) μ m² and an incidence angle of $\alpha_i = 0.38^\circ$ (just below the critical angle for total external reflection of Ir which is 0.42° at 11 keV). The intensity scattered by the surface was collected at wide angle (GIXD) using a 2D pixel detector (Maxipix). Slits (0.5 mm, parallel to the surface) have been placed well before the detector (slit-sample distance of 190 mm, compared to a detector-sample distance of 640 mm). The reference for the normalized scattered intensities (NSIs) is the incident beam whose intensity has been measured by a monitor placed before the sample. The intensity scattered at small angle (GISAXS) was collected using a high grade charge-coupled device 16-bit camera (Photonic Science; 2.25 Mpixels pixel size of 43.965μ m²). The sample to detector distance was set to 525 ± 5 mm. The *h*, *k*, *l* indexes in relative lattice unit are referred to the Ir(111) hexagonal surface unit cell ($a_s = b_s = 2.715$ Å; $c_s = 6.65$ Å).

References

- Chen, M. S. & Goodman, D. W. The Structure of Catalytically Active Gold on Titania. *Science* **306**, 252–255; doi: 10.1126/science.1102420 (2004).
- Eustis, S. & El-Sayed, M. A. Why gold nanoparticles are more precious than pretty gold: noble metal surface plasmon resonance and its enhancement of the radiative and nonradiative properties of nanocrystals of different shapes. *Chem. Soc. Rev.* **35**, 209–217 (2006).
- Knickerbein, M. B. Experimental Observation of Superparamagnetism in Manganese Clusters. *Phys. Rev. Lett.* **86**, 5255–5257; doi: 10.1103/PhysRevLett.86.5255 (2001).
- Boyen, H.-G. Oxidation-Resistant Gold-55 Clusters. *Science* **297**, 1533–1536; doi: 10.1126/science.1076248 (2002).
- Lopez, N. *et al.* On the origin of the catalytic activity of gold nanoparticles for low-temperature CO oxidation. *J. Catal.* **223**, 232–235; doi: 10.1016/j.jcat.2004.01.001 (2004).
- Si, Y. & Samulski, E. T. Exfoliated Graphene Separated by Platinum Nanoparticles. *Chem. Mater.* **20**, 6792–6797; doi: 10.1021/cm801356a (2008).
- Kreibig, U. & Vollmer, M. in *Optical Properties of Metal Clusters* (Springer, 1995).
- Binz, S. M. *et al.* High Island Densities and Long Range Repulsive Interactions: Fe on Epitaxial Graphene. *Phys. Rev. Lett.* **109**, 026103; doi: 10.1103/PhysRevLett.109.026103 (2012).
- Weiss, N. *et al.* Uniform Magnetic Properties for an Ultrahigh-Density Lattice of Noninteracting Co Nanostructures. *Phys. Rev. Lett.* **95**, 157204; doi: 10.1103/PhysRevLett.95.157204 (2005).
- Yoo, E. *et al.* Enhanced Electrocatalytic Activity of Pt Subnanoclusters on Graphene Nanosheet Surface. *Nano Lett.* **9**, 2255–2259; doi: 10.1021/nl900397t (2009).
- Nesselberger, M. *et al.* The effect of particle proximity on the oxygen reduction rate of size-selected platinum clusters. *Nat. Mater.* **12**, 919–924; doi: 10.1038/nmat3712 (2013).
- Heiz, U. & Landman, U. in *Nanocatalysis* (Springer, 2006).
- Guo, S., Dong, S. & Wang, E. Three-Dimensional Pt-on-Pd Bimetallic Nanodendrites Supported on Graphene Nanosheet: Facile Synthesis and Used as an Advanced Nanoelectrocatalyst for Methanol Oxidation. *ACS Nano* **4**, 547–555; doi: 10.1021/nn9014483 (2010).
- Sun, S. *et al.* Single-atom Catalysis Using Pt/Graphene Achieved through Atomic Layer Deposition. *Sci. Rep.* **3**, 1775; doi: 10.1038/srep01775 (2013).
- Voloshina, E. N. *et al.* Electronic structure and imaging contrast of graphene moiré on metals. *Sci. Rep.* **3**, doi: 10.1038/srep01072 (2013).
- Soldano, C., Mahmood, A. & Dujardin, E. Production, properties and potential of graphene. *Carbon* **48**, 2127–2150; doi: 10.1016/j.carbon.2010.01.058 (2010).
- Wintterlin, J. & Bocquet, M.-L. Graphene on metal surfaces. *Surf. Sci.* **603**, 1841–1852; doi: 10.1016/j.susc.2008.08.037 (2009).
- Martocchia, D. *et al.* Graphene on Ru(0001): A 25×25 Supercell. *Phys. Rev. Lett.* **101**, 126102; doi: 10.1103/PhysRevLett.101.126102 (2008).
- Sutter, P. W., Flege, J.-I. & Sutter, E. A. Epitaxial graphene on ruthenium. *Nat. Mater.* **7**, 406–411; doi: 10.1038/nmat2166 (2008).
- Coraux, J., N'Diaye, A. T., Busse, C. & Michely, T. Structural Coherency of Graphene on Ir(111). *Nano Lett.* **8**, 565–570; doi: 10.1021/nl0728874 (2008).
- Busse, C. *et al.* Graphene on Ir(111): Physisorption with Chemical Modulation. *Phys. Rev. Lett.* **107**, 036101; doi: 10.1103/PhysRevLett.107.036101 (2011).
- Coraux, J. *et al.* Growth of graphene on Ir(111). *New J. Phys.* **11**, 023006; doi: 10.1088/1367-2630/11/2/023006 (2009).
- Pletikosić, I. *et al.* Dirac Cones and Minigaps for Graphene on Ir(111). *Phys. Rev. Lett.* **102**, 056808; doi: 10.1103/PhysRevLett.102.056808 (2009).
- Gastel, R. van *et al.* Selecting a single orientation for millimeter sized graphene sheets. *Appl. Phys. Lett.* **95**, 121901; doi: 10.1063/1.3225554 (2009).
- Jean, F. *et al.* Effect of preparation on the commensurabilities and thermal expansion of graphene on Ir(111) between 10 and 1300 K. *Phys. Rev. B* **88**, 165406; doi: 10.1103/PhysRevB.88.165406 (2013).
- Blanc, N., Coraux, J., Vo-Van, C., Geaymond, O. & Renaud, G. Local deformations and incommensurability of high-quality epitaxial graphene on a weakly interacting transition metal. *Phys. Rev. B* **86**, 235439 (2012).
- Sutter, E. *et al.* Arrays of Ru nanoclusters with narrow size distribution templated by monolayer graphene on Ru. *Surf. Sci.* **605**, 1676–1684; doi: 10.1016/j.susc.2011.01.026 (2011).
- Donner, K. & Jakob, P. Structural properties and site specific interactions of Pt with the graphene/Ru(0001) moiré overlayer. *J. Chem. Phys.* **131**, 164701–164701–10; doi:10.1063/1.3246166 (2009).
- Zhang, H., Fu, Q., Cui, Y., Tan, D. & Bao, X. Fabrication of metal nanoclusters on graphene grown on Ru(0001). *Chin. Sci. Bull.* **54**, 2446–2450; doi: 10.1007/s11434-009-0411-0 (2009).
- Pan, Y., Gao, M., Huang, L., Liu, F. & Gao, H.-J. Directed self-assembly of monodispersed platinum nanoclusters on graphene Moiré template. *Appl. Phys. Lett.* **95**, 093106; doi: 10.1063/1.3223781 (2009).
- Liao, Q. *et al.* Nucleation and growth of monodispersed cobalt nanoclusters on graphene moiré on Ru(0001). *Nanotechnology* **22**, 125303; doi: 10.1088/0957-4484/22/12/125303 (2011).
- N'Diaye, A. T., Bleikamp, S., Feibelman, P. J. & Michely, T. Two-Dimensional Ir Cluster Lattice on a Graphene Moiré on Ir(111). *Phys. Rev. Lett.* **97**, 215501; doi: 10.1103/PhysRevLett.97.215501 (2006).
- N'Diaye, A. T. *et al.* A versatile fabrication method for cluster superlattices. *New J. Phys.* **11**, 103045; doi: 10.1088/1367-2630/11/10/103045 (2009).
- Gerber, T. *et al.* CO-Induced Smoluchowski Ripening of Pt Cluster Arrays on the Graphene/Ir(111) Moiré. *ACS Nano*; doi: 10.1021/nn400082w (2013).
- Franz, D. *et al.* Atomic Structure and Crystalline Order of Graphene-Supported Ir Nanoparticle Lattices. *Phys. Rev. Lett.* **110**, 065503; doi: 10.1103/PhysRevLett.110.065503 (2013).
- Wang, B. *et al.* Size-Selected Monodisperse Nanoclusters on Supported Graphene: Bonding, Isomerism, and Mobility. *Nano Lett.* **12**, 5907–5912; doi: 10.1021/nl303319f (2012).
- Tainoff, D. *et al.* Self-Organization of Size-Selected Bare Platinum Nanoclusters: Toward Ultra-dense Catalytic Systems. *J. Phys. Chem. C* **112**, 6842–6849; doi: 10.1021/jp710216s (2008).
- Bardotti, L., Tournus, F., Mélinon, P., Pellarin, M. & Broyer, M. Self organisation of Pt and Au clusters deposited on graphite: the role of reactivity. *Eur. Phys. J. D* **63**, 221–224; doi: 10.1140/epjd/e2011-10579-4 (2011).
- Meyer, J. C., Girit, C. O., Crommie, M. F. & Zettl, A. Hydrocarbon lithography on graphene membranes. *Appl. Phys. Lett.* **92**, 123110; doi: 10.1063/1.2901147 (2008).
- Banhart, F., Kotakoski, J. & Krasheninnikov, A. V. Structural Defects in Graphene. *ACS Nano* **5**, 26–41; doi: 10.1021/nn102598m (2011).
- Bardotti, L., Tournus, F., Mélinon, P., Pellarin, M. & Broyer, M. Mass-selected clusters deposited on graphite: Spontaneous organization controlled by cluster surface reaction. *Phys. Rev. B* **83**, 035425 (2011).

42. Ishigami, M., Chen, J. H., Cullen, W. G., Fuhrer, M. S. & Williams, E. D. Atomic Structure of Graphene on SiO₂. *Nano Lett.* **7**, 1643–1648; doi: 10.1021/nl070613a (2007).
43. Chepulskii, R. V. & Curtarolo, S. Ab Initio Insights on the Shapes of Platinum Nanocatalysts. *ACS Nano* **5**, 247–254; doi: 10.1021/nn102570c (2010).
44. Baletto, F. & Ferrando, R. Structural properties of nanoclusters: Energetic, thermodynamic, and kinetic effects. *Rev. Mod. Phys.* **77**, 371–423; doi: 10.1103/RevModPhys.77.371 (2005).
45. Doye, J. & Calvo, F. Entropic Effects on the Size Dependence of Cluster Structure. *Phys. Rev. Lett.* **86**, 3570–3573; doi: 10.1103/PhysRevLett.86.3570 (2001).
46. Tournus, F. Random nanoparticle deposition: inter-particle distances in 2D, 3D, and multilayer samples. *J. Nanoparticle Res.* **13**, 5211–5223; doi: 10.1007/s11051-011-0506-9 (2011).
47. Renaud, G. *et al.* Real-Time Monitoring of Growing Nanoparticles. *Science* **300**, 1416–1419; doi: 10.1126/science.1082146 (2003).
48. Lazzari, R. ISGISAXS: a program for grazing-incidence small-angle X-ray scattering analysis of supported islands. *J. Appl. Crystallogr.* **35**, 406–421; doi: 10.1107/S0021889802006088 (2002).
49. Renaud, G., Lazzari, R. & Leroy, F. Probing surface and interface morphology with Grazing Incidence Small Angle X-Ray Scattering. *Surf. Sci. Rep.* **64**, 255–380; doi: 10.1016/j.surfrep.2009.07.002 (2009).
50. Leroy, F., Renaud, G., Létoublon, A. & Lazzari, R. Growth of Co on Au(111) studied by multiwavelength anomalous grazing-incidence small-angle x-ray scattering: From ordered nanostructures to percolated thin films and nanopillars. *Phys. Rev. B* **77**, 235429; doi: 10.1103/PhysRevB.77.235429 (2008).
51. Leroy, F. *et al.* Kink ordering and organized growth of Co clusters on a stepped Au(111) surface: A combined grazing-incidence x-ray scattering and STM study. *Phys. Rev. B* **77**, 045430; doi: 10.1103/PhysRevB.77.045430 (2008).
52. Hosemann, R. & Bagchi, S. N. in *Direct analysis of diffraction by matter* (North-Holland, 1962).
53. Hattab, H. *et al.* Interplay of Wrinkles, Strain, and Lattice Parameter in Graphene on Iridium. *Nano Lett.* **12**, 678–682; doi: 10.1021/nl203530t (2012).
54. Baudoing-Savois, R. *et al.* A new UHV diffractometer for surface structure and real time molecular beam deposition studies with synchrotron radiations at ESRF. *Nucl. Instrum. Methods Phys. Res. Sect. B Beam Interact. Mater. At.* **149**, 213–227; doi: 10.1016/S0168-583X(98)00628-4 (1999).
55. Renaud, G. BM32. at <<http://www.esrf.eu/UsersAndScience/Experiments/CRG/BM32>>, (2014) (Date of acces 09/10/2014)
56. PLYRA. Plateforme PLYRA. *Plateforme PLYRA* at <<http://plyra.univ-lyon1.fr/>>, (2014) (Date of acces 09/10/2014)
57. Alayan, R. *et al.* Application of a static quadrupole deviator to the deposition of size-selected cluster ions from a laser vaporization source. *Rev. Sci. Instrum.* **75**, 2461–2470; doi: 10.1063/1.1764607 (2004).

Acknowledgments

We thank O. Boisron (ILM), O. Geaymond, and the staff of the BM32 beamline. Research supported by French ANR Contract No. ANR-2010-BLAN-1019-NMGEM.

Author Contributions

L.B., F.T. and G.R. initiated the study. F.J. and T.Z. performed the graphene synthesis; S.L., C.A., F.T. and L.B. involved in the clusters synthesis and deposition; T.Z., F.J., G.R., S.L. and F.T. performed the x-rays measurements; L.B. performed the STM imaging; C.A. designed and build the UHV transfer device. S.L. wrote the manuscript and prepared the figures. T.Z., F.J., G.R., S.L., L.B. and F.T. participated to the scientific discussion, analysed the data, reviewed the manuscript and the figures.

Additional Information

Supplementary information accompanies this paper at <http://www.nature.com/srep>

Competing financial interests: The authors declare no competing financial interests.

How to cite this article: Linas, S. *et al.* Moiré induced organization of size-selected Pt clusters soft landed on epitaxial graphene. *Sci. Rep.* **5**, 13053; doi: 10.1038/srep13053 (2015).



This work is licensed under a Creative Commons Attribution 4.0 International License. The images or other third party material in this article are included in the article's Creative Commons license, unless indicated otherwise in the credit line; if the material is not included under the Creative Commons license, users will need to obtain permission from the license holder to reproduce the material. To view a copy of this license, visit <http://creativecommons.org/licenses/by/4.0/>

Chapitre 2 : Modélisation et analyse de courbes de magnétométrie, pour une caractérisation précise des propriétés magnétiques de nanoparticules

Dans un souci de détermination la plus précise possible des propriétés magnétiques intrinsèques de nanoparticules, à partir de mesures macroscopiques sur des assemblées de particules diluées en matrice, nous avons développé (principalement en collaboration avec Alexandre Tamion) une méthodologie d'analyse et de modélisation de différents types de mesures de magnétométrie SQUID. Les questions auxquelles nous souhaitons répondre dans le cas des échantillons que nous étudions sont notamment : dans quelle mesure les interactions entre les particules affectent-elles le signal mesuré ? Quelle est la distribution de taille magnétique des particules ? Quelle est leur anisotropie magnétique ?

J'ai établi un modèle semi-analytique permettant de décrire de façon réaliste et efficace la réponse d'une assemblée de macrospins sans interactions lors d'une mesure de susceptibilité à bas champ selon le protocole ZFC/FC (zero-field cooled/ field cooled). Contrairement au modèle habituellement utilisé, qui suppose une transition abrupte entre le régime bloqué et le régime superparamagnétique, j'ai développé un modèle appelé « progressive crossover model » qui prend en compte le caractère progressif de l'évolution d'un régime bloqué vers un régime d'équilibre en fonction de la température [Tournus2011g, Tournus2011h]. À partir de l'expression de la susceptibilité (linéaire) d'une assemblée de macrospins, on peut en effet établir une équation différentielle simple décrivant le processus de mesure avec le protocole ZFC/FC, et l'on peut alors trouver des solutions approchées à cette équation, qu'il est possible de comparer aux solutions exactes. Afin de présenter plus en détail ce travail de modélisation, la publication « **Magnetic susceptibility curves of a nanoparticle assembly, I: Theoretical model and analytical expressions for a single magnetic anisotropy energy** » est reproduite ci-dessous.

Un des principaux résultats présentés dans cet article est la forme analytique approchée de la courbe ZFC, qui constitue une excellente approximation (cf. Fig. 1 de l'article). Cette expression reflète clairement le passage progressif entre le régime bloqué (moment magnétique M_b) et le régime d'équilibre (moment magnétique M_{eq}) :

$$M_{ZFC}^0(T) = M_b e^{-v\delta t} + M_{eq}(1 - e^{-v\delta t})$$

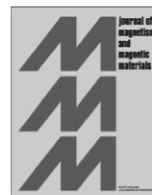
où intervient la fréquence de retournement des macrospin (modèle de Néel), qui dépend fortement de l'anisotropie K et de la température T : $v(T) = v_0 \exp\left(-\frac{K}{k_B T}\right)$, ainsi qu'un *temps de mesure effectif* δt lui-même dépendant de différents paramètres (notamment la température et la vitesse de balayage en température lors de la mesure, v_T) : $\delta t(T) \simeq 0.6727 \frac{T}{v_T} \left(\frac{K}{k_B T}\right)^{-0.9}$

Cet article discute également la notion de température de blocage, et examine le lien entre celle-ci (ou une température de transition, ainsi que la largeur de la transition) et les différents paramètres.



Contents lists available at ScienceDirect

Journal of Magnetism and Magnetic Materials

journal homepage: www.elsevier.com/locate/jmmm

Magnetic susceptibility curves of a nanoparticle assembly, I: Theoretical model and analytical expressions for a single magnetic anisotropy energy

F. Tournus^{a,b,*}, E. Bonet^c^a Université de Lyon, F-69000, France^b Univ. Lyon 1, Laboratoire PMCN, CNRS, UMR 5586, F69622 Villeurbanne Cedex, France^c CNRS/UJF, Institut Néel, BP 166, 38042 Grenoble Cedex 9, France

ARTICLE INFO

Available online 20 November 2010

Keywords:

Magnetic nanoparticle
Magnetic anisotropy
Magnetic susceptibility
Superparamagnetism
ZFC/FC curve

ABSTRACT

We study a model system made of non-interacting monodomain ferromagnetic nanoparticles, considered as macrospins, with a randomly oriented uniaxial magnetic anisotropy. We derive a simple differential equation governing the magnetic moment evolution in an experimental magnetic susceptibility measurement, at low field and as a function of temperature, following the well-known Zero-Field Cooled/Field Cooled (ZFC/FC) protocol. Exact and approximate analytical solutions are obtained, together for the ZFC curve and the FC curve. The notion of blocking temperature is discussed and the influence of various parameters on the curves is investigated. A *crossover temperature* is defined and a comparison is made between our *progressive crossover model* (PCM) and the crude “two states” or *abrupt transition model* (ATM), where the particles are assumed to be either fully blocked or purely superparamagnetic. We consider here the case of a single magnetic anisotropy energy (MAE), which is a prerequisite before considering the more realistic and experimentally relevant case of an assembly of particles with a MAE distribution (cf. part II that follows).

© 2010 Elsevier B.V. All rights reserved.

1. Introduction

The acquisition of magnetic susceptibility curves, following the zero field-cooled/field-cooled (ZFC/FC) protocol, is a common tool to investigate the magnetic behavior of nanoparticle assemblies. In these experiments, the separation between the FC and ZFC curves at a given temperature, together with a peak in the ZFC curve at T_{\max} is a signature of the magnetic anisotropy of the particles. This peak corresponds schematically to the transition from a blocked state to a superparamagnetic state. These measurements are widely used because they provide information on the magnetic anisotropy energy (MAE) of nanoparticles. This key parameter corresponds to the energy barrier that needs to be overcome to flip the magnetic moment from a direction of easy magnetization to the opposite direction: it then governs the stability of a nanomagnet.

Although a few theoretical studies have been devoted to ZFC/FC curves [1–7], to our knowledge, no theoretical derivation of an analytical expression of the magnetic moment for the entire temperature range for the ZFC and FC curves has been reported. Despite the fact that they are widespread in the nanomagnetism literature, ZFC/FC susceptibility curves remain in many cases underexploited. Experimental curves are often just qualitatively

analyzed, the only point of interest being the value of T_{\max} . When a fit of the entire curve is considered, the crude model proposed by Wohlfarth [8] with an abrupt blocked to superparamagnetic transition is always used [9–13]. In this model, a particle is supposed to be blocked (its magnetic moment does not change with T) as long as the temperature is below its *blocking temperature* T_B , and superparamagnetic (the macrospin switching is so frequent that the equilibrium value of the magnetic moment is observed) for $T > T_B$. T_B is taken as the temperature for which the relaxation frequency ν is equal to $1/\tau_{\text{meas}}$, where τ_{meas} is the measuring time of an isothermal experiment [14]. The “blocking” of a macrospin then clearly depends on the MAE of a particle (and thus, on its volume V), but also on the measuring time. One may wonder what is the “measuring time” in the case of a ZFC/FC experiment with a dynamical temperature sweep. Other questions one may ask are: how exactly is T_B related to the susceptibility peak? Can the progressive nature of the blocked to superparamagnetic crossover still be neglected for samples with a sharp size distribution? Moreover, the temperature of the ZFC peak, T_{\max} , is very often identified as the blocking temperature of an entire assembly of particles. Is this procedure right? What is the link between T_{\max} and the MAE? To answer these questions, a first necessary step is to investigate the behavior of an assembly of particles with a single MAE value. Then, we will be able to simulate ZFC/FC curves in order to reach a more precise determination of the MAE distribution from experimental curves.

In this paper, we establish a simple differential equation that allows to describe the progressive crossover from the blocked

* Corresponding author at: Univ. Lyon 1, Laboratoire PMCN, CNRS, UMR 5586, F69622 Villeurbanne Cedex, France.

E-mail address: florent.tournus@univ-lyon1.fr (F. Tournus).

regime to the superparamagnetic one. This framework fully takes into account the dynamical aspect of the ZFC/FC measurement. We find exact and approximate analytical solutions describing the ZFC/FC curves. The influence of each parameter is then investigated to get a comprehensive view on the susceptibility curves. Finally, the obtained results are compared with the crude “two states” or ATM model.

We consider here an assembly of magnetic particles having the same magnetic moment μ and the same MAE K . For the following, we make these simplifying assumptions. The ferromagnetic nanoparticles are treated as uniaxial macrospins, meaning that the individual spins are always colinear within one particle, with a coherent magnetization reversal between the two opposite easy magnetization directions: this is the well-known Stoner–Wohlfarth model [15] which is well-suited for small monodomain particles [16,17]. We also assume that the particles are far enough from each other so that they are not interacting (this corresponds to diluted samples of clusters embedded in a matrix, as those of Refs. [18–20]). The easy magnetization axes are supposed to be randomly oriented, as is the case in most experiments. The applied field H is supposed to be low enough so that the system displays a simple linear response (this approximation is discussed later). Finally, since the effect of temperature is mainly in the exponential variation of the relaxation frequency $\nu = \nu_0 \exp[-K/(k_B T)]$, we neglect the dependence of μ , K and ν_0 with T . In most cases, these variations only have a marginal effect on the curves: for pathological cases, they could easily be included in the model we describe (differential equation), however, precluding the use of analytical expressions.

2. Differential equation governing the magnetic moment evolution

2.1. Parallel and perpendicular susceptibility

For the linear response of a magnetic particle to an applied field, the following relation holds in the case of an angle ϕ between the magnetic field direction and the anisotropy axis:

$$\chi(\phi) = \cos^2 \phi \chi_{\parallel} + \sin^2 \phi \chi_{\perp}$$

which gives for an assembly of randomly oriented macrospins, upon averaging over all angles ϕ ,

$$\tilde{\chi} = \frac{1}{3} \chi_{\parallel} + \frac{2}{3} \chi_{\perp}$$

The equilibrium susceptibility can be calculated, as a function of the dimensionless parameter $\sigma = K/(k_B T)$, and can be expressed as [21,22]

$$\chi_{\parallel} = \chi_0(1+2S) \quad \text{and} \quad \chi_{\perp} = \chi_0(1-S)$$

where $\chi_0 = \mu_0 \mu^2 / (3k_B T V)$ and S is the average of the second Legendre polynomial, which depends on σ [21,22]. Note that the particle volume V is involved since the susceptibility, which is a dimensionless quantity, is defined as the ratio between the *magnetization* and the applied field H . As it can be seen from these expressions, we recover the well-known result

$$\tilde{\chi} = \chi_0 = \frac{\mu_0 \mu^2 / V}{3k_B T}$$

which shows that the equilibrium susceptibility of a randomly oriented assembly of macrospins simply follows the Curie law and does not depend on the magnetic anisotropy value. Note that, on the other hand, the parallel and perpendicular components of the susceptibility depends on σ : if we use the asymptotic expression of S including the first order correction in $1/\sigma$, namely $S \simeq 1 - 3/(2\sigma)$, we can write for $\sigma \gg 1$

$$\chi_{\parallel} \simeq \frac{\mu_0 \mu^2 / V}{k_B T} - \frac{\mu_0 \mu^2 / V}{K} \quad \text{and} \quad \chi_{\perp} \simeq \frac{\mu_0 \mu^2 / V}{2K}$$

2.2. Dynamical behavior and average susceptibility

The previous expressions have been established for the equilibrium case, while we are concerned by a dynamical phenomenon in the case of ZFC/FC curves. By introducing the relaxation times τ_{\parallel} and τ_{\perp} , we can write [21–23]

$$\chi_{\parallel}(\omega) = \frac{\chi_{\parallel}}{1+i\omega\tau_{\parallel}} \quad \text{and} \quad \chi_{\perp}(\omega) = \frac{\chi_{\perp}}{1+i\omega\tau_{\perp}}$$

where τ_{\parallel} is related to the interwell mode (macrospin switching) while τ_{\perp} is related to intrawell relaxation. These two relaxation times are then completely different: in particular, τ_{\parallel} grows as $\exp(\sigma)$ for large σ , whereas τ_{\perp} remains of the order of $\tau_0 = 1/\nu_0$ (relaxation time of the Larmor precession). Since τ_0 is very small, typically of the order of 10^{-10} s, it is then legitimate to set $\omega\tau_{\perp} \ll 1$ in the above equation, especially when dealing with “quasistatic” measurements such as ZFC/FC curves. The average dynamic susceptibility then reads, replacing τ_{\parallel} by τ for simplicity,

$$\tilde{\chi}(\omega) = \frac{1}{3} \frac{\chi_{\parallel}}{1+i\omega\tau} + \frac{2}{3} \chi_{\perp} = \frac{\chi_0 + i\omega\tau \frac{2}{3} \chi_{\perp}}{1+i\omega\tau}$$

We can also write,

$$\tilde{\chi}(\omega) = \frac{\chi_{eq} + i\omega\tau\chi_b}{1+i\omega\tau} \quad (1)$$

with $\chi_{eq} = \chi_0$ and $\chi_b = 2\chi_{\perp}/3$. This makes very clear the crossover from the equilibrium regime ($\omega\tau \ll 1$ and $\tilde{\chi} \simeq \chi_{eq}$) to the blocked regime ($\omega\tau \gg 1$ and $\tilde{\chi} \simeq \chi_b$). This equation has been used many times in the frame of AC susceptibility measurements [21–26].

2.3. Differential equation and solution for a fixed temperature

Knowing $\tilde{\chi}$ allows us to express the total magnetic moment of the sample, M (the letter M will always refer to a moment and not a magnetization). For the sake of simplicity we omit, as we will always do in the following, the total number of particles N_{tot} which simply appears as a prefactor in the value of M . Considering the magnetic moment component $M(\omega) = V\tilde{\chi}(\omega)H(\omega)$ which gives, according to Eq. (1),

$$M(\omega)(1+i\omega\tau) = V(\chi_{eq} + i\omega\tau\chi_b)H(\omega)$$

Going from a frequency representation to a time representation, we obtain the following differential equation for the magnetic moment of an assembly of randomly oriented macrospins

$$\frac{1}{\nu} \frac{dM}{dt} + M = V \left(\chi_{eq} H + \frac{1}{\nu} \chi_b \frac{dH}{dt} \right) \quad (2)$$

We have used here the relaxation frequency $\nu = 1/\tau$ instead of the relaxation time.

In the case of a ZFC/FC susceptibility measurement the applied field H is constant, so that the last term in the right hand side of Eq. (2) disappears. It only plays a role in the initial setting of the field at low temperature, after zero field-cooling and before starting the ZFC curve acquisition: χ_b will just control the initial value (at $T \rightarrow 0$) of the magnetic moment. We then obtain a very simple differential equation governing the magnetic moment behavior during a ZFC/FC measurement:

$$\frac{1}{\nu} \frac{dM}{dt} + M = \frac{\mu_0 \mu^2 H}{3k_B T} \quad (3)$$

with the initial condition $M(t \rightarrow 0) = M(T \rightarrow 0) = M_b$, where

$$M_b = V\chi_b H = \frac{\mu_0 \mu^2 H}{3K}$$

and the relaxation frequency ν given by

$$\nu(T) = \nu_0 \exp\left(-\frac{K}{k_B T}\right)$$

This result is the central equation from which we will derive the expressions of ZFC and FC curves. It is valid as long as the observation/evolution time is much longer than τ_0 ($\omega\tau_0 \ll 1$ condition). Note that it is valid at any temperature, not only for low temperature (when $\sigma \gg 1$): in particular it simply gives $M = M_{eq}$ when $\sigma \rightarrow 0$. The only use of the $\sigma \gg 1$ assumption is for the simplified expression of χ_b (up to the $1/\sigma$ order), which just appears in the initial condition i.e. at very low temperature (typically 2 K) where it is highly reasonable. Moreover, it is always possible to use higher order developments of $\chi_{\perp}(\sigma)$ for a tiny gain of precision in the initial value M_b . Note also that for the ν_0 frequency we can either assume that it is a constant, as we will do here, or use more elaborate expressions where it varies with σ [27–29]. However, such an expression would certainly preclude the obtention of an analytical solution of Eq. (3). In addition, since the main variation of ν with temperature T comes from the exponential term, a temperature variation of ν_0 has almost no visible effect on the ZFC/FC curves.

The integration of Eq. (3) is straightforward for a fixed temperature. When the value of the magnetic moment for $T \rightarrow 0$ is taken as the initial condition, we can write

$$\begin{aligned} M(t) &= \frac{\mu_0 \mu^2 H}{3K} e^{-\nu t} + \frac{\mu_0 \mu^2 H}{3k_B T} (1 - e^{-\nu t}) \\ &= M_b e^{-\nu t} + M_{eq} (1 - e^{-\nu t}) \end{aligned}$$

This expression makes clear the crossover, with increasing time, from the blocked magnetic moment $M_b = \mu_0 \mu^2 H / (3K)$ to the equilibrium (i.e. superparamagnetic) moment $M_{eq} = \mu_0 \mu^2 H / (3k_B T)$.

3. Solution in the case of a temperature sweep

We now assume that the temperature is varied at a constant rate $dT/dt = \nu_T$. The time t can then be removed from the differential equation and we have

$$\frac{\nu_T}{\nu(T)} \frac{dM}{dT} + M = M_{eq}(T)$$

We will first put a particular emphasis on the case of a ZFC curve (i.e. $\nu_T > 0$), and we will obtain approximate analytical solutions by deriving expressions of general and particular solutions of the differential equation. Indeed, let us remind the reader that a solution of this first order linear differential equation is given by the sum of two terms:

$$M = M_g + M_p$$

where the *general* solution M_g is the solution with the right-hand-side term equal to zero, and M_p is a particular solution of the complete equation.

Further, by using a different method, we will derive exact expressions (but much more complicated) both for the ZFC and the FC curve.

3.1. General and particular solutions

The general solution can be written

$$M_g = \alpha \exp\left[-\int_0^T \frac{\nu(u)}{\nu_T} du\right]$$

and we will try to get a simple expression of the integral term

$$\int_0^T \frac{\nu(u)}{\nu_T} du = F(T) - F(0)$$

In fact, using the incomplete gamma function Γ , we can express exactly $F(T)$ as

$$F(T) = \frac{\nu(T)T}{\nu_T} - \frac{K\nu_0}{k_B\nu_T} \Gamma\left(0, \frac{K}{k_B T}\right)$$

which can be written, using the dimensionless ratio $\sigma = K/(k_B T)$,

$$F(T) = \frac{\nu(T)T}{\nu_T} p(\sigma) \quad \text{where} \quad p(\sigma) = 1 - \sigma e^{\sigma} \Gamma(0, \sigma)$$

For $\sigma \gg 1$, we have $p(\sigma) \simeq 1/\sigma$ and we can simply write

$$F(T) = \nu(T)\delta t \quad \text{with} \quad \delta t \simeq \frac{k_B T^2}{\nu_T K}$$

This approximate result has already been derived by Chantrell and Wohlfarth [1], who had investigated the effect of the temperature sweeping rate on the field-cooled magnetization. However, we can develop further $p(\sigma)$ in powers of $1/\sigma$, or alternatively fit $p(\sigma)$ with a power law which is a better approximation, and on a much wider range of σ values (i.e. of temperatures). This provides a different, but still convenient, expression for δt

$$\delta t(T) \simeq 0.6727 \frac{T}{\nu_T} \left(\frac{K}{k_B \nu_T}\right)^{-0.9} \quad (4)$$

Since $p(\sigma) \rightarrow 0$ when $\sigma \rightarrow \infty$, $F(0) = 0$ and we finally get this simple expression for the general solution of the differential equation:

$$M_g = \alpha \exp[-\nu(T)\delta t(T)] \quad (5)$$

We now come to the particular solution of the differential equation. Without any loss of generality, we can write

$$M_p = f(T) \exp\left[-\int_0^T \frac{\nu(u)}{\nu_T} du\right]$$

where the function $f(T)$ must satisfy

$$\frac{df}{dT} = M_{eq}(T) \frac{\nu(T)}{\nu_T} \exp\left[\int_0^T \frac{\nu(u)}{\nu_T} du\right]$$

which corresponds to

$$f(T) = \int_0^T M_{eq}(T_0) \frac{\nu(T_0)}{\nu_T} e^{F(T_0)} dT_0$$

Then, by using $F_0 = F(T_0)$ instead of the integration variable T_0 , and noting that $dF_0/dT_0 = \nu(T_0)/\nu_T$, we obtain

$$f(T) = \int_0^F M_{eq}(F_0) e^{F_0} dF_0$$

where we use the simple notation F for $F(T)$. In the end, this leads to a quite simple expression, which is exact at this point, for a particular solution of the differential equation:

$$M_p = \int_0^F M_{eq}(F_0) \exp(F_0 - F) dF_0 \quad (6)$$

3.2. Zeroth and first order approximations

Since the term $\exp(F_0 - F)$ in Eq. (6) decreases extremely fast when F_0 moves away from F , we can neglect the variation of M_{eq} with F_0 and simply replace it with $M_{eq}(F)$. This is what we call the *zeroth order approximation*. M_{eq} can then be taken out of the integral, which can be immediately calculated to give

$$M_p = M_{eq}(T) [1 - e^{-F(T)}]$$

Using the expression of the general solution (see Eq. (5)) and taking into account the initial condition $M(T=0) = M_b$, we obtain a simple analytical expression, to the zeroth order, for the evolution

of the magnetic moment of the ZFC curve:

$$M_{ZFC}^0(T) = \frac{\mu_0 \mu^2 H}{3K} e^{-v\delta t} + \frac{\mu_0 \mu^2 H}{3k_B T} (1 - e^{-v\delta t}) \quad (7)$$

that we can write, as for the solution at a fixed temperature:

$$M_{ZFC}^0(T) = M_b e^{-v\delta t} + M_{eq}(1 - e^{-v\delta t})$$

This shows in a very transparent way the crossover between the blocked magnetic moment and the superparamagnetic one, as a function of temperature. Remarkably, the expression is exactly the same as for a fixed temperature, with the time t replaced by the timescale δt , which depends on T and on other parameters (in particular the temperature sweeping rate v_T , see Eq. (4)). Thus, measuring the moment at temperature T after a sweep from zero temperature is equivalent to immediately set the temperature to T and wait for a time δt . As will be discussed further, the crossover between the two regimes corresponds to a susceptibility peak around a temperature usually referred as the *blocking temperature*, whose definition and significance will be discussed later.

We can obtain a more accurate approximation, inevitably at the expense of a more complicated expression, by taking into account the variation of M_{eq} in the integral involved in M_p . If we make a first order development of M_{eq} around F , we obtain

$$M_{eq}(F_0) \simeq M_{eq}(F) - \frac{M_b}{F}(F_0 - F)$$

where we have used the approximate value $\delta t \simeq k_B T^2 / (v_T K)$ in the expression of $F(T) = v(T)\delta t(T)$ to calculate the derivative

$$\frac{dM_{eq}}{dF_0} = \frac{dM_{eq}}{dT_0} \left(\frac{dF_0}{dT_0} \right)^{-1}$$

This allows us to write $M_p^1 = M_p^0 + \delta M_p$, corresponding to the *first order approximation*, where M_p^0 is the zeroth order solution seen before and

$$\delta M_p = \frac{M_b}{F(T)} \int_0^F u e^{-u} du$$

Consequently, the first order correction term can be expressed as

$$\delta M_p(T) = M_b \frac{1 - e^{-v\delta t}(1 + v\delta t)}{v\delta t}$$

which is always positive and goes to zero when $T \rightarrow 0$ and $T \rightarrow \infty$: it only modifies the ZFC curve around the crossover from the blocked to

the superparamagnetic state. However, it remains negligible since the ratio $\delta M_p / M_{ZFC}^0$ never exceeds 2%. Nevertheless, looking at the detail of the curve around the susceptibility peak, the first order approximation is necessary if we want to correctly reproduce the crossing between the exact ZFC and FC curves (see further and Fig. 1). Since the correction δM_p does not alter the initial value of the magnetization at $T = 0$, it simply adds to the zeroth order solution and we can write, within the first order approximation:

$$M_{ZFC}^1(T) = M_b e^{-v\delta t} + M_{eq}(1 - e^{-v\delta t}) + \delta M_p(T) \quad (8)$$

3.3. Exact solution: expressions for the FC and ZFC curves

We will now use another strategy to derive an expression for the solutions of the differential equation. Let us consider the temperature sweep as a succession of “plateaus” where the differential equation can be solved exactly. The magnetic moment at the end of a plateau is then used as the initial condition for the determination of M on the following temperature plateau.

We will first consider the case of the FC curve where the starting point is at a high enough temperature T_m for which the system is superparamagnetic and the magnetic moment is simply $M \simeq M_{eq}$. We can then easily write the value of $M(T_m - dT, t)$ and then $M(T_m - 2dT, t)$ and so on. This allows us to reach, in the limit of $dT \rightarrow 0$ while keeping $dT/dt = v_T$, a general expression of $M_{FC}(T)$:

$$M_{FC}(T) = \int_T^{T_m} -\frac{M_b K}{k_B T_0^2} e^{-\int_T^{T_0} v(u) du / v_T} dT_0 + M_{eq}(T)$$

We can rewrite the integral in the exponential term and let $T_m \rightarrow \infty$ to get a more condensed expression:

$$M_{FC}(T) = \int_T^\infty \frac{M_b K}{k_B T_0^2} (1 - e^{[v(T)\delta t(T) - v(T_0)\delta t(T_0)]}) dT_0$$

Note that this analytical expression constitutes an *exact* solution of the differential equation (what can quite easily be verified by calculating dM/dT). However, the fact that it involves an integral makes it difficult to implement efficiently in numerical calculations.

By applying the same method, with a succession of temperature plateaus, starting from $M = M_b$ at $T = 0$ K, we can establish the general expression of the ZFC curve. We find

$$M_{ZFC}(T) = M_b e^{-v\delta t} + M_{eq}(1 - e^{-v\delta t}) + \Delta(T)$$

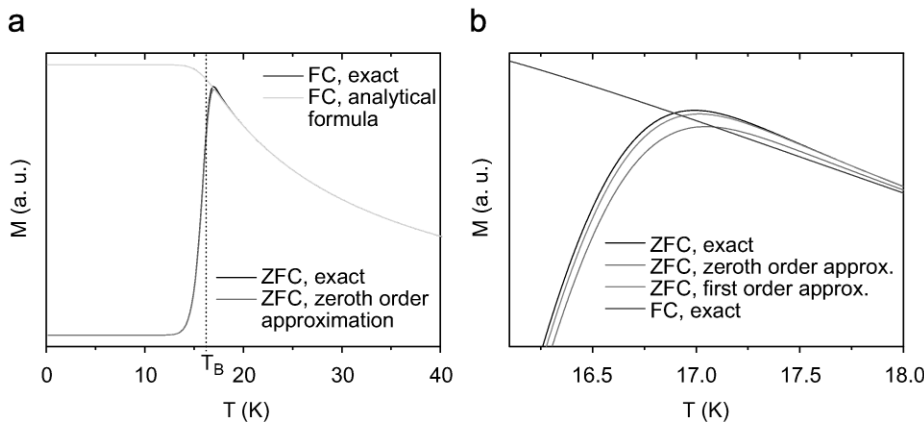


Fig. 1. (a) Comparison between the exact ZFC and FC curves (obtained by direct integration of the differential equation) and the analytical formulas (see text). For the ZFC curve, only M_{ZFC}^0 is displayed since analytical ZFC curves of higher precision are undistinguishable from the exact one. Note that the exact FC curve is undistinguishable from the analytical one. (b) Comparison between the exact ZFC curve (black line), the zeroth order approximation M_{ZFC}^0 (red line) and the first order approximation M_{ZFC}^1 (pink line), in a very narrow temperature range around the susceptibility peak. These curves differ by the way they cross the FC curve (blue line). The calculations correspond to the case of particles with a 4 nm diameter, a saturation magnetization $M_{sat} = 7.45 \times 10^5$ A/m and an anisotropy constant $K_{eff} = 1.6 \times 10^5$ J/m³, $v_T = 0.018$ K/s and $v_0 = 10^9$ Hz, which corresponds to a blocking temperature $T_B \simeq 16$ K. (For interpretation of the references to colour in this figure legend, the reader is referred to the web version of this article.)

where the function $\Delta(T)$ appears as a correction to the zeroth order solution, and is defined by

$$\Delta(T) = M_b e^{-v(T)\delta t(T)} \int_0^T \frac{K}{k_B T_0^2} [e^{v(T_0)\delta t(T_0)} - 1] dT_0$$

Whereas the previous expressions of the ZFC curve were approximations, it is important to note that this solution is *exact* (once more, this can be verified by calculating dM/dT). However, as for the FC curve, using this exact expression involves costly numerical calculations, while the $\Delta(T)$ term only appears as a minor correction to M_{ZFC}^0 . Therefore, the zeroth order approximation, which is very convenient to manipulate and completely intuitive (a simple balance between M_b and M_{eq} , changing with temperature), will be accurate enough in most practical cases and should thus be preferred (see Fig. 1).

4. Discussion

4.1. Maximum of the ZFC and ZFC/FC curve crossing

The value of the ZFC curve maximum (susceptibility peak), which occurs at a temperature T_{max} can be directly derived from the differential equation. Indeed, by setting $dM/dT = 0$, we obtain the exact relation:

$$M_{ZFC}(T_{max}) = \frac{\mu_0 \mu^2 H}{3k_B T_{max}} = M_{eq}(T_{max})$$

For $T > T_{max}$, the ZFC curve is decreasing and $dM/dT < 0$ which means that, according to the differential equation, $M_{ZFC}(T) > M_{eq}(T)$. On the other hand, since the FC curve is always decreasing with temperature, the consequence is that $M_{FC}(T) \leq M_{eq}(T)$ for any T . These remarks show that for $T = T_{max}$ the ZFC curve is necessarily *above* the FC curve and remains so for higher temperatures. Since at low temperature we have on the contrary $M_{ZFC} < M_{FC}$, there must be a crossing between the two curves at a given temperature just below T_{max} . This feature, which has never been discussed to our knowledge, is completely unintuitive (we are not talking here of an artificial curve crossing coming from experimental artefacts, which may have already been observed). Moreover, as noted previously, the zeroth order approximation of the ZFC curve does not allow to reproduce satisfactorily this crossing between the FC and ZFC curves, whereas the first order approximation appears to be much more successful (see Fig. 1).

4.2. Final value of the FC curve for $T \rightarrow 0$ K

The final value, for $T \rightarrow 0$ K, of the magnetic moment for the FC curve, noted M_0 , can be calculated with the exact formula

$$M_0 = \int_0^\infty \frac{M_b K}{k_B T^2} [1 - e^{-v(T)\delta t(T)}] dT$$

where, for practical numerical evaluation, is it of course neither necessary to perform the integration from $T=0$ K (the integrand is almost zero) nor to go to $T \rightarrow \infty$ (the exponential term becomes rapidly negligible).

This integral expression of M_0 allows us to study the influence of the various parameters, without the need to compute entire FC curves by a direct numerical integration of the differential equation. The quite simple formula of M_0 does in fact not allow us to see “at a glance” its evolution with the parameters of the problem. For instance, the factor $M_b K$, which is proportional to V^2 (since it is proportional to μ^2) could let us think that M_0 shows the same proportionality with V . As we will see further, it is, however, not the case: M_0 is instead almost proportional to V , which comes from the fact that v and δt also depends on V .

4.3. Is the FC curve similar to a ZFC curve? Irreversibility of the FC curve

Even if the magnetic moment satisfies the same differential equation for the ZFC and FC curve (it should still be noted that the sign of the v_T term is changed), the M_{FC} curve has no reason to be identical to a M_{ZFC} curve starting from a moment M_0 at 0 K. As a matter of fact, when both curves are simulated (by a direct numerical integration of the differential equation, or by using the above formulae), we see a clear difference between the two curves around the blocking temperature. Whereas the true FC curve is monotonous, the ZFC starting from M_0 shows a small peak (see Fig. 2). This demonstrates that increasing the temperature after having measured a FC curve down to $T \simeq 0$ K does not produce the same curve: there is *irreversibility*.

Nevertheless, for experimental measurements on real samples where there is necessarily an anisotropy dispersion, this irreversibility may not be visible. In fact, the FC curve is even often recorded with an increasing temperature sweep, for practical reasons. This apparent loss of irreversibility can be explained by some kind of “blurring” effect [30] due to the dispersion of the various parameters: the irreversibility which exists for a single anisotropy energy may be extremely difficult to observe experimentally. Moreover, a ZFC curve

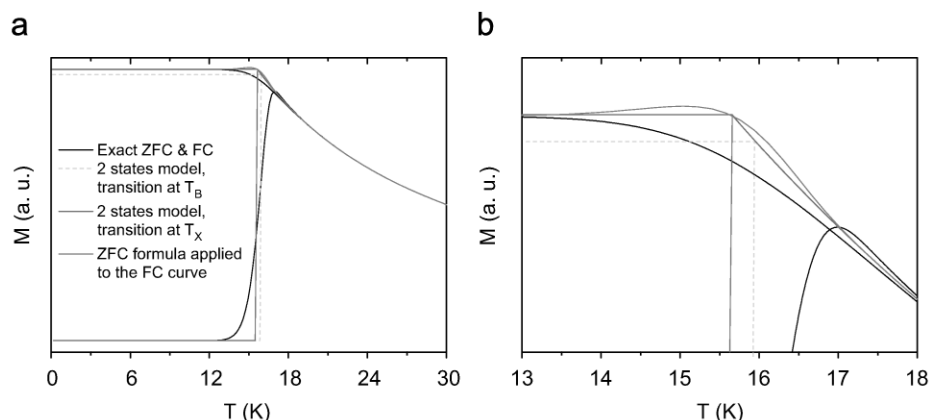


Fig. 2. (a) Comparison between the exact ZFC/FC curves (black lines) and the two states model with an abrupt transition between the blocked regime and the superparamagnetic one. In one case the transition is at the blocking temperature T_B (green line), whereas in the other case it is at T_X (red line), which is obviously a better choice. A FC curve, computed with the M_{ZFC}^0 formula, starting from an initial moment M_0 is also shown (pink curve): it appears to be very close to the two states model. (b) Enlarged view of the same curves as in (a), around the crossover temperature. The calculation parameters are the same as those of Fig. 1. (For interpretation of the references to colour in this figure legend, the reader is referred to the web version of this article.)

starting from M_0 is not too bad an approximation of the FC curve since it has the correct behavior both for $T \rightarrow 0$ K and for $T \rightarrow \infty$. It is then obvious that the deviation will be significant only in the region of the crossover between the blocked regime and the superparamagnetic regime.

4.4. Definition and meaning of the blocking temperature T_B

The blocking temperature T_B is usually defined by the relation [14]

$$T_B = \frac{K}{k_B \ln(v_0 \tau_{\text{meas}})} \quad (9)$$

where τ_{meas} is an effective time of measurement of the magnetic moment, typically around 100 s (it can vary between less than a second to a few hundreds of seconds). By taking $\ln(v_0 \tau_{\text{meas}}) \simeq 25$, which corresponds to $\tau_{\text{meas}} \simeq 7$ s with a v_0 of 10^{10} Hz, we recover the relation $K \simeq 25k_B T_B$ frequently met in the literature. Eq. (9) simply states the fact that for $T = T_B$, the relaxation frequency of the macrospins is equal to the inverse of the measurement time: $\nu(T_B) = 1/\tau_{\text{meas}}$. It is then obvious that the blocking temperature depends on the experimental technique and the procedure used.

In the case of ZFC/FC susceptibility curves, there is a dynamical measurement with a temperature sweep and not a static measurement at a fixed temperature during a time τ_{meas} . On the other hand, the approximate analytical expression (to the zeroth order) of the ZFC curve is identical to the one established for a fixed temperature, but with a term δt that can be considered as an effective measurement time, which depends on the temperature. Since the ZFC magnetic moment at temperature T , after a temperature sweep, is the same as the one we would have measured after having immediately set the temperature from 0 to T and then waited during a time δt , the term *effective waiting time* would be more appropriate for δt . By reproducing the initial definition of T_B , we can then define the blocking temperature of a dynamical ZFC curve [1] with the relation

$$\nu(T_B) \delta t(T_B) = 1 \quad \text{i.e.} \quad T_B = \frac{K}{k_B \ln(v_0 \delta t)} \quad (10)$$

Eq. (10) is in fact an implicit relation on T_B since δt depends on T . Even with approximate expressions for δt , it cannot be solved in a direct way. However, it is possible to determine T_B from this equation by a self-consistent resolution scheme. In addition, we will derive later an approximate analytical relation between T_B and the parameters involved in this problem (v_0 , K , ν_T).

Qualitatively, the blocking temperature corresponds to the temperature where the system goes from a blocked regime to the superparamagnetic one, but we know that this is in fact a progressive crossover, even for a single anisotropy energy. On the ZFC curve, T_B is related to the susceptibility peak, but it should be kept in mind that it is not identical to the temperature T_{max} where the maximum is reached. With the above definition, T_B is slightly below T_{max} but it is neither the inflection point of the curve, nor the point situated at the half the maximum value (see Fig. 1). Moreover, as established before, the ZFC expression (at the zeroth order) can be viewed as a mixing of two components corresponding to the two extreme behaviors: blocked, i.e. with a constant magnetic moment; and superparamagnetic, i.e. with a moment varying as $1/T$. The “weight” of the blocked contribution is given by $\exp[-\nu(T)\delta t(T)]$ and is consequently equal to $1/e \simeq 0.37$ when $T = T_B$. This shows that T_B is not the temperature for which the system is “half blocked” and “half superparamagnetic”: at T_B , we are closer to the superparamagnetic regime than to the blocked one. We insist on the fact that in the case of a single anisotropy energy, even if T_{max} and T_B are very close to one another (see further), these two temperatures are not identical, contrary to what is often believed. The temperature dependent T_B may seem quite unphysical or even useless.

We, however, emphasize that its definition exactly reflects the usual one where the time needed to reach temperature T is neglected.

4.4.1. Evolution of T_B with the parameters

In our model, five parameters (H , μ , K , v_0 and ν_T) entirely determine the susceptibility curves. The influence of H is trivial because we assume that it is small enough to be in the linear response frame: it just changes the amplitude of the curves, not their shape. The scaling with μ is also obvious from the analytical expressions of the curves: they vary proportionally to μ^2 , as it was expected from the values of M_b and M_{eq} . Therefore, the three parameter set (K , v_0 , ν_T) controls the shape of the ZFC/FC curves, and in particular the value of T_B . Moreover, we expect T_B to be roughly proportional to the anisotropy energy K , i.e. to the ratio K/k_B which has the right dimension. Without any loss of generality, we can then write $T_B = (K/k_B) \times f(y)$, where $f(y)$ is a function of the dimensionless number $y = v_0 K / (k_B \nu_T)$ that can be constructed with the three parameters.

In order to get an analytical relation between T_B and the various parameters, $f(y)$ needs to be determined. This function can be inferred from the computed value of T_B for a great number of parameters sets. We find from numerical studies that f can be modelled, to an excellent approximation on a very wide range of parameters, by a linear function of $\ln(y)$. Thus, a best fit provides the useful relation

$$T_B = \frac{K/k_B}{0.927 \ln\left(\frac{v_0 K}{k_B \nu_T}\right) - 4.19} \quad (11)$$

which allows us to directly compute T_B , with a high precision, for a given set of parameters. We can see that the ratio $x = K/(k_B T_B)$ is not a constant (usually assumed to be equal to 25) but slightly depends on the MAE itself and other parameters. Therefore, the intuitive idea that the blocking temperature is directly proportional to the anisotropy K is true only to some extent. This means that, strictly speaking, the anisotropy distribution of an assembly is not identical to the blocking temperature distribution. Another way to account for this feature is to consider that the effective measurement time τ_{meas} , that must be used to compute T_B (using Eq. (9)), depends on the parameters, and especially on K .

4.5. Comparison with the “two states model”: temperature and width of the crossover

A quite crude model, that we shall call the “two states model” or ATM (abrupt transition model), is widely used in the literature [8–13] when dealing with superparamagnetic nanoparticles. It corresponds to the case of an extremely abrupt transition: particles are either fully blocked (constant magnetic moment), or purely superparamagnetic (magnetic moment varying as $1/T$ [31]). This model completely dismisses the detailed evolution of the magnetic moment around the crossover (i.e. near T_B): we know that in fact the crossover between the two regimes is gradual. Nevertheless, this simple model appears to be very easy to handle, especially to simulate the behavior of an assembly of particles with a MAE distribution. The case of such an assembly will be addressed in the following article (part. II) [30], but here we compare the more elaborate expressions we have derived, which constitutes the *progressive crossover model* (PCM), to the simple ATM. Let us emphasize that, even if this model captures the essential variations of the resulting magnetic moment with temperature, a better description of the detailed behavior around T_B could be relevant for the investigation of well-defined samples with a low MAE dispersion (whereas we expect this crude model to be successful in the

case of samples with a broad dispersion, thanks to a “blurring” effect [30]).

In the “two states model”, the blocking temperature is always taken as the transition temperature: as far as the ZFC is concerned, $M=M_b$ for $T < T_B$ and $M=M_{eq}$ for $T > T_B$. This is indeed quite a good approximation because the two limits ($T \rightarrow 0$ K and $T \rightarrow \infty$) are correctly described. For the FC curve, which is rarely considered, it is assumed that the blocked value is given by $M_{eq}(T_B)$. This assumption is in fact slightly erroneous: the final value of the magnetic moment in the blocked state M_0 is different from $M_{eq}(T_B)$, as it can be seen on Fig. 2. On the other hand, it is convenient to define a *crossover temperature* T_X such that $M_0 = M_{eq}(T_X)$, which is equivalent to $T_X = \mu_0 \mu^2 H / (3k_B M_0)$. Using T_X as the “frontier” between the blocked and superparamagnetic regime will then correspond to an improved ATM, having the correct behavior for $T \rightarrow 0$ K and $T \rightarrow \infty$ both for the ZFC and FC curves (see Fig. 2).

In the same way that for T_B , we can study numerically the variation of M_0 with the parameters. We find that the relation $M_0 = M_b [0.9283 \ln(y) - 3.69]$ produces a very good agreement with the numerical simulations (note that this means that M_0 is almost proportional to V). This corresponds to

$$T_X = \frac{K/k_B}{0.9283 \ln\left(\frac{v_0 K}{k_B v_T}\right) - 3.69}$$

This also corresponds to $T_B/T_X = 1.0015 + 0.5/x$, with $x = K/(k_B T_B)$, which gives $T_X \approx 0.98T_B$ in realistic cases where $x \approx 25$.

Whereas the transition from the blocked to the superparamagnetic regime is abrupt within the ATM, it is in fact gradual within a more realistic description (PCM): even for a single anisotropy energy, the crossover has a finite width. We will see how this width is controlled by the various parameters. Let us denote ΔM the difference $M_{FC} - M_{ZFC}$, $T_{10\%}$ the temperature for which we have $\Delta M = 0.1\Delta M(0)$, and $T_{90\%}$ $\Delta M = 0.9\Delta M(0)$. The temperature interval $\Delta T = T_{10\%} - T_{90\%}$ is then used as a numerical quantity to measure the crossover “width”. A large set of simulations shows that ΔT is almost proportional to T_B , and allows us to derive the following analytical relation (coming from a fit):

$$\frac{\Delta T}{T_B} = \frac{1.1075}{1 + 0.3548x}$$

where $x = K/(k_B T_B)$ is usually taken to be 25, but in fact may vary (see Eq. (11)) moderately for realistic systems (typically from 20 to 30). This shows that ΔT varies approximately linearly with K (or T_B), and we can keep in mind that, as long as $x \approx 25$, $\Delta T/T_B$ is around 10%. The knowledge of this crossover width will be of great help to decide whether it can be neglected or not, in the case of real systems with an anisotropy dispersion.

4.6. Position and amplitude of the ZFC peak

The crude relation $K \approx 25k_B T_B$ is often used as a simple “rule of thumb” method to infer the value of the magnetic anisotropy from the “blocking temperature” observed in an experimental ZFC curve. However, as mentioned earlier, the blocking temperature does not correspond to any remarkable point of the ZFC susceptibility peak: consequently, T_B is in fact identified to the temperature T_{max} of the peak. It is thus interesting to study how T_{max} is related to T_B . Numerical simulations allows us to establish, with an excellent approximation, an analytical expression of the ratio T_B/T_{max} as a function of the parameter $x = K/(k_B T_B)$:

$$\frac{T_B}{T_{max}} = 0.9844 - \frac{1.0415}{x}$$

As for the crossover temperature T_X , this ratio is almost constant, as long as realistic physical systems are concerned (with x around 25).

Thus, we may apply this simple relation for most cases of interest:

$$T_{max} \approx 1.06T_B$$

Moreover, we can establish [32] that, as for T_B , T_{max} does not vary strictly linearly with K contrary to common belief.

Let us now turn to the susceptibility peak height $M_{max} = M_{ZFC}(T_{max})$. As demonstrated above, we can write exactly $M_{max} = M_{eq}(T_{max})$, which corresponds to $M_{max} = M_b K / (k_B T_{max})$. Finally, according to the analytical expression of T_{max} , we can write

$$M_{max} = M_b (0.9844x - 1.0415)$$

which shows that M_{max} is almost proportional to M_b . The factor of proportionality is approximately 23.6 (value corresponding to the “reference” case where $x = 25$).

4.7. Influence of experimental parameters: temperature sweeping rate and residual magnetic field

The influence of the temperature sweeping rate on FC curves has already been investigated by Chantrell and Wohlfarth [1], in a search to qualitatively reproduce experimental observations. v_T is indeed a parameter that can easily be controlled in an experiment, which is not the case of K or v_0 . The investigation of a particular system at various sweeping rates will therefore present an opportunity to confront theoretical predictions to experimental measurements.

Unfortunately, because of experimental limitations (temperature stabilization, acquisition time, duration of the experiment), v_T cannot take either extremely high or extremely low values: the range of accessible values is at most two orders of magnitude. As v_T is involved in the various analytical expressions through a logarithm, a large variation will in fact have a limited impact on the susceptibility curves. Nevertheless, our theoretical model predicts that a v_T variation should have small but visible effects on the curves. In particular, a decrease of v_T results in a lowering of T_B and on the contrary, in an increase of M_0 : a relative change around 10% is expected when v_T is increased tenfold. This also shows that, in order to really make an accurate MAE determination from a ZFC curve, the temperature sweeping rate should be taken into account. Note also that, since the accessible dynamic range is much wider in AC susceptibility measurements, they are better suited for the determination of v_0 for instance, through measurements at different frequencies.

Another experimental parameter can modify the ZFC curve, without being controlled: a small magnetic field may indeed remain while the sample is cooled in the magnetometer, to reach the starting point of the ZFC. In fact, such a residual field H_{res} is unavoidable and it is worthwhile to examine its effect using the theoretical model we have developed. The starting point M_{ini} of the ZFC curve is then related to the final point of a FC curve with an applied field H_{res} , which corresponds to a magnetic moment

$$M_{res} = \alpha M_{b,res} \quad \text{with} \quad \alpha = 0.9283 \ln\left(\frac{v_0 K}{k_B v_T}\right) - 3.69$$

where $M_{b,res} = \mu_0 \mu^2 H_{res} / (3K)$. Thus, we can write for the initial point of the ZFC curve [33]

$$M_{ini} = M_{res} - M_{b,res} + M_b$$

which corresponds to

$$M_{ini} = \frac{\mu_0 \mu^2}{3K} [H + (\alpha - 1)H_{res}] \quad (12)$$

This shows that the effect of a residual cooling field can be neglected only if $(\alpha - 1)H_{res} \ll H$. In the “reference” case where $x = K/(k_B T_B) = 25$, we have $\alpha - 1 \approx 24.5$ so that this condition reads $H_{res} \ll H/24.5$ which is highly stringent. For instance, a measurement with $H = 50$ Oe should correspond to a residual cooling

field much smaller than 2 Oe, otherwise H_{res} will impact the ZFC curve.

If this condition is not fulfilled, the expression of the ZFC curve must be modified to take into account the correct starting point, which is not M_b but the M_{ini} of Eq. (12):

$$M_{\text{ZFC}}(T) = M_{\text{ini}}e^{-\nu\delta t} + M_{\text{eq}}(1 - e^{-\nu\delta t})$$

It should be noted that the modification of the curve is not simply a rigid shift: the shape of the curve itself is modified, because the existence of H_{res} only affects the “blocked” part of the curve. We emphasize that although there is no modification of the ZFC peak position for a single MAE, the residual field will modify T_{max} in the case of an assembly with a MAE distribution. The problem of a residual cooling field is thus fully relevant for the interpretation of experimental data.

4.8. Remark on the influence of the magnetic field amplitude

In the theory developed above, we have made the assumption that the applied magnetic field H was low enough so that the system response remains linear: the susceptibility $\chi = M/(HV)$ is then independent from the magnitude of the field. Such an assumption can be verified experimentally, and from our experience, a field around 25 or 50 Oe (i.e. $\mu_0 H$ around 2.5 or 5 mT) is often low enough to fulfill this condition.

Nevertheless, it is interesting to see how the theoretical expressions are altered when the field magnitude is not negligible. H plays a role in two different features. First, it modifies the height of the energy barrier needed to flip the magnetic moment of a nanoparticle thus changing the value of ν [34]. This effect scales with the parameter $(1-h)$ where $h = H/H_{\text{ani}}$, the anisotropy field being given by $H_{\text{ani}} = 2K/(\mu_0\mu)$. Second, it affects the equilibrium magnetic moment M_{eq} . The non-linearity becomes non-negligible when the condition $\xi \ll 1$ is no longer fulfilled, with $\xi = \mu_0\mu H/(k_B T)$. The dimensionless parameters h and ξ are related to $\sigma = K/(k_B T)$ through the equality $\xi = 2\sigma h$. Then, around the ZFC susceptibility peak ($\sigma \simeq 25$), we have $\xi \simeq 50 h$. This shows that the non-linearity of M_{eq} can be significant while h remains small, H having therefore a negligible effect on the switching energy barrier. In addition, the non-linearity of M_{eq} is not simply that of a Langevin function but depends on σ . In particular, the equilibrium cubic susceptibility χ_3 of randomly oriented macrospins varies a lot with σ [23,35,22]: around the ZFC peak ($\sigma \simeq 25$) it strongly deviates from the Langevin value (by almost a factor 3).

These considerations underline the fact that the non-linear effects due to the use of a too high measuring field cannot be simply reproduced by replacing the Curie expression of M_{eq} by a Langevin function. The situation is much more complex than assumed by several authors. Keeping a low value for h does not prevent non-linearities of M_{eq} that can significantly reduce the final value M_0 of the FC curve. Even if the influence of H may be taken into account with ad-hoc modified theoretical expressions, relying on much weaker theoretical basis [36], it is always preferable to perform experiments using a low enough magnetic field so that the linear response theory remains valid.

5. Conclusion

Starting from the expression of the dynamical linear susceptibility of an assembly of randomly oriented macrospins, we have established a simple differential equation governing the magnetic moment behavior for an assembly of non-interacting particles having the same MAE. This equation, which in the case of a ZFC/FC

susceptibility measurement simply reads

$$\frac{dM}{dt} = \frac{M_{\text{eq}} - M}{\tau}$$

has then been solved analytically for the entire FC and ZFC curves, taking into account the dynamical temperature variation (sweeping) that is met in experimental measurements.

Exact solutions as well as approximate ones have been obtained. In particular, an analytical expression for the ZFC curve, intuitive and very easy to handle, has been shown to be an excellent approximation: the system evolves gradually from a blocked regime to a superparamagnetic (equilibrium) regime with increasing temperature. This is the first time, to our knowledge, that an analytical expression describing the progressive blocked to superparamagnetic crossover is provided. An effective measuring time δt , which depends on temperature and other parameters, has been introduced and led us to clarify the notion of blocking temperature in the case of a dynamical measurement (which is not isothermal).

Various features of the ZFC/FC curves have been discussed (ZFC peak position, intensity and width, final point of the FC curve...) together with the influence of the different parameters involved in the model. This helps to get a comprehensive view on low field susceptibility curves, which is a prerequisite to correctly analyze experimental data obtained on real nanoparticle assemblies (i.e. with a dispersion of parameters, and in particular MAE). In the next article (part II that follows) [30], these results will be applied to the case of realistic systems with a dispersion of anisotropy energy, coming for instance from a size dispersion of the particles. The comparison with the commonly used ATM will be continued.

Acknowledgments

The authors acknowledge A. Gerardin, E. Jal, S. Rohart and A. Tamion for fruitful discussions and N. Blanchard for reading the manuscript. This work has been partially funded by the “Agence Nationale de la Recherche” (ANR DYSC).

References

- [1] R.W. Chantrell, E.P. Wohlfarth, Phys. Stat. Sol. A 91 (1985) 619.
- [2] J.-O. Andersson, C. Djurberg, T. Jonsson, P. Svedlindh, P. Nordblad, Phys. Rev. B 56 (1997) 13983.
- [3] R.W. Chantrell, N. Walmsley, J. Gore, M. Maylin, Phys. Rev. B 63 (2000) 024410.
- [4] M.A. Chuev, JETP Lett. 85 (2007) 611.
- [5] Y.L. Raikher, V.I. Stepanov, J. Magn. Magn. Mater. 316 (2007) 348.
- [6] Z. Mao, D. Chen, Z. He, J. Magn. Magn. Mater. 320 (2008) 2335.
- [7] A.A. Timopheev, Low Temp. Phys. 34 (2008) 446.
- [8] E.P. Wohlfarth, Phys. Lett. 70A (1979) 489.
- [9] R.W. Chantrell, M. El-Hilo, K. O'Grady, IEEE Trans. Magn. 27 (1991) 3570.
- [10] H. Pfeiffer, R.W. Chantrell, J. Magn. Magn. Mater. 120 (1993) 203.
- [11] M. Respaud, J.M. Broto, H. Rakoto, A.R. Fert, L. Thomas, B. Barbara, M. Verelst, E. Snoeck, P. Lecante, A. Mosset, J. Osuna, T. Ould Ely, C. Amiens, B. Chaudret, Phys. Rev. B 57 (1998) 2925.
- [12] C. Antoniak, J. Lindner, M. Farle, Europhys. Lett. 70 (2005) 250.
- [13] H.T. Yang, D. Hasegawa, M. Takahashi, T. Ogawa, Appl. Phys. Lett. 94 (2009) 013103.
- [14] C.P. Bean, J.D. Livingston, J. Appl. Phys. 30 (1959) 120S.
- [15] E.C. Stoner, E.P. Wohlfarth, Phil. Trans. R. Soc. London A 240 (1948) 599.
- [16] M. Jamet, W. Wernsdorfer, C. Thirion, D. Mailly, V. Dupuis, P. Mélinon, A. Pérez, Phys. Rev. Lett. 86 (2001) 4676.
- [17] R. Skomski, J. Phys. Condens. Matter 15 (2003) R841.
- [18] S. Rohart, C. Raufast, L. Favre, E. Bernstein, E. Bonet, V. Dupuis, Phys. Rev. B 74 (2006) 104408.
- [19] F. Tournus, A. Tamion, N. Blanc, A. Hannour, L. Bardotti, B. Prével, P. Ohresser, E. Bonet, T. Epiciér, V. Dupuis, Phys. Rev. B 77 (2008) 144411.
- [20] A. Tamion, C. Raufast, M. Hillenkamp, E. Bonet, J. Jouanguy, B. Canut, E. Bernstein, O. Boisron, W. Wernsdorfer, V. Dupuis, Phys. Rev. B 81 (2010) 144403.
- [21] M.I. Shliomis, V.I. Stepanov, J. Magn. Magn. Mater. 122 (1993) 176.

- [22] J.L. García-Palacios, On the statics and dynamics of magnetoanisotropic nanoparticles, in: I. Prigogine, S.A. Rice (Eds.), *Advances in Chemical Physics*, vol. 112, Wiley & Sons, Inc., 2000, p. 1.
- [23] Y.L. Raikher, V.I. Stepanov, *Phys. Rev. B* 55 (1997) 15005.
- [24] J.I. Gittleman, B. Abeles, S. Bozowski, *Phys. Rev. B* 9 (1974) 3891.
- [25] P. Svedlindh, T. Jonsson, J.L. García-Palacios, *J. Magn. Magn. Mater.* 169 (1997) 323.
- [26] Y.L. Raikher, V.I. Stepanov, *Phys. Rev. B* 66 (2002) 214406.
- [27] L. Néel, *Ann. Geophys.* 5 (1949) 99.
- [28] W.F. Brown, *Phys. Rev.* 130 (1963) 1677.
- [29] W.T. Coffey, D.S.F. Crothers, Y.P. Kalmykov, E.S. Massawe, J.T. Waldron, *Phys. Rev. E* 49 (1994) 1869.
- [30] F. Tournus, A. Tamion, *J. Magn. Magn. Mater.* (2010), this issue, doi:10.1016/j.jmmm.2010.11.057.
- [31] Instead of using a Curie-type equilibrium magnetic moment, a Langevin function is sometimes assumed to be a better approximation.
- [32] We find $T_{\max} = \frac{k}{k_B} [0.9125 \ln(\gamma) - 5.166]$.
- [33] $M_{b,\text{res}}$ and M_b correspond respectively to a reversible response to the field H_{res} and H , while $M_{\text{res}} - M_{b,\text{res}}$ is the irreversible part of the final moment (at $T \rightarrow 0$) after cooling under a residual field.
- [34] The value of v_0 also changes with H .
- [35] J.L. García-Palacios, F.J. Lázaro, *Phys. Rev. B* 55 (1997) 1006.
- [36] Since the correct dynamical non-linear effects should be considered, which dramatically complicates the analysis [23,26].



Corrigendum

Corrigendum to “Magnetic susceptibility curves of a nanoparticle assembly I: Theoretical model and analytical expressions for a single magnetic anisotropy energy” [J. Magn. Magn. Mater. 323 (9) (2010) 1109–1117]

F. Tournus^{a,b,*}, E. Bonet^c

^a Université de Lyon, F-69000, France

^b Université de Lyon 1, Laboratoire PMCN, CNRS, UMR 5586, F69622 Villeurbanne Cedex, France

^c CNRS/UJF, Institut Néel, BP 166, 38042 Grenoble Cedex 9, France

The authors regret to inform that their recently published article “Magnetic susceptibility curves of a nanoparticle assembly, I: Theoretical model and analytical expressions for a single magnetic anisotropy energy” [J. Magn. Magn. Mater. 323/(2011) 1109–1117] had a typing error in Eq. (4). It should read $\delta t(T) \simeq 0.6727 \frac{T}{v_T} \left(\frac{K}{k_B T} \right)^{-0.9}$. This typo had no influence on the remaining of the article. The authors would like to apologise for any inconvenience caused.

DOI of original article: 10.1016/j.jmmm.2010.11.056

* Corresponding author at: Université de Lyon 1, Laboratoire PMCN, CNRS, UMR 5586, F69622 Villeurbanne Cedex, France. Tel.: +33 4 72 43 28 31.
E-mail address: florent.tournus@univ-lyon1.fr (F. Tournus).

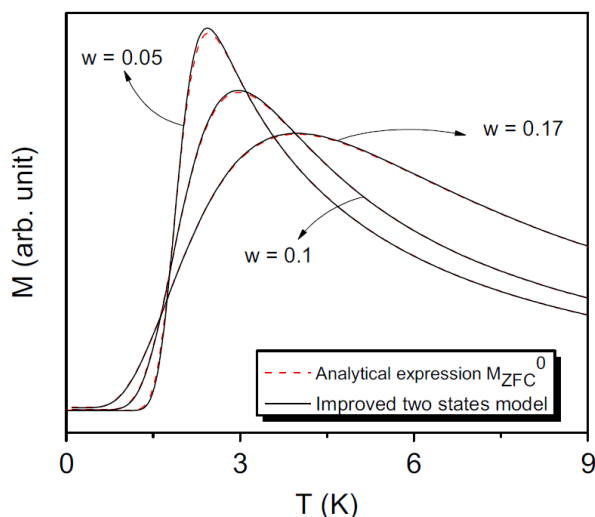
Cette description théorique des courbes de susceptibilité ZFC/FC permet ainsi de décrire de manière claire l'effet des différents paramètres sur les courbes expérimentales (cf. Table 1, tirée de [Tournus2011h]). Il est également possible de faire le lien avec le modèle habituel « à deux états » (c'est-à-dire où les particules sont soit complètement bloquées soit à l'équilibre dans le régime superparamagnétique), en établissant un modèle « à deux états, amélioré » (improved two states model, cf. Fig. 9) qui tient compte notamment de la vitesse de balayage en température.

Table 1

Influence of the anisotropy constant K_{eff} and the particle volume V on the various features of ZFC/FC curves for an assembly with a single magnetic anisotropy energy $K=K_{\text{eff}}V$.

	K_{eff}	V
$M_{\text{ZFC}}(0), M_{\text{FC}}(0)$	Inversely proportional	Proportional
T_B, T_X, T_{max}	Proportional	Proportional
Absolute width of the ZFC peak	Proportional	Proportional
Amplitude of the ZFC peak	Inversely proportional	Proportional
Superparamagnetic signal	–	Proportional to V^2

Fig. 9 : Comparaison entre le « improved two states model » et le « progressive crossover model » (expression analytique) pour des courbes de susceptibilité ZFC dans le cas d'assemblées de nanoparticules présentant une distribution de taille lognormale avec différentes valeurs du paramètre de dispersion w . Figure tirée de [Tournus2011h].



De plus, ce formalisme peut être utilisé dans la procédure d'ajustement que l'on appelle « triple fit » consistant à ajuster simultanément des courbes ZFC/FC et un cycle $m(H)$ à température ambiante (et donc, dans le régime superparamagnétique dans notre cas) : cette méthode permet une détermination précise des caractéristiques d'un échantillon [Tamion2009, Tournus2011b, Tamion2012a]. Comme illustré sur la Figure 10, cette approche permet de discriminer efficacement entre différentes distributions de taille proches (qui donneraient quasiment la même réponse $m(H)$ dans le régime superparamagnétique), et par conséquent on obtient une plus grande fiabilité concernant la valeur de constante d'anisotropie magnétique K_{eff} . Comme les courbes ZFC dépendent fortement de la distribution d'énergie d'anisotropie (produit $K=K_{\text{eff}}V$ où V est le volume des particules), elles permettent également de mettre en évidence des effets fins concernant la distribution de taille magnétique dans un échantillon de nanoparticules : par exemple un effet de couche morte [Tamion2011], l'absence de coalescence lors d'un recuit [Tournus2011a] ou encore l'influence des multimères [Tournus2011].

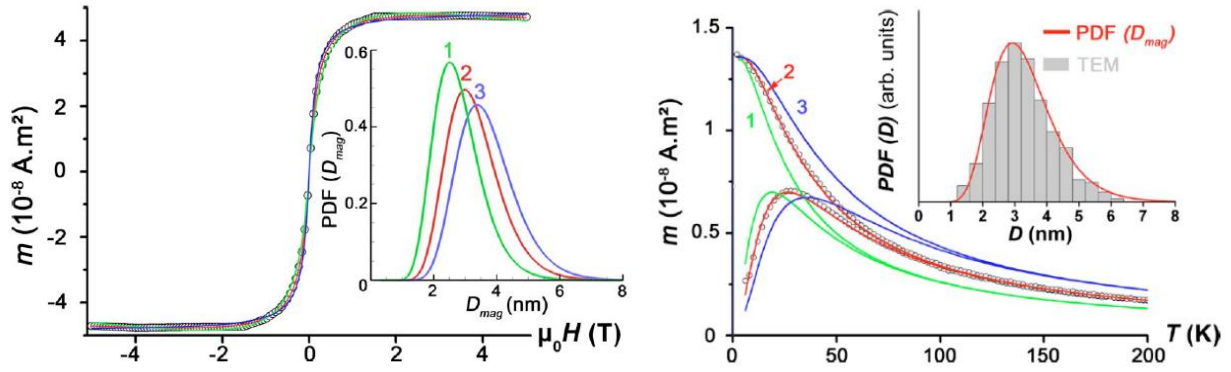


Fig. 10 : À gauche, courbe $m(H)$ expérimentale (points) à 300 K, pour un échantillon de nanoparticules de Co en matrice d'or. La courbe peut être reproduite de manière satisfaisante avec différentes distributions de taille (lognormales), représentées en insert. À droite, comparaison entre les courbes ZFC/FC simulées avec les différentes distributions de taille et les mesures expérimentales (points). Seule la distribution n°2 donne un bon accord à la fois pour les courbes ZFC/FC et $m(H)$ à 300 K. Cette distribution de taille est par ailleurs en excellent accord avec l'histogramme de taille déduit des observations MET (cf. en insert). Figure tirée de [Tamion2009].

De plus, nous avons montré comment modéliser efficacement les courbes d'hystérésis, dans un cadre déterministe et à température non nulle, pour des assemblées de particules avec une distribution de taille et une anisotropie pouvant comporter une composante bi-axiale [Tamion2012] (cf. Fig. 11). Avec les mêmes ingrédients (modèle de Néel pour la relaxation des macrospins à température non nulle, et modèle de Stoner-Wohlfarth) nous avons étendu notre approche de modélisation des courbes de susceptibilité aux mesures AC [Hillion2012, DeToro2013, DeToro2013a] (cf. Fig. 12).

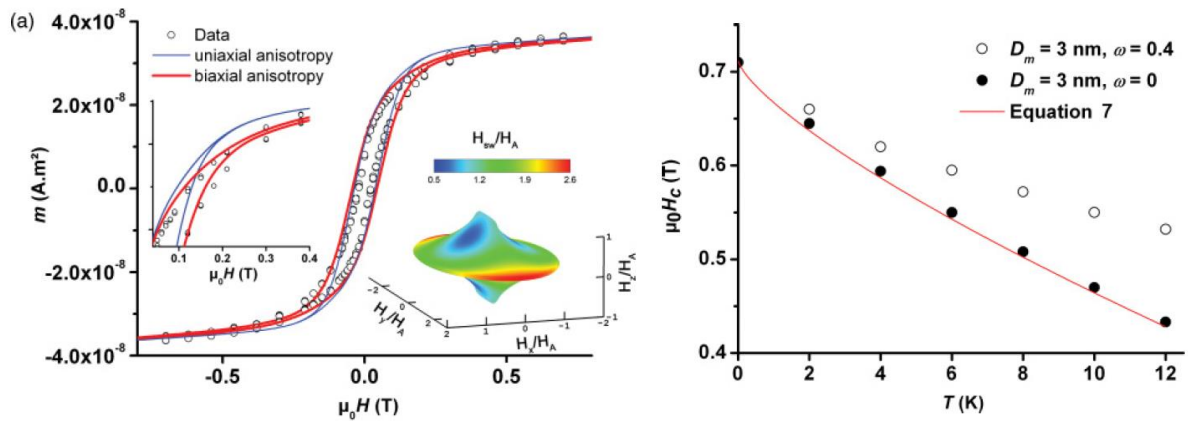
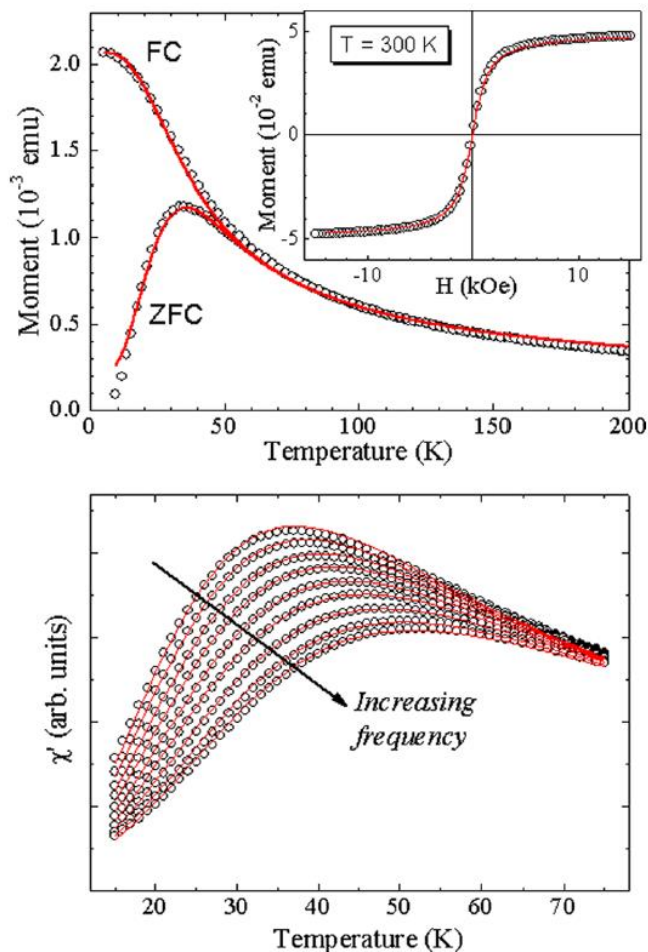


Fig. 11 : À gauche, cycle d'hystérésis mesuré à 2 K (points) pour un échantillon de nanoparticules de Co dans une matrice de C, comparé à des simulations avec (courbe rouge) et sans (courbe bleue) composante bi-axiale pour l'anisotropie des particules. En insert est représentée l'astroïde correspond au meilleur accord (avec une anisotropie bi-axiale non négligeable). À droite, évolution du champ coercitif en fonction de la température calculée pour une assemblée de particules sans dispersion en taille ($\omega=0$, ronds pleins) et avec une dispersion de taille (lognormale avec $\omega=0.4$, ronds vides). La courbe rouge, qui correspond à la formule de Scharrock (souvent utilisée pour déterminer l'anisotropie à partir des valeurs de champ coercitif), c'est-à-dire une dépendance du champ coercitif en $(T/K)^{3/4}$, ne donne une bonne description que dans le cas de particules de taille identique. Figure tirée de [Tamion2012].

Fig. 12 : Ajustement (courbes) des mesures expérimentales (points) pour un échantillon de nanoparticules ferrimagnétiques de maghémite ($\gamma\text{-Fe}_2\text{O}_3$) entourées d'une coquille de silice. Les ajustements portent à la fois sur le cycle $m(H)$ à 300 K (en haut en insert), les courbes ZFC/FC (mesures DC, en haut) et la susceptibilité AC à différentes fréquences (partie réelle, en bas). Un même jeu de paramètres permet de rendre compte de l'ensemble des différentes mesures. Figure tirée de [DeToro2013a].



Par ailleurs, je me suis penché sur la question des effets non-linéaires dans la susceptibilité des particules superparamagnétiques [Tournus2013], qui apparaissent lorsque les mesures ZFC/FC (en régime DC) sont faites avec un champ appliqué suffisant pour s'écarter d'une simple réponse linéaire. Contrairement à ce que l'on pourrait penser, l'effet prépondérant (le premier effet non-linéaire à se manifester lorsqu'on augmente le champ de mesure) n'est pas lié à une modification de la barrière de retournement des macrospins mais provient de la susceptibilité d'ordre 3 des nanoparticules superparamagnétiques (i.e. à l'équilibre). Comme cette susceptibilité dépend de la température et de l'énergie d'anisotropie (donc de la taille des particules), on observe un régime où les courbes ZFC/FC peuvent être sensiblement affectées (y compris avec un décalage du pic de la ZFC) tandis que le champ appliqué reste très petit devant le champ d'anisotropie des particules (et donc, garde un effet négligeable sur les barrières de retournement). Cet effet peut être rationalisé et inclus de manière relativement simple dans la modélisation des courbes ZFC/FC, de façon à mieux appréhender les mesures expérimentales. La publication « **Effect of nonlinear superparamagnetic response on susceptibility curves for nanoparticle assemblies** » [Tournus2013] reproduite ci-dessous présente ce travail en détail.

Effect of nonlinear superparamagnetic response on susceptibility curves for nanoparticle assembliesF. Tournus,^{*} A. Hillion, A. Tamion, and V. Dupuis*Institut Lumière Matière, UMR5306 Université Lyon 1-CNRS, Université de Lyon 69622 Villeurbanne cedex, France*

(Received 21 February 2013; revised manuscript received 11 April 2013; published 3 May 2013)

We examine the effect of the applied magnetic field amplitude on zero field-cooled/field-cooled (ZFC/FC) curves, through the nonlinear susceptibility of superparamagnetic particles (i.e., at thermodynamic equilibrium, but taking into account the magnetic anisotropy). This nonlinear effect is shown to be the first to manifest itself when going away from the linear response regime (i.e., when the magnetic moment is simply proportional to the applied field), largely before the modification of the macrospin switching energy due to the external field. We demonstrate that it has a significant impact on ZFC/FC curves, especially for the low-temperature behavior of the FC curve, even in usual experimental conditions. We then show how this nonlinearity can be taken into account, in an easy way, to obtain a better modeling of the susceptibility curves and consequently a more reliable determination of the nanoparticles' magnetic properties. The theoretical considerations are confronted in a series of experimental measurements on Co nanoparticles.

DOI: 10.1103/PhysRevB.87.174404

PACS number(s): 75.75.-c, 75.50.Tt, 75.20.-g, 75.30.Gw

I. INTRODUCTION

The numerous potential applications of magnetic nanoparticles, in areas ranging from medicine to catalysis, are driving research on nanoparticle synthesis and characterization.¹⁻⁶ In this context, low field susceptibility curves, following the so-called zero field-cooled/field-cooled (ZFC/FC) protocol, are widely used for the determination of the nanoparticle properties, in particular the distribution of magnetic anisotropy energy (MAE) and particle size.

This technique consists in measuring the magnetic moment of a nanoparticle assembly, under a low applied field (typically 50 Oe), as a function of temperature. The ZFC curve starts from low temperature (typically 2 K), with a demagnetized sample cooled down from room temperature under no applied field. In contrast, for the FC curve the temperature is decreased from room to low temperature while the magnetic moment is measured, keeping the applied field constant. The obtained curves then reflect the progressive crossover, as a function of temperature T , between the blocked regime and the superparamagnetic (SP) regime (i.e., where the magnetic moments are at thermodynamic equilibrium). The main characteristic features of these susceptibility curves are the existence of a peak in the ZFC curve, occurring at a temperature T_{\max} , and the merging of the ZFC and FC curves when all the particles are in the superparamagnetic regime. The value of T_{\max} is often used to characterize and compare, with a single figure, the magnetic anisotropy of nanoparticle samples. However, such a usage may be hazardous because both the magnetic anisotropy and the details of the size distribution control the shape of the ZFC/FC curves.⁷

In order to perform a more reliable analysis of these magnetization curves, a full modeling is yet possible both for the ZFC and the FC curve, using either a “two-states model” (or abrupt transition model, where the particles are supposed to be either blocked or SP),⁸⁻¹¹ or a more elaborate “progressive crossover model.”^{7,12,13} These two semianalytic models are equivalent as long as the MAE dispersion is large enough and with a carefully defined transition temperature (i.e., “blocking temperature”).⁷ One of the basic hypotheses of these models

is that the applied magnetic field is low enough to observe a linear response of the nanoparticle assembly, which means that its magnetic moment (response) is simply proportional to the external field (i.e., the response scales linearly with the excitation). If we are in such a linear response regime, then the normalized ZFC/FC curves measured with various field amplitudes H should all be superimposed, as the total magnetic moment simply scales with H . However, this assumption is far from being systematically verified. Anyway, from an experimental point of view, a compromise needs to be found between having a fair signal-to-noise ratio and remaining close enough to the linear response regime.

On the other hand, it is well known that for applied magnetic fields of increasing amplitudes, the T_{\max} value is shifting.¹⁴ The nonintuitive fact that this ZFC peak shift can be nonmonotonous has been discussed in the literature.¹⁵⁻¹⁷ In particular, Zheng *et al.*¹⁷ have pointed out that it can be explained by the contribution of SP particles with a size distribution. The influence of the applied field on the equilibrium magnetic moment is sometimes considered through a Langevin function,¹⁷⁻¹⁹ which is only justified at high temperature^{20,21} (i.e., far above the blocked-superparamagnetism crossover, when the anisotropy can be neglected).

In this paper, we examine the effect of the applied magnetic field amplitude on ZFC/FC curves, through the nonlinear susceptibility of SP particles (i.e., at thermodynamic equilibrium, but taking into account the MAE). This nonlinear effect is shown to be the first to manifest itself when going away from the linear response regime, largely before the modification of the macrospin switching energy due to the external field. We demonstrate that it has a significant impact on ZFC/FC curves, especially for the low-temperature behavior of the FC curve, even in usual experimental conditions. We then show how this nonlinearity can be taken into account, in an easy way, to obtain a better modeling of the susceptibility curves and consequently a more reliable determination of the nanoparticles' magnetic properties. The theoretical considerations are confronted in a series of experimental measurements on Co nanoparticles.

II. THEORETICAL ANALYSIS

A. Framework

In the following, we make the usual assumption that magnetic nanoparticle samples can be described by independent macrospins of magnetic moment $\mu = M_S V$ and a uniaxial anisotropy corresponding to a MAE $K = K_{\text{eff}} V$. Here M_S is the saturation magnetization, V is the particle volume, and K_{eff} is the effective anisotropy constant. We also assume that the easy magnetization axes of the nanoparticles are randomly oriented. The macrospin switching time is given by the Néel model: $\tau = \tau_0 \exp(\frac{\Delta E}{k_B T})$, where ΔE is the switching energy barrier, i.e., simply equal to K in the absence of any external magnetic field. Moreover, the evolution of K_{eff} , M_S , and τ_0 with temperature is neglected in the range of interest for ZFC/FC curves. It must be noted that the analysis presented in the following can still be applied to more complicated situations (texture of the macrospin orientations, dispersion of K_{eff} , evolution of M_S , K_{eff} , or τ_0 with T), at the expense of a higher computational cost. The hypothesis of a macrospin behavior is crucial but is well verified for few-nanometer-diameter particles.^{22–24} From an experimental point of view, the most stringent hypothesis is certainly the absence of interparticle interactions, which requires particles far enough from each other (i.e., high dilution in the case of particles embedded in a nonmagnetic material).^{12,25–27}

Before considering the realistic case of a nanoparticle assembly with a particle-size distribution, we discuss the case of a monodisperse assembly of randomly oriented macrospins. In a simplified model, which we call the “abrupt transition model,” the macrospins of a given MAE are supposed to be either fully blocked (with a magnetic moment m_b) or fully superparamagnetic, that is, at thermodynamic equilibrium (with a magnetic moment m_{eq}). The expressions of m_b and m_{eq} are discussed further later. Then, the ZFC curve is given by $m_{\text{ZFC}} = m_b$ for $T < T_B$ and $m_{\text{ZFC}} = m_{\text{eq}}$ for $T \geq T_B$, where the blocking temperature T_B establishes a transition between the two behaviors. The transition temperature corresponds to the situation when the measurement time τ_m (or *effective* measurement time, in the case of a continuous acquisition during a temperature sweep^{13,28}) is equal to the switching time τ , which means

$$T_B = \frac{\Delta E}{k_B \ln(\tau_m/\tau_0)}.$$

On the other hand, we have for the FC curve $m_{\text{FC}} = m_{\text{eq}}(T_B)$ for $T < T_B$ and $m_{\text{FC}} = m_{\text{eq}}$ for $T \geq T_B$.

One can distinguish the different effects of the applied magnetic field on the ZFC/FC curves (beyond the simple proportionality to the field, which does not modify the curves shape). The field amplitude H will modify the macrospin switching time through a variation of τ_0 ²⁹ (this has only a small incidence) and more importantly through a change of ΔE in the exponential.^{14,30,31} In the end this will affect the blocking temperature of particles of a given MAE. Besides, the equilibrium (SP) magnetic moment m_{eq} also depends on H and the deviation from the linear behavior $m_{\text{eq,lin}} = \mu_0 \mu^2 H / (3k_B T)$ will contribute to modify the ZFC/FC curves shape when the applied field is increased. Interestingly, it should be noted that the blocked moment m_b is strictly linear

in H (because it is related to the transverse susceptibility¹³), as long as the saturation is not reached:

$$m_b = \frac{\mu_0 \mu^2 H}{3K}.$$

While the magnetic field effect on ΔE and even τ_0 has already been considered in previous studies,^{14,16,17,30,32} the dependence of m_{eq} upon H has been under-rated. Let us emphasize that $m_{\text{eq}}(H)$ does not correspond to a simple Langevin function. Indeed, the Langevin function is the thermodynamic equilibrium response of a particle assembly only in the case of a vanishing magnetic anisotropy.^{20,21,28} This is a crucial point: The particles’ anisotropy still plays a role in the SP contribution, especially close to T_B . In particular, we can expect it to have a strong impact on the FC curve, because $m_{\text{eq}}(T_B)$ is involved (see above).

These observations also hold for the more elaborate progressive crossover model, where we can write¹³

$$m_{\text{ZFC}} = m_b e^{-\delta t/\tau} + m_{\text{eq}}(1 - e^{-\delta t/\tau})$$

and

$$m_{\text{FC}} = m_{\text{eq}}(T_B) e^{-\delta t/\tau} + m_{\text{eq}}(1 - e^{-\delta t/\tau}),$$

δt being an effective waiting time related to the temperature sweeping rate r_T . As explained in Ref. 13, δt depends on the anisotropy and on the temperature [$\delta t \simeq 0.6727 (T/r_T)(k_B T/K)^{0.9}$], which means that it varies among the particles and along the ZFC/FC curves. In this case, we have (for a negligible applied field)¹³

$$T_B \simeq \frac{K/k_B}{0.9283 \ln\left(\frac{K}{k_B \tau_0 r_T}\right) - 3.69}.$$

To go further, we can point out that the effects of the applied field H on the macrospin switching time are controlled by the dimensionless parameter $h = H/H_A$, where H_A is the anisotropy field defined by $H_A = 2K_{\text{eff}}/(\mu_0 M_S)$. These effects are then negligible as long as $h \ll 1$. On the other hand, the deviation of m_{eq} from a linear response to the applied magnetic field is controlled by another dimensionless parameter (ratio between Zeeman and thermal energies)³³:

$$\xi = \frac{\mu_0 M_S V H}{k_B T}.$$

Therefore, the linear approximation for m_{eq} is acceptable as long as $\xi \ll 1$, where we can write $m_{\text{eq}} \simeq m_{\text{eq,lin}}$. By introducing a third dimensionless parameter $\sigma = K_{\text{eff}} V / (k_B T)$, which reflects the relative importance of anisotropy vs thermal effects, we can see how h and ξ are related: $\xi = 2\sigma h$. The SP regime (equilibrium response) takes place typically for $\sigma \leq 25$ [this comes from the fact that for ZFC/FC measurements we have $\ln(\tau_m/\tau_0) \simeq 25$]. This means that around T_B , at the onset of the SP regime, we can write $\xi \simeq 50h$. For instance, we can have a situation where $h = 0.01$, and hence T_B will not be noticeably changed, while $\xi \simeq 0.5$ around T_B so that the SP contribution will clearly deviate from $m_{\text{eq,lin}}$. This demonstrates that the applied field amplitude H modifies m_{eq} much before having a sizable effect on the blocking temperature (through the macrospin switching time τ).

As a consequence, there exists an intermediate regime where $h \ll 1$ but ξ is no more negligible, and hence

the nonlinear effects in m_{eq} start to be significant (i.e., we are facing a nonlinear superparamagnetic response) while the macrospin switching is almost unaffected by H . In the following, we consider this particular regime, which is the first to appear when one deviates from the linear response regime (at low field).

B. Third-order magnetic susceptibility and ZFC/FC simulation

We consider a system of randomly oriented uniaxial macrospins, having the same volume V , and consequently the same magnetic moment $\mu = M_S V$ and MAE $K = K_{\text{eff}} V$. We can determine its equilibrium response (component along the applied field direction, m_{eq}) to an external field H , at a temperature T . This can be done numerically without any difficulty, as reported in several studies,^{20,21,33,34} using statistical physics formulations involving the system partition function.

Then, a Taylor expansion can be made as a function of ξ in reduced units. One can write

$$m_{\text{eq}}/m_S = \frac{\xi}{3} + \alpha \xi^3 + \dots,$$

where m_S is the sample saturation magnetic moment. Thus, the first nonlinear term is proportional to the *reduced third-order susceptibility* α . This coefficient depends only on the parameter σ . In the limit of small σ or large σ values, $\alpha(\sigma)$ can be expressed analytically using power series of σ or $1/\sigma$. We can write³³

$$\alpha = -\frac{1}{45} - \frac{8}{10125} \sigma^2 + \dots \quad \text{for } \sigma \ll 1$$

and

$$\alpha = -\frac{1}{15} + \frac{2}{15\sigma} + \dots \quad \text{for } \sigma \gg 1.$$

The extreme cases correspond to a Langevin function ($\sigma = 0$, no anisotropy barrier) and to a Ising function ($\sigma \rightarrow \infty$, only two possible orientations) with respectively $\alpha = -1/45$ and $\alpha = -1/15$. In the case relevant for ZFC/FC measurements, we are mostly interested in knowing the α value for σ around 20–25. Let us insist on the fact that in this range m_{eq} is closer to a Ising function than to a Langevin function. Note that limiting the nonlinear expansion of m_{eq} to the third-order susceptibility is a good approximation up to $\xi \simeq 0.5$ – 1 , which corresponds to an applied field $H/H_A \simeq 0.01$ – 0.02 . Figure 1 indeed displays the error on m_{eq} induced by such a truncation to the third-order susceptibility. It also compares this truncation to the linear approximation and a Langevin function. Note also that because ξ is inversely proportional to T , the truncation becomes a better approximation when going away from the blocking temperature. Beyond the fact that m_{eq} does not correspond to a Langevin function (see Fig. 1), taking into account the true third-order magnetic susceptibility constitutes an essential improvement because the dependence of α on σ (i.e., on the particle anisotropy and size) is then considered. This will be very important for a correct description of the ZFC/FC curves in the case of a particle-size distribution.

In order to efficiently incorporate this third-order susceptibility effect in ZFC/FC simulations, one needs an analytical expression of $\alpha(\sigma)$ in the entire range of interest for SP

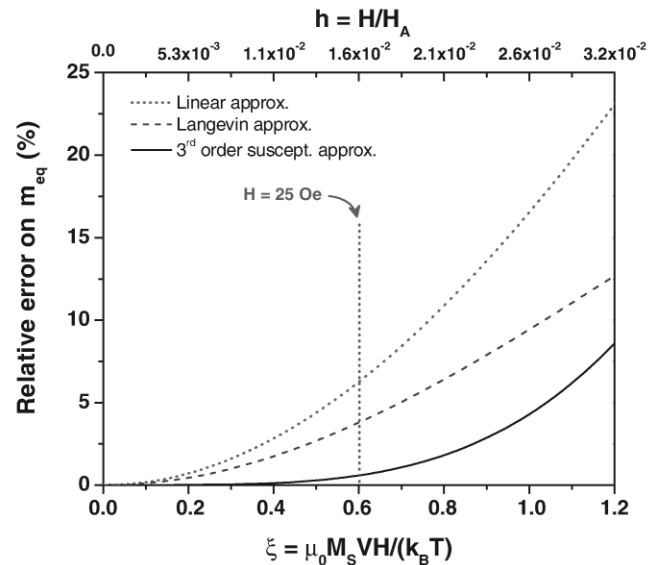


FIG. 1. (Color online) Relative error on the equilibrium magnetic moment m_{eq} , as a function of the dimensionless parameter ξ , for different approximations: the linear response approximation (red [gray] dotted line), the Langevin approximation (blue [gray] dashed line), and the true nonlinear response truncated to the third-order susceptibility (black solid line). The calculations are done for particles of 5-nm diameter, with $M_S = 1.35 \times 10^6$ A/m, $K_{\text{eff}} = 100$ kJ/m³ (which corresponds to $T_B \simeq 18$ K and $H_A \simeq 1500$ Oe), at a temperature of 25 K (i.e., $\sigma \simeq 19$).

particles (i.e., from $\sigma = 0$ to about 25). Because we can already describe with high precision the two extreme regimes ($\sigma \ll 1$ and $\sigma \gg 1$), we propose a linear interpolation³⁵ between the values $\alpha(\sigma_{\text{min}})$ and $\alpha(\sigma_{\text{max}})$, where σ_{min} and σ_{max} are the boundary values where the extreme regimes approximations start to fail. As shown in Fig. 2, one can find very good polynomial fits in either σ or $1/\sigma$ (these fits are slightly different from the Taylor expansions but allow us to extend the domain of applicability), up to $\sigma \simeq 2$ on the low- σ side and down to $\sigma \simeq 5.5$ on the high- σ side: The linear interpolation is then limited to $\sigma \in [2, 5.5]$ and appears very satisfactory.

We now turn to ZFC/FC simulations, incorporating the applied field effect on m_{eq} through the analytical expression of the reduced third-order susceptibility discussed above. As already mentioned, two models can be used to describe the evolution from the blocked regime to the SP regime:¹³ The abrupt transition model (ATM), where there is a discontinuity for the ZFC at the transition temperature (in a case of a single MAE), or the progressive crossover model (PCM), where the evolution between the two regimes is gradual, resulting in continuous ZFC curves even for a single MAE. In both formulations (see above), the equilibrium magnetic moment m_{eq} appears in a very transparent way, so that there is no difficulty to add the third-order susceptibility contribution (analytical approximation) to the usual linear response $m_{\text{eq,lin}} = \mu_0 \mu^2 H / (3k_B T)$.

Figure 3(a) shows the effect of the applied field amplitude on the ZFC/FC curves, for a single MAE (corresponding typically to Co clusters in the fcc phase with a 5-nm diameter, under a 25-Oe magnetic field). Different approximations for

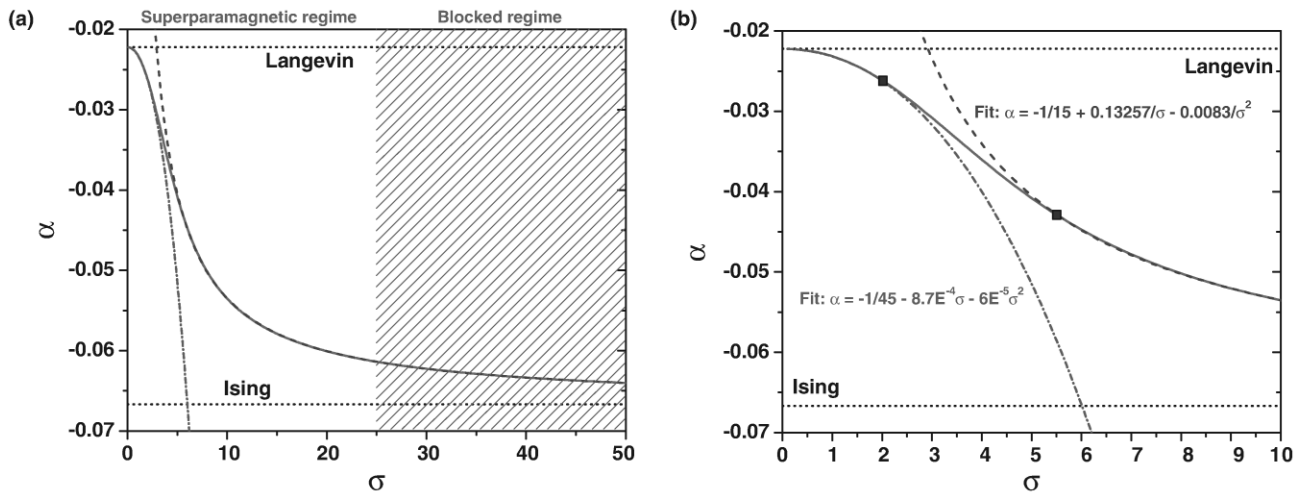


FIG. 2. (Color online) (a) Numerical calculation of the reduced third-order susceptibility α (red [gray] solid line) as a function of σ , compared to the low- σ and high- σ analytical approximations (blue [gray] dashed line and green [gray] dash-dotted line). The extreme cases, corresponding to a Langevin or a Ising function, are indicated with horizontal dotted lines. In a ZFC/FC measurement, the superparamagnetic regime (i.e., thermodynamic equilibrium) is observed typically for $\sigma \leq 25$, whereas the region $\sigma > 25$ (hatched region) corresponds to the blocked regime. (b) Closer view, for σ between 0 and 10, of the numerically determined $\alpha(\sigma)$ value (red [gray] solid line) and the low- σ and high- σ analytical approximations (blue [gray] dashed line and green [gray] dash-dotted line). The two black squares indicate the σ_{\min} and σ_{\max} values and materialize the range where a linear interpolation will be used for $\alpha(\sigma)$.

the equilibrium response are compared (see the Appendix for the analytical expression of the curves for each approximation): The linear approximation, the Langevin approximation, and the third-order susceptibility approximation. In this case, in addition to simulations using the PCM, what would be obtained for the more common ATM is also displayed. Note that the illustrative case considered here corresponds to $h \simeq 0.017$, a blocking temperature $T_B \simeq 18$ K, a σ value

around 26 at T_B , and $\xi \simeq 0.9$ at T_B . We are thus typically in the regime described previously, where the nonlinearity cannot be neglected while the energy barrier (and consequently T_B) is almost unaffected ($h \ll 1$ is still satisfied). One can immediately see that there is a clear deviation from the linear case (i.e., what would be obtained with a very low applied field), especially around the ZFC peak. As far as the FC curve is concerned, the most striking effect is the significant decrease of

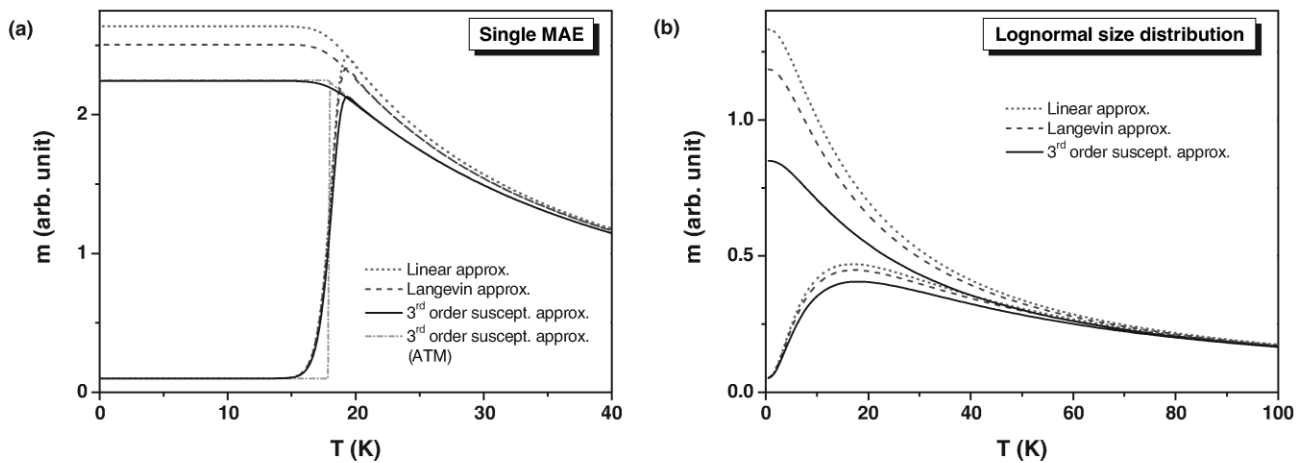


FIG. 3. (Color online) ZFC/FC curves simulations using the progressive crossover model (PCM), for a single MAE (a) or for a MAE distribution due to a log-normal particle-size distribution (b). Different approximations for m_{eq} are compared (the analytical expressions are summarized in the Appendix): the linear response approximation (red [gray] dotted line), the Langevin approximation (blue [gray] dashed line), and the true nonlinear response truncated to the third-order susceptibility (black solid line). The calculations are done for particles with $M_S = 1.35 \times 10^6$ A/m, $K_{\text{eff}} = 100$ kJ/m³ (which corresponds to $H_A \simeq 1500$ Oe), with a 25-Oe applied magnetic field (i.e., $h \simeq 0.017$). τ_0 is fixed to 10^{-10} s and the temperature sweeping rate is $r_T = 0.033$ K/s. The particle diameter is equal to 5 nm (single MAE case, case a), while it follows a log-normal distribution (case b) with a median diameter of 3 nm and a dispersion parameter of 0.3. For the single MAE case, the curves corresponding to the abrupt transition model (ATM, dash-dotted line) are also shown. In the case of a significant MAE distribution (as in case b) the ATM and PCM are equivalent.

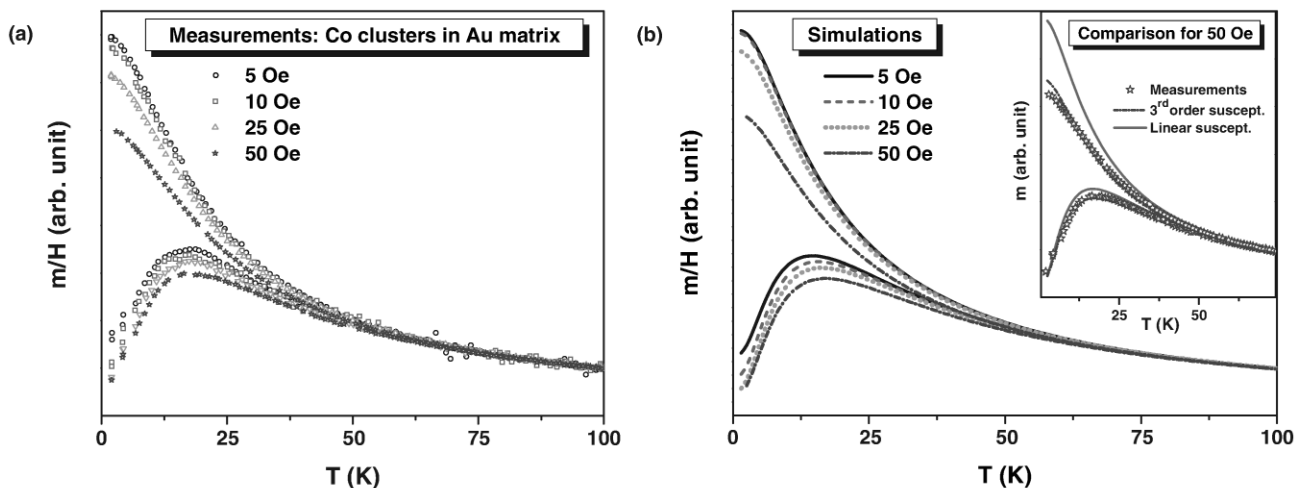


FIG. 4. (Color online) Normalized ZFC/FC curves measured for a sample of Co nanoparticles embedded in a gold matrix, with different applied field amplitudes (a). Simulated ZFC/FC curves, taking into account the third-order susceptibility in the superparamagnetic contribution, for different applied magnetic fields (b). In insert, the experimental curves with a 50-Oe applied field are compared to the curves simulated with the third-order susceptibility approximation and the linear response approximation. The nanoparticles have a log-normal size distribution (median diameter of 2.75 nm and dispersion parameter of 0.26) and a $K_{\text{eff}} = 162 \text{ kJ/m}^3$. A residual field of 0.7-Oe is included.

the low temperature limit, which can easily be explained by the fact that the third-order susceptibility is always negative (i.e., it decreases the response magnitude as compared to the linear regime). The inability of a Langevin description to correctly account for the applied field effects is also clearly visible. In Fig. 3(b), the same comparison between the different approximations (linear response, Langevin function, and response including the third-order susceptibility) for the superparamagnetic particles response is done for the more realistic case of a particle-size distribution (log-normal in this case). The same type of behavior as for a single particle size is observed: The FC curve slope is significantly decreased, and the ZFC peak has a reduced amplitude. Note that the beginning of the ZFC (low temperature) remains unchanged (because of m_b linearity), as well as the high-temperature limit, where both σ and ξ go to zero so that the system's response is simply given by the linear susceptibility of a paramagnet (i.e., $1/T$ evolution).

This theoretical analysis demonstrates that the nonlinearity of the SP contribution must be considered in order to accurately analyze experimental curves. Using a Langevin function does not at all constitute a reliable solution. Of course, for applied field amplitudes that are too large, considering only the third-order susceptibility is not enough and the simple approach presented here cannot be applied (moreover, in this case the blocking temperatures are also significantly affected by the magnetic field). From an experimental point of view, however, there is no real interest in choosing such conditions, highly deviating from the linear response regime.

III. EXPERIMENTAL STUDY

The evolution of the ZFC/FC curves' shapes, when varying the applied magnetic field amplitude, has been experimentally studied on a Co nanoparticle assembly. The sample consists of Co nanoparticles (around 3 nm in diameter, with a log-normal size distribution) synthesized by laser vaporization and deposited in ultra-high-vacuum conditions using low-

energy cluster beam deposition (LECBD).^{36,37} During particle deposition, a gold matrix is codeposited (by electron beam evaporation) so that the magnetic clusters are embedded in Au with a high dilution (0.5% in volume), resulting in negligible interparticle interactions.²⁶

ZFC/FC measurements have been performed with different applied field amplitudes, using a superconducting quantum interference device (SQUID) magnetometer (Quantum Design MPMS 5XL). As can be seen in Fig. 4(a), there is a striking evolution of the curves' shapes (normalized by the applied field) with a flattening of the FC curve (low-temperature limit) and a decrease of the ZFC peak amplitude when the magnetic field is increased from 5 to 50 Oe. A first observation is that, as far as the FC curve is concerned, the linear response (invariance of the curves shape) is satisfied up to a 10-Oe applied field in the present case. The fact that ZFC curves are not superimposed, as is the case for FC curves (5- and 10-Oe curves, and it almost holds for the 25-Oe FC too), may seem surprising. Indeed, let us remember that the blocked contribution is not affected by the applied field (simple linear behavior) so that when all the particles are blocked (which is almost the case at the lowest temperature of 2 K) the normalized ZFC curves should have the same value.

The downshift of the ZFC at low temperature, when the field is increased, can fully be explained by the existence of a small residual field in the SQUID when cooling the sample in supposedly "zero field-cooled" conditions. As it has been discussed previously, a tiny residual field of the order of $1/25$ (i.e., 4%) of the measurement field amplitude is enough to perturb the low-temperature part of a ZFC curve.¹³ The effect of the residual field H_{res} can be taken into account in the simulations: We first compute the low-temperature limit of a FC curve with H_{res} as the applied field and then use this value as the starting point of the experimental ZFC curve. Here, we find that the measurements are consistent with a 0.7-Oe residual field, which would be fully negligible for many measurements but has a detectable impact in the case of ZFC curves acquired

with a small amplitude field: Such a H_{res} represents around 14% of the measurement field in the case of $H = 5$ Oe and 7% for $H = 10$ Oe. When the applied field becomes large enough, this residual field has a negligible effect on the ZFC starting point, which is precisely what we observe for 25-Oe and 50-Oe measurements.

The other features (flattening of the FC curve and decrease of the ZFC peak) are well reproduced by the simulations [see Fig. 4(b)], using the framework exposed above, which includes the third-order susceptibility in the equilibrium magnetic response. These effects then result only from the nonlinearity of m_{eq} . Interestingly, we have found that it is often possible to fit ZFC/FC curves, even in the nonlinear regime discussed here, with the simple linear response formulation. As has just been demonstrated above, such a successful fit does not prove in any way that the magnetic response to the external field is indeed linear. The series of experimental curves [Fig. 4(a)] can be fitted using the previously reported “triple-fit” method (simultaneous fit of the 300-K superparamagnetic $m(H)$ curve and ZFC/FC susceptibility curves).¹² The FC flattening is in fact not prohibitive for the fit using linear expressions, because the low- T limit of the FC is treated as an adjustable parameter (it is chosen to give the experimental value). However, depending on which measurement field is considered, the parameters obtained by a best-fit procedure are not exactly identical. While the impact on the deduced particle-size distribution is very limited (0.1-nm change in the median diameter and 0.01 variation in the log-normal dispersion), the anisotropy constant increases from $K_{\text{eff}} = 162$ kJ/m³ for $H = 5$ Oe to $K_{\text{eff}} = 178$ kJ/m³ for $H = 50$ Oe. In contrast, a fit with the third-order nonlinear susceptibility provides a constant $K_{\text{eff}} = 162$ kJ/m³ value. In the case of a 50-Oe measurement, and for this particular sample, neglecting the nonlinearity of m_{eq} would result in a 10% overestimation of the magnetic anisotropy constant. The inset in Fig. 4(b) displays the best fit of the experimental curves with the third-order susceptibility approximation and shows how important the nonlinear effects are (the linear susceptibility approximation gives drastically different curves).

Note that neglecting the effect of the residual field for low-field measurements is worse and can easily lead to a 20% error on K_{eff} , which is then underestimated. More generally, taking into account the nonlinearity effect allows one to avoid the potentially significant error (even when remaining in the regime where $h \ll 1$) on the magnetic anisotropy constant that would be inferred from a fit based on a linear response model. For instance, including the third-order susceptibility would avoid a 18% overestimation in the case displayed in Fig. 3(b), while in other cases errors up to 30% on K_{eff} can be avoided. A nonlinear modeling is then clearly beneficial for the accuracy of the magnetic parameters determined from experimental curves. It is also important to note that a slight shift of the ZFC curve maximum temperature T_{max} can be observed as a function of the applied field, even if the macrospin switching energy barriers are not affected (i.e., h remains very small). Such a shift can be obtained with a particle-size distribution, simply because there exists a nonlinearity in m_{eq} , and may be amplified by the existence of a tiny residual field in the magnetometer during the zero field-cooling step.

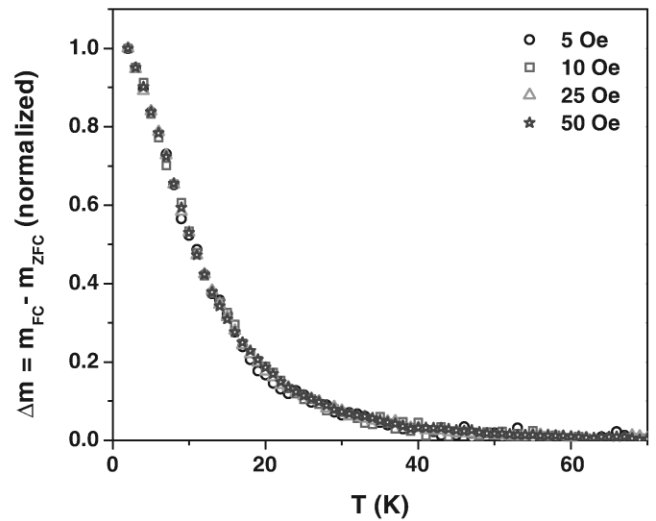


FIG. 5. (Color online) Experimental normalized $\Delta m = m_{\text{FC}} - m_{\text{ZFC}}$ curves for the sample of Co nanoparticles embedded in a gold matrix, with the different applied field amplitudes.

According to the ZFC/FC curve expressions,^{7,13} both the effect of a residual field and of a nonlinearity in m_{eq} should vanish when considering the difference $\Delta m = m_{\text{FC}} - m_{\text{ZFC}}$. As expected, in sharp contrast with the change in the ZFC/FC curves with the applied field amplitude, the normalized Δm curves are found to be almost identical (see Fig. 5). These curves are the signature of the gradual unblocking of the particles with increasing temperature: They are similar to remanence $m_R(T)$ measurements and only bear the signature of the blocked nanoparticles. Δm is also directly related to the distribution of blocking temperatures in the nanoparticle assembly,⁷ and thus it reflects the switching energy distribution in the sample. The fact that in the present experimental case Δm does not evolve with the applied field, in the range considered here, is a proof that we are still in the $h \ll 1$ regime where the field effect on the energy barriers can be neglected. This justifies the use of the framework exposed above where only the equilibrium contribution is modified by H .

One may want to take advantage of these properties of the $\Delta m = m_{\text{FC}} - m_{\text{ZFC}}$ curve, namely the insensitivity to a residual field and to a nonlinearity in m_{eq} . Indeed, as already evoked in a previous work,⁷ $\Delta m(T)$ can be fitted directly using a semianalytical model. In the case of a particle-size distribution function $\rho(V)$, one can write for the progressive crossover model

$$\Delta m \propto \frac{\mu_0 M_S^2 H}{3K_{\text{eff}}} \int_0^\infty V e^{-\delta t/\tau} \rho(V) dV,$$

where both τ and δt (to a much lesser extent) depend on T and V . Similarly, with the abrupt transition model, one can write

$$\Delta m \propto \frac{\mu_0 M_S^2 H}{3K_{\text{eff}}} \int_{V_{\text{lim}}}^\infty V \rho(V) dV,$$

with $V_{\text{lim}}(T) = \ln(\tau_m/\tau_0)k_B T/K_{\text{eff}}$, which corresponds typically to $V_{\text{lim}} \simeq 25k_B T/K_{\text{eff}}$. There is thus no difficulty

to fit an experimental Δm curve, which can give access to the particle-size distribution and the anisotropy constant. However, going from two curves (FC and ZFC) to only one results in a loss of information (contribution of the equilibrium magnetic moments) and transforms a highly discriminating feature (the ZFC peak) into a smooth curve, which appears to be less sensitive to a parameter variation. In the end, we believe that directly analyzing ZFC/FC curves is preferable.

Finally, this study stresses that special attention must be paid to the choice of the applied field for ZFC/FC susceptibility measurements. A compromise has to be found between a high signal (and consequently a better quality of the experimental curves) and a strong deviation from linearity, which precludes a simple theoretical modeling of the curves. It is then strongly advisable to check in which regime we are (linear response, moderate nonlinear response with $h \ll 1$, highly nonlinear response) when analyzing a particular sample. Some conditions may be suited for one case and not for another one: In particular, according to the material considered, the anisotropy field H_A can vary a lot, thus changing substantially the value of h and the parameter ξ around the blocking temperature. It must be kept in mind that with a fixed acquisition magnetic field, the nonlinearity effects will be more pronounced for systems with a small H_A . By evaluating the maximum value of ξ corresponding to a given experimental situation, one can ensure that a reliable modeling of the curves is then possible.

IV. CONCLUSION

We have shown how the applied magnetic field amplitude can alter the shape of ZFC/FC susceptibility curves of a nanoparticle assembly. The first effect, when deviating from the linear response regime valid at very low acquisition field, is to modify the magnetic behavior of superparamagnetic particles: A nonlinearity appears in the equilibrium magnetic moment m_{eq} , the third-order susceptibility being the first component that needs to be considered. Such a nonlinear effect can be significant while the impact of the applied magnetic field on the switching energy distribution (and hence on the particles blocking temperatures) can safely be neglected.

In this moderate nonlinear regime, a simple theoretical modeling of this nonlinear effect is possible with an accurate analytical approximation of the reduced third-order equilibrium susceptibility. This framework is then fully compatible with the usual theoretical description of ZFC/FC curves (ATM or PCM) and only involves a marginal additional computational cost. Unfortunately, a simple and reliable theoretical description seems impossible for large applied field amplitudes, where the third-order susceptibility is not sufficient and where the switching energy barrier are also affected.

The most visible effect of the appearance of a m_{eq} nonlinearity is the flattening of the FC curve (lowering of the low-temperature limit). In the case of a particle-size distribution, a slight shift of the ZFC peak temperature with the field is also possible, even if the individual particle blocking temperatures remain unchanged. It must be noted that the use of a Langevin function to describe the field dependence of the superparamagnetic contribution is not physically sound, as it misses the dependence of the nonlinear susceptibility

on the parameter $\sigma = K_{\text{eff}}V/(k_B T)$. As long as the applied field is not too high, taking into account the nonlinear behavior of the equilibrium magnetic response enables a more accurate determination of the nanoparticles' magnetic properties from the fit of experimental ZFC/FC curves. This has been illustrated on a sample of Co nanoparticles embedded in a gold matrix, characterized with an applied magnetic field ranging from 5 to 50 Oe. In this case, the linear response regime is only met at low acquisition fields ($H \leq 10$ Oe).

Experimentally, when choosing the applied field amplitude for ZFC/FC measurements, it is advisable to find a good compromise between having an intense signal and keeping a moderate nonlinearity in the nanoparticles' magnetic response. The existence of a very small residual field in the magnetometer (even less than 1 Oe), during the zero field-cooling step, has been shown to be critical in the case of low acquisition field amplitudes (for instance, 5 or 10 Oe). With these considerations, we think that in many cases the most judicious choice is to use a 25-Oe applied field for ZFC/FC measurements, keeping in mind that the conditions of validity of the different approximations ($h \ll 1$, small ξ) vary with the experimental situation considered (in particular with the material). Interestingly, and as expected from the theoretical description, the quantity $\Delta m = m_{\text{FC}} - m_{\text{ZFC}}$ appears to be insensitive to the nonlinearity in the superparamagnetic response and to the effect of a residual field. Since it can also be easily modeled, this curve which reflects the unblocking of the particles as a function of temperature may be useful in some cases.

Finally, the flattening of the FC curve with increasing field amplitude is reminiscent of the effect of interparticle interactions. This should be related to the existence, in concentrated samples, of an internal effective field reflecting the dipolar interactions among the nanomagnets.

ACKNOWLEDGMENTS

The authors acknowledge D. Ferrah and E. Bonet for fruitful discussions, the PLYRA for nanoparticle sample preparation, and the CML for SQUID magnetometry measurements.

APPENDIX: SUMMARY OF THE ANALYTICAL EXPRESSIONS USED FOR ZFC/FC MODELLING

In the present article, analytical expressions have been used to describe the evolution of the magnetic moment, in a ZFC/FC measurement, for an assembly of particles having the same volume V and consequently the same anisotropy $K = K_{\text{eff}}V$ and magnetic moment $\mu = M_S V$. For a particle assembly with a size distribution, these analytical expressions are numerically integrated over the particle volume.

The *progressive crossover model* described in Ref. 13 allows us to write

$$m_{\text{ZFC}} = m_b e^{-\delta t/\tau} + m_{\text{eq}}(1 - e^{-\delta t/\tau})$$

and

$$m_{\text{FC}} = m_{\text{eq}}(T_B) e^{-\delta t/\tau} + m_{\text{eq}}(1 - e^{-\delta t/\tau})$$

with

$$m_b = \frac{\mu_0 \mu^2 H}{3K}, \quad T_B = \frac{K/k_B}{0.9283 \ln\left(\frac{K}{k_B \tau_0 r_T}\right) - 3.69},$$

$$\delta t = 0.6727 \frac{T}{r_T} \left(\frac{k_B T}{K}\right)^{0.9}, \quad \text{and} \quad \tau = \tau_0 \exp\left(\frac{K}{k_B T}\right).$$

Different approximations can then be used for the equilibrium magnetic moment m_{eq} .

(1) Linear response approximation:

$$m_{\text{eq}} = \frac{\mu_0 \mu^2 H}{3k_B T}.$$

(2) Langevin approximation:

$$m_{\text{eq}} = \mu \left[\coth\left(\frac{\mu_0 \mu H}{k_B T}\right) - \frac{k_B T}{\mu_0 \mu H} \right].$$

(3) Third-order susceptibility approximation:

$$m_{\text{eq}} = \frac{\mu_0 \mu^2 H}{3k_B T} + \alpha \mu \left(\frac{\mu_0 \mu H}{k_B T}\right)^3,$$

where the coefficient α (reduced third-order susceptibility) depends on the value of the dimensionless parameter $\sigma = K/(k_B T)$:

$$\alpha = -\frac{1}{45} - 8.7 \times 10^{-4} \sigma - 6 \times 10^{-5} \sigma^2 \quad \text{if } \sigma < 2,$$

$$\alpha = -0.01355 - 0.00532 \sigma \quad \text{if } \sigma \in [2, 5.5],$$

$$\alpha = -\frac{1}{15} + \frac{0.13257}{\sigma} - \frac{0.0083}{\sigma^2} \quad \text{if } \sigma > 5.5.$$

Note that these approximations for m_{eq} can also be used in the framework of the *abrupt transition model* where we have

$$\text{for } T \geq T_B : \quad m_{\text{ZFC}} = m_{\text{FC}} = m_{\text{eq}},$$

$$\text{for } T < T_B : \quad m_{\text{ZFC}} = m_b \quad \text{and} \quad m_{\text{FC}} = m_{\text{eq}}(T_B).$$

*florent.tournus@univ-lyon1.fr

¹D. Weller, A. Moser, L. Folks, M. E. Best, W. Lee, M. F. Toney, M. Schwickert, J. U. Thiele, and M. F. Doerner, IEEE Trans. Magn. **36**, 10 (2000).

²A. Moser, K. Takano, D. T. Margulies, M. Albrecht, Y. Sonobe, Y. Ikeda, S. Sun, and E. E. Fullerton, J. Phys. D: Appl. Phys. **35**, R157 (2002).

³S. Mornet, S. Vasseur, F. Grasset, and E. Duguet, J. Mater. Chem. **14**, 2161 (2004).

⁴C. Xu and S. Sun, Polym. Int. **56**, 821 (2007).

⁵A. H. Lu, E. L. Salabas, and F. Schüth, Angew. Chem. Int. Ed. **46**, 1222 (2007).

⁶K. M. Krishnan, IEEE Trans. Magn. **46**, 2523 (2010).

⁷F. Tournus and A. Tamion, J. Magn. Magn. Mater. **323**, 1118 (2011).

⁸E. P. Wohlfarth, Phys. Lett. A **70**, 489 (1979).

⁹R. W. Chantrell, M. El-Hilo, and K. O'Grady, IEEE Trans. Magn. **27**, 3570 (1991).

¹⁰H. Pfeiffer and R. W. Chantrell, J. Magn. Magn. Mater. **120**, 203 (1993).

¹¹M. Respaud, J. M. Broto, H. Rakoto, A. R. Fert, L. Thomas, B. Barbara, M. Verelst, E. Snoeck, P. Lecante, A. Mosset *et al.*, Phys. Rev. B **57**, 2925 (1998).

¹²A. Tamion, M. Hillenkamp, F. Tournus, E. Bonet, and V. Dupuis, Appl. Phys. Lett. **95**, 062503 (2009).

¹³F. Tournus and E. Bonet, J. Magn. Magn. Mater. **323**, 1109 (2011).

¹⁴M. El-Hilo, K. O'Grady, and R. W. Chantrell, J. Magn. Magn. Mater. **114**, 307 (1992).

¹⁵R. Sappey, E. Vincent, N. Hadacek, F. Chaput, J. P. Boilot, and D. Zins, Phys. Rev. B **56**, 14551 (1997).

¹⁶H. Kachkachi, W. T. Coffey, D. S. F. Crothers, A. Ezzir, E. C. Kennedy, M. Noguès, and E. Tronc, J. Phys.: Condens. Matter **12**, 3077 (2000).

¹⁷R. K. Zheng, H. Gu, B. Xu, and X. X. Zhang, J. Phys.: Condens. Matter **18**, 5905 (2006).

¹⁸The Langevin function $\mathcal{L}(x) = \coth(x) - 1/x$ gives the thermodynamic equilibrium response $m(H)$ for an assembly of paramagnetic

spins (or macrospins, when their magnetic anisotropy can be neglected) of individual moment μ : We have $m(H) = m_S \mathcal{L}(\xi)$ with the dimensionless parameter $\xi = \frac{\mu_0 \mu H}{k_B T}$ and m_S as the saturation magnetic moment. For macrospins with a size distribution $\rho(V)$, we note that $\mu = M_S V$, where V is the particle size and M_S is the saturation magnetization, so that the total magnetic moment is obtained by integration of Langevin functions: $m = m_S \int \mathcal{L}_V \rho(V) dV$.

¹⁹Y. Shiratsuchi and M. Yamamoto, Phys. Rev. B **76**, 144432 (2007).

²⁰M. Respaud, J. Appl. Phys. **86**, 556 (1999).

²¹H. Mamiya and I. Nakatani, IEEE Trans. Magn. **34**, 1126 (1998).

²²W. Wernsdorfer, E. B. Orozco, K. Hasselbach, A. Benoit, B. Barbara, N. Demoncey, A. Loiseau, H. Pascard, and D. Mailly, Phys. Rev. Lett. **78**, 1791 (1997).

²³M. Jamet, W. Wernsdorfer, C. Thirion, D. Mailly, V. Dupuis, P. Mélinon, and A. Pérez, Phys. Rev. Lett. **86**, 4676 (2001).

²⁴A. Tamion, E. Bonet, F. Tournus, C. Raufast, A. Hillion, O. Gaier, and V. Dupuis, Phys. Rev. B **85**, 134430 (2012).

²⁵F. Tournus, N. Blanc, A. Tamion, M. Hillenkamp, and V. Dupuis, J. Magn. Magn. Mater. **323**, 1868 (2011).

²⁶A. Hillion, A. Tamion, F. Tournus, J.-B. Flament, M. Hillenkamp, E. Bonet, and V. Dupuis, IEEE Trans. Magn. **47**, 3154 (2011).

²⁷A. Hillion, M. Pauly, A. Tamion, F. Tournus, M. Hillenkamp, B. P. Pichon, S. Begin-Colin, and V. Dupuis, J. Appl. Phys. **112**, 123902 (2012).

²⁸N. A. Usov, J. Appl. Phys. **109**, 023913 (2011).

²⁹W. F. Brown Jr., Phys. Rev. **130**, 1677 (1963).

³⁰J. L. Dormann, D. Fiorani, and M. El Yamani, Phys. Lett. A **120**, 95 (1987).

³¹W. X. Fang, Z. H. He, D. H. Chen, and Y. Z. Shao, J. Magn. Magn. Mater. **321**, 4032 (2009).

³²L. E. Wenger and J. A. Mydosh, Phys. Rev. B **29**, 4156 (1984).

³³J. L. García-Palacios and F. J. Lázaro, Phys. Rev. B **55**, 1006 (1997).

³⁴N. A. Usov and Y. B. Grebenshchikov, J. Appl. Phys. **106**, 023917 (2009).

³⁵The linear interpolation of $\alpha(\sigma)$ between $\sigma = 2$ and $\sigma = 5.5$ is given by $\alpha \simeq -0.01355 - 0.00532 \sigma$.

- ³⁶A. Perez, P. Melinon, V. Dupuis, L. Bardotti, B. Masenelli, F. Tournus, B. Prevel, J. Tuaillon-Combes, E. Bernstein, A. Tamion, N. Blanc, D. Tainoff, O. Boisron, G. Guiraud, M. Broyer, M. Pellarin, N. Del Fatti, F. Vallee, E. Cottancin, J. Lerme, J-L. Vialle, C. Bonnet, P. Maioli, A. Crut, C. Clavier, J. L. Rousset, F. Morfin, *Int. J. Nanotech.* **7**, 523 (2010).
- ³⁷A. Tamion, C. Raufast, M. Hillenkamp, E. Bonet, J. Jouanguy, B. Canut, E. Bernstein, O. Boisron, W. Wernsdorfer, and V. Dupuis, *Phys. Rev. B* **81**, 144403 (2010).

Récemment, nous avons poursuivi ce travail de modélisation et d'analyse des mesures de magnétométrie en nous intéressant aux courbes de rémanence isothermes (courbes IRM et DcD, « Isothermal Remanent Magnetization » et « Direct current Demagnetization »). Ces courbes sont particulièrement intéressantes puisqu'elles mettent en jeu le retournement (irréversible) des macrospins sous un champ appliqué, et sont donc complémentaires des mesures ZFC/FC où le retournement se fait sous l'effet de la température (passage d'un régime bloqué à superparamagnétique). De plus, elles permettent de caractériser les interactions entre particules dans une assemblée (courbe δM). Ce travail nous permet d'être en mesure de simuler de manière fiable et rapide des courbes IRM pour des assemblées réalistes de nano-aimants (avec distribution de taille notamment), et d'utiliser des courbes expérimentales pour en tirer des informations fines (comme l'existence d'une dispersion d'anisotropie, ou d'une anisotropie bi-axiale) sur les propriétés magnétiques intrinsèques des particules [Hillion2013a].

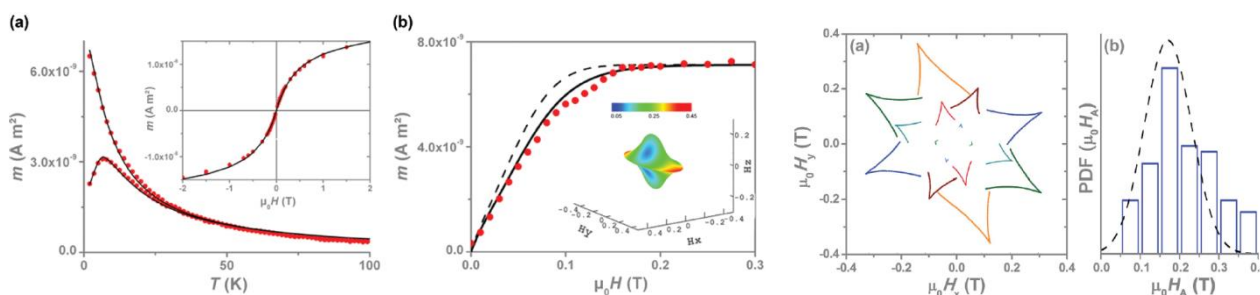


Fig. 13 : À gauche : a) courbes ZFC/FC et $m(H)$ à 300 K expérimentales (points) et ajustées (courbes) b) courbe IRM expérimentale à 2 K (points) et ajustement avec (courbe en trait plein) ou sans contribution bi-axiale à l'anisotropie (courbe en pointillés). Il est la fois nécessaire d'inclure une distribution de constante d'anisotropie et une contribution bi-axiale pour reproduire les courbes expérimentales. L'échantillon est constitué de particules de Co diluées dans une matrice de carbone amorphe. À droite : a) exemple de mesures d'astroïdes (permettant de déduire le champ de retournement) de particules individuelle, obtenues par la technique micro-SQUID (collab. W. Wernsdorfer, Institut Néel à Grenoble) sur les mêmes particules. b) Comparaison entre la distribution de champ d'anisotropie déduite d'une centaine de mesures micro-SQUID sur particules de Co individuelles (histogramme) et la distribution déduite de l'ajustement des mesures conventionnelles de magnétométrie (incluant la courbe IRM). Figure tirée de [Hillion2013a]

Un gros travail de modélisation théorique des mesures IRM a été effectué, en se basant sur une description des assemblées de nanoparticules magnétiques comme des macrospins à anisotropie uniaxiale (pouvant par la suite être étendu au cas d'une anisotropie bi-axiale), orientés aléatoirement et sans interaction. L'effet de la température est pris en compte à l'aide d'un temps de retournement des macrospins (relaxation de Néel) qui dépend de manière exponentielle du rapport $\Delta E/k_B T$ où ΔE représente la barrière d'énergie pour le retournement de l'aimantation. La combinaison de ce modèle de relaxation de Néel et de macrospin (modèle de Stoner-Wohlfarth) permet d'établir des formules analytiques pour les courbes IRM et d'étudier l'influence de chacun des paramètres. Là encore, comme on peut le voir avec la publication « **Modelling of isothermal remanence magnetisation curves for an assembly of macrospins** » [Tournus2015] reproduite ci-dessous, ce travail permet de mieux appréhender les mesures expérimentales ainsi que la mise en place de procédures d'ajustement pour déterminer les propriétés magnétiques d'assemblées de nano-aimants [Hillion2014, Oyarzun2015, Tournus2016].



Modelling of isothermal remanence magnetisation curves for an assembly of macrospins



F. Tournus

Institut Lumière Matière, UMR5306 Université Lyon 1-CNRS, Université de Lyon 69622 Villeurbanne Cedex, France

ARTICLE INFO

Article history:

Received 4 December 2013

Received in revised form

30 April 2014

Available online 26 September 2014

Keywords:

Magnetic nanoparticle

Remanence curve

Magnetic anisotropy

Nanoparticle assembly

Switching field distribution

ABSTRACT

We present a robust and efficient framework to compute isothermal remanent magnetisation (IRM) curves for magnetic nanoparticle assemblies. The assembly is modelled by independent, randomly oriented, uniaxial macrospins and we use a Néel model to take into account the thermal relaxation. A simple analytic expression is established for a single size, in a sudden switching approximation, and is compared to more evolved models. We show that for realistic samples (necessarily presenting a size dispersion) the simple model is very satisfactory. With this framework, it is then possible to reliably simulate IRM curves, which can be compared to experimental measurements and used in a best fit procedure. We also examine the influence of several parameters on the IRM curves and we discuss the link between the irreversible susceptibility and the switching field distribution.

© 2014 Elsevier B.V. All rights reserved.

1. Introduction

Among the various magnetic measurements used to characterise a nanomagnet assembly (or a granular system), Isothermal Remanent Magnetisation (IRM) is a long-established protocol which is however rarely quantitatively exploited [1–5]. Originally, it was used to evaluate the switching field distribution (SFD) or, combined with Direct Current Demagnetisation (DCD) measurements, to detect the nature of interactions via the parameter Δm or via a Henkel plot [6–18]. In order to perform a IRM measurement, the nanomagnet sample is first demagnetised (zero field cooling from the superparamagnetic state). Then, a magnetic field H is applied for a given time before going back to zero: the isothermal remanent magnetic moment is then acquired. By increasing successively H , we can obtain a full IRM(H) curve, starting from 0, and going up to a maximum value which is simply the remanent moment m_R obtained after saturation (i.e. the same remanent state as for the major hysteresis loop). IRM curves only reflect the *irreversible* switching of magnetic nanoparticles and the signal, which is always measured at zero field, is free of any other magnetic contribution. This means that there is no effect of superparamagnetic particles, paramagnetic substrate or diamagnetic impurities for instance, making this measurement of particular interest. Moreover, since the underlying phenomenon (irreversible switching of macrospins, under an applied field) is qualitatively different from low field susceptibility measurements

(where we detect a thermal relaxation), IRM curves appear to be complementary to the widely used zero field-cooled/field-cooled (ZFC/FC) curves [5,8,19–21].

In this paper, we will discuss the modelling of IRM curves for model nanoparticle assemblies. Our goal here is to provide a simple way to efficiently simulate realistic curves, which can then be compared to experimental measurements and be used for a best fit procedure, in order to determine some intrinsic properties of the nanomagnets. It is indeed possible to experimentally study samples of magnetic nanoparticles diluted in a non-magnetic matrix, where the inter-particle interactions can safely be neglected, and therefore well described by the theoretical framework exposed in this paper. In the following, such an assembly will be modelled by independent, randomly oriented, uniaxial macrospins. We will first consider the case of zero temperature measurement and a single magnetic anisotropy, before taking into account the effect of temperature, still for a single particle size and anisotropy. Finally, we will address the more realistic case of measurements, at a given temperature, on a nanomagnet assembly displaying a size distribution and/or a magnetic anisotropy distribution.

2. IRM curves at zero temperature

2.1. Stoner–Wohlfarth model and magnetisation switching

Let us remind the reader some of the results derived from the well known Stoner–Wohlfarth macrospin model. We will consider

E-mail address: florent.tournus@univ-lyon1.fr

an assembly of identical particles behaving as uniaxial macrospins, of magnetic moment $\mu = M_S V$ and anisotropy energy $K = K_{\text{eff}} V$, where V is the particle volume, M_S the saturation magnetisation and K_{eff} the magnetic anisotropy constant. When a given particle is submitted to an external magnetic field H , its energy can be written as

$$E = K \sin^2 \theta - \mu_0 H \cos(\theta - \varphi)$$

where θ is the angle between the macrospin magnetic moment and its easy axis and φ the angle between the magnetic field and the macrospin easy axis. With zero applied field, the system has two degenerate minima ($\theta = 0$ and $\theta = \pi$) separated by a maximum ($\theta = \pi/2$), corresponding to an energy barrier K . When a magnetic field is applied, one minimum is rising, becoming metastable, while the other is going down. The barrier to overcome, in order to go from the metastable configuration to the stable one, is decreasing with H . When the maximum (top of the energy barrier) reaches the metastable position, it means that the barrier is vanishing and the system will inevitably switch to the one and only stable orientation. This condition is equivalent to having, at the same time,

$$\frac{\partial E}{\partial \theta} = 0 \quad \text{and} \quad \frac{\partial^2 E}{\partial \theta^2} = 0 \quad (1)$$

The orientation θ_0 of the macrospin when the switching occurs thus verifies

$$K \sin(2\theta_0) = -\mu_0 H \mu \sin(\theta_0 - \varphi) \quad \text{and} \quad 2K \cos(2\theta_0) = -\mu_0 H \mu \cos(\theta_0 - \varphi)$$

which gives $\tan(2\theta_0) = 2 \tan(\theta_0 - \varphi)$. Using trigonometry identities, we can establish that the switching orientation is directly related to the angle φ between the applied field and the easy axis, through

$$\tan \theta_0 = -\tan^{1/3} \varphi \quad (2)$$

The two equations deriving from condition (1) can also be used to determine the switching field, called H_{sw}^0 . By keeping the switching angle θ_0 in the equations, we can write

$$H_{\text{sw}}^0 = H_A \frac{(1 - \tan^2 \theta_0 + \tan^4 \theta_0)^{1/2}}{1 + \tan^2 \theta_0} \quad (3)$$

where the anisotropy field H_A is given by $H_A = 2K/(\mu_0 \mu) = 2K_{\text{eff}}/(\mu_0 M_S)$. Because we know how θ_0 is related to φ , this expression can then be written in an elegant way (through trigonometry manipulations), where the dependence on φ is explicit:

$$H_{\text{sw}}^0 = H_A (\sin^{2/3} \varphi + \cos^{2/3} \varphi)^{-3/2} \quad (4)$$

This result is well known, much more than the above expression involving θ_0 which can however be useful. We can see from the equation, and in Fig. 1a, that $H_{\text{sw}}^0(\varphi)$ is symmetric with respect to $\varphi = \pi/4$ where it has its minimum value [$H_{\text{sw}}^0(\pi/4) = H_A/2$], and reaches its maximum value of H_A for $\varphi = 0$ and $\varphi = \pi/2$. Note that we have restricted here φ in the interval $[0, \pi/2]$, but by symmetry we have $H_{\text{sw}}^0(\pi - \varphi) = H_{\text{sw}}^0(\varphi)$.

2.2. Analytical expression of the IRM curve for a randomly oriented macrospin assembly

From the Stoner–Wohlfarth expression of the switching field, we know that no particle will switch until H reaches $H_A/2$ and that all the particles will have switched when H reaches H_A . This means that we have $\text{IRM}(H) = 0$ for $H \leq H_A/2$ and $\text{IRM}(H) = m_R$ for $H \geq H_A$. In the interval $[H_A/2, H_A]$, we need to determine which particles in the assembly will switch for a given applied field H . From the shape of the H_{sw}^0 curve, we can tell that the particles with an angle φ between the field and the easy magnetisation direction in the

interval $[\varphi_1, \varphi_2]$ where $H > H_{\text{sw}}^0(\varphi)$ will switch. Since the switching field curve is symmetric, we have $\varphi_1 = \pi/4 - \delta$ and $\varphi_2 = \pi/4 + \delta$ where δ depends on H (it goes from zero for $H = H_A/2$ to $\pi/4$ for $H = H_A$).

Let us now express the value of $\text{IRM}(H)$, taking into account the random orientation of the easy axis in the particle assembly. The probability density function of φ (defined in the $[0, \pi]$ interval) is given by $\rho(\varphi) = \sin \varphi/2$. The contribution to the IRM signal of the switching of particles having an orientation between φ and $\varphi + d\varphi$ is then equal to $2N_{\text{tot}} \mu \cos \varphi \rho(\varphi) d\varphi$. Here, N_{tot} is the total number of particles, and the factor 2 comes from the fact that particles having switched and particles already in the most favourable orientation will contribute to the remanence [22]. We then have

$$\text{IRM}(H) = 2 \int_{\pi/4-\delta}^{\pi/4+\delta} N_{\text{tot}} \mu \cos \varphi \frac{\sin \varphi}{2} d\varphi = m_R \int_{\pi/4-\delta}^{\pi/4+\delta} \sin(2\varphi) d\varphi$$

where we have used $m_R = N_{\text{tot}} \mu/2$. By simple integration, we thus find

$$\text{IRM}(H) = m_R \sin(2\delta) = m_R \cos(2\varphi_1)$$

φ_1 being the solution below $\pi/4$ of the equation $H_{\text{sw}}^0(\varphi) = H$. In order to solve this equation, we use the expression (3) established above and we can introduce the dimensionless parameters $h = H/H_A$ and $x = \tan^2 \theta_0 = \tan^{2/3} \varphi$ to write

$$h = \frac{(1 - x + x^2)^{1/2}}{1 + x}$$

This corresponds to a second order equation $x^2(1 - h^2) - x(1 + 2h^2) + (1 - h^2) = 0$ and the smallest solution is given by

$$x_1 = \frac{1 + 2h^2 - \sqrt{12h^2 - 3}}{2(1 - h^2)} \quad (5)$$

Finally we can deduce φ_1 from the relation $\varphi_1 = \arctan(x_1^{3/2})$. Further, a simple analytical expression can be obtained for the IRM curve by writing $\cos(2\varphi_1) = \cos^2 \varphi_1 - \sin^2 \varphi_1$ and then use the trigonometric relations $\cos^2 = 1/(1 + \tan^2)$ and $\sin^2 = \tan^2/(1 + \tan^2)$ together with the fact that $\tan^2 \varphi_1 = x_1^3$. In the end, we have established a compact equation for $\text{IRM}(H)$:

$$\text{IRM}(H) = m_R \frac{1 - x_1^3}{1 + x_1^3} \quad \text{for } H \in [H_A/2, H_A] \quad (6)$$

This curve is represented in Fig. 1b, and we note that there is an angular point at $H = H_A/2$. We will see in the following how this formalism can be extended to non-zero temperature and to the case of a particle size and/or anisotropy distribution. Note that, since neither the anisotropy field H_A nor the switching field at zero temperature depend on the particle size, the IRM curve at zero temperature is independent of the size distribution (just as for the Stoner–Wohlfarth hysteresis loop), provided that the particles all have the same M_S and K_{eff} .

An analytical expression can also be derived for the DCD protocol. For a non-interacting macrospin assembly, we have the relation [23] $\text{DCD}(H) = m_R - 2\text{IRM}(H)$. This only reflects the fact that for the initial state used for the DCD measurement all the macrospins are preliminarily brought in the metastable orientation and will thus eventually switch when the field is applied, while for the IRM already half of the macrospin are in the more favourable orientation. We then have

$$\text{DCD}(H) = m_R \frac{3x_1^3 - 1}{1 + x_1^3} \quad \text{for } H \in [H_A/2, H_A] \quad (7)$$

while $\text{DCD}(H) = m_R$ for $H \leq H_A/2$ and $\text{DCD}(H) = -m_R$ for $H \geq H_A$. Note that because the sample is preliminarily saturated in one

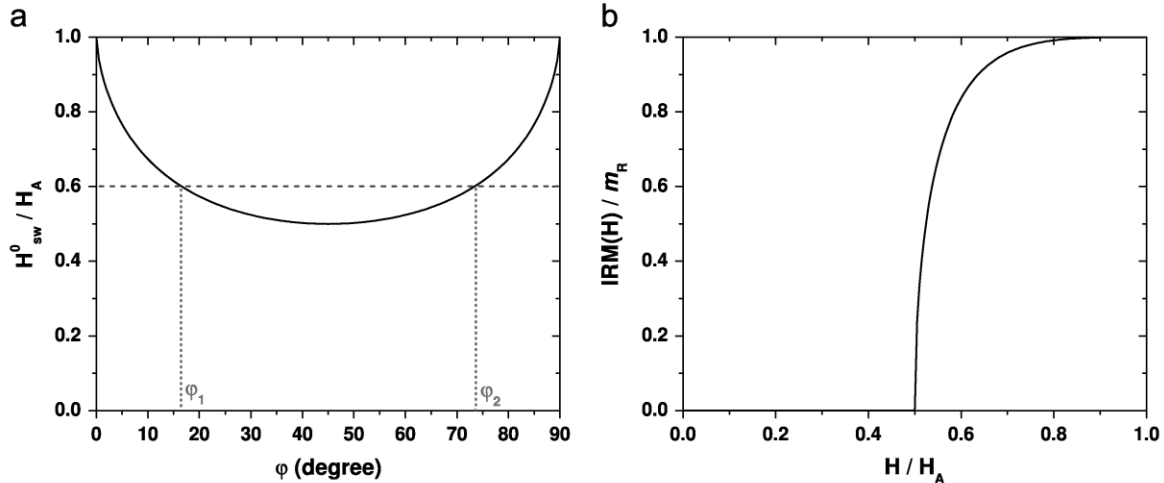


Fig. 1. (a) Zero-temperature switching field H_{sw}^0 as a function of the angle φ between the applied field and the macrospin easy axis. As an example, the angles φ_1 and φ_2 , defining the range of particles which will be able to switch for an applied magnetic field $H = 0.6 H_A$, are shown. (b) IRM(H) curve, for an assembly of randomly oriented identical macrospins. This curve can be analytically described (see text).

direction and then the reversal field is applied in the opposite direction, the DCD curve is in fact DCD($|H|$). We can also write down the exact field that has to be applied in order to have DCD(H_R) = 0 (this defines the DC demagnetising field), and we find for this assembly of identical macrospins at zero temperature:

$$H_R = H_A \frac{\sqrt{1 - x_R + x_R^2}}{1 + x_R} \quad \text{with } x_R = 3^{-1/3}$$

corresponding to $H_R \simeq 0.524 H_A$. This field is not related to any particular switching field and is slightly different from the coercive field of the Stoner–Wohlfarth hysteresis loop, as originally pointed out by Wohlfarth [23].

2.3. Irreversible susceptibility and switching field distribution

Because the IRM curve reflects the irreversible switching of nanomagnets, it seems convenient and physically meaningful to define the *irreversible* susceptibility χ_{irr} as $\chi_{irr} = dIRM/dH$ [4,7,9,10,12,15,17,24–26]. From the expressions established before, we can write

$$\chi_{irr} = -2m_R \sin(2\varphi_1) \frac{d\varphi_1}{dH}$$

which corresponds to

$$\chi_{irr} = -2m_R \sin(2\varphi_1) \left[\frac{dH_{sw}^0}{d\varphi}(\varphi_1) \right]^{-1} \quad (8)$$

This shows that when $dH_{sw}^0/d\varphi$ goes to zero then the irreversible susceptibility diverges: it corresponds to a peak occurring at $\varphi_1 = \pi/4$, that is $H = H_A/2$. Using the analytical expression of the IRM curve, we can also determine the evolution of χ_{irr} in the interval $H \in [H_A/2, H_A]$ and we have:

$$\chi_{irr} \propto h^{-5/3} (1 + x_1^3)^{-2/3} \frac{x_1^2}{1 - x_1^2} \quad (9)$$

where we remind that h is defined by $h = H/H_A$ and x_1 is given by Eq. (5). For $H < H_A/2$ or $H > H_A$ we simply have $\chi_{irr} = 0$.

It is often considered [4,7,9,10,12,15,17,24–26] that the derivative of the IRM curve (or what is closely related, of the DCD curve) represents the switching field distribution (SFD), ρ_{sw} of the nanomagnets in a sample. But does $\chi_{irr}(H)$ really reflect $\rho_{sw}(H)$? We will show that for an assembly of randomly oriented particles these two quantities are not strictly proportional, even at zero

temperature (i.e. when there is no influence of the particle size distribution). In the situation considered, the SFD is the direct consequence of the orientation distribution $\rho(\varphi)$. Since by definition we have

$$H_{sw}^0[\varphi_1(H)] = H_{sw}^0[\varphi_2(H)] = H$$

it means that $\varphi_1(H)$ and $\varphi_2(H)$ are the reciprocal functions of $H_{sw}^0(\varphi)$, defined respectively on the interval $[0, \pi/4]$ and $[\pi/4, \pi/2]$. Then, the proportion of particles having a switching field in the interval $[H, H + dH]$, which is $\rho_{sw}(H)dH$, is equal to the proportion of particles verifying $\varphi \in [\varphi_1 + d\varphi_1, \varphi_1]$ or $\varphi \in [\varphi_2, \varphi_2 + d\varphi_2]$. Consequently, we can write (note that $d\varphi_1/dH$ is negative):

$$\rho_{sw}(H) dH = -\rho(\varphi_1) d\varphi_1 + \rho(\varphi_2) d\varphi_2$$

which gives

$$\rho_{sw}(H) = -\frac{\sin \varphi_1 + \sin \varphi_2}{2} \left[\frac{dH_{sw}^0}{d\varphi}(\varphi_1) \right]^{-1} = -\frac{\sqrt{1 + \sin(2\varphi_1)}}{2} \left[\frac{dH_{sw}^0}{d\varphi}(\varphi_1) \right]^{-1}$$

This expression is very similar to Eq. (8) established for χ_{irr} , but it is not identical. Therefore, the two quantities will not display the same precise variation with H . However, the main evolution comes from the $(dH_{sw}^0/d\varphi)^{-1}$ term, so that both χ_{irr} and ρ_{sw} will show a peak (divergence) at $H = H_A/2$ (see Fig. 2). Another way to see the difference between the two quantities is to write that

$$\chi_{irr} \propto -\frac{d\varphi_1}{dH} \cos \varphi_1 \rho(\varphi_1) + \frac{d\varphi_2}{dH} \cos \varphi_2 \rho(\varphi_2)$$

while we have for ρ_{sw} :

$$\rho_{sw} = -\frac{d\varphi_1}{dH} \rho(\varphi_1) + \frac{d\varphi_2}{dH} \rho(\varphi_2)$$

Comparing these two expressions, we clearly see that a cosine factor appears in the irreversible susceptibility but not in the SFD. This shows that, as long as the particles have different easy axis orientations, there is a difference between the two curves [24]. In addition, we can obtain an analytical expression for the SFD for $h \in [1/2, 1]$:

$$\rho_{sw} \propto h^{-5/3} (1 + x_1^3)^{-2/3} \frac{\sqrt{x_1}}{1 - x_1^2} (1 + x_1^3 + 2x_1^{3/2})$$

Although at zero temperature the difference between χ_{irr} and ρ_{sw} appears to be quite marginal, we will see in the following sections that at a non-zero temperature, for an assembly of particles with a size distribution, the two quantities can widely differ.

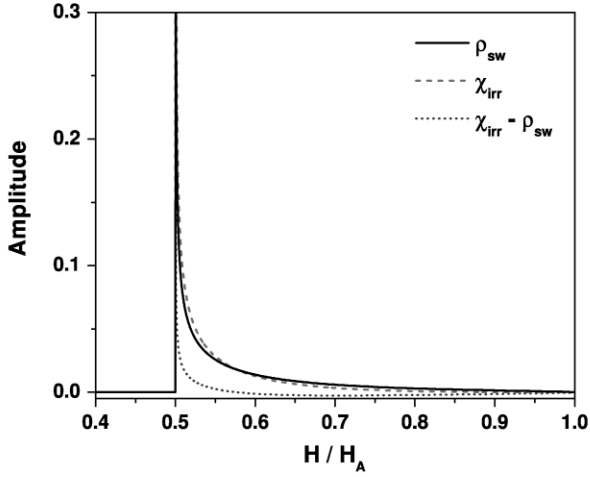


Fig. 2. Comparison between the irreversible susceptibility χ_{irr} and the switching field distribution ρ_{sw} , for an assembly of randomly oriented identical macrospins at zero temperature.

3. IRM modelling taking into account the temperature, for a single size and magnetic anisotropy

We now consider the effect of temperature on the macrospin switching. As before, the sample is supposed to be made of independent (i.e. noninteracting) uniaxial macrospins, with the same size, magnetic moment and anisotropy energy, and a random orientation of the easy axis direction. At zero temperature, the energy barrier has to vanish in order for a macrospin to switch from the metastable orientation to the stable one. At a given temperature, it becomes possible to overcome the barrier and to observe switching with an applied field which does not completely suppress it. The only effect of temperature that we will consider here is this statistical crossing (supposed to occur only from the metastable state to the stable one, this approximation will be examined further). We will also assume that macrospins only populate the lowest energetic configuration of the potential wells (i.e. the metastable and the stable orientations). In that sense, each macrospin is supposed to consist of a two state system. This is a highly reasonable approximation, given the fact that the depth of each potential well is much larger than the thermal energy $k_B T$.

3.1. Switching rate

The switching time of a macrospin, representing the occurrence of a statistical jump over the energy barrier ΔE due to thermal agitation, can be written using a Néel expression:

$$\tau_{\text{sw}} = \tau_0 \exp\left(\frac{\Delta E}{k_B T}\right) \quad (10)$$

where τ_0 is typically of the order of 10^{-10} s. Since the energy barrier separating the metastable state from the stable state will be reduced when a magnetic field of increasing amplitude is applied, this will strongly affect the switching time τ_{sw} which can become smaller than the “measurement time” τ_m . Note that, in the IRM protocol, this measurement time is the duration of application of the field H (typically a few seconds) before going back to remanence where the acquisition of IRM(H) is performed (within a time which is supposed for the moment to have no influence: the relaxation at zero field will only be discussed later). If the condition $\tau_{\text{sw}} = \tau_m$ is fulfilled, then it means that statistically the macrospin will have switched for the given applied magnetic field. Therefore, at a given temperature T , the switching field H_{sw}

will be defined as the field for which we have

$$\tau_{\text{sw}}(H_{\text{sw}}, T) = \tau_m \quad (11)$$

Note that this condition means that, when the switching occurs, the energy barrier is still much larger than $k_B T$. It indeed corresponds to $\Delta E/(k_B T) = \ln(\tau_m/\tau_0) \simeq 25$, if we consider a typical value of $\tau_m = 5$ s which is many orders of magnitude larger than τ_0 (around 10^{-10} s). In any case, the value of the parameter $\epsilon_{\text{sw}} = \ln(\tau_m/\tau_0)$ will be somewhere between 20 and 30.

In order to determine the evolution of τ_{sw} with the applied magnetic field, we need to know the variation of the barrier ΔE with H . This evolution depends on the angle φ between the field and the macrospin easy axis. While for $\varphi = 0$ and $\varphi = \pi/2$ it is easy to establish the analytical expression $\Delta E = K(1 - H/H_A)^2$, there is no exact analytical expression for the general case. Nevertheless, it is convenient to write

$$\Delta E(H, \varphi) = K \left[1 - \frac{H}{H_{\text{sw}}^0(\varphi)} \right]^{\alpha(\varphi)} \quad (12)$$

where $\alpha(\varphi)$ is chosen to provide the best fit of numerical calculations of the barrier. It should be noted that the best choice of α depends on the range considered: for small barriers, i.e. for $H \rightarrow H_{\text{sw}}^0$, we have $\alpha \rightarrow 3/2$ for all the angles [27] except $\varphi = 0$ and $\pi/2$; but if the entire range is considered (from $\Delta E = K$ to 0) the best fit gives values which depends on φ and which can significantly differ from $\alpha = 3/2$. Pfeiffer has thus proposed an approximate expression [28] for $\alpha(\varphi)$ which follows the shape of $H_{\text{sw}}^0(\varphi)$ between the two extreme values ($\alpha = 2$ for $\varphi = 0$ and $\pi/2$ and $\alpha = 1.43$ for $\varphi = \pi/4$):

$$\alpha(\varphi) \simeq 0.86 + 1.14 \frac{H_{\text{sw}}^0(\varphi)}{H_A} \quad (13)$$

Another approach is to write

$$\Delta E(H, \varphi) = XK \left[1 - \frac{H}{H_{\text{sw}}^0(\varphi)} \right]^{\alpha} \quad (14)$$

and consider that the coefficient X and/or α depend(s) on φ and H . One can then chose to fix $\alpha = 3/2$ and incorporate all the remaining dependence on φ and H in the prefactor X , which deviates the more from unity, the larger φ differs from $\pi/4$ and the closer H goes to $H_{\text{sw}}^0(\varphi)$ [29]. In the end, since we are interested in efficiently modelling the response of an entire assembly of randomly oriented macrospins, we will use in the following the constant $\alpha = 3/2$ approximation, which means that the energy barrier is supposed to vary as

$$\Delta E(H, \varphi) = K \left[1 - \frac{H}{H_{\text{sw}}^0(\varphi)} \right]^{3/2} \quad (15)$$

The impact of this approximation on the simulated IRM curves will be examined, in comparison with the more precise Pfeiffer approximation. Since the major contribution to IRM curves comes from particles with φ around $\pi/4$, we can anticipate that the $\alpha = 3/2$ approximation is fully satisfying (especially in the case of a particle size and/or anisotropy distribution, which will “blur” the details of the individual curves).

3.2. Sudden switching approximation

We will consider here that there is a *sudden switching* of the macrospins: as long as $\tau_{\text{sw}} > \tau_m$ there is no switching at all, and therefore no change in the IRM, while the switching is inevitable for $\tau_{\text{sw}} \leq \tau_m$. This means that the switching is not gradual, it is assumed to be somehow deterministic instead of statistical. By doing this approximation, we replace the probability to observe a switching event during the time τ_m , which in fact varies continuously between

0 and 1 as τ_{sw} decreases (i.e. as H increases), by a step function having a discontinuity from 0 to 1 at $H = H_{sw}$. This approximation will be discussed in the next section and it appears to be very reasonable in many cases.

The condition of switching (Eq. (11)) corresponds to

$$\frac{\Delta E(H_{sw})}{k_B T} = \ln(\tau_m / \tau_0) \quad (16)$$

Taking into account the expression of ΔE , we can write

$$\tau_0 \exp\left\{\frac{K}{k_B T} \left[1 - \frac{H_{sw}(T)}{H_{sw}^0}\right]^\alpha\right\} = \tau_m$$

which gives

$$H_{sw}(T) = H_{sw}^0 \left\{1 - \left[\frac{k_B T}{K} \ln\left(\frac{\tau_m}{\tau_0}\right)\right]^{1/\alpha}\right\} \quad (17)$$

By using the dimensionless parameters $\sigma = K/(k_B T)$ and $\epsilon_{sw} = \ln(\tau_m / \tau_0)$, we then have

$$\frac{H_{sw}(T)}{H_{sw}^0} = 1 - \left(\frac{\epsilon_{sw}}{\sigma}\right)^{1/\alpha} \quad (18)$$

In the simplest approximation of a constant $\alpha = 3/2$, independent of the angle φ , the effect of temperature is just a reduction of the zero-temperature switching field H_{sw}^0 by a coefficient

$$C(T) = \frac{H_{sw}(T)}{H_{sw}^0} = 1 - \left[\frac{\epsilon_{sw}}{\sigma(T)}\right]^{2/3} \quad (19)$$

which is the same for every macrospin orientation. In such a case, the shape of the astroid curve (polar representation of the switching field as a function of the angle φ) would remain unchanged when the temperature is varied: an increasing temperature would just lead to the shrinking of a macrospin astroid. This feature is not exact, since we know that the exponent α varies with φ , however the true astroid deformation is minor so that this approximation is not too crude [30].

From Eq. (18), it can be seen that the switching field is zero for $\epsilon_{sw} = \sigma$, which corresponds to $K = \epsilon_{sw} k_B T$. This corresponds to the well known blocking temperature concept. Indeed, by defining T_B so that we have

$$K = \epsilon_{sw} k_B T_B \quad (20)$$

where we remind that $\epsilon_{sw} = \ln(\tau_m / \tau_0)$ is typically around 25, we then find that for $T \geq T_B$ the particles are superparamagnetic: they can switch (during the measurement time), without the need of an external magnetic field. Such particles can then reach thermal equilibrium, they do not display any average remanent magnetic moment and therefore they do not contribute to the IRM curve. The coefficient $C(T)$ can also be expressed in a convenient way using the blocking temperature T_B :

$$C(T) = \frac{H_{sw}(T)}{H_{sw}^0} = 1 - \left(\frac{T}{T_B}\right)^{2/3} \quad (21)$$

The corresponding evolution as a function of T/T_B is shown in Fig. 3.

All this shows that, provided T is lower than the blocking temperature T_B , the IRM curve of a randomly oriented macrospin assembly will have the same type of expression as the one derived for zero temperature. The only effect of temperature is the rescaling (reduction) of the switching field (Eq. (19)), so that we can derive the same analytical expression just by changing the definition of the reduced field h to

$$h = \frac{H}{H_A C(T)} \quad (22)$$

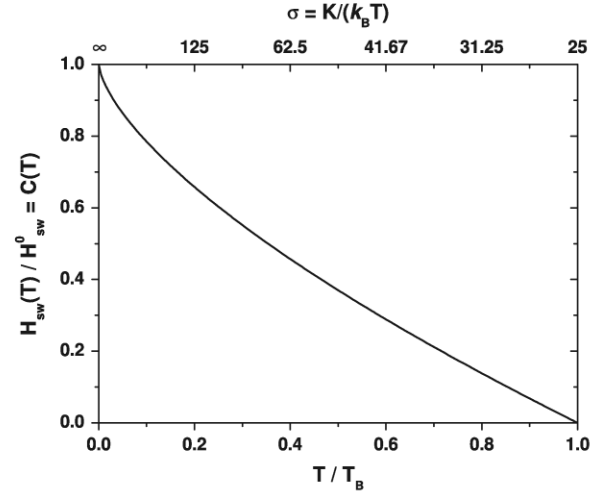


Fig. 3. Evolution of the ratio $H_{sw}(T)/H_{sw}^0$ as a function of T/T_B . Here, the approximation of a constant $\alpha = 3/2$ coefficient is used.

Then, we can write for the assembly, at a non-zero temperature:

$$\text{IRM}(H, T) = m_R \frac{1 - x_1^3}{1 + x_1^3} \quad \text{for } h \in \left[\frac{1}{2}, 1\right] \quad (23)$$

with, as before,

$$x_1 = \frac{1 + 2h^2 - \sqrt{12h^2 - 3}}{2(1 - h^2)} \quad (24)$$

Of course, we still have $\text{IRM}(H, T) = 0$ for $H < H_A C(T)/2$ and $\text{IRM}(H, T) = m_R$ for $H > H_A C(T)$. Note that, for the moment, and since we consider the case of $T < T_B$, we suppose that the remanent moment of the assembly m_R does not vary with temperature.

3.3. Statistical switching model

As already evoked in the preceding section, the switching of a macrospin (transition from the metastable orientation to the stable one) is a statistical process. The probability, for a particle to switch during the interval τ_m is

$$P_{sw} = 1 - \exp\left(-\frac{\tau_m}{\tau_{sw}}\right) \quad (25)$$

where τ_{sw} is the Néel switching time introduced earlier (Eq. (10)). Since we know the variation of τ_{sw} with H (through the variation of ΔE), we can examine how the curve $P_{sw}(H)$ looks like (see Fig. 4a). In the sudden switching approximation, we had approximated this smooth curve by a step function going from 0 to 1 at H_{sw} , while in reality the crossover from 0 to 1 is gradual. There is thus a “statistical spread” or the macrospin switching. It is interesting to characterise this transition width, to see in which case it can be neglected (in particular with respect to the dependence of the switching field on the orientation φ and on the particle size and magnetic anisotropy in the case of an assembly made of non-identical particles).

By introducing the dimensionless parameters

$$c = \frac{\Delta E}{k_B T} \quad \text{and} \quad z = \epsilon_{sw} - c \quad (26)$$

one can express the switching probability: $P_{sw} = 1 - \exp(-e^z)$. Let us now consider the switching probability density (or rate) $p_{sw}(z)$, which means that $p_{sw}(z) dz$ represents the probability for a macrospin to switch, in a time τ_m , in the interval $[z, z + dz]$. However, experimentally we do not control directly the z value but the applied field H . When H goes from 0 to H_{sw}^0 , the energy barrier goes from K to 0 and then ϵ varies from σ to 0: this means

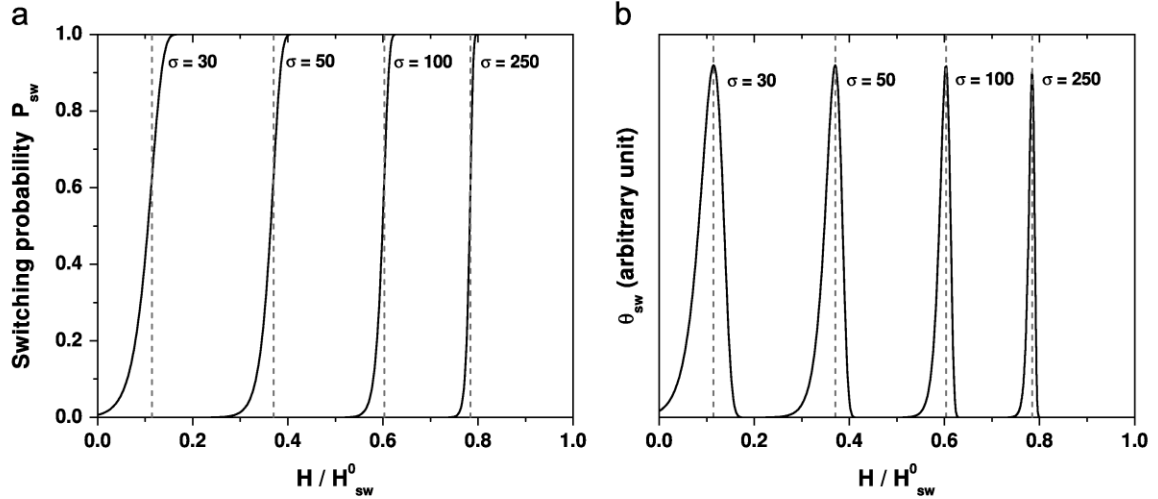


Fig. 4. Evolution of the switching probability P_{sw} (a) and probability density θ_{sw} (b) as a function of H/H_{sw}^0 , for different values of the σ parameter (ϵ_{sw} has been fixed to 25). The dotted lines indicate, for each σ , the switching field H_{sw} corresponding to the sudden switching approximation. The width of the θ_{sw} peaks corresponds to ΔH_p .

that the parameter z goes from a negative value ($\epsilon_{sw} - \sigma$, which is necessarily negative otherwise the particles would be superparamagnetic) to a quite large positive value (ϵ_{sw}). The switching rate θ_{sw} , as a function of the variable H is then equal to

$$\theta_{sw}(H) = p_{sw}(z) \frac{dz}{dH}$$

and we can write

$$\theta_{sw}(H) = p_{sw}(z) \frac{\sigma \alpha}{H_{sw}^0} \left(1 - \frac{H}{H_{sw}^0}\right)^{\alpha-1} = e^z \exp(-e^z) \frac{\sigma \alpha}{H_{sw}^0} \left(1 - \frac{H}{H_{sw}^0}\right)^{\alpha-1}$$

The switching probability density θ_{sw} is thus the product of two terms: one shows a strong variation with H , first increasing and then decreasing (term corresponding to p_{sw}), and the other one softly varies with H , always decreasing (term corresponding to dz/dH). The result is that $\theta_{sw}(H)$ displays a peak shape and is almost indistinguishable from p_{sw} . Therefore we can make the approximation $\theta_{sw} \simeq p_{sw}$ to find the peak position of the switching probability density. This corresponds to the condition $dp_{sw}/dz = 0$, which is equivalent to $1 - e^z = 0$. The solution is simply $z = 0$, which means that the peak occurs for

$$\epsilon = \epsilon_{sw} = \ln(\tau_m/\tau_0)$$

In the end, we find that the macrospin switching probability density is maximal when

$$\frac{\Delta E}{k_B T} = \ln(\tau_m/\tau_0)$$

which is precisely the condition defining the switching field (Eq. (16)) in the sudden switching approximation. This shows that it is physically sound to consider that the macrospin switching occurs when the applied magnetic field is equal to the previously defined H_{sw} .

The switching probability density peak is not only characterised by its position, but also by its width. Still considering that $\theta_{sw} \simeq p_{sw}$, we can determine the z value for which we have $p_{sw}(z) = p_{sw}(0)/2$ (half of the maximum of the peak). This corresponds to the self-consistent equation $z = e^z - \ln(2e)$, the solutions of which are $z_1 \simeq 0.99$ and $z_2 \simeq -1.46$ (note that this is mathematical and fully independent of any parameter of the system). In order to determine the width of the peak (spread of the statistical switching) with the magnetic field as variable, ΔH_p , we just need to determine the fields verifying $z(H_1) = z_1$ and $z(H_2) = z_2$ and to consider that

$\Delta H_p = H_1 - H_2$. Noting that we have $\epsilon(H_1) = \epsilon_{sw} - 0.99$ and $\epsilon(H_2) = \epsilon_{sw} + 1.46$ while $\epsilon(H_{sw}) = \epsilon_{sw}$, we obtain

$$\frac{\Delta H_p}{H_{sw}} = \frac{1(\epsilon_{sw} + 1.46)^{1/\alpha} - (\epsilon_{sw} - 0.99)^{1/\alpha}}{2(\sigma^{1/\alpha} - \epsilon_{sw}^{1/\alpha})}$$

One can then write that the macrospin switching occurs for an applied field $H = H_{sw} \pm \Delta H_p$, i.e. with a statistical dispersion even for identical particles. Note that this dispersion only depends on the parameter σ (provided τ_m and τ_0 are fixed). From the expression above, we can see that the relative dispersion is decreasing with σ : a large values of σ will correspond to a reduced switching range (and at the same time, the switching field is getting close to the zero-temperature switching field). On the contrary, we can see that for particles approaching the superparamagnetic limit, i.e. for $\sigma \rightarrow \epsilon_{sw}$, the relative width of the switching probability peak becomes very large (it diverges, because $H_{sw} \rightarrow 0$). Concerning the absolute width in magnetic field, we can establish that

$$\Delta H_p = A H_{sw}^0 \left(1 - \frac{H_{sw}}{H_{sw}^0}\right) \quad (27)$$

where the factor A is a simple constant (as soon as ϵ_{sw} is fixed, i.e. for fixed τ_m and τ_0). Typically we have $A \simeq 0.033$ for $\epsilon_{sw} = 25$ (A only varies from 0.027 to 0.041, for $\epsilon \in [20, 30]$). As a function of the parameter σ , we can also write

$$\Delta H_p = B H_{sw}^0 \sigma^{-1/\alpha}$$

where B also depends only on ϵ_{sw} and is typically around 0.28 (it remains in the interval $[0.26, 0.30]$ for $\epsilon_{sw} \in [20, 30]$). Finally, taking into account these results, it is important to keep in mind that

$$H_{sw} \rightarrow H_{sw}^0 \quad \text{implies} \quad \Delta H_p \rightarrow 0$$

while

$$H_{sw} \rightarrow 0 \quad \text{implies} \quad \Delta H_p \rightarrow A H_{sw}^0$$

The statistical spread of the switching is at most around 3% of the zero-temperature switching field (i.e. ΔH_p remains, in realistic situations, always lower than 3% of the anisotropy field).

On one hand the probabilistic nature of magnetic moment switching will correspond to a certain width of the irreversible susceptibility peak (even for a single angle φ), and on the other hand, the variety of orientations φ in a macrospin assembly will also imply a width of the χ_{irr} peak (even in the sudden switching

approximation). We can compare this broadening due to probabilistic switching, ΔH_p with the one coming from the existence of various orientations, ΔH_φ . We can define ΔH_φ as the difference between the field $H_{90\%}$ where the IRM reaches 90% of its maximum value and H_{peak} which corresponds to the point where the IRM starts to grow (divergence of χ_{irr}). We then know that H_{peak} corresponds to $h = 1/2$ (the particles with $\varphi = \pi/4$ are the first to switch) while $H_{90\%}$ corresponds to h such that $(1 - x^3)/(1 + x^3) = 0.9$, and hence $h \simeq 0.637$. This means that

$$\Delta H_\varphi \simeq 0.273 H_{\text{peak}} \quad \text{with } H_{\text{peak}} = \frac{H_A}{2} C(T)$$

or written differently:

$$\frac{\Delta H_\varphi}{H_A} = 0.637 \frac{H_{\text{sw}}}{H_{\text{sw}}^0} = 0.637 \left[1 - \left(\frac{\epsilon_{\text{sw}}}{\sigma} \right)^{1/\alpha} \right]$$

This equation shows that the relative width $\Delta H_\varphi/H_{\text{peak}}$ is constant. Moreover, we can see that when $\sigma \rightarrow \epsilon_{\text{sw}}$, i.e. when the particles reach the superparamagnetic limit, the switching field dispersion due to the random orientations goes to zero. This case (particles close to the superparamagnetic regime) corresponds, on the contrary to the largest statistical width ΔH_p . Thus, except for particles having large σ values (i.e. large magnetic anisotropy energy compared to the thermal energy), the statistical broadening can become quite significant compared to the effect of random macrospin axis orientation. One can for instance write that (here we consider the particles with $\varphi = \pi/4$ for the expression of ΔH_p , because they correspond to the peak at H_{peak}):

$$\frac{\Delta H_p}{\Delta H_\varphi} \simeq 0.12 \left[\frac{1}{C(T)} - 1 \right] = 0.12 \frac{\epsilon_{\text{sw}}^{1/\alpha}}{\sigma^{1/\alpha} - \epsilon_{\text{sw}}^{1/\alpha}}$$

However, as soon as σ is a few times larger than ϵ_{sw} , the statistical nature of the macrospin switching has a very minor effect on the IRM curves. Let us emphasise that it is useful to have an idea of these switching field broadening, to evaluate their relevance in the case of an anisotropy distribution.

3.4. Discussion

In the framework of the statistical macrospin switching model, the IRM curve for an assembly of nanoparticles can be written as

$$\text{IRM}(H) = 2N_{\text{tot}}\mu \int_0^{\pi/2} P_{\text{sw}}(H, \varphi) \cos \varphi \rho(\varphi) d\varphi \quad (28)$$

which gives for the case of a random orientation of the easy axis [then $\rho(\varphi) = \sin \varphi/2$ and $m_R = N_{\text{tot}}\mu/2$]:

$$\text{IRM}(H) = m_R \int_0^{\pi/2} P_{\text{sw}}(H, \varphi) \sin(2\varphi) d\varphi \quad (\text{probabilistic switching}) \quad (29)$$

where P_{sw} is the switching probability defined earlier in this section.

In the sudden switching approximation, the probability goes from 0 to 1 when $H = H_{\text{sw}}(\varphi)$. The above expression then becomes, by introducing φ_1 and φ_2 the angles verifying $H_{\text{sw}}(\varphi_1) = H_{\text{sw}}(\varphi_2) = H$:

$$\text{IRM}(H) = m_R \int_{\varphi_1}^{\varphi_2} \sin(2\varphi) d\varphi \quad (\text{sudden switching}) \quad (30)$$

which is the integral expression that we had used to derive the analytical IRM formula. If the probabilistic nature of the macrospin switching is taken into account, it is unfortunately not possible anymore to express $\text{IRM}(H)$ analytically. Nevertheless, numerical calculations can be performed (using the above integral formulation) to compare the curves simulated with and without the sudden switching approximation.

In Fig. 5, the different approximations for the exponent α governing the evolution of $\Delta E(H)$ are compared (the constant $\alpha = 3/2$ and $\alpha = 1.43$ approximations and the analytical expression of $\alpha(\varphi)$ proposed by Pfeiffer [28]), for a realistic case of face-centred-cubic (fcc) cobalt nanoparticles of a single size. As it can be seen there are slight differences which, at the onset of the IRM curve, appear to be less important when the particles are smaller (i.e. smaller σ value). We can easily imagine that the difference between these approximations will be blurred when we will consider an assembly of particles showing a size distribution and/or an anisotropy distribution.

In Fig. 6a, we show the modification of the IRM curve for different particle sizes (note that the particle volume controls the magnitude of m_R , i.e. the maximum of the IRM curve), at a measurement temperature of 2 K. As expected, the macrospin switching occurs at lower applied fields for smaller particle sizes (because they correspond to a smaller σ and hence the influence of the thermal agitation is greater). Moreover, the deviation between the sudden switching approximation and the statistical switching is visible only at the onset of the IRM curve for the smallest particle sizes. In the same way, we can observe the difference between these two models on the simulated IRM curves for different temperatures (Fig. 6b). The increase in measurement temperature goes with a decrease of the field where the IRM starts to rise, and is accompanied by a smoother onset of the curve. We can also see here that, as far as we do not approach the blocking temperature (around 5 K in the case of Fig. 6b), the sudden switching approximation is already very satisfactory, even in the case of a single particle size.

3.5. Influence of the relaxation, beyond irreversible switching

The IRM measurement is performed at zero field, but it is not instantaneous. The system then stays during a time τ_{zero} (of the order of a few seconds, just as τ_m) at remanence, so that it can potentially relax. This is exactly what happens for the remanence versus time $m_R(t)$ curves, where the observed decrease reflects the anisotropy energy of the particles in the sample. Note that this relaxation only concerns the particles which are close to the superparamagnetic limit, on the τ_{zero} timescale, i.e. corresponding to a σ close to $\ln(\tau_{\text{zero}}/\tau_0)$. For simplicity, and since they are very similar (they are related to the characteristics of the magnetometer used for the measurements), we will consider in the following that we have $\tau_{\text{zero}} = \tau_m$, so that $\ln(\tau_{\text{zero}}/\tau_0) = \epsilon_{\text{sw}}$.

In the absence of any external magnetic field, the temporal evolution of the magnetic moment m of a macrospin assembly is given by the simple differential equation [31]:

$$\frac{dm}{dt} + \frac{m}{\tau} = 0 \quad (31)$$

where τ is the Néel switching time without applied field, that is

$$\tau = \tau_{\text{sw}}(H = 0) = \tau_0 \exp\left(\frac{K}{k_B T}\right)$$

After a time τ_{zero} , the magnetic moment has evolved from its initial value m_0 to

$$m(\tau_{\text{zero}}) = m_0 e^{-\tau_{\text{zero}}/\tau}$$

Therefore, compared to the situation where we had neglected this zero field relaxation, the remanent moment (prefactor in the expression of the IRM curves) is simply reduced by a factor

$$\eta = \frac{m(\tau_{\text{zero}})}{m_0} = \exp(-e^{\epsilon_{\text{sw}} - \sigma}) \quad (32)$$

It should be noted that this reduction factor is the same, whatever the amplitude of the applied field before coming back to

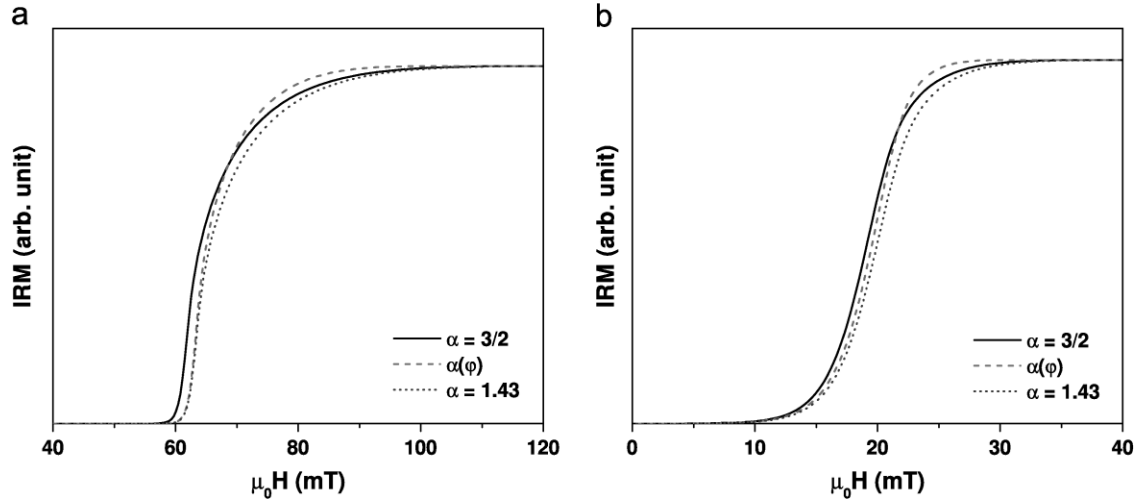


Fig. 5. IRM curves simulated at $T=2$ K, with the statistical switching framework and for different approximations concerning the evolution of the energy barrier with the applied field. Solid lines correspond to the constant $\alpha=3/2$ model, while dashed lines correspond to the $\alpha(\varphi)$ expression proposed by Pfeiffer [28], and the dotted lines correspond to a constant $\alpha=1.43$. The calculations have been performed for fcc Co nanoparticles of 4 nm diameter (a) or 2.5 nm diameter (b), with $K_{\text{eff}}=120$ kJ/m³, $M_S=1.35 \times 10^6$ A/m, and $\epsilon_{\text{sw}}=25$.

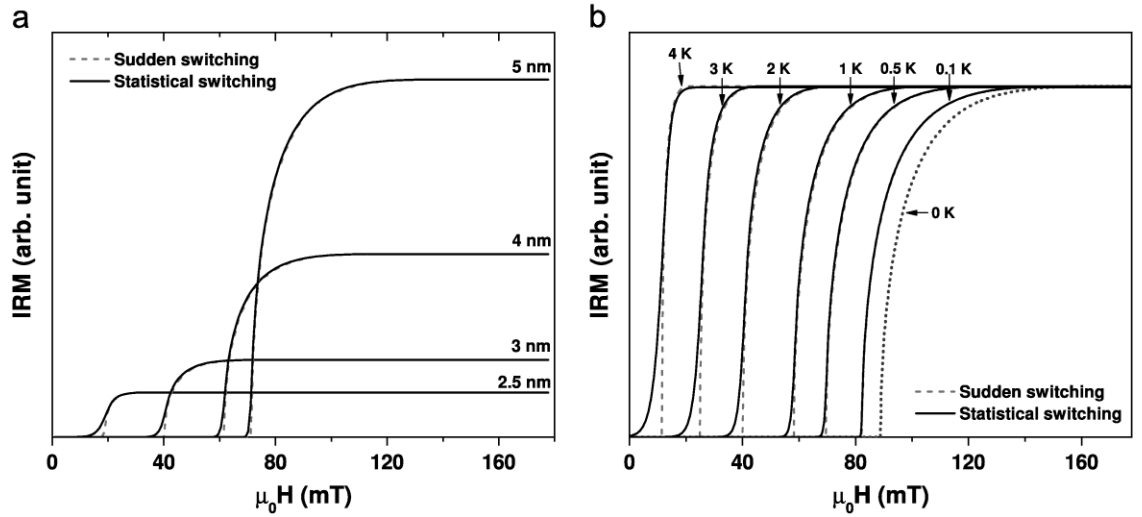


Fig. 6. (a) IRM curves simulated at $T=2$ K for different particle sizes (from 2.5 to 5 nm diameter). (b) IRM curves of 3 nm diameter particles simulated for different temperatures (from 0 to 4 K). The simulations correspond to fcc Co nanoparticle assemblies, with $K_{\text{eff}}=120$ kJ/m³, $M_S=1.35 \times 10^6$ A/m, and $\epsilon_{\text{sw}}=25$, with the constant $\alpha=3/2$ assumption for both sudden switching (dashed lines) or statistical switching (solid lines) models.

remanence for the IRM(H) acquisition. Thus, taking into account the zero-field relaxation just consists in a rescaling of the IRM amplitude. Moreover, this correction by a factor η is only necessary when σ is close to ϵ_{sw} : for instance, as soon as $\sigma > \epsilon_{\text{sw}} + 5$ we have $\eta > 0.99$ (the error of neglecting the relaxation is less than 1%).

Until now, we have considered that the magnetic moment switching was only occurring from the metastable orientation to the stable one, irreversibly. By noting 1 the metastable state and 2 the stable one, we have assumed that the energy barrier between these two states can be overcome in the direction $1 \rightarrow 2$ but not from $2 \rightarrow 1$. This is perfectly justified in the case of a strong asymmetry between 1 and 2, i.e. when the switching occurs under a strong magnetic field. The energy barriers indeed correspond respectively to $\Delta E_{1 \rightarrow 2} = E_{\text{max}} - E_1$ and $\Delta E_{2 \rightarrow 1} = E_{\text{max}} - E_2$, where E_{max} is the energy at the top of the barrier (saddle point), and the difference between E_1 and E_2 is increasing with H (moreover, the energy barrier controls the switching rate through an exponential). Taking into account the switching in the $2 \rightarrow 1$ direction will be relevant only in the case of small applied fields, and if such a

small field is enough to observe a significant amount of macrospin switching; once again, this corresponds to particles close to the superparamagnetic limit.

One can write $\Delta E_{2 \rightarrow 1}$ in a similar form as $\Delta E_{1 \rightarrow 2}$ but with a change of sign [32]:

$$\Delta E_{2 \rightarrow 1} = K(1 + H/H_{\text{sw}}^0)^\alpha \quad (33)$$

The ratio between the two switching times is thus given by

$$r = \frac{\tau_{1 \rightarrow 2}}{\tau_{2 \rightarrow 1}} = \exp\{-\sigma[(1 + h_{\text{sw}})^\alpha - (1 - h_{\text{sw}})^\alpha]\} \quad (34)$$

where we have introduced the reduced field $h_{\text{sw}} = H/H_{\text{sw}}^0$. In the range of h_{sw} we are interested in, we thus have (by developing to the first order in h_{sw} , and replacing α by $3/2$):

$$r \simeq \exp(-3\sigma h_{\text{sw}})$$

From this equation, we can deduce at which condition it can be useful to take into account the $2 \rightarrow 1$ transition. For instance, in order to have $r > 10^{-3}$, we need to have $\sigma h_{\text{sw}} < \ln 10$, which

corresponds approximately to

$$H < \frac{3}{\sigma} H_{sw}^0$$

Note that, because σ is at least equal to $\epsilon_{sw} \simeq 25$ (otherwise the particles are superparamagnetic and do not contribute to the IRM), we indeed find that this relaxation effect is only a correction appearing at low field. One can also find another condition to decide if it is pertinent or not to consider the $2 \rightarrow 1$ transition. Even if the switching time $\tau_{2 \rightarrow 1}$ becomes significant with respect to $\tau_{1 \rightarrow 2}$ it does not mean that it will have an influence on the IRM curve. For this, it should be comparable to the time τ_m otherwise the resulting transition probability remains marginal. One can for instance decide to consider the $2 \rightarrow 1$ transition only if P_{sw} is larger than 10^{-3} . This corresponds to the constraint $\epsilon_{sw} - \epsilon > -3 \ln 10$, which can then be approximately written

$$\sigma \left(1 - \frac{3}{2} h_{sw} \right) < \epsilon_{sw} + 7$$

By combining the previous constraint on h_{sw} (h_{sw} is at most equal to $3/\sigma$) to this one, it is possible to limit the consideration of $2 \rightarrow 1$ transitions to the case:

$$\sigma < \epsilon_{sw} + 11$$

In the end, we can use the previous theoretical expressions of the IRM curve (where this relaxation from 2 to 1 is neglected) as long as the particles verify $\sigma \geq \epsilon_{sw} + 11$. On the other hand, for particles having lower values of σ , the transition $2 \rightarrow 1$ should be taken into account at low field (for $H < 3H_{sw}^0/\sigma$).

Let us examine how the IRM signal can be modelled when both $1 \rightarrow 2$ and $2 \rightarrow 1$ transitions can occur. Among the N_φ particles, for which the orientation is in the $[\varphi, \varphi + d\varphi]$ interval, N_1 particles are in the potential well number 1 (metastable state) and N_2 in the potential well number 2 (stable state). By introducing the proportions $n_1 = N_1/N_\varphi$ and $n_2 = N_2/N_\varphi$, we can write the following set of differential equations:

$$\frac{dn_1}{dt} = -\frac{n_1}{\tau_{1 \rightarrow 2}} + \frac{n_2}{\tau_{2 \rightarrow 1}}$$

$$\frac{dn_2}{dt} = -\frac{n_2}{\tau_{2 \rightarrow 1}} + \frac{n_1}{\tau_{1 \rightarrow 2}}$$

Since $n_2 = 1 - n_1$, and by introducing the frequency

$$\tilde{\nu} = \frac{1}{\tau_{1 \rightarrow 2}} + \frac{1}{\tau_{2 \rightarrow 1}} = \frac{e^{-\sigma(1-h_{sw})^\alpha} + e^{-\sigma(1+h_{sw})^\alpha}}{\tau_0} \quad (35)$$

we then have

$$\frac{dn_1}{dt} + \tilde{\nu} n_1 = \frac{1}{\tau_{2 \rightarrow 1}}$$

This can be solved, taking into account the initial condition $n_1(t=0) = 1/2$ (for the IRM protocol, the sample has been initially demagnetised and the two potential wells are equally populated), and we can express the n_1 proportion after a time τ_m :

$$n_1 = \frac{1}{2} e^{-\tilde{\nu} \tau_m} + \frac{1 - e^{-\tilde{\nu} \tau_m}}{\tilde{\nu} \tau_{2 \rightarrow 1}}$$

The asymmetry between the state 2 and the state 1 is thus

$$S = n_2 - n_1 = 1 - 2n_1 = (1 - e^{-\tilde{\nu} \tau_m}) \left(1 - \frac{2}{\tilde{\nu} \tau_{2 \rightarrow 1}} \right) \quad (36)$$

and the contribution to the IRM signal is simply $\mu N_\varphi \cos \varphi S$. For randomly oriented macropins (here all the particles are described with a φ in the interval $[0, \pi/2]$), we have $N_\varphi = N_{tot} \sin \varphi d\varphi$, so

that we can finally write

$$IRM(H) = m_R \int_0^{\pi/2} S(H, \varphi) \sin(2\varphi) d\varphi \quad (\text{two states relaxation}) \quad (37)$$

The term $S(H, \varphi)$ is given by Eq. (36) and can also be written as

$$S = \left\{ 1 - \exp[-e^{\epsilon_{sw} - \sigma(1-h_{sw})^\alpha} - e^{\epsilon_{sw} - \sigma(1+h_{sw})^\alpha}] \right\} \frac{1-r}{1+r}$$

where r is the switching time ratio defined by Eq. (34) and $h_{sw} = H/H_{sw}^0$.

We can remark that when $\tau_{2 \rightarrow 1} \rightarrow \infty$, i.e. when $r \rightarrow 0$ and $\tilde{\nu} \rightarrow 1/\tau_{sw}$, the term $S(H, \varphi)$ becomes identical to the switching probability $P_{sw}(H, \varphi)$ exposed earlier. Therefore, S is just a more advanced expression of P_{sw} taking into account the reverse $2 \rightarrow 1$ transition and it can be computed without any difficulty. The advantage of this expression is that it gives the correct limit at $H \rightarrow 0$ (see Fig. 7): we indeed have $2/\tau_{2 \rightarrow 1} \rightarrow \tilde{\nu}$ when $h_{sw} \rightarrow 0$, and thus $S \rightarrow 0$.

4. IRM curves at non-zero temperature, with a distribution of particle size

4.1. General expression

In the case of a particle size distribution $f(D)$ [or $f(V)$ as a function of the particle volume V instead of the diameter D], there is no difficulty to express the total IRM signal as the sum over the different sizes. We thus have

$$IRM(H) = \int_0^\infty IRM(V, H) f(V) dV$$

It is important to note that the magnetic moment of each particle size $\mu = M_S V$ appears as a prefactor in $IRM(V, H)$, so that the contribution of each size will be weighted by the corresponding volume. This means for instance that, in the case of a single anisotropy constant K_{eff} , the largest particles in an assembly will have a greater switching field and at the same time a more important contribution to the resulting IRM curve than the small particles. Moreover, for each particle size, the contribution is multiplied by the reduction factor η (see Eq. (32)) which accounts

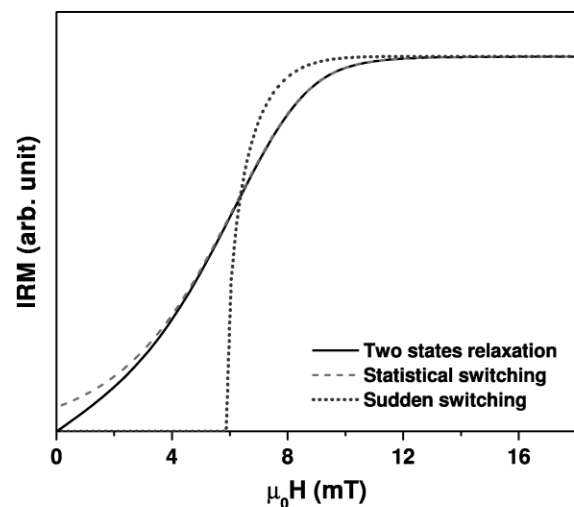


Fig. 7. IRM curves simulated at $T=2$ K with different frameworks: the sudden switching and statistical switching approximations, and the 2 states relaxation model (with the constant $\alpha = 3/2$ approximation). The particles considered are very close to the superparamagnetic limit ($\sigma \simeq 28$ while $\epsilon_{sw} = 25$). The simulations correspond to a 2.3 nm diameter fcc Co nanoparticle assembly, with $K_{eff} = 120$ kJ/m³ and $M_S = 1.35 \times 10^6$ A/m.

for the relaxation at zero field (only significant close to the superparamagnetic limit).

From what we have seen in the preceding section, the most general expression of the IRM curve [which can also be applied for any distribution of the easy axes $\rho(\varphi)$] is then

$$IRM(H) = 2N_{tot}M_S \int_0^\infty \eta V \int_0^{\pi/2} S(V, H, \varphi) \cos \varphi \rho(\varphi) d\varphi f(V) dV \quad (38)$$

where we can see that the only dependence on the applied field H is through the term $S(V, H, \varphi)$. If the relaxation (transition both from and to the metastable orientation) is neglected, then this term should simply be replaced by the switching probability $P_{sw}(V, H, \varphi)$. Further, if we consider the sudden switching approximation, the probability is replaced by a step function (Heaviside function) going from 0 to 1 at $H = H_{sw}(V, \varphi)$. In this case, as we have shown, the integral over φ can be performed analytically and we get

$$IRM(H) = 2N_{tot}M_S \int_0^\infty \eta V \mathcal{F}(V, H) f(V) dV \quad (\text{sudden switching}) \quad (39)$$

where \mathcal{F} is the function $(1 - x_1^3)/(1 + x_1^3)$ which depends both on V and H through the x_1 parameter (defined in Eq. (24)).

4.2. Comparison of the different approximations

From the discussion of the preceding sections, we can tell that: the higher the σ , the closer are the results of simulations using the sudden or statistical switching approximation; on the other hand, the higher the σ , the more the difference between the constant $\alpha = 3/2$ and $\alpha(\varphi)$ approximations is visible. As it can be seen in Figs. 8 and 9, the effect of considering $\alpha(\varphi)$, as well as the probabilistic aspect of switching becomes insignificant in the case of a particle size distribution of increasing dispersion. Moreover, the two states relaxation model (taking into account the transition from the stable to the metastable orientation) appears useless in the case of a size dispersion, even if it was required to correctly describe a monodispersed assembly close to the superparamagnetic regime.

In realistic cases, where the nanoparticle samples necessarily present a size distribution having a significant width (in almost any case the relative diameter dispersion is larger than 5 or 10%), and given the experimental measurement uncertainties, one can conclude that the simplest model (sudden switching and constant $\alpha = 3/2$ approximation) is perfectly suited for the theoretical description of IRM curves. This framework, due to its low computational cost, is also well adapted to best fit procedures that can be used to analyse experimental magnetic measurements.

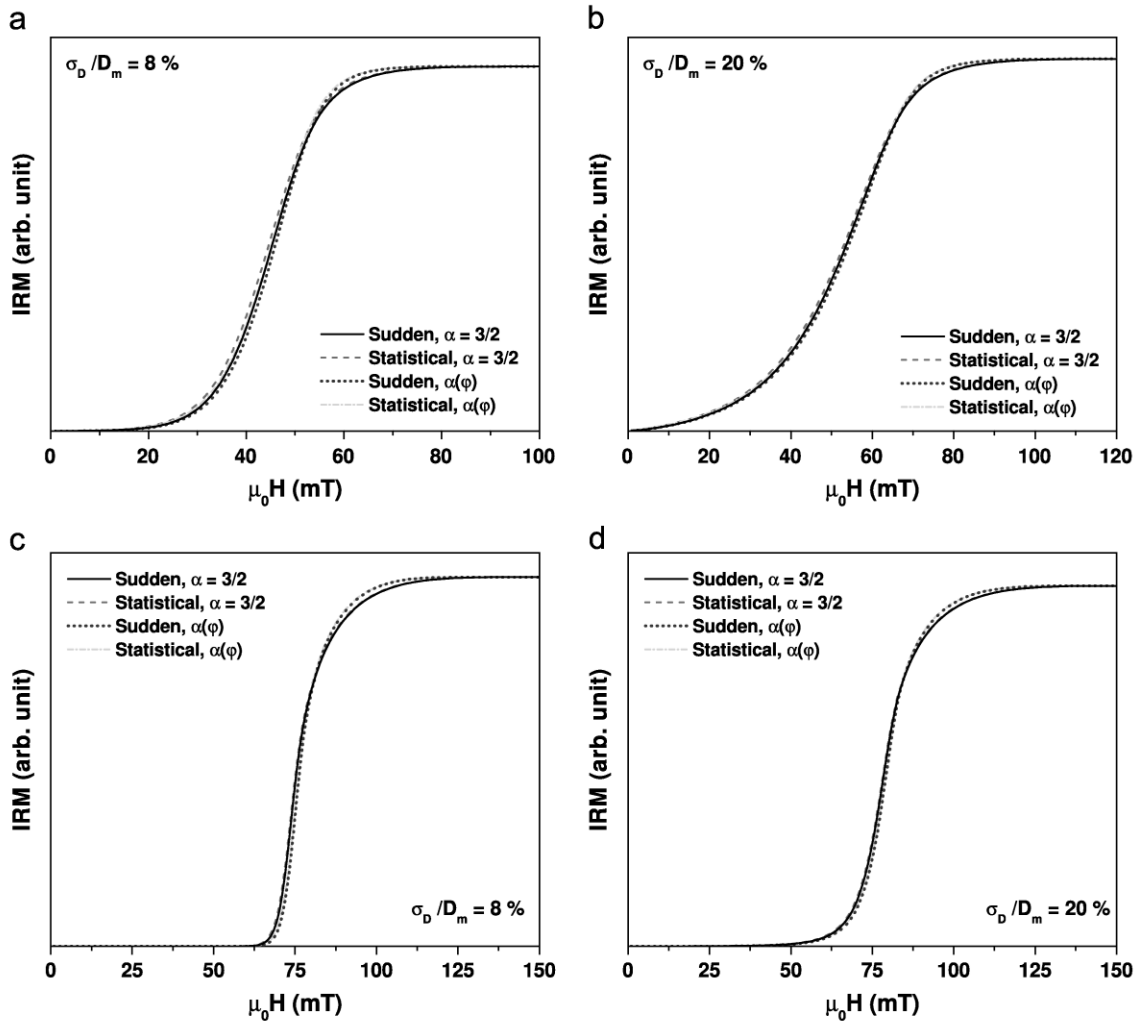


Fig. 8. IRM curves simulated at $T=2$ K with different frameworks: the sudden switching or statistical switching model, with the constant $\alpha = 3/2$ or $\alpha(\varphi)$ approximation. The simulations correspond to a gaussian particle size distribution, centred on $D_m=3$ nm and with a relative dispersion $\sigma_D/D_m = 8\%$ (a) or 20% (b), or centred on $D_m=5$ nm with $\sigma_D/D_m = 8\%$ (c) or 20% (d). The parameters correspond to fcc Co nanoparticles, with $K_{eff} = 120$ kJ/m³ and $M_S = 1.35 \times 10^6$ A/m, while $\epsilon_{sw} = 25$.

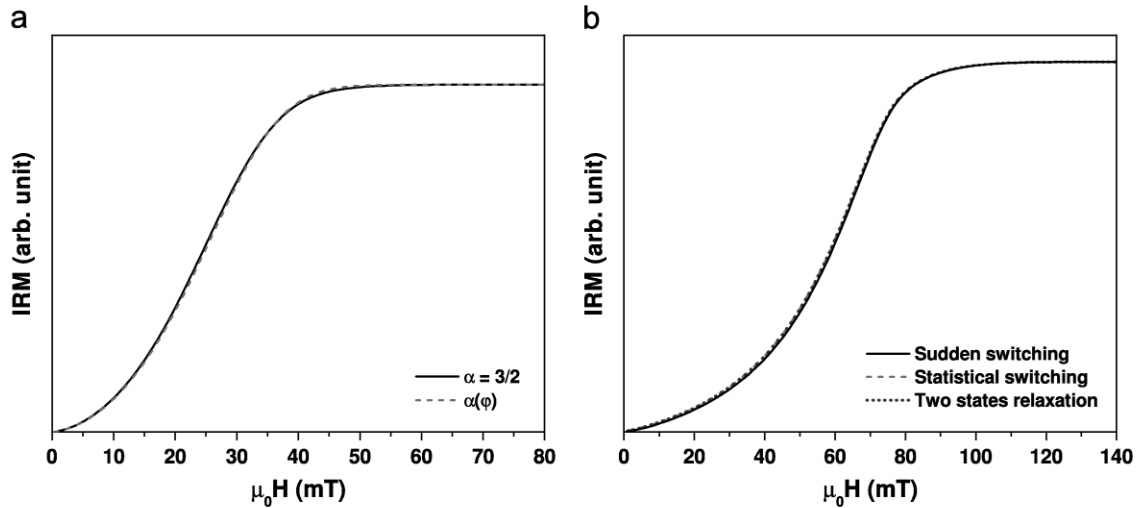


Fig. 9. (a) IRM curves simulated at $T=2$ K for a gaussian distribution of particles diameter (centred on $D_m=2.5$ nm, with a relative dispersion $\sigma_D/D_m=8\%$), where the constant $\alpha=3/2$ approximation is compared to the $\alpha(\varphi)$ approximation (in the sudden switching framework). (b) IRM curves simulated at $T=2$ K for a gaussian distribution of particles diameter (centred on $D_m=2.3$ nm, with a relative dispersion $\sigma_D/D_m=50\%$) with different frameworks: the sudden switching, statistical switching, or two states relaxation model (with the constant $\alpha=3/2$ approximation). The parameters correspond to fcc Co nanoparticles, with $K_{\text{eff}}=120$ kJ/m³ and $M_S=1.35 \times 10^6$ A/m, while $\epsilon_{\text{sw}}=25$, which means that the superparamagnetic limit is around a 2.2 nm diameter.

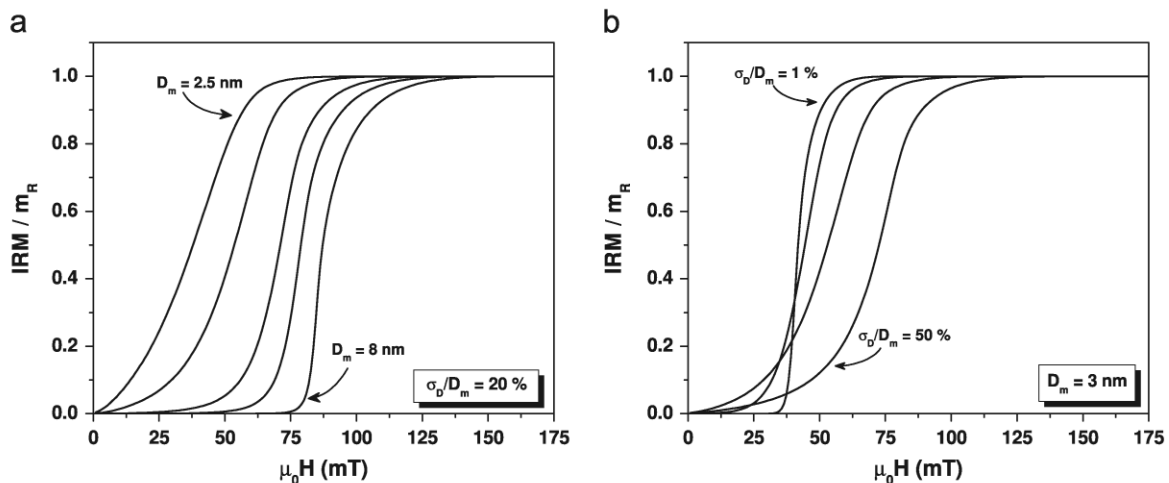


Fig. 10. IRM curves simulated at 2 K (sudden switching model with the $\alpha=3/2$ approximation), normalised with respect to m_R for assemblies of particles with different gaussian size distributions. (a) Variation of the mean diameter D_m (successively 2.5 nm, 3 nm, 4 nm, 5 nm and 8 nm) with a fixed relative dispersion $\sigma_D/D_m=20\%$. (b) Variation of the relative dispersion (successively 1%, 8%, 20% and 50%) with a fixed median diameter $D_m=3$ nm. In each case, the parameters correspond to fcc Co nanoparticles, with $K_{\text{eff}}=120$ kJ/m³ and $M_S=1.35 \times 10^6$ A/m, while $\epsilon_{\text{sw}}=25$.

4.3. Overview of the impact of different parameters on the IRM curves

It is instructive to have an overview of the influence of different parameters (mean particle size, size dispersion, magnetic anisotropy constant, measurement temperature) on the IRM curves. In Fig. 10, the impact of a variation of the particle size distribution on the IRM curve shape is displayed. As expected, a larger median diameter goes with a shift to higher magnetic fields of the inflexion point, and also with a steeper increase of the curve. The reduced width of the transition (from 0 to m_R) reflects the increase of the mean σ value (σ scales proportionally to D^3 , where D is the particle diameter). It should be noticed that the displacement of the IRM inflexion point is very moderate: for instance, when going from a 3 nm to 8 nm median diameter (i.e. an increase in anisotropy energy of nearly a factor 20), the field corresponding to the maximum slope is less than doubled. This shows that IRM curves are much less sensitive than ZFC/FC curves to the

parameters of the particle size distribution [20,19]. In the same way, a change of a few percent of the relative dispersion has no dramatic effect on the IRM curve while it would deeply affect ZFC/FC curves (both the ZFC peak temperature and the merging point between FC and ZFC curves [20]). The influence of the relative size dispersion σ_D/D_m is indeed shown in Fig. 10b. In addition to a widening of the transition, an increase of the diameter standard deviation σ_D (at a fixed median diameter D_m) results in a shift of the IRM inflexion point to higher magnetic fields (this is due to the existence of particles in the assembly having higher σ values, and consequently higher switching fields).

The effect of temperature is shown in Fig. 11, for a representative case of a nanoparticle assembly with a gaussian size distribution. A temperature increase results in both a lowering of the high field limit of the IRM curve (i.e. m_R) and a modification of the curve shape: the evolution from 0 to m_R is smoother for a higher measurement temperature and the inflexion point is displaced to lower fields. In the example shown, the effect of temperature is

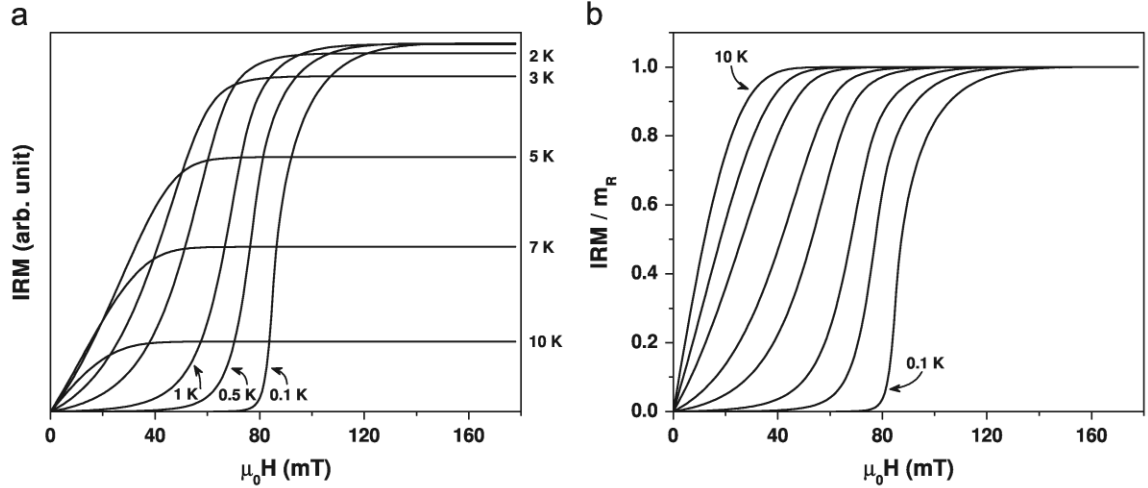


Fig. 11. IRM curves simulated at 2 K (sudden switching model with the $\alpha=3/2$ approximation) for an assembly of particles with a gaussian size distribution (median diameter $D_m = 3$ nm and relative dispersion $\sigma_D/D_m = 20\%$), for different measurement temperatures: 0.1, 0.5, 1, 2, 3, 5, 7, and 10 K. While in (a) the curves have not been rescaled, in (b) they have been normalised with respect to the remanent magnetic moment $m_R(T)$. In each case, the parameters correspond to fcc Co nanoparticles, with $K_{\text{eff}} = 120$ kJ/m³ and $M_S = 1.35 \times 10^6$ A/m, while $\epsilon_{\text{sw}} = 25$.

quite drastic and the IRM curve is significantly modified even for a 1 K temperature variation.

The impact of the anisotropy constant K_{eff} on the IRM curve is also illustrated in Fig. 12, for the same representative case of a nanoparticle assembly with a gaussian size distribution. At zero temperature, the inflexion point would scale linearly with the anisotropy constant (because H_{sw}^0 is directly proportional to K_{eff}). Here it is not exactly the case because, for each particle size the switching field is $H_{\text{sw}} = H_{\text{sw}}^0 C(T)$, where the factor $C(T)$ depends on the product $K_{\text{eff}}V$. This means that the effect of a K_{eff} modification is not the same for each particle size. Another important feature is illustrated in Fig. 12b (here with a single particle size): keeping the same σ value, a modification of the anisotropy constant cannot be compensated by a change of the particle size. The couples of parameters (K_{eff}, V) and ($K_{\text{eff}}/2, 2V$) give fully different curves and can therefore be easily discriminated. On the contrary, for ZFC low field susceptibility measurements, the shape of the curve is controlled by the magnetic anisotropy energy (i.e. the product $K_{\text{eff}}V$), so that the two couples of parameters are indistinguishable [31,20]. This makes the IRM protocol very complementary to ZFC/FC curves for nanoparticle assemblies [5].

4.4. Irreversible susceptibility and switching field distribution

Starting from the expression of the IRM curve involving a Heaviside function (i.e. within the sudden switching approximation framework), it is easy to write down the irreversible susceptibility $\chi_{\text{irr}} = d\text{IRM}/dH$. Indeed, the only dependence on the applied field H is through the Heaviside function, so that derivation results in a Dirac peak term $\delta(H - H_{\text{sw}})$. We then have

$$\chi_{\text{irr}}(H) = 2N_{\text{tot}}M_S \int_0^\infty \eta V \int_0^{\pi/2} \delta[H - H_{\text{sw}}(V, \varphi)] \cos \varphi \rho(\varphi) d\varphi f(V) dV \quad (40)$$

On the other hand, the switching field distribution among the particle assembly can be written

$$\rho_{\text{sw}}(H) = \int_0^\infty \int_0^{\pi/2} \delta[H - H_{\text{sw}}(V, \varphi)] \rho(\varphi) d\varphi f(V) dV \quad (41)$$

From these two expressions, we can see that χ_{irr} and ρ_{sw} are highly similar but not equal (the term $2N_{\text{tot}}M_S$ has no importance, it is just a scaling factor). For χ_{irr} , the contribution of each switching field is multiplied by a factor $\cos \varphi$ (experimentally,

what is measured is the projection of the magnetic moment along the applied field direction) and a factor ηV . This implies that χ_{irr} will not have the same shape as the switching field distribution: for a given temperature, larger particles will correspond to a larger σ and thus a larger switching field, and at the same time they will have a more important contribution to χ_{irr} (because of factor V). Even more striking is the impact of the reduction factor η (which reflects the thermal relaxation at zero field, i.e. which goes from 1 to 0 when a particle evolves from a blocked to a superparamagnetic regime): particles close to (and of course those below) the superparamagnetic limit will almost not contribute to χ_{irr} . For instance, we may have in the assembly a majority of particles having a very low switching field without producing a peak in χ_{irr} , because they correspond to a vanishing η . Note that even for a single particle size (or for $T \rightarrow 0$) there is a slight difference between χ_{irr} and ρ_{sw} due to the $\cos \varphi$ term, as discussed before.

All this shows that χ_{irr} does not reflect the switching field distribution ρ_{sw} [33]. This is illustrated in Figs. 13 and 14 where we can see how the curves can differ, and how a peak in χ_{irr} may dramatically overestimate the true median switching field. Contrary to what is often assumed [7,9,10,12,15], a peak in χ_{irr} cannot be used to conclude that it corresponds to a peak in the switching field distribution. Such a peak in the irreversible susceptibility does neither correspond to a mean, nor a median, nor a most probable switching field in a nanomagnet assembly (even in the ideal case of non-interacting particles!). Abusive identifications should then be avoided, especially in the case of broad or long-tailed particle size distributions (for instance log-normal size distribution, where even the very small number of marginally large particles can have a significant impact on χ_{irr}). In the end, it is unfortunately not possible to directly infer the switching field distribution just from an experimental irreversible susceptibility curve. In order to determine ρ_{sw} , it is necessary to perform a fit of the experimental IRM curve, which is of course much more demanding.

4.5. The case of an anisotropy constant distribution

Sticking for simplicity to the sudden switching approximation, we can examine the case of an anisotropy constant distribution. In this case, instead of a single K_{eff} value, we consider a statistical distribution $\rho(K_{\text{eff}})$ of the anisotropy constant. Such a distribution can be introduced to reflect the differences (in shape or atomic

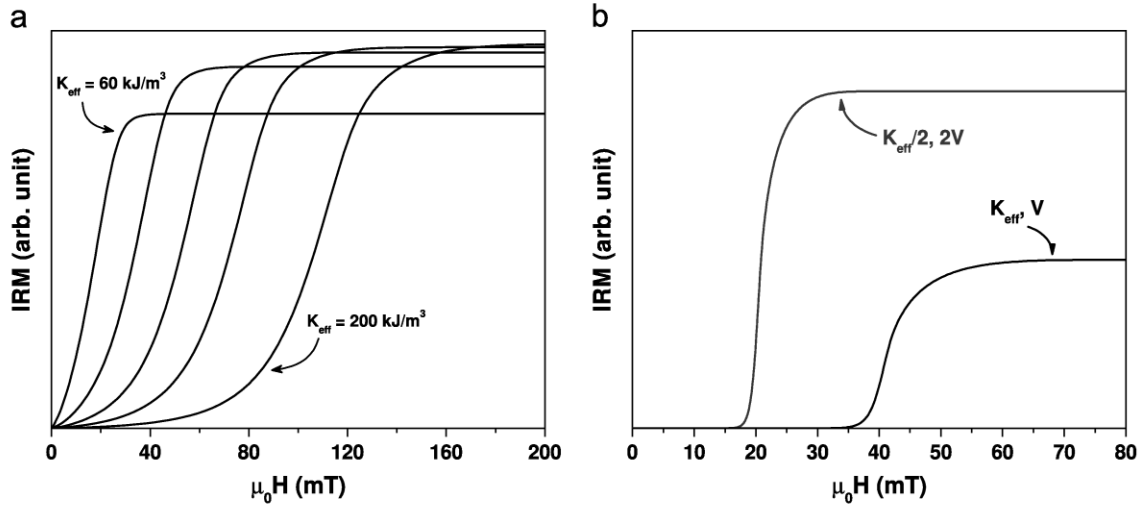


Fig. 12. (a) Simulated IRM curves (sudden switching model with the $\alpha = 3/2$ approximation) for an assembly of particles with a gaussian size distribution (median diameter $D_m = 3$ nm and relative dispersion $\sigma_D/D_m = 20\%$), for different values of the anisotropy constant: 60, 90, 120, 150, and 200 kJ/m³. (b) IRM curves simulated (statistical switching model with the $\alpha = 3/2$ approximation) for a single particle size corresponding to the couple of parameters (K_{eff}, V) [reference case with a 120 kJ/m³ anisotropy constant and a 3 nm particle diameter] and ($K_{\text{eff}}/2, 2V$). In each case we have $M_S = 1.35 \times 10^6$ A/m, while $\epsilon_{\text{sw}} = 25$ and the temperature is 2 K.

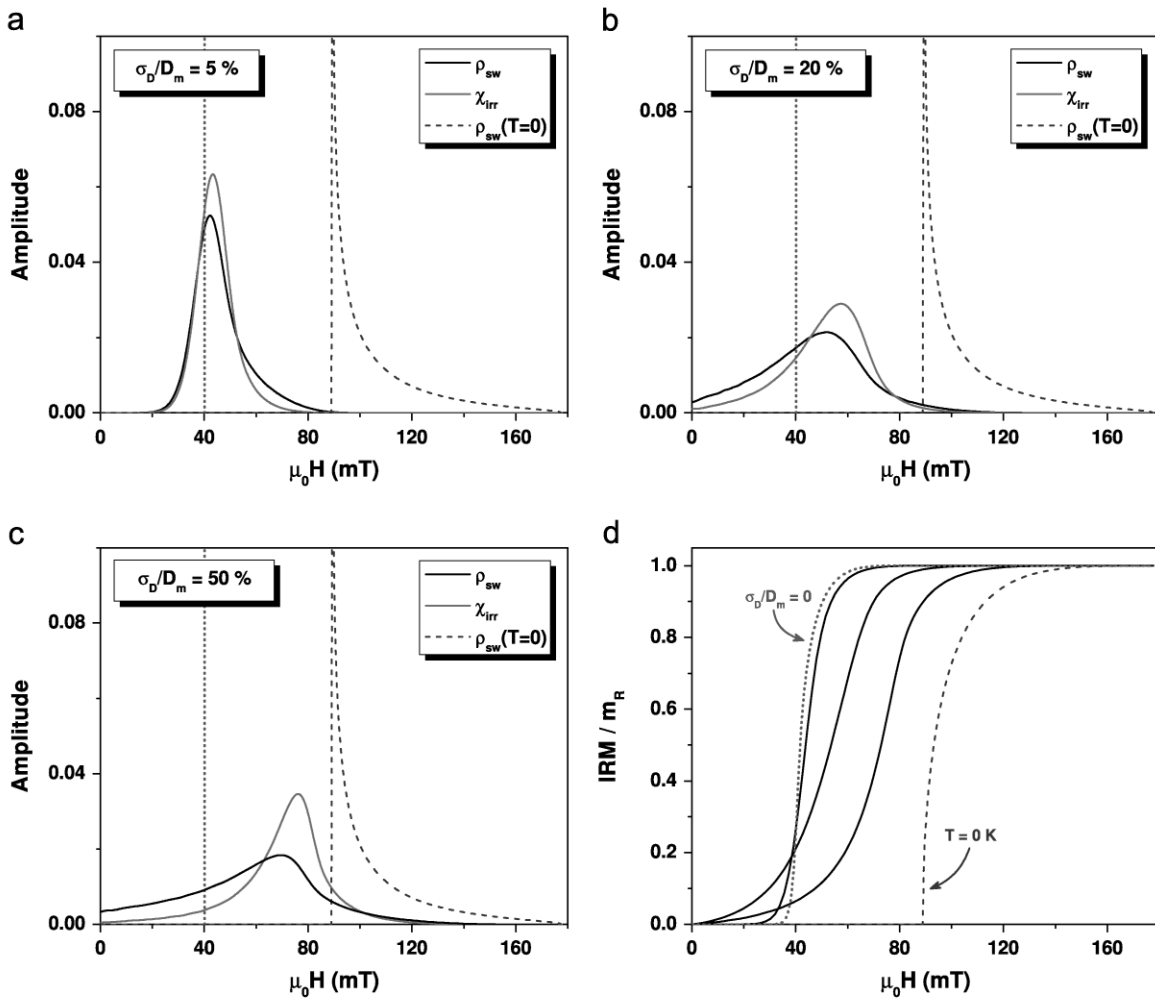


Fig. 13. Comparison of χ_{irr} , ρ_{sw} and $\rho_{\text{sw}}(T=0)$ for an assembly of particles with a gaussian size distribution centred on $D_m = 3$ nm. In each case we have $M_S = 1.35 \times 10^6$ A/m and $K_{\text{eff}} = 120$ kJ/m³, while $\epsilon_{\text{sw}} = 25$ and the temperature is 2 K. Calculations have been done for a relative size dispersion σ_D/D_m of 5% (a), 20% (b) and 50% (c). The vertical dotted line indicates the position of the switching field distribution peak for the median size [i.e. $H_{\text{sw}}(D = D_m, \varphi = \pi/4)$, which is roughly the median switching field]. The corresponding normalised IRM curves are shown in (d), compared to the curve at zero temperature and the one without size dispersion.

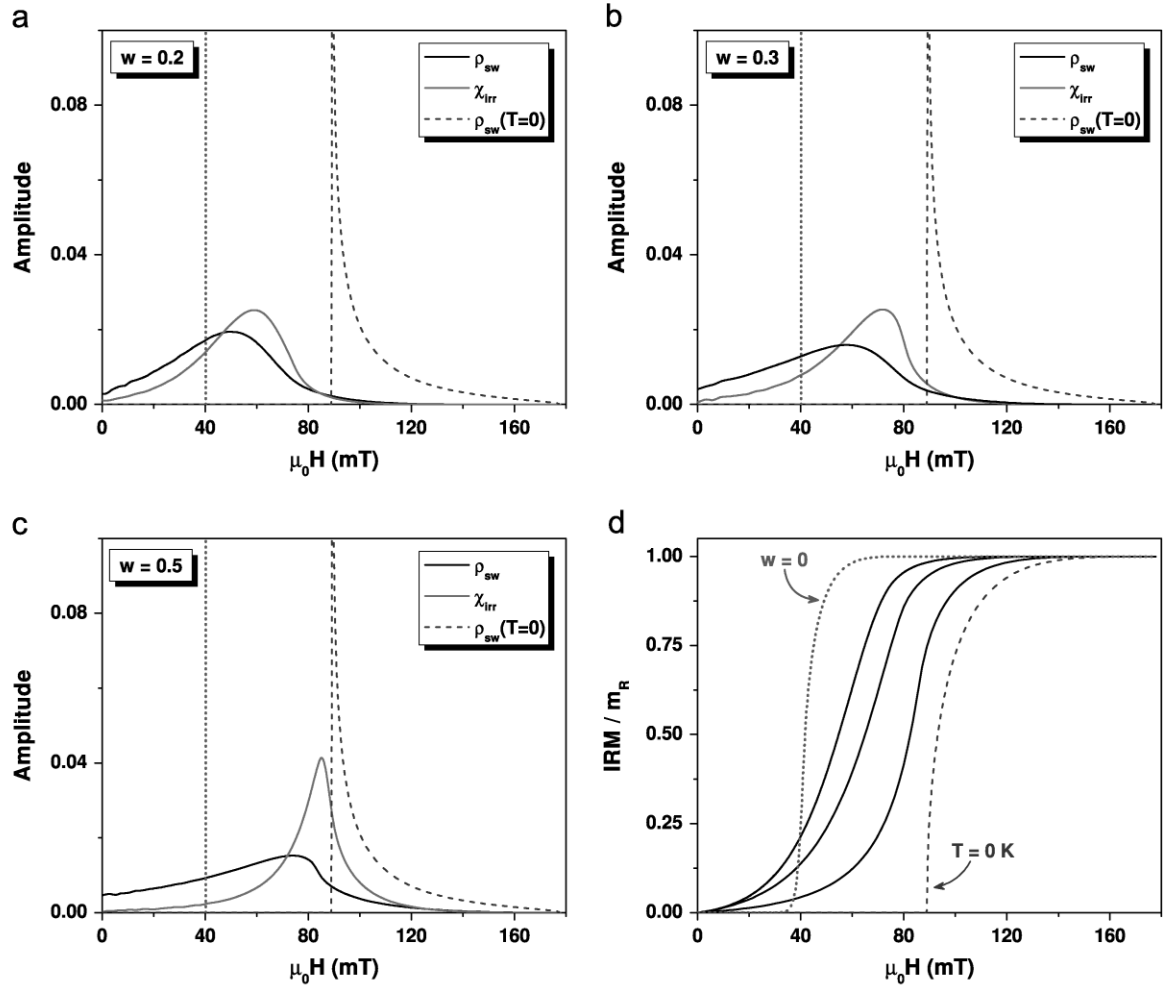


Fig. 14. Comparison of χ_{irr} , ρ_{sw} and $\rho_{\text{sw}}(T=0)$ for an assembly of particles with a lognormal size distribution centred on $D_m=3$ nm. In each case we have $M_S = 1.35 \times 10^6$ A/m and $K_{\text{eff}} = 120$ kJ/m³, while $\epsilon_{\text{sw}} = 25$ and the temperature is 2 K. Calculations have been done for a dispersion parameter w of the lognormal equal to 0.2 (a), 0.3 (b) and 0.5 (c). The vertical dotted line indicates the position of the switching field distribution peak for the median size [i.e. $H_{\text{sw}}(D = D_m, \varphi = \pi/4)$, which is roughly the median switching field]. The corresponding normalised IRM curves are shown in (d), compared to the curve at zero temperature and the one without size dispersion.

structure for instance) among particles of a same size in an assembly, resulting in a dispersion of the magnetic anisotropy energy [34–36,5]. We then have, for a single particle size:

$$\text{IRM}(H) = 2N_{\text{tot}}\mu \int_0^\infty \eta \mathcal{F}(K_{\text{eff}}, H) \rho(K_{\text{eff}}) dK_{\text{eff}} \quad (42)$$

where μ is the magnetic moment of a particle, \mathcal{F} the function $(1 - x_1^2)/(1 + x_1^2)$ which depends on both K_{eff} and H through x_1 , and η is the reduction factor (relaxation) also depending on K_{eff} . Thus, there is no difficulty to compute IRM curves in such a case of an anisotropy constant distribution. As shown in Fig. 15, the K_{eff} dispersion broadens the transition zone of the IRM without significant displacement of its inflexion point (contrary to the case of a size dispersion, here each K_{eff} value equally contributes to the total curve, as soon as the particles are far from being superparamagnetic). The irreversible susceptibility χ_{irr} is also very close to the switching field distribution ρ_{sw} (see Fig. 15), which was not the case for an assembly of particles with a size distribution. Here, with only a K_{eff} dispersion, both χ_{irr} and ρ_{sw} display a peak at a position corresponding to the median K_{eff} value, and it is much reasonable to consider that χ_{irr} reflects the switching field distribution.

In the most general case, the magnetic particle assembly displays both a size distribution $f(V)$ and an anisotropy constant

distribution $\rho(K_{\text{eff}})$. Then, the IRM expression is given by

$$\text{IRM}(H) = 2N_{\text{tot}}M_S \int_0^\infty \int_0^\infty \eta \mathcal{F} V f(V) dV \rho(K_{\text{eff}}) dK_{\text{eff}} \quad (43)$$

where the reduction factor η depends on K_{eff} and V and the function \mathcal{F} depends on K_{eff} , V and H through the parameter x_1 . This means that there is no particular difficulty, except the potentially large computational time, to calculate the IRM curve of such a nanomagnet assembly. Fig. 16 illustrates the influence of a K_{eff} distribution on the IRM curve. When the relative dispersion is increased, the curve gets smoother with almost no change of the inflexion point. As for the case of a single anisotropy constant, the irreversible susceptibility χ_{irr} deduced from the IRM curve can strongly differ from the switching field distribution ρ_{sw} (see Fig. 16b). This is mainly due to the size distribution (each particle size will not equally contribute to the resulting IRM curve, while it is almost the case for each K_{eff}). Let us insist again on the fact that χ_{irr} should not be interpreted as a switching field distribution, nor as a reflect of the magnetic anisotropy distribution or of the particle size distribution.

Another general remark is that there is, a priori, no unique set of parameters to produce a given IRM curve: a particular size distribution and a single K_{eff} can result in the same curve as with another size distribution and using a K_{eff} dispersion. However, the two situations would correspond to a different switching field distribution. There is

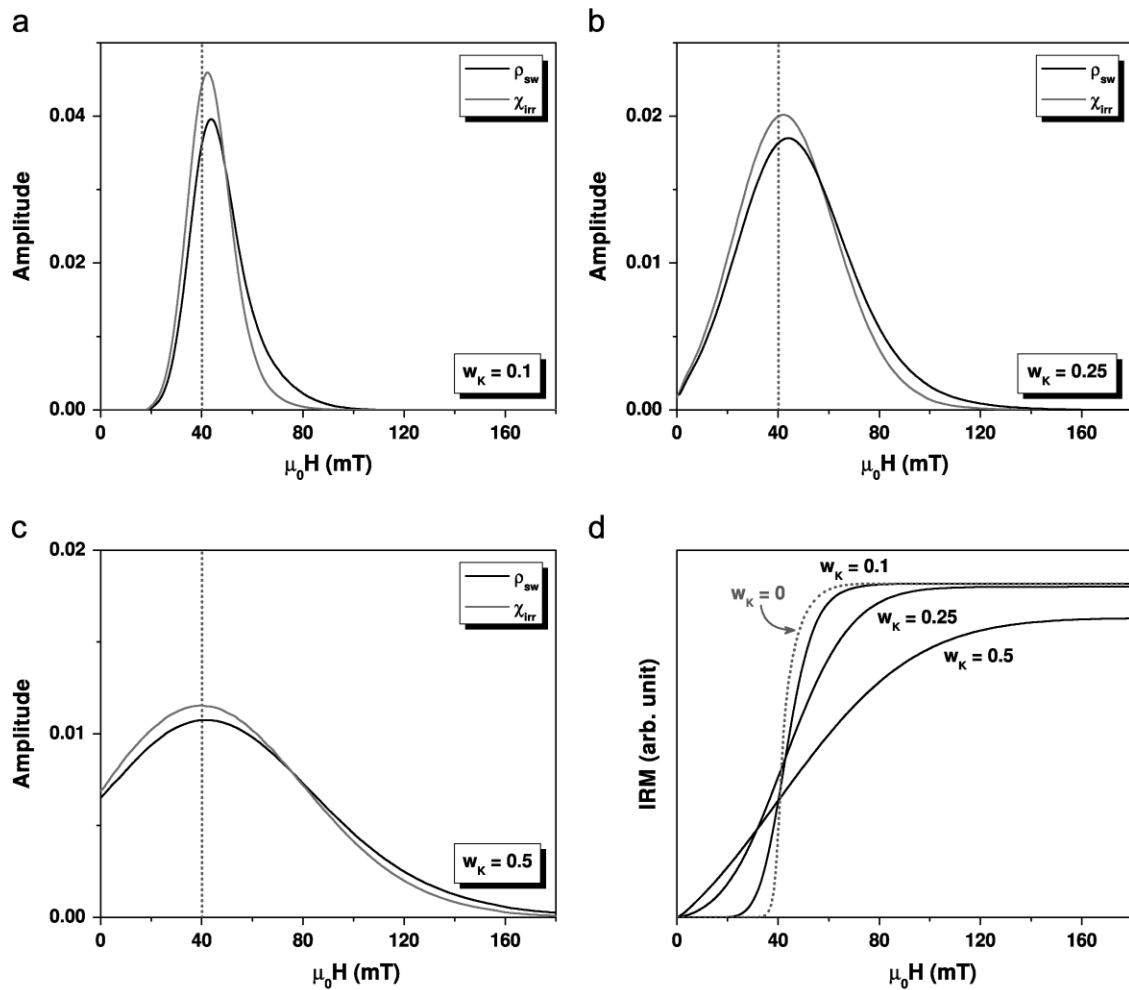


Fig. 15. Comparison of χ_{irr} and ρ_{sw} for an assembly of monodispersed particles (diameter $D_m=3$ nm) with a gaussian distribution of anisotropy constants, centred on $\overline{K_{eff}} = 120$ kJ/m³ and of various standard deviations σ_K . Calculations have been done for a relative dispersion $w_K = \sigma_K/\overline{K_{eff}}$ equal to 0.1 (a), 0.25 (b) and 0.5 (c). The vertical dotted line indicates the position of the switching field distribution peak for the median anisotropy constant (i.e. without K_{eff} dispersion). The corresponding IRM curves are shown in (d), compared to the curve without K_{eff} dispersion. In each case we have $M_S = 1.35 \times 10^6$ A/m, while $\epsilon_{sw} = 25$ and the temperature is 2 K.

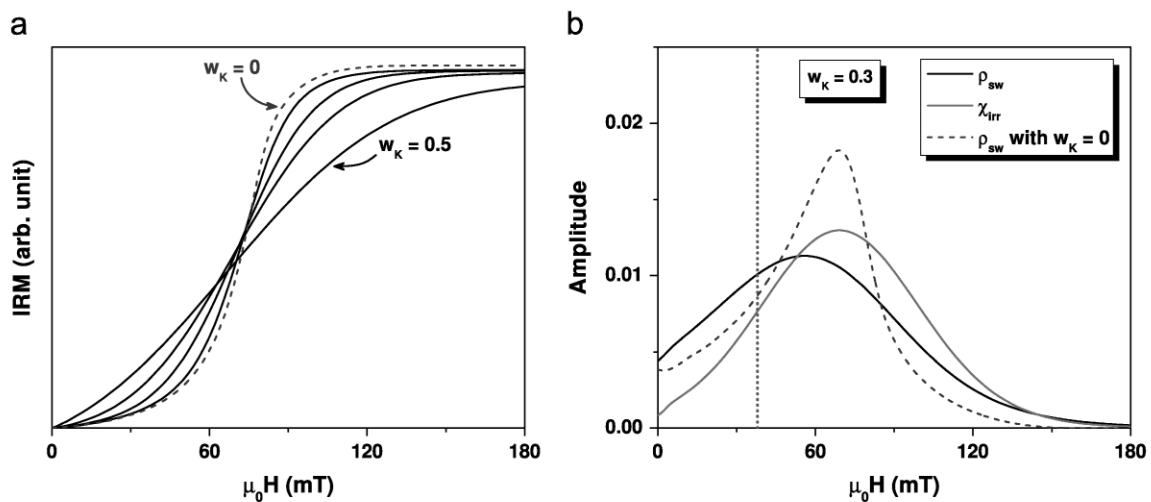


Fig. 16. (a) IRM curves, calculated at $T=2$ K, for an assembly of particles with both a diameter distribution (gaussian distribution centred on $D_m=3$ nm and with a relative dispersion $\sigma_D/D_m = 50\%$) and a distribution of anisotropy constants (gaussian distribution centred on $\overline{K_{eff}} = 120$ kJ/m³ and of various standard deviations σ_K). Calculations have been done for a relative dispersion $w_K = \sigma_K/\overline{K_{eff}}$ equal to 0.1, 0.2, 0.3, and 0.5. The curve for a single anisotropy constant ($w_K=0$) is also shown. (b) Comparison of χ_{irr} and ρ_{sw} for the $w_K=0.3$ case. The switching field distribution without K_{eff} dispersion is also shown (dashed line), and the vertical dotted line indicates the position of the switching field distribution peak for the median anisotropy constant and the median diameter (it is close to the median switching field). In each case we have $M_S = 1.35 \times 10^6$ A/m, while $\epsilon_{sw} = 25$.

no way to separate the contribution of a size distribution and of a K_{eff} distribution just from an experimental IRM curve. In order to infer the physical parameters of a magnetic particle assembly, one then must consider several types of magnetic measurements. Using their complementarity (for instance, IRM, ZFC/FC and magnetisation loops), it is finally possible to determine the intrinsic nanomagnet properties from a combined best fit procedure. This has been done recently for a diluted Co nanoparticle assembly, providing original information [5].

5. Conclusion

We have presented a robust and efficient framework to compute IRM curves for magnetic nanoparticle assemblies. The assembly is modelled by independent, randomly oriented, uniaxial macrospins and we use a Néel model to take into account the thermal relaxation. The simple analytic expression established for a single size, in a sudden switching approximation, has been compared to more evolved models. We have shown that for realistic samples (necessarily presenting a size dispersion) the simple model is very satisfactory. With this framework, it is then possible to reliably simulate IRM curves, which can be compared to experimental measurements and used in a best fit procedure. We have examined the influence of several parameters on the curves and discussed the link between the irreversible susceptibility and the switching field distribution. We have thus emphasized that these two quantities in fact significantly differ (especially for broad size distributions), so that the derivative of an experimental IRM curve does not directly reflect the switching field distribution.

The semi-analytical modelling of IRM curves enables the determination of some intrinsic nanomagnet properties, especially when complementary measurements are considered (ZFC/FC curves, magnetisation loops...). Isothermal remanence magnetisation curves are powerful tools, very complementary to more widespread measurements on particle assemblies, and the theoretical framework presented in this paper allows us to fully exploit them, from a quantitative point of view. It can also be used to verify the validity of some underlying assumptions (for instance, the uniaxial character of the anisotropy, or the use of a single anisotropy constant). Let us insist on the fact that the model we have developed only applies to non-interacting assemblies of particles, which can be experimentally difficult to prepare.

Acknowledgements

The author acknowledges A. Tamion for fruitful discussions.

References

- [1] S.W. Charles, R. Chandrasekhar, K. O'Grady, M. Walker, *J. Appl. Phys.* 64 (1988) 5840.
- [2] A. Stancu, C. Papusoi, *IEEE Trans. Magn.* 30 (1994) 2750.
- [3] C. Papusoi, E.N. Abarra, T. Suzuki, *J. Appl. Phys.* 92 (2002) 7373.
- [4] J.M. Martínez Huerta, J. De La Torre Medina, L. Piraux, A. Encinas, *J. Appl. Phys.* 111 (2012) 083914.
- [5] A. Hillion, A. Tamion, F. Tournus, O. Gaier, E. Bonet, C. Albin, V. Dupuis, *Phys. Rev. B* 88 (2013) 094419.
- [6] O. Henkel, *Phys. Stat. Solid. (b)* 7 (1964) 919–929.
- [7] P.E. Kelly, K. O'Grady, P.I. Mayo, R.W. Chantrell, *IEEE Trans. Magn.* 25 (1989) 3881.
- [8] K. O'Grady, *IEEE Trans. Magn.* 26 (1990) 1870.
- [9] P.I. Mayo, K. O'Grady, R.W. Chantrell, J.A. Cambridge, I.L. Sanders, T. Yogi, J. K. Howard, *J. Magn. Mater.* 95 (1991) 109.
- [10] K. O'Grady, M. El-Hilo, R.W. Chantrell, *IEEE Trans. Magn.* 29 (1993) 2608.
- [11] A.D.C. Viegas, J. Geshev, L.S. Dorneles, J.E. Schmidt, M. Knobel, *J. Appl. Phys.* 82 (1997) 3047.
- [12] X. Batlle, M. García del Muro, A. Labarta, *Phys. Rev. B* 55 (1997) 6440–6445.
- [13] J. García-Otero, M. Porto, J. Rivas, *J. Appl. Phys.* 87 (2000) 7376.
- [14] J. Rivas, A. Kazadi Mukenga Bantu, G. Zaragoza, M. Blanco, M. López-Quintela, *J. Magn. Mater.* 249 (2002) 220–227.
- [15] B. Rellinghaus, S. Stappert, M. Acet, E.F. Wassermann, *J. Magn. Mater.* 266 (2003) 142.
- [16] S.A. Majetich, M. Sachan, *J. Phys. D: Appl. Phys.* 39 (2006) R407–R422.
- [17] O. Hellwig, A. Berger, T. Thomson, E. Dobisz, Z.Z. Bandic, H. Yang, D.S. Kercher, E.E. Fullerton, *Appl. Phys. Lett.* 90 (2007) 162516.
- [18] S. Laureti, G. Varvaro, A.M. Testa, D. Fiorani, E. Agostinelli, G. Piccaluga, A. Musinu, A. Ardu, D. Peddis, *Nanotechnology* 21 (2010) 315701.
- [19] A. Tamion, M. Hillenkamp, F. Tournus, E. Bonet, V. Dupuis, *Appl. Phys. Lett.* 95 (2009) 062503.
- [20] F. Tournus, A. Tamion, *J. Magn. Mater.* 323 (2011) 1118.
- [21] F. Tournus, A. Hillion, A. Tamion, V. Dupuis, *Phys. Rev. B* 87 (2013) 174404.
- [22] A more rigorous expression would be $2N_{\text{tot}}\mu \cos(\pi - \varphi)\rho(\varphi) d\varphi$ and considering φ in the interval $[\pi/2, \pi]$, because the particles for which $\varphi \in [0, \pi/2]$ are already in the most favorable orientation.
- [23] E.P. Wohlfarth, *J. Appl. Phys.* 29 (1958) 595.
- [24] R.W. Chantrell, K. O'Grady, A. Bradbury, S.W. Charles, N. Hopkins, *IEEE Trans. Magn.* 23 (1987) 204.
- [25] R.J.M. van de Veerdonk, X. Wu, D. Weller, *IEEE Trans. Magn.* 38 (2002) 2450.
- [26] R.J.M. van de Veerdonk, X. Wu, D. Weller, *IEEE Trans. Magn.* 39 (2003) 590.
- [27] R.H. Victora, *Phys. Rev. Lett.* 63 (1989) 457.
- [28] H. Pfeiffer, *Phys. Stat. Solid. (a)* 118 (1990) 295–306.
- [29] J.W. Harrell, *IEEE Trans. Magn.* 37 (2001) 533.
- [30] C. Thirion, W. Wernsdorfer, M. Jamet, V. Dupuis, P. Mélinon, A. Pérez, D. Mailly, *J. Appl. Phys.* 91 (2002) 7062.
- [31] F. Tournus, E. Bonet, *J. Magn. Mater.* 323 (2011) 1109.
- [32] This is not exact for $\varphi = \pi/2$ where the barriers are identical, but it is true for $\varphi = 0$ and we are interested in small H values. We will also use the constant $\alpha = 3/2$ approximation.
- [33] Except in the very particular case where all the nanomagnets have the same easy axis orientation (perfect texture) and with a particle size distribution fully independent of the anisotropy distribution. This may be a reasonable assumption for bit patterned magnetic media [26,17].
- [34] F. Tournus, S. Rohart, V. Dupuis, *IEEE Trans. Magn.* 44 (2008) 3201.
- [35] F. Tournus, N. Blanc, A. Tamion, M. Hillenkamp, V. Dupuis, *Phys. Rev. B* 81.
- [36] A. Tamion, E. Bonet, F. Tournus, C. Raufast, A. Hillion, O. Gaier, V. Dupuis, *Phys. Rev. B* 85 (2012) 134430.

Les résultats de cette activité de recherche, s'appuyant sur un travail de modélisation aussi rigoureux que possible, nous permettent aujourd'hui d'exploiter de manière quantitative et précise les mesures magnétiques sur des assemblées de nano-aimants. Un ensemble de mesures expérimentales peut ainsi être ajusté afin de déterminer un jeu de paramètres magnétiques consistant (cf. Figure 14). La motivation de ce travail était d'être capable de déduire les propriétés magnétiques intrinsèques de nanoparticules à partir de mesures sur des systèmes dilués, mais aussi de tester les modèles couramment utilisé dans la communauté. Dans cette optique, nos échantillons de nanoparticules fabriquées de manière bien contrôlée ont été pleinement exploités, et nous avons pu montrer qu'ils constituaient des systèmes modèles pour des études fines de nano-magnétisme (notamment, en s'assurant de l'absence d'interactions magnétiques entre particules). Des résultats originaux ont été obtenus sur des nanoparticules de Co pures [Tamion2012, Hillion2013a, Oyarzun2015] (cf. Fig. 15) mais aussi bien sûr sur des systèmes plus complexes comme les nanoparticules bimétalliques (cf. chapitre 3). Il est toujours possible d'aller plus loin (cf. perspectives), en particulier en s'intéressant aux interactions entre particules au sein d'une assemblée, en complexifiant le système (texturation de la direction des axes d'anisotropie par exemple) ou en considérant d'autres types de mesures magnétiques complémentaires.

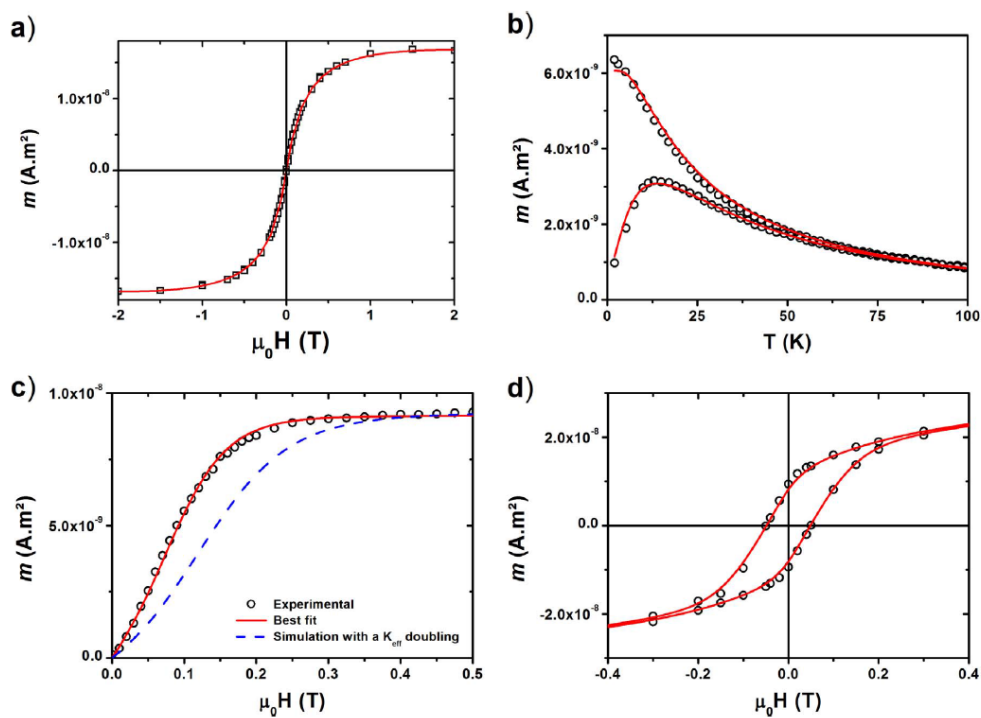
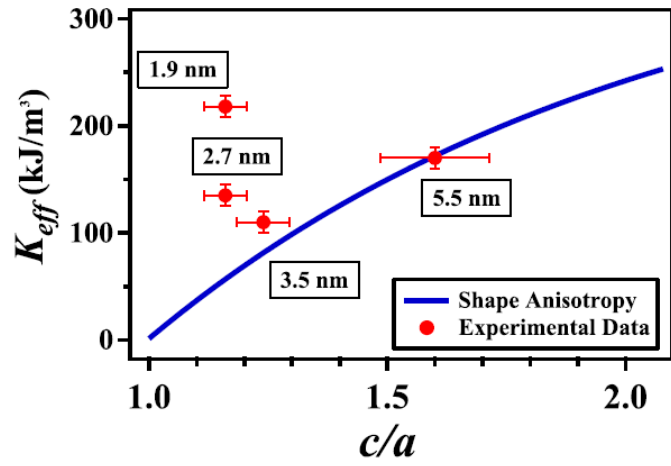


Fig. 14 : Courbes expérimentales (points) $m(H)$ à 300 K (a), ZFC/FC (b), IRM à 2 K (c) et cycle $m(H)$ à 2 K (d) mesurées sur un échantillon de nanoparticules de Co diluées dans une matrice de carbone et recuites. L'ensemble des mesures peut être ajusté (courbes en trait plein) avec un même jeu de paramètres magnétiques. Figure tirée de [Tournus2016].

Fig. 15 : Constante d'anisotropie K_{eff} pour des nanoparticules de Co de différentes tailles, déterminée par un ajustement simultané de différentes mesures de magnétométrie (cycle $m(H)$ à 300 K et à 2 K, ZFC/FC et IRM à 2 K). On observe une forte variation avec la taille, qui peut s'expliquer par un effet de forme pour les plus grosses particules (la courbe indique l'anisotropie de forme en fonction du rapport c/a des ellipsoïdes correspondant aux nanoparticules), et par un effet de surface (facettage des particules) pour les plus petites tailles. Figure tirée de [Oyarzun2015].



Chapitre 3 : Nanoparticules bimétalliques, propriétés structurales, magnétiques et réactivité

A) Nanoparticules de CoPt

L'étude des nanoparticules de CoPt est intéressante à plusieurs titres [Andreazza2015]. D'un point de vue magnétique d'abord, en particulier en vue d'applications pour l'enregistrement magnétique à ultra haute densité, puisque lorsqu'il est chimiquement ordonné dans la phase $L1_0$ (alternance de plans atomiques purs Co et purs Pt selon la direction $[001]$) l'alliage CoPt présente une anisotropie magnéto-cristalline énorme, du moins pour le matériau massif. De plus, la mise en ordre chimique (cf. Fig. 16) et la structure de petites nanoparticules mixtes font l'objet de nombreuses études théoriques et différentes géométries, parfois « exotiques », ont été envisagées. Parallèlement aux mesures magnétiques, je me suis attaché à étudier en détail la structure des échantillons, en raison du lien étroit entre l'arrangement cristallographique et le magnétisme dans les alliages de métaux de transition.

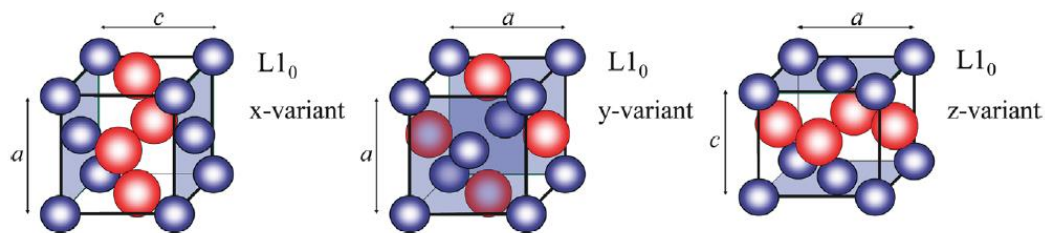


Fig. 16 : Représentation de la cellule unitaire du CoPt (ou FePt) chimiquement ordonné dans la phase $L1_0$, correspondant à une alternance de plans purs Co (ou Fe) et Pt. Le paramètre de maille vaut $c \neq a$ dans la direction de l'ordre chimique. À partir d'une maille cubique-faces-centrées (cfc, pour la phase A1 chimiquement désordonnée), l'ordre peut s'établir selon 3 directions équivalentes (x,y, ou z) correspondant à 3 différents variants. Les jonctions entre différents variants donnent alors lieu à des défauts planaires d'ordre chimique. Figure tirée de [Andreazza2015].

Nous avons étudié des assemblées de particules de CoPt (non triées en taille dans un premier temps) diluées dans une matrice de carbone amorphe. Alors que le dépôt de nanoparticules se fait à température ambiante, un recuit (typiquement 2 h à 750 K) est effectué pour promouvoir la mise en ordre chimique des particules, tout en évitant la coalescence. Au cours de la thèse de Nils Blanc que j'ai encadrée, nous avons ainsi démontré que les nanoparticules de CoPt pouvaient s'ordonner dans la phase $L1_0$, y compris jusqu'à un diamètre aussi petit que 2 nm. Nous avons observé la signature de la mise en ordre chimique au travers d'une évolution des propriétés magnétiques (moments atomiques déterminés par XMCD, anisotropie magnétique déterminée d'après les mesures de magnétométrie) couplée à une évolution de la structure cristallographique observée par METHR [Tournus2008]. Étonnamment, même si le recuit induit une augmentation significative de l'anisotropie magnétique, celle-ci reste largement inférieure (environ un ordre de grandeur) à celle de la phase $L1_0$ massive. La publication « **Evidence of $L1_0$ chemical order in CoPt nanoclusters: Direct observation and magnetic signature** » [Tournus2008], reproduite ci-dessous, présente de manière détaillée ces résultats.



Evidence of $L1_0$ chemical order in CoPt nanoclusters: Direct observation and magnetic signature

Florent Tournus,^{1,*} Alexandre Tamion,¹ Nils Blanc,¹ Abdelkrim Hannour,¹ Laurent Bardotti,¹ Brigitte Prével,¹ Philippe Ohresser,² Edgar Bonet,³ Thierry Epicier,⁴ and Véronique Dupuis¹

¹Université de Lyon, F-69000, France

and Université Lyon 1, Laboratoire PMCN, CNRS, UMR 5586, F-69622 Villeurbanne Cedex, France

²Synchrotron SOLEIL, BP 48, 91192 Gif-sur-Yvette, France

³CNRS/UJF, Institut Néel, BP 166, 38042 Grenoble Cedex 9, France

⁴MATEIS, UMR CNRS 5510, INSA-Lyon, Université de Lyon, F-69621 Villeurbanne Cedex, France

(Received 11 January 2008; revised manuscript received 21 February 2008; published 10 April 2008)

We report the synthesis and characterization of well-defined CoPt clusters with a mean diameter of 3 nm, produced in ultrahigh vacuum conditions following a physical route. Samples made of diluted layers of CoPt clusters embedded in amorphous carbon have been studied by transmission electron microscopy. High-resolution observations have revealed the appearance of $L1_0$ chemical order upon annealing, even for clusters with a 2 nm diameter, without cluster coalescence. The magnetic properties of both chemically disordered and ordered CoPt clusters embedded in amorphous carbon have then been measured by x-ray magnetic circular dichroism and superconducting quantum interference device magnetometry. Despite a striking change of the Co magnetic moment, the magnetic anisotropy of chemically ordered nanoparticles increases, with respect to the chemically disordered A1 phase, in much lower proportions than what is observed for the bulk.

DOI: 10.1103/PhysRevB.77.144411

PACS number(s): 75.75.+a, 61.46.Df, 75.30.Gw, 68.37.Og

I. INTRODUCTION

Magnetic particles of a few nanometers diameter have attracted much attention both for their fundamental interest (the magnetic properties of low-coordinated atoms can display dramatic changes^{1,2}) and for their potential applications. In particular, small permanent magnets at the nanoscale would make possible ultrahigh density magnetic storage devices.³ However, at such a size, the magnetization direction of a particle usually fluctuates at room temperature. Consequently, each ferromagnetic particle is in fact equivalent to a paramagnetic moment, with a vanishing average remanent magnetization. This phenomenon, which must be overcome for practical applications, is called superparamagnetism. In order to increase the thermal stability (or equivalently, to increase the magnetization relaxation time), great efforts have been directed toward an enhancement of the nanoparticles magnetic anisotropy. One of the preferred routes is to use magnetic alloys.

In this context, there have been considerable progresses in the synthesis procedures of FePt (Refs. 4–15) or CoPt (Refs. 16–31) nanoparticles. These alloys can all crystallize in the chemically ordered $L1_0$ phase, corresponding to very high magnetocrystalline anisotropy for the bulk.^{32,33} Among these materials, we have investigated the specific case of CoPt. Unfortunately, despite significant advances, it is still very difficult to produce well-defined nanoparticles in the $L1_0$ phase. Although this phase is the stable one at room temperature, an additional difficulty may come from the lowering of the order-disorder transition temperature (from the $L1_0$ phase to the chemically disordered A1 phase) due to the size reduction of the particles.^{34–42} Chemical order in small particles could then be thermodynamically unstable at room temperature. Moreover, chemical ordering is in general obtained by annealing, which goes with problems of pollution or coalescence, difficult to avoid.^{20,43–46}

As a consequence, in spite of a huge number of results presented on these systems, there exists, to our knowledge, no convincing experimental study reporting a value of the intrinsic magnetic anisotropy for well-characterized $L1_0$ CoPt nanoparticles.⁴⁷ Indeed, it is a tricky task to ensure that CoPt nanoparticles have a well-known magnetic size, are chemically ordered, are noninteracting, etc., to correctly deduce the intrinsic properties of well-defined nanoparticles from macroscopic magnetic measurements. As a matter of fact, we may never be able to reach a magnetic anisotropy as high as the bulk one, for CoPt particles of a few nanometers diameter. This would constitute a serious setback for the expected technological applications.

In this paper, we report the synthesis and characterization of well-defined CoPt clusters with a mean diameter of ≈ 3 nm. After a short description of our original synthesis technique, following a physical route, and of the samples studied, we present transmission electron microscopy (TEM) observations revealing the appearance of the $L1_0$ phase upon annealing, without particle coalescence. Then we show the results of magnetic measurements, by x-ray magnetic circular dichroism (XMCD) and superconducting quantum interference device (SQUID) magnetometry, on assemblies of both chemically disordered and ordered CoPt clusters embedded in amorphous carbon. We show that, despite a striking change of the Co magnetic moment, the magnetic anisotropy of chemically ordered nanoparticles increases in much lower proportions than what is observed for the bulk, with respect to the chemically disordered phase.

II. SAMPLE PREPARATION

CoPt nanoparticles are synthesized using a physical technique, as opposed to chemical synthesis of colloidal particles. We use the low energy cluster beam deposition

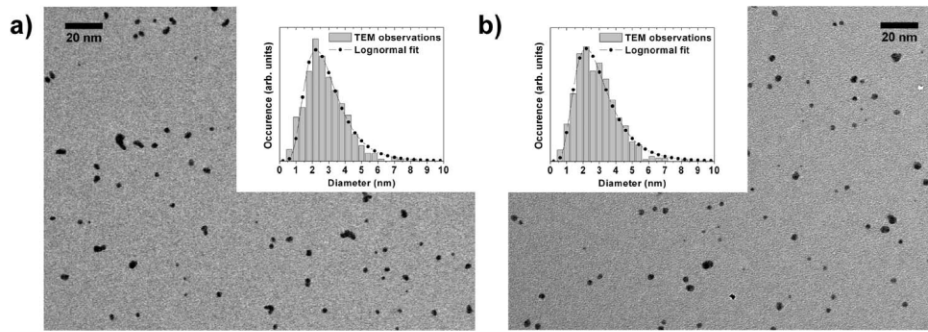


FIG. 1. TEM images of a 2D film of CoPt clusters (equivalent thickness ≈ 0.5 Å) embedded in amorphous carbon, as prepared (a) and after annealing (b). The size histograms deduced by TEM images analysis, together with the best fits corresponding to a log-normal size distribution, are shown in the inset. The fit parameters [see Eq. (1)] are $d_m=2.58$ nm, $w=0.42$ and $d_m=2.67$ nm, $w=0.47$, respectively, for as-prepared and annealed clusters.

(LECBD) technique^{48,49} that allows us to grow thin films of nanoparticles deposited on a substrate. We will give a short description of this original technique.

Clusters are produced in a laser vaporization-gas condensation source similar to the one developed by Dietz *et al.*, Milani and deHeer.^{50,51} Briefly, a plasma created by the impact of a Nd:YAG (yttrium aluminum garnet) laser beam focused on a rod is thermalized by injection of a continuous flow of helium at low pressure (typically 30 mbar) inducing the clusters growth. Clusters are subsequently stabilized and cooled down in the supersonic expansion taking place at the exit nozzle of the source. A low-energy cluster beam is then obtained, with clusters of different sizes, mostly neutral but also ionized (typically 1% of ions), allowing the growth of thin cluster films on a substrate.

The main key points of this technique are the following. The samples are produced under ultrahigh vacuum conditions (base static pressure of 10^{-10} mbar, and around 10^{-8} mbar during deposition, due to the use of helium as carrier gas). This means that, contrary to other techniques, in particular the chemical synthesis involving ligands, the clusters surface is not altered. Moreover, as mentioned further, the samples can be protected by a capping layer in order to avoid any pollution or oxidation when they are exposed to air for subsequent characterizations. It is important to note that the clusters composition is determined by the one of the target used for laser vaporization. This means that the particles stoichiometry can easily be adjusted by simply changing the target. In the present case, we use an equiatomic CoPt rod, leading to nanoparticles with a composition very close to $\text{Co}_{0.5}\text{Pt}_{0.5}$. Indeed, Rutherford backscattering spectrometry (RBS) experiments⁵² indicate that the mean stoichiometry of the clusters films is $\text{Co}_{0.56}\text{Pt}_{0.44}$. Energy dispersive x-ray spectroscopy (EDX) measurements on individual particles are in agreement with this result and show, within the precision of this technique, that the composition dispersion is quite low (around 10%).

Another important feature of the LECBD technique is that the clusters arrive on the substrate in a soft-landing regime, following a random deposition scheme. Consequently, as long as there is no significant diffusion on the substrate, which is the case in this study, the interparticle distance is entirely controlled by the clusters density: The surface den-

sity for two-dimensional (2D) samples or the volume density for three-dimensional samples where the clusters are embedded in a matrix. This allows us to adjust the strength of interparticle interactions and, by synthesizing highly diluted samples, to obtain thin films of clusters behaving as nearly isolated nanoparticles. Oppositely, there is, to our knowledge, no reported study on samples obtained from colloidal CoPt nanoparticles solutions where interparticle interactions are negligible. Moreover, the LECBD technique is highly versatile since clusters can be deposited on a large variety of substrates. For this study, we have used copper grids coated by a thin amorphous-carbon (a-C) layer, for TEM observations, and silicon substrates for magnetic measurements.

We have produced different samples of CoPt nanoparticles: 2D samples of CoPt clusters on a-C; 2D samples of CoPt clusters embedded in a-C, using an a-C capping layer; “sandwich” samples with two layers of CoPt particles embedded in a-C; and “mille-feuille” samples, on a silicon substrate, made of a large number of CoPt clusters layers (28 successive 2D cluster depositions) separated by a-C layers (a few nanometers thick). These two identical samples, used for magnetic characterizations, consist of diluted CoPt cluster layers, each one with an equivalent thickness of about 0.5 Å, corresponding to a cluster density around 2500 clusters per μm^2 and a mean interparticle distance of 10 nm. On the other hand, samples for TEM observations have been produced with various concentrations (i.e., cluster surface densities).

The size distribution of the deposited clusters is relatively sharp and corresponds to a log-normal curve. It slightly varies with the experimental conditions and depends on the material constituting the clusters. In the present case of CoPt nanoparticles, the clusters size, as deduced from size histograms measured by TEM (see Fig. 1), is well described by a log-normal function,

$$f(d) = \frac{1}{w\sqrt{2\pi}d} \exp\left[-\frac{1}{2}\left(\frac{\ln(d/d_m)}{w}\right)^2\right], \quad (1)$$

with a median diameter $d_m=2.6 \pm 0.1$ nm and a dispersion $w=0.42 \pm 0.05$ (corresponding to a mean diameter $\bar{d} \approx 2.9$ nm and a standard deviation $\sigma \approx 1.2$ nm).

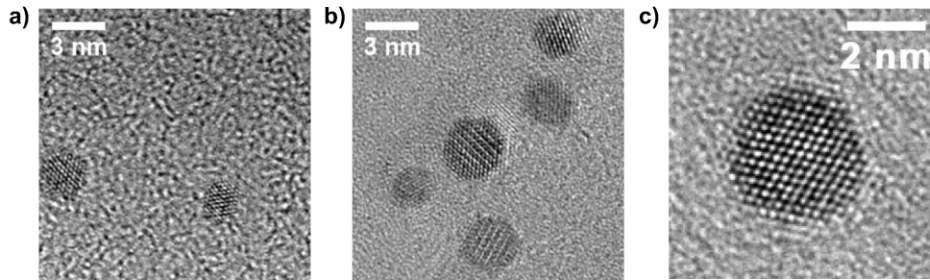


FIG. 2. HRTEM images of CoPt clusters of 2D films on amorphous carbon. (a) As-prepared clusters in the chemically disordered fcc A1 phase. (b,c) Annealed clusters: Some of them are in an orientation where $L1_0$ chemical order is visible, whereas some others appear as chemically disordered crystals (c).

III. TRANSMISSION ELECTRON MICROSCOPY OBSERVATIONS

There is a double advantage of using a matrix, in our case a-C, in which the clusters are embedded. Indeed, on the one hand, it acts as a spacer, preventing clusters to come into contact both during the thin film growth and during an eventual post-deposition annealing (as discussed later); and on the other hand, it protects the clusters from pollution and oxidation, allowing us to expose the samples to air without any alteration of the CoPt particles properties.

Keeping this in mind, the choice of a-C as embedding matrix appears to be sound. Carbon indeed does not form any stable carbide with Co and Pt, nor is it appreciably soluble in these elements, it is an efficient protection against oxidation, and most of all, it is transparent enough to electrons so that direct TEM observations are possible. We emphasize that, whereas other materials can represent interesting matrices (normal metals, or superconducting metals for particular applications⁵³), a-C is really attractive because it is a light element and it is amorphous (contrary to nanocrystalline metallic or oxide matrices²⁶): Having a direct observation of embedded clusters is of great help to ensure that the samples are made of well-separated nanoparticles of well-known size, and that these characteristics are preserved upon annealing.

Following the widely used procedure, various CoPt clusters samples were annealed (2D films of bare clusters, 2D films coated by a-C, and “sandwich” samples) in order to promote $L1_0$ chemical order in nanoparticles. Two hours annealing periods were performed at a 650 °C temperature and under high vacuum (pressure lower than 10^{-7} mbar), with or without a preliminary air exposure.

As it can be seen in Fig. 1, there is almost no clusters coalescence upon annealing when clusters are embedded in a-C: The size distribution is nearly the same, as well as the cluster density. There is, however, a noticeable change in the clusters shape: The circularity of the clusters projected surface increases with annealing, meaning that the nanoparticles are becoming more spherical. In addition, high resolution TEM (HRTEM) images (see Fig. 2) show that both as-prepared and annealed clusters are well crystallized and display the typical $\{100\}$ and $\{111\}$ facets of a truncated octahedron.

Due to the smallness of inter-reticular distances change between the chemically disordered A1 and the ordered $L1_0$

phase,³² a distance measurement cannot be used to determine if the particles are in the $L1_0$ phase. Moreover, there is no assurance that at such small sizes the interatomic distances are the same, or evolves in the same way, as in the bulk material. A similar cautiousness prevents us from using a tetragonalization measurement (the c/a ratio, as determined for instance from d_{111} and d_{200} distances) to quantify the nanoparticles chemical order.

The best criteria to ensure that particles are not chemically disordered is to be able to observe a contrast which is not visible for face-centered-cubic (fcc) crystals [(001) or (110) for instance]. Indeed, the $L1_0$ structure corresponds to successive pure Co and pure Pt atomic planes in the (001) direction. However, the particles must be in some particular orientations to allow such a contrast to manifest itself. This means that, even if the clusters are chemically ordered, only a small fraction will display a contrast corresponding to the Co-Pt alternation, because they are randomly oriented on the substrate. We would like to stress that, besides the statistical difficulty of finding correctly oriented particles, obtaining good quality HRTEM images of clusters with a diameter of only a few nanometers is highly challenging: Particles can move under the electron beam, they can even transform (Co evaporation for instance, as it is observed with nanobeam EDX analysis); the a-C layer can deform itself or even break down; a pollution can appear very quickly, and sometimes we observe the formation of an oxide shell around the clusters.

For annealed samples, we have been able to successfully observe nanoparticles in different orientations revealing a $L1_0$ -type contrast [not only a (001) contrast but also a (110) contrast]. For some particular particles, such as the one displayed in Fig. 3, which shows a remarkable (001) contrast, we have performed HRTEM images simulations. We have used the multislice method and the dynamical scattering theory, as implemented in the JEMS software.^{54,55} Simulations are in remarkable agreement with the experiment when considering a perfectly $L1_0$ -ordered cluster of the same size and orientation as the one observed by HRTEM (see Fig. 3). We can then positively conclude that such a contrast is not an artifact: It is a direct signature of the chemical order inside CoPt clusters after annealing.⁵⁶ We also emphasize that the observation of a $L1_0$ -type contrast for annealed samples is not marginal at all: Although it is difficult to observe particles with an orientation revealing two different crystallographic planes, it is quite common to observe a (001) con-

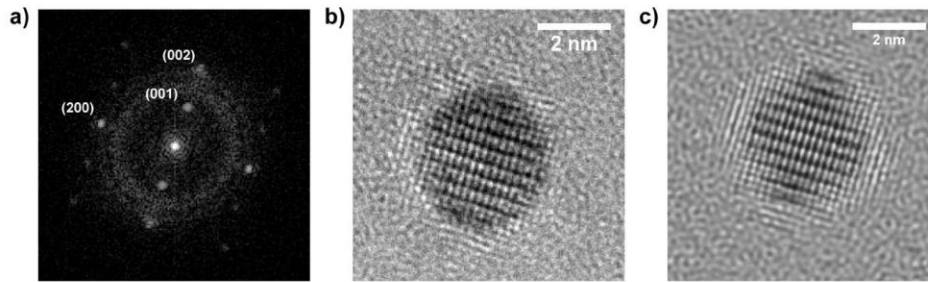


FIG. 3. (a) Fourier transform corresponding to the HRTEM image of the annealed CoPt cluster shown in (b). The (001) peak is the signature of $L1_0$ chemical order corresponding to the strong contrast modulation visible in (b). (c) HRTEM image simulation obtained with a perfectly $L1_0$ chemically ordered CoPt cluster, observed along the [010] direction, with a slight tilt.

trast alone. Nevertheless, since we can hardly evaluate the proportion of clusters displaying a $L1_0$ contrast, the question of an incomplete chemical ordering in the sample will be addressed in Sec. V. At the opposite, for as-prepared samples, we have not been able to observe any $L1_0$ contrast in HRTEM images. It shows that annealing is needed to promote chemical order in the nanoparticles, and that they are being produced in the chemically disordered fcc A1 phase.

The observation of a $L1_0$ contrast on HRTEM images constitutes direct evidence that individual particles are chemically ordered. HRTEM then appears as a powerful technique to investigate the $A1 \rightarrow L1_0$ transformation in nanoparticles. Other methods like x-ray or electron diffraction may not be suited for samples made of diluted 2D assemblies of CoPt clusters with a diameter of 3 nm or less. Indeed, we have also succeeded in observing a (001) contrast in clusters of a 2 nm diameter (see Fig. 4). To our knowledge, chemical order had never been observed in so small CoPt nanoparticles. This result must be taken into account when examining thermodynamic predictions obtained from theoretical models.⁵⁷ Note that the observation of these small $L1_0$ clusters implies that they are thermodynamically stable, not only at room temperature, but at higher temperature since annealing has turned room temperature A1 clusters into room temperature $L1_0$ clusters. This pushes down the limit, and

even questions the existence, of a critical particle size where chemical order would become unstable at room temperature.

IV. MAGNETIC PROPERTIES

A. XMCD measurements

XMCD measurements were performed at the UE56/2-PGM-2 beamline of the BESSY synchrotron (Berlin), at the Co $L_{2,3}$ edges. We used a collinear geometry where the applied magnetic field is parallel to the incident photon beam. The x-ray absorption spectroscopy (XAS) signal was monitored using the total electron yield detection mode, with an applied field of 5 T (which is high enough to fully saturate the sample magnetization, as it has been verified by acquiring hysteresis loops). Measurements were performed at 300 K, on both as-prepared and annealed (2 h at 650 °C, as for TEM samples) “mille-feuille” samples.

As it can be seen from the XAS spectra (Fig. 5), the a-C matrix appears as an efficient protection against oxidation and corresponds to a low x-ray attenuation, which ensures a high signal-to-noise ratio: The Co L_3 edge is sharp and does not include any detectable oxide contribution.²⁶ Moreover, there is no significant difference in the edges profiles between as-prepared and annealed CoPt particles. Hence, a drastic modification of the Co chemical environment (as carbon diffusion in the clusters) is very unlikely.

The mean orbital and spin magnetic moments per Co atom, μ_L and μ_S , have been determined using the well-known sum rules.^{59,60} Note that, since the samples are made of randomly oriented crystallized nanoparticles, the magnetic dipole term μ_T , which reflects the asphericity of the spin moment distribution around the absorbing Co atom, averages to zero.⁶¹ Therefore, the effective spin moment $\mu_S^{\text{eff}} = \mu_S + 7\mu_T$, evaluated from the XMCD signal, is in fact the true spin magnetic moment.

This assertion can still be moderated, taking into account the fact that the μ_T cancellation may not apply in materials with a strong spin-orbit coupling: In such a case, the dipole term does not only result from the crystal field and consequently cannot be eliminated using angle-dependent XMCD measurements^{61,62} (or, as in the present case, with randomly oriented particles). Moreover, even in materials with a negligible bulk spin-orbit coupling, going to low-dimensional

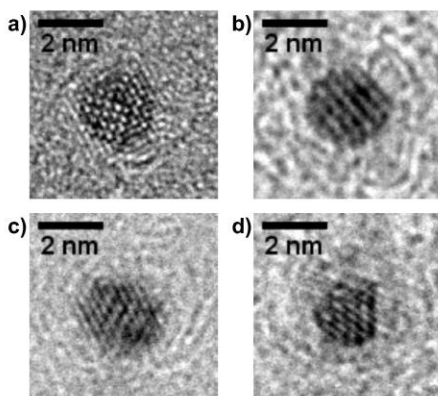


FIG. 4. Small annealed CoPt clusters, around 2 nm in diameter, showing a $L1_0$ chemical order contrast: (110) in the case of image (a) and (001) for images (b,c,d). Samples corresponding to images (c) and (d) are capped with an a-C layer.

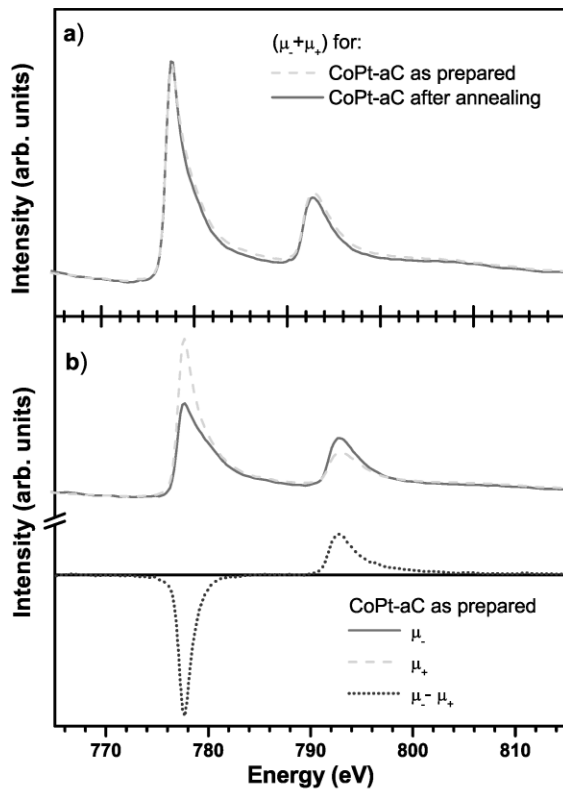


FIG. 5. (Color online) (a) XAS spectra at the Co L_3 and L_2 edges for the as-prepared and annealed samples. (b) XAS signals (μ_- and μ_+ corresponding to the two different circular polarizations) for the as-prepared sample, and the corresponding XMCD curve ($\mu_- - \mu_+$).

systems can result in a failure of the μ_T cancellation.⁶² The reason is that spin-orbit coupling effects are enhanced for low-coordinated atoms. As a matter of fact, even the strict application of the sum rules can be questioned in peculiar situations⁶³ (interfaces, low-dimensional systems, etc.). However, contrary to the Fe case, it has been shown that both the μ_T cancellation and the sum rules remain verified in the case of low-dimensional Co systems.^{64,65} Anyway, following previously presented studies^{58,66,67} [even for the questionable case of FePt (Refs. 68–70)], we will assume that the sum rules can safely be applied in the case of CoPt nanoparticles.

The Co magnetic moments, deduced from XMCD, are reported in Table I. There is a striking change of the spin magnetic moment upon annealing: the μ_S value is enhanced

by 12%. In addition, both the orbital magnetic moment and the μ_L/μ_S ratio increase significantly. The high μ_S value of the as-prepared sample is consistent with the fact that every Co atom is magnetically ordered, i.e., that there is no dead layer at the clusters surface. To all appearances, the average magnetic moment per Co atom corresponds to the real Co moment in CoPt: It is not the result of a balance between some populations of Co atoms with different magnetic moments. The magnetic moment augmentation upon annealing must then be related to an intraparticle change.⁷¹ According to TEM observations, we claim that this striking evolution is a signature of the structural transition from the chemically disordered to the $L1_0$ phase in CoPt nanoparticles. Amazingly, the net Co magnetic moment is increasing upon chemical ordering, which seems in contradiction with the bulk behavior where the magnetization is decreasing when going from A1 to $L1_0$ phase.³² However, this effect could be due to the small size of the particles, or an extensive Pt magnetic moment reduction could compensate the Co magnetic moment variation. Note also that a change in the number of d holes per Co atom, upon annealing, can result in a modification of the Co magnetic moment, as deduced from XMCD. However, since there is also a significant evolution of the μ_L/μ_S ratio, a variation of the number of d holes cannot explain by itself the observed results. In any case, even if such a variation can play a role,⁷² the conclusion remains the same: Annealing has a significant effect on the XMCD signal of CoPt nanoparticles.

Surprisingly, our result significantly differs from the one reported by Grange *et al.*⁵⁸ In their study, they have determined the Co and Pt magnetic moments of $L1_0$ CoPt thin films, using XMCD. Assuming their CoPt film is fully chemically ordered (which, according to the authors, is not guaranteed), the discrepancy between the reported value and the present one implies a tremendous size effect. Indeed, such a magnetic moment enhancement is known to happen only at much lower size: The deviation from the bulk behavior occurs around 400 atoms,⁷³ whereas in our case, the mean CoPt cluster size corresponds to 800 atoms.

Interestingly, the magnetic moment values measured for as-prepared CoPt nanoparticles are very close to those obtained by Grange *et al.* for a presumably $L1_0$ thin film. A possible interpretation is that chemical order is in fact similar for both CoPt samples: Chemical order in as-prepared CoPt clusters may be higher than expected (partial order, due to a finite size effect, as discussed by Rohart *et al.*⁷⁴) and/or chemical order in the CoPt thin film may be much lower than

TABLE I. Geometric and magnetic size parameters (d_m and w) deduced, respectively, from TEM and from SQUID measurements; Co spin and orbital magnetic moments [μ_S and μ_L are calculated, following Grange *et al.*, assuming that the number of holes per Co atom is $n_h=2.628$ (Ref. 58)]; CoPt clusters MAEs (K_{eff}) and maximum susceptibility temperatures (T_{max}) determined from ZFC curves.

	TEM d_m (nm)	TEM w	SQUID d_m (nm)	SQUID w	μ_S ($\mu_B/\text{at.}$)	μ_L ($\mu_B/\text{at.}$)	μ_L/μ_S	K_{eff} (kJ/m ³)	T_{max} (K)
CoPt as-prepared	2.60 ± 0.1	0.42 ± 0.05	2.55 ± 0.2	0.36 ± 0.1	1.70	0.12	0.071	193 ± 20	28
CoPt annealed	2.63 ± 0.1	0.45 ± 0.05	2.45 ± 0.2	0.35 ± 0.1	1.91 (1.76) ^a	0.18 (0.11) ^a	0.094 (0.063) ^a	385 ± 20	52

^aFrom Grange *et al.* (Ref. 58), for a presumably $L1_0$ thin film.

expected. As a consequence, if as-prepared clusters are already partially chemically ordered (however, TEM observations do not substantiate any sizeable chemical order in as-prepared particles), it means that the $A1 \rightarrow L1_0$ transition must have an even higher impact on the Co magnetic moment.

Unfortunately, there is, to our knowledge, no reported value of the Co magnetic moments for the bulk CoPt $A1$ phase that could have been compared to the present results. On the other hand, Imperia *et al.*⁶⁷ have recently determined the μ_L/μ_S ratio for disordered Co-Pt alloy nanoparticles. They have found that μ_L/μ_S is significantly higher in their case than in ours. However, due to missing experimental details and characterization, a direct comparison with our system is difficult: The particle size is unknown (the question of an eventual coalescence during sample growth is not evoked), the particles structure and composition are not described, and the use of an oxide capping layer may result in a partial Co oxidation. This oxidation can give rise to a μ_L/μ_S enhancement, as previously demonstrated.⁷⁵ Moreover, we have also observed that CoPt embedded in an oxide matrix (MgO) exhibit a higher μ_L/μ_S ratio than in a-C,²⁶ which is consistent with the very high interface magnetic anisotropy measured in MgO matrix²⁸ (as it is expected that a high μ_L goes with a high anisotropy^{76,77}). Since we are more interested in the intrinsic CoPt nanoparticles magnetic properties, the choice of an a-C matrix seems to be more judicious than an oxide one.

XMCD measurements have allowed us to detect a Co orbital moment augmentation, which lets us think of a concomitant magnetic anisotropy increase. However, the magnitude of the μ_L evolution upon annealing ($\approx 50\%$) sheds doubt on the possibility to reach a magnetic anisotropy enhancement as high as in the bulk, where a $\approx 10\,000\%$ augmentation is observed.³² Nevertheless, additional experiments are needed in order to obtain a quantitative evaluation of CoPt nanoparticles magnetic anisotropy energy (MAE).

B. SQUID magnetometry measurements

Magnetic measurements at various temperatures have been performed on the “mille-feuille” samples, using a SQUID magnetometer. The high temperature (300 K) hysteresis loops (see Fig. 6), for as-prepared and annealed samples, do not show any coercivity, which is typical of an assembly of superparamagnetic particles. The magnetization curves can be successfully fitted using a simple Langevin function, taking into account the clusters size distribution and the Co magnetic moment deduced from XMCD results.⁷⁸ This allows us to check that the clusters magnetic size is the same (within error bars) as the geometric size observed by TEM, even for the annealed sample (see Table I). This is another evidence that no coalescence is taking place upon annealing. Moreover, the fact that the magnetic size dispersion is very similar to the geometrical one, shows that the clusters composition distribution must be quite sharp: Indeed, a significant stoichiometry variation among the particles would result in a broadened distribution of magnetic moment per cluster. Besides, since the same Langevin fit can be used for 300 K

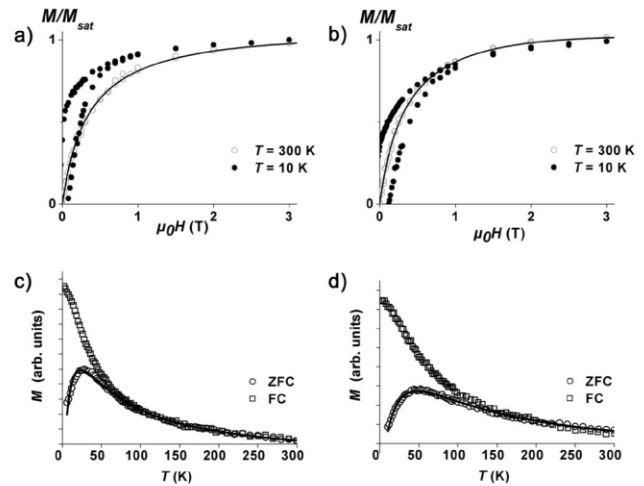


FIG. 6. Hysteresis loops of the as-prepared (a) and annealed (b) sample, at 300 K (○) and 10 K (●). The solid line corresponds to a fit using a Langevin function, with a log-normal clusters size distribution (parameters given in Table I). ZFC-FC magnetization curves of the as-prepared (c) and annealed (d) sample. The solid line corresponds to a fit using a theoretical semianalytical model (see text), with the same clusters size distribution as for the high temperature cycles fit.

and 200 K hysteresis cycles, it means that anisotropy effects are negligible at such temperatures.

Oppositely, magnetization cycles at low temperature (10 K) exhibit a coercive field and a remanent to saturation magnetization ratio $M_r/M_{sat} \approx 0.4$ (see Fig. 6). Note that the maximum magnetic field ($\mu_0H = 5$ T) is largely sufficient to saturate the magnetization. According to the Stoner-Wohlfarth model,⁷⁹ M_r/M_{sat} must be lower than 0.5 for an assembly of randomly oriented macrospins without interaction. This gives an indication that the interparticle distance in the samples is large enough to consider that the CoPt clusters are isolated.

The effect of annealing (i.e., chemical ordering) is immediately visible on the low temperature cycle: The coercive field μ_0H_C increases twofold (from 0.07 T to 0.12 T), meaning that the magnetic anisotropy is enhanced. In order to get a quantitative estimation of the MAE, we have performed magnetic susceptibility measurements following the zero-field-cooled and/or field-cooled (ZFC-FC) procedure. We use a 50 Oe (i.e., 0.005 T) magnetic field, applied in a direction parallel to the sample plane. As it can be seen in Fig. 6, the ZFC curves show a transition from ferromagnetic to superparamagnetic regime, as evidenced by the susceptibility peak around a given T_{max} temperature. The $1/T$ behavior, for high enough temperature (T slightly larger than T_{max}), is consistent with the picture of rapidly switching macrospins without interaction. Just as for H_C , the T_{max} value is doubled upon annealing, which is another signature of a strong MAE augmentation.

The simple relation $K_{eff}V = 25k_B T_{max}$ is used in many studies to derive the anisotropy constant K_{eff} (MAE) from the measured value of T_{max} and knowing the typical particles volume V . However, the application of this “rule of thumb” equation can be highly uncertain: The particles size disper-

sion can only be approximately taken into account (and is not considered in most cases); the use of T_{\max} instead of the blocking temperature (which is hard to define for particle distributions) is an approximation; and the value of the prefactor (usually 25) is not well established and varies among the authors.

Nevertheless, this crude expression can be used to get a first MAE estimation and gives in the present case $K_{\text{eff}} = 0.25 \text{ MJ/m}^3$ ($0.25 \times 10^7 \text{ erg/cm}^3$) and $K_{\text{eff}} = 0.50 \text{ MJ/m}^3$ ($0.50 \times 10^7 \text{ erg/cm}^3$), respectively, for the chemically disordered and chemically ordered CoPt nanoparticles. Following Dormann *et al.*⁸⁰ (as Petit *et al.* did⁸¹), we have used the effective volume $V_{\text{eff}} = \langle V^2 \rangle / \langle V \rangle$ in the equation.

A more elaborate approach is yet possible, where the entire ZFC curve is adjusted by a semianalytical model (described in Ref. 28), which fully takes into account the particles size distribution and the dynamic temperature sweep during the experimental acquisition. The only adjustable parameter is then the anisotropy constant K_{eff} : The corresponding energy barrier of a cluster with volume V is simply written as $\Delta E = K_{\text{eff}} V$. This widely used expression implicitly supposes that the clusters size distribution is the major source of dispersion for the magnetization switching energy barrier. As a matter of fact, this assumption is not firmly justified, especially in the case of an alloy: In addition to the usual surface and shape distribution effects (additional facets on a perfect truncated octahedron for instance⁸²), compositional variation and chemical order distribution^{83,84} (or even, as discussed by Rohart *et al.*,⁷⁴ the statistical atomic distribution at a fixed chemical order parameter) can deeply modify the MAE. Moreover, it is the standard procedure to also neglect any temperature variation of the MAE and of the cluster magnetization, which is quite justified in the temperature range considered here.^{85,86} Anyway, since the simple relation $\Delta E = K_{\text{eff}} V$ appears to be satisfactory in the present case, we will not go further into a cluster anisotropy analysis in this study. An additional degree of freedom, using a surface anisotropy term (i.e., $\Delta E = K_V V + K_S S$, where S is the cluster surface), does not change the results and just leads to $K_S \approx 0$.

This semianalytical model has been applied to adjust the ZFC curves, using a log-normal function for the clusters magnetic size distribution, with the parameters d_m and w [see Eq. (1)] determined from the Langevin fit of high temperature hysteresis loops. We have been able to precisely reproduce the experimental curves (see Fig. 6), the best fit giving a MAE value of $K_{\text{eff}} = 0.19 \text{ MJ/m}^3$ ($0.19 \times 10^7 \text{ erg/cm}^3$) for chemically disordered CoPt nanoparticles and $K_{\text{eff}} = 0.38 \text{ MJ/m}^3$ ($0.38 \times 10^7 \text{ erg/cm}^3$) for $L1_0$ ones. The 100% MAE relative variation found with this model is consistent with the T_{\max} doubling, if we simply consider the “rule of thumb” relation previously mentioned (since, in the present case, we know that the clusters size distribution is the same for as-prepared and annealed samples).

V. DISCUSSION

The TEM observations, together with the magnetic measurements previously presented show that the CoPt nanopar-

ticles evolve upon annealing: The structure changes from $A1$ to $L1_0$; the Co magnetic moment is enhanced as well as the μ_L/μ_S ratio; and the MAE increases (consequently, the blocking temperature is higher). Let us emphasize that the particles embedded in a-C remain almost isolated with no significant change in size, so that the magnetic properties evolution really reflects the behavior of individual CoPt nanoparticles. Surprisingly, although the anisotropy is found to increase with chemical ordering, the determined MAE value is quite small as compared to the bulk.^{32,33} The magnitude of the corresponding MAE variation is significant but dramatically lower than the two orders of magnitude augmentation reported for the bulk!

In order to fix the ideas, the blocking temperature of a 3 nm particle with the same MAE as the bulk CoPt $L1_0$ one (5 MJ/m^3) would be $\approx 200 \text{ K}$. Conversely, the particle size that would account for the observed blocking temperature (52 K), if the MAE was the bulk one, would be 1.9 nm in diameter.

Our unexpected results can be compared to previous magnetic measurements carried on CoPt nanoparticles.^{16–24,27–30,81,87} Many researchers have reported extremely high coercivity for annealed CoPt samples and some have derived MAE values.^{21,81,87} However, to our knowledge, among the previously presented results, there is not any case where the system was made of noninteracting particles (as it can be seen from the remanence to saturation ratio M_r/M_{sat} which, according to the isolated macrospin model,⁷⁹ should be 0.5 at 0 K and then decrease with temperature). In most cases, the impact of annealing on the particles size (in particular, coalescence) has not been investigated. Moreover, very often, there is no definite proof that the system is made of chemically ordered CoPt nanoparticles, so that the evolution of the magnetic properties, which is ascribed to $L1_0$ chemical ordering, could come (at least, partly) from particle growth and interparticle interactions. It must also be noted that the CoPt particles studied in the present case are among the smallest ever reported. Here, contrary to other works, several characterizations have been made on the very same system (and even on the same sample for XMCD and SQUID measurements). Therefore, our conclusions must be particularly reliable.

One can envisage various effects to account for the striking difference between the MAE of the bulk $L1_0$ phase and the one of annealed CoPt nanoparticles. Indeed, one may think that (i) the clusters magnetic size is smaller than expected; (ii) there are interparticle interactions; (iii) the particles are not fully chemically ordered; (iv) the MAE reduction is a finite size effect; (v) the MAE reduction is due to the a-C matrix. We will discuss these different points in the following.

(i) The magnetic size could indeed be different (smaller in fact), than the diameter observed by TEM. However, as said before, to be compatible with the bulk $L1_0$ MAE, the mean magnetic diameter should be around 1.9 nm. This would imply that the major part of Co atoms are in fact nonmagnetic (“dead-layer” effect), which is not compatible with XMCD observations. Moreover, as presented in the section reporting SQUID results, the size distribution determined from TEM is able to reproduce the high temperature superparamagnetic

magnetization cycles. Clusters with a much smaller magnetic size would definitely not produce a correct magnetization curve. This explanation can then be rejected.

(ii) Magnetic interactions between particles can modify the blocking temperature and change the magnetization curves.^{88–90} However, for blocked particles, interactions would broaden the switching field distribution and shift it toward higher values⁹¹ (as if the particles volume was greater, thus increasing the energy barrier for magnetization reversal): If there were some interactions between particles, the presently measured MAE would be overestimated meaning that the true MAE reduction, as compared to the bulk, is in fact even higher. Consequently, the possibility of nonvanishing interparticle interactions cannot account for the observed effect.

(iii) The $L1_0$ chemical order could be incomplete and/or some particles (the smallest ones) may still be in the A1 phase. However, if it is the case, it means that the Co magnetic moment enhancement, which is an average value over all Co atoms, is even greater for a complete $A1 \rightarrow L1_0$ transition. Moreover, since a $L1_0$ -type contrast is highly visible by HRTEM and since a perfectly ordered nanocrystal is in very good agreement with experimental images (see Fig. 3), the chemical order parameter must be significant.⁹² In addition, we can safely assume that a 2 h annealing at 650 °C is enough to reach thermodynamic equilibrium, so that there is no reason for identical particles to be in different phases. Nevertheless, it cannot be excluded that, because of the size dependence of the transition temperature, the smallest particles in the sample remain chemically disordered.

Following this idea, we have tried to determine a critical diameter under which the particles would remain in the A1 phase, by fitting the ZFC curve with the bulk MAE value for $L1_0$ clusters (largest particles) and the previously determined MAE for A1 clusters (smallest particles). We have found that it is definitely impossible to account for the experimental observations with a part of the clusters size distribution corresponding to particles having the bulk $L1_0$ MAE. Conversely, assuming that the critical diameter is 2 nm (chemically ordered particles of this size have been observed by TEM), we have determined the MAE of the largest clusters, which are in the $L1_0$ phase: It does not change, within the uncertainty, the MAE value previously determined by assuming that all the particles are in the ordered phase. In the end, even if some particles in the annealed sample are still partially disordered, it does not change the conclusion that the MAE of $L1_0$ CoPt nanoparticle is much lower than the bulk one.

(iv) The finite size of the CoPt clusters, and the corresponding high surface to volume ratio could be responsible for the striking MAE reduction observed in the case of $L1_0$ nanoparticles. Actually, Rohart *et al.*⁷⁴ recently predicted, using an empirical Néel anisotropy model, that the MAE of $L1_0$ particles should decrease when going to small clusters. This counterintuitive result can be written in term of a finite size correction to the anisotropy: $K_{\text{eff}}(N) = K_{\infty} + K_{\text{fs}}/N^{-\alpha}$, where N is the number of atoms in the cluster, and K_{∞} and K_{fs} are, respectively, the bulk MAE and the finite size contribution to the MAE. These two terms, together with the α exponent, vary with the cluster chemical order parameter. The Néel

model predicts that K_{fs} is negative for CoPt clusters with a significant chemical order parameter (and in particular for perfect $L1_0$ particles), while it is positive for chemically disordered clusters. This is qualitatively consistent with our results where as-prepared particles display a higher MAE⁹³ than the bulk (according to Ref. 32, the bulk MAE of the CoPt A1 phase is around 0.06 MJ/m³), whereas it is the opposite for chemically ordered nanoparticles.

However, the magnitude of the calculated finite size effect is not in agreement with the MAE reduction observed in the present case. This may be due to other contributions neglected in the crude Néel theoretical model. In particular, magnetoelastic effects could dominate and have strong repercussions on the size dependence of the MAE. For instance, the crystallographic structure of CoPt nanoparticles can be slightly different from the bulk one, the tetragonalization can differ from the one observed in the bulk, resulting in modified nearest-neighbor distances. A consequence could be a significative lowering of the magnetic anisotropy. Even so, such a weak structural distortion is hard to detect, and its precise impact on the magnetic properties is even more difficult to determine, so that such a magnetoelastic effect is quite speculative. Another possibility is that some particles may not be made of a single $L1_0$ domain: Twinned clusters for instance could correspond to particles with various c axes (easy magnetization direction), leading to a strong MAE diminution.⁷ Nevertheless, if some twinned (and multiply twinned) particles have indeed been detected by TEM, the observation of such structures remains exceptional, especially in the annealed sample. These considerations show how size reduction effects could play a major role in the MAE decrease of CoPt $L1_0$ nanoparticles. However, it also implies that a complete analysis should explicitly consider that the MAE is in fact size dependent.⁹⁴

(v) The last possibility is that the a-C matrix⁹⁵ strongly modifies the clusters magnetic properties and in particular the magnetic anisotropy. Even if such a hypothesis cannot be firmly discarded, some elements tend to show that carbon does not have such an impact on CoPt nanoparticles. First, as mentioned earlier, no alloying effect (carbide formation) is detected from the core level absorption peak of Co. This is also consistent with the fact that, at the macroscopic scale, the formation of cobalt and platinum carbide is not favorable. Second, the use of a carbon matrix has no detectable effect on the structure of CoPt clusters, even after annealing: $L1_0$ clusters are observed both with and without the a-C matrix. Third, as demonstrated by the high Co magnetic moment value measured by XMCD, carbon does not quench cobalt magnetism (contrary to other elements, oxygen in particular). Moreover, if the carbon matrix induces a pure interface effect, we expect that it could be accounted for with a surface anisotropy term in the ZFC curves fit. Since it is not the case, a supposed magnetic effect of carbon should have repercussions on the volume magnetic anisotropy. It is still possible to envisage carbon diffusion in the CoPt clusters core, resulting in interstitial carbon atoms with a dramatic effect on the magnetic anisotropy, but such an unprecedented phenomenon remains highly speculative.

The true explanation of the observed reduced magnetic anisotropy of CoPt $L1_0$ clusters, as compared to the bulk,

may be a combination of the various envisaged effects. Identifying these physical mechanisms, and trying to control them, is a prerequisite to be able to overcome the intrinsic, and unexpected, limitations on the magnetic anisotropy of CoPt nanoparticles.

VI. CONCLUSION

In conclusion, we have studied the structural and magnetic properties of CoPt nanoparticles synthesized by the LECBD technique, in ultrahigh vacuum conditions. The produced samples are made of nearly isolated nanoparticles embedded in amorphous carbon. The $A1 \rightarrow L1_0$ phase transformation takes place upon annealing, without particle coalescence, as evidence by TEM. A chemical contrast revealing the $L1_0$ order has been observed by HRTEM, even for CoPt particles as small as 2 nm in diameter. XMCD measurements have shown that chemical ordering is accompanied by a striking enhancement of the Co magnetic moment. A 100% magnetic anisotropy increase has also been evidenced by SQUID magnetometry measurements on the very same samples. However, the MAE of annealed clusters, for which the $L1_0$ chemical order has been evidenced, ap-

pears to be much lower than the bulk one (by more than one order of magnitude).

A careful examination of the previously presented results reveals that the present study is the first intrinsic magnetic characterization of well-known CoPt nanoparticles. This means that the stimulating results reported for CoPt particles samples may in fact have been over interpreted. Therefore, one can legitimately question the ability of CoPt to keep its promises: The intrinsic magnetic anisotropy of chemically ordered CoPt nanoparticles may never be high enough to ensure a magnetization thermal stability compatible with practical applications. Let us note that the same problem could be met for FePt nanoparticles, where the even more numerous magnetic characterizations reported should be cautiously examined.

ACKNOWLEDGMENTS

The authors gratefully acknowledge E. Bernstein, A. Perez, O. Boisron, and G. Guiraud for stimulating discussions and for their support. The authors acknowledge support through the BESSY IA-SFS program (Contracts No. BESSY-ID.07.1.672 and No. RII 3CT-2004-506008).

*ftournus@ipmcn.univ-lyon1.fr

- ¹I. M. L. Billas, A. Chatelain, and W. A. de Heer, *Science* **265**, 1682 (1994).
- ²P. Gambardella, S. Rusponi, M. Veronese, S. S. Dhesi, C. Grazioli, A. Dallmeyer, I. Cabria, R. Zeller, P. H. Dederichs, K. Kern, C. Carbone, and H. Brune, *Science* **300**, 1130 (2003).
- ³D. J. Sellmyer, M. Yu, and R. D. Kirby, *Nanostruct. Mater.* **12**, 1021 (1999).
- ⁴S. H. Sun, C. B. Murray, D. Weller, L. Folks, and A. Moser, *Science* **287**, 1989 (2000).
- ⁵S. H. Sun, S. Anders, T. Thomson, J. E. E. Baglin, M. F. Toney, H. F. Hamann, C. B. Murray, and B. D. Terris, *J. Phys. Chem. B* **107**, 5419 (2003).
- ⁶S. Stoyanov, Y. Huang, Y. Zhang, V. Skumryev, G. C. Hadjipanayis, and D. Weller, *J. Appl. Phys.* **93**, 7190 (2003).
- ⁷B. Rellinghaus, S. Stappert, M. Acet, and E. F. Wassermann, *J. Magn. Magn. Mater.* **266**, 142 (2003).
- ⁸B. Stahl, J. Ellrich, R. Theissmann, M. Ghafari, S. Bhattacharya, H. Hahn, N. S. Gajbhiye, D. Kramer, R. N. Viswanath, J. Weissmüller, and H. Gleiter, *Phys. Rev. B* **67**, 014422 (2003).
- ⁹S. Stappert, B. Rellinghaus, M. Acet, and E. F. Wassermann, *J. Cryst. Growth* **252**, 440 (2003).
- ¹⁰H.-G. Boyen, K. Fauth, B. Stahl, P. Ziemann, G. Kästle, F. Weigl, F. Banhart, M. Hessler, G. Schütz, N. Gajbhiye, J. Ellrich, H. Hahn, M. Büttner, M. G. Garnier, and P. Oelhafen, *Adv. Mater.* **17**, 574 (2005).
- ¹¹K. Elkins, D. Li, N. Poudyal, V. Nandwana, Z. Jin, K. Chen, and J. P. Liu, *J. Phys. D* **38**, 2306 (2005).
- ¹²M. Takahashi, T. Ogawa, D. Hasegawa, and B. Jeyadevan, *J. Appl. Phys.* **97**, 10J307 (2005).
- ¹³H. Nguyen, L. Howard, G. Stinton, S. Giblin, B. Tanner, I. Terry, A. Hughes, I. Ross, A. Serres, and J. Evans, *Chem. Mater.* **18**, 6414 (2006).
- ¹⁴V. Nandwana, K. E. Elkins, N. Poudyal, G. S. Chaubey, K. Yano, and J. P. Liu, *J. Phys. Chem. C* **111**, 4185 (2007).
- ¹⁵Chuan-bing Rong, N. Poudyal, G. S. Chaubey, V. Nandwana, R. Skomski, Y. Q. Wu, M. J. Kramer, and J. P. Liu, *J. Appl. Phys.* **102**, 043913 (2007).
- ¹⁶M. Yu, Y. Liu, and D. J. Sellmyer, *J. Appl. Phys.* **87**, 6959 (2000).
- ¹⁷A. C. C. Yu, M. Mizuno, Y. Sasaki, H. Kondo, and K. Hiraga, *Appl. Phys. Lett.* **81**, 3768 (2002).
- ¹⁸Y. Xu, Z. G. Sun, Y. Qiang, and D. J. Sellmyer, *J. Magn. Magn. Mater.* **266**, 164 (2003).
- ¹⁹C. N. Chinnasamy, B. Jeyadevan, K. Shinoda, and K. Tohji, *J. Appl. Phys.* **93**, 7583 (2003).
- ²⁰Y. Sui, L. Yue, R. Skomski, X. Z. Li, J. Zhou, and D. J. Sellmyer, *J. Appl. Phys.* **93**, 7571 (2003).
- ²¹X. Sun, Z. Y. Jia, Y. H. Huang, J. W. Harrell, D. E. Nikles, K. Sun, and L. M. Wang, *J. Appl. Phys.* **95**, 6747 (2004).
- ²²L. Castaldi, K. Giannakopoulos, A. Travlos, D. Niarchos, S. Boukari, and E. Beaurepaire, *J. Magn. Magn. Mater.* **290-291**, 544 (2005).
- ²³M. Mizuno *et al.*, *J. Appl. Phys.* **97**, 10J301 (2005).
- ²⁴J.-M. Qiu, Y.-H. Xu, J. H. Judy, and J.-P. Wang, *J. Appl. Phys.* **97**, 10P704 (2005).
- ²⁵A. Hannour, L. Bardotti, B. Prevel, E. Bernstein, P. Melinon, A. Perez, J. Gierak, E. Bourhis, and D. Mailly, *Surf. Sci.* **594**, 1 (2005).
- ²⁶L. Favre *et al.*, *Phys. Rev. B* **74**, 014439 (2006).
- ²⁷T. Seto, K. Koga, H. Akinaga, F. Takano, T. Orii, and M. Hirasawa, *J. Nanopart. Res.* **8**, 371 (2006).
- ²⁸S. Rohart, C. Raufast, L. Favre, E. Bernstein, E. Bonet, and V. Dupuis, *Phys. Rev. B* **74**, 104408 (2006).

- ²⁹J. H. Kim, J. Kim, N. Oh, Y.-H. Kim, C. K. Kim, C. S. Yoon, and S. Jin, *Appl. Phys. Lett.* **90**, 023117 (2007).
- ³⁰D. M. Newman, M. L. Wears, M. Jollie, and D. Choo, *Nanotechnology* **18**, 205301 (2007).
- ³¹D. Alloyeau, C. Langlois, C. Ricolleau, Y. L. Bouar, and A. Loiseau, *Nanotechnology* **18**, 375301 (2007).
- ³²R. A. McCurrie and P. Gaunt, *Philos. Mag.* **13**, 567 (1966).
- ³³G. Hadjipanayis and P. Gaunt, *J. Appl. Phys.* **50**, 2358 (1979).
- ³⁴Y. K. Takahashi, T. Ohkubo, M. Ohnuma, and K. Hono, *J. Appl. Phys.* **93**, 7166 (2003).
- ³⁵Y. K. Takahashi, T. Koyama, M. Ohnuma, T. Ohkubo, and K. Hono, *J. Appl. Phys.* **95**, 2690 (2004).
- ³⁶S. Fukami and N. Tanaka, *Philos. Mag. Lett.* **84**, 33 (2004).
- ³⁷T. Miyazaki, O. Kitakami, S. Okamoto, Y. Shimada, Z. Akase, Y. Murakami, D. Shindo, Y. K. Takahashi, and K. Hono, *Phys. Rev. B* **72**, 144419 (2005).
- ³⁸R. V. Chepulskii and W. H. Butler, *Phys. Rev. B* **72**, 134205 (2005).
- ³⁹B. Yang, M. Asta, O. N. Mryasov, T. J. Klemmer, and R. W. Chantrell, *Scr. Mater.* **53**, 417 (2005).
- ⁴⁰B. Yang, M. Asta, O. N. Mryasov, T. J. Klemmer, and R. W. Chantrell, *Acta Mater.* **54**, 4201 (2006).
- ⁴¹C.-b. Rong, D. Li, V. Nandwana, N. Poudyal, Y. Ding, Z. Wang, H. Zeng, and J. Liu, *Adv. Mater.* **18**, 2984 (2006).
- ⁴²M. Muller, P. Erhart, and K. Albe, *Phys. Rev. B* **76**, 155412 (2007).
- ⁴³Z. Dai, S. Sun, and Z. Wang, *Nano Lett.* **1**, 443 (2001).
- ⁴⁴T. Thomson, S. L. Lee, M. F. Toney, C. D. Dewhurst, F. Y. Ogrin, C. J. Oates, and S. Sun, *Phys. Rev. B* **72**, 064441 (2005).
- ⁴⁵B. Yao, R. V. Petrova, R. R. Vanfleet, and K. R. Coffey, *J. Appl. Phys.* **99**, 08E913 (2006).
- ⁴⁶H. Wang, Y. Huang, Y. Zhang, G. Hadjipanayis, D. Weller, and A. Simopoulos, *J. Magn. Magn. Mater.* **310**, 22 (2007).
- ⁴⁷As discussed further in this paper.
- ⁴⁸P. Melinon, V. Paillard, V. Dupuis, A. Perez, P. Jensen, A. Hoareau, M. Broyer, J. L. Vialle, M. Pellarin, B. Baguenard, and J. Lerme, *Int. J. Mod. Phys. B* **9**, 339 (1995).
- ⁴⁹A. Perez, P. Melinon, V. Dupuis, B. Prevel, L. Bardotti, J. Tuaille-Combes, B. Masenelli, M. Treilleux, M. Pellarin, J. Lerme, E. Cottancin, M. Broyer, M. Jamet, M. Negrier, F. Tournus, and M. Gaudry, *Mater. Trans.* **42**, 1460 (2001).
- ⁵⁰T. G. Dietz, M. A. Duncan, D. E. Powers, and R. E. Smalley, *J. Chem. Phys.* **74**, 6511 (1981).
- ⁵¹P. Milani and W. A. deHeer, *Rev. Sci. Instrum.* **61**, 1835 (1990).
- ⁵²A. Hannour, Ph.D. thesis, Université Lyon 1, 2006.
- ⁵³M. Jamet, W. Wernsdorfer, C. Thirion, D. Mailly, V. Dupuis, P. Mélinon, and A. Pérez, *Phys. Rev. Lett.* **86**, 4676 (2001).
- ⁵⁴P. Stadelmann, *Microsc. Microanal.* **9**, 60 (2003).
- ⁵⁵HRTEM multislice calculations are performed using a “sliced” CoPt cluster (slice thickness of 1.902 Å) on amorphous carbon (3 nm thick), with a supercell of a 9.95 nm side length. The electron scattering potential and the wave-function transmission are calculated with a 1024×1024 fast-Fourier-transform (maximum spatial frequency $\approx 10 \text{ \AA}^{-1}$) corresponding to a pixel size of $\approx 0.1 \text{ \AA}$ in the simulated image. For the high-resolution image formation, the microscope parameters are fixed to the value corresponding to the experimentally used electron microscope (JEOL 2010F).
- ⁵⁶Note that in Ref. 29 there are claims to having observed $L1_0$ CoPt particles by HRTEM, whereas no such contrast was visible on their images, etc.
- ⁵⁷To our knowledge, models only exist for the very similar FePt system (see Refs. 34–42).
- ⁵⁸W. Grange, I. Galanakis, M. Alouani, M. Maret, J.-P. Kappler, and A. Rogalev, *Phys. Rev. B* **62**, 1157 (2000).
- ⁵⁹B. T. Thole, P. Carra, F. Sette, and G. van der Laan, *Phys. Rev. Lett.* **68**, 1943 (1992).
- ⁶⁰P. Carra, B. T. Thole, M. Altarelli, and X. Wang, *Phys. Rev. Lett.* **70**, 694 (1993).
- ⁶¹J. Stöhr, *J. Electron Spectrosc. Relat. Phenom.* **75**, 253 (1995).
- ⁶²C. Ederer, M. Komelj, J. W. Davenport, and M. Fähnle, *J. Electron Spectrosc. Relat. Phenom.* **130**, 97 (2003).
- ⁶³C. Ederer, M. Komelj, M. Fähnle, and G. Schütz, *Phys. Rev. B* **66**, 094413 (2002).
- ⁶⁴M. Komelj, C. Ederer, J. W. Davenport, and M. Fähnle, *Phys. Rev. B* **66**, 140407(R) (2002).
- ⁶⁵C. Ederer, M. Komelj, and M. Fähnle, *Phys. Rev. B* **68**, 052402 (2003).
- ⁶⁶W. Grange, M. Maret, J.-P. Kappler, J. Vogel, A. Fontaine, F. Petroff, G. Krill, A. Rogalev, J. Goulon, M. Finazzi, and N. B. Brookes, *Phys. Rev. B* **58**, 6298 (1998).
- ⁶⁷P. Imperia, P. Andreatza, D. Schmitz, J. Penuelas, and C. Andreatza-Vignolle, *J. Magn. Magn. Mater.* **310**, 2417 (2007).
- ⁶⁸C. Antoniak, J. Lindner, M. Spasova, D. Sudfeld, M. Acet, M. Farle, K. Fauth, U. Wiedwald, H.-G. Boyen, P. Ziemann, F. Wilhelm, A. Rogalev, and S. Sun, *Phys. Rev. Lett.* **97**, 117201 (2006).
- ⁶⁹O. Dmitrieva, M. Spasova, C. Antoniak, M. Acet, G. Dumpich, J. Kastner, M. Farle, K. Fauth, U. Wiedwald, H.-G. Boyen, and P. Ziemann, *Phys. Rev. B* **76**, 064414 (2007).
- ⁷⁰N. Jaouen, D. Babonneau, J. M. Tonnerre, D. Carbone, F. Wilhelm, A. Rogalev, T. K. Johal, and G. van der Laan, *Phys. Rev. B* **76**, 104421 (2007).
- ⁷¹Considering only the XMCD results, one could think of a Co segregation at the clusters surface, which could result in a magnetic moment increase. However, this hypothesis is not compatible with the HRTEM observations: With a Co segregation, the $L1_0$ phase formation in the clusters core would not be possible (problem of composition).
- ⁷²Unfortunately, we are not aware of any experimental or theoretical determination of the evolution of the number of d holes per Co atom, when going from the chemically disordered to the chemically ordered phase of CoPt.
- ⁷³I. M. L. Billas, A. Chatelain, and W. A. de Heer, *J. Magn. Magn. Mater.* **168**, 64 (1997).
- ⁷⁴S. Rohart, F. Tournus, and V. Dupuis (unpublished).
- ⁷⁵P. Imperia, D. Schmitz, H. Maletta, N. S. Sobal, and M. Giersig, *Phys. Rev. B* **72**, 014448 (2005).
- ⁷⁶P. Bruno, *Phys. Rev. B* **39**, 865 (1989).
- ⁷⁷G. van der Laan, *J. Phys.: Condens. Matter* **10**, 3239 (1998).
- ⁷⁸For Pt, we use the value reported in Ref. 58.
- ⁷⁹E. C. Stoner and E. P. Wohlfarth, *Philos. Trans. R. Soc. London, Ser. A* **240**, 599 (1948).
- ⁸⁰J. L. Dormann, F. D’Orazio, F. Lucari, E. Tronc, P. Prené, J. P. Jolivet, D. Fiorani, R. Cherkaoui, and M. Noguès, *Phys. Rev. B* **53**, 14291 (1996).
- ⁸¹C. Petit, S. Rusponi, and H. Brune, *J. Appl. Phys.* **95**, 4251 (2004).
- ⁸²M. Jamet, W. Wernsdorfer, C. Thirion, V. Dupuis, P. Melinon, A. Perez, and D. Mailly, *Phys. Rev. B* **69**, 024401 (2004).
- ⁸³S. S. A. Razeq, J. B. Staunton, B. Ginatempo, E. Bruno, and F. J.

- Pinski, Phys. Rev. B **64**, 014411 (2001).
- ⁸⁴J. B. Staunton, S. Ostanin, S. S. A. Razee, B. Gyorffy, L. Szunyogh, B. Ginatempo, and E. Bruno, J. Phys.: Condens. Matter **16**, S5623 (2004).
- ⁸⁵J. B. Staunton, S. Ostanin, S. S. A. Razee, B. L. Gyorffy, L. Szunyogh, B. Ginatempo, and E. Bruno, Phys. Rev. Lett. **93**, 257204 (2004).
- ⁸⁶O. N. Mryasov, U. Nowak, K. Y. Guslienko, and R. W. Chantrell, Europhys. Lett. **69**, 805 (2005).
- ⁸⁷R. K. Rakshit and R. C. Budhani, J. Phys. D **39**, 1743 (2006).
- ⁸⁸R. W. Chantrell, N. Walmsley, J. Gore, and M. Maylin, Phys. Rev. B **63**, 024410 (2000).
- ⁸⁹J. M. Vargas, W. C. Nunes, L. M. Socolovsky, M. Knobel, and D. Zanchet, Phys. Rev. B **72**, 184428 (2005).
- ⁹⁰W. Figueiredo and W. Schwarzacher, J. Phys.: Condens. Matter **19**, 276203 (2007).
- ⁹¹O. A. Chubykalo and R. W. Chantrell, J. Magn. Magn. Mater. **272–276**, E1169 (2004).
- ⁹²We are currently working on a quantitative determination of the chemical order parameter of a single particle from HRTEM images.
- ⁹³The MAE is also higher than some values reported for other as-prepared CoPt particles (see Refs. 81 and 87).
- ⁹⁴It seriously complicates the MAE determination from ZFC curves fit. Unless the expected size dependence of the MAE is well established, the results will not gain in precision by just adding adjustable parameters. Therefore, we think it is wiser to keep using the simple $\Delta E = K_{\text{eff}}V$ model when it is successful. The best way to directly study the MAE size dependence would be to use samples made of size-selected particles: We are currently working in this direction.
- ⁹⁵Or some undetected impurities.

On peut noter que l'utilisation de la matrice de carbone constitue un choix tout à fait pertinent puisqu'elle n'entraîne pas de problème de miscibilité, qu'elle protège efficacement les particules de l'oxydation [Tournus2008a] (cf. Fig. 17 où l'on compare la matrice de MgO et celle de C), qu'elle empêche la coalescence lors du recuit [Tournus2011a], et qu'elle autorise des observations par microscopie électronique en transmission à haute résolution (METHR).

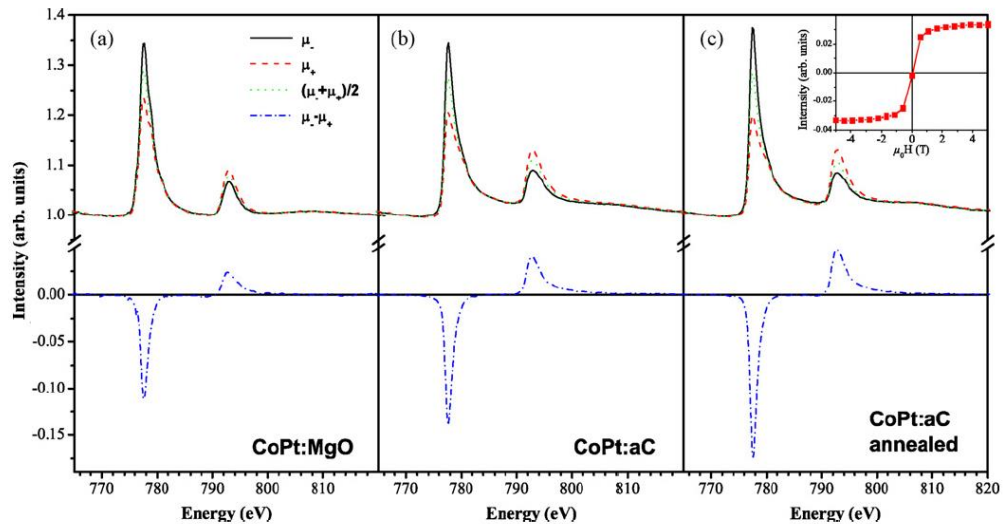


Fig. 17 : Spectres d'absorption X (selon chacune des polarisations circulaires, ainsi que spectre moyen) et signal dichroïque (XMCD) aux seuils $L_{2,3}$ du Co, pour des particules de Co (non triées) noyées dans une matrice de MgO et dans une matrice de carbone amorphe (aC) avant et après recuit. Les mesures ont été effectuées à 300 K. Figure tirée de [Tournus2008a].

En ce qui concerne la question de l'existence (ou pas) d'une taille limite pour la mise en ordre dans la phase $L1_0$, mais aussi de la quantification du paramètre d'ordre à longue distance (ce dernier peut varier continument de 0 à 1, d'une phase A1 complètement désordonnées à une phase $L1_0$ parfaitement ordonnée chimiquement), nous avons développé une méthode, basée sur l'analyse et la simulation d'images METHR, permettant de déterminer de manière quantitative le paramètre d'ordre chimique d'une nanoparticule individuelle de diamètre inférieur à 4 nm. L'article « **Measuring the $L1_0$ chemical order parameter of a single CoPt nanoparticle smaller than 4 nm** » [Blanc2011], reproduit ci-dessous, présente ce travail.

Measuring the $L1_0$ chemical order parameter of a single CoPt nanoparticle smaller than 4 nm

Nils Blanc, Florent Tournus,* and Véronique Dupuis

LPMCN, UMR 5586 CNRS and Université de Lyon, Université Lyon 1, F-69622 Villeurbanne, France

Thierry Epicier

MATEIS, UMR 5510 CNRS and INSA-Lyon, Université de Lyon, F-69621 Villeurbanne, France

(Received 2 December 2010; revised manuscript received 13 January 2011; published 16 March 2011)

We discuss the possibility of $L1_0$ chemical order parameter quantification for an individual particle of CoPt, using transmission electron microscopy. While “usual” approaches are found to be unapplicable for small particles (less than 4 nm in diameter), we present a method based on the comparison between an experimental high-resolution image and simulated ones with various degrees of chemical order.

DOI: 10.1103/PhysRevB.83.092403

PACS number(s): 75.50.Cc, 61.46.Df, 68.37.Og, 61.66.Dk

The chemical order phase transition in alloy nanoparticles such as CoPt or FePt has recently motivated a lot of experimental and theoretical studies.^{1–11} In addition to its fundamental aspects, a good knowledge of this transition is relevant for the study of magnetic properties: in particular, the magnetic anisotropy is intimately related to the degree of chemical order,¹² and the extremely high magnetocrystalline anisotropy of the bulk $L1_0$ phase originates from the stacking of pure Co (or Fe) and Pt atomic planes in the [001] direction.¹³ Even if this ordered phase is thermodynamically stable at room temperature, nanoparticles are generally synthesized in the face-centered-cubic (fcc) chemically disordered phase $A1$, which is metastable. Annealing is then required to promote atomic diffusion and reach a chemically ordered state; however, without exceeding the $L1_0 \rightarrow A1$ transition temperature. This temperature is very high for the bulk but must be significantly decreased by size reduction effects: this opens up a question on the existence of a lower size limit for $L1_0$ ordering in nanoparticles.^{3,5,14} Moreover, the finite size is also expected to change the type of transition^{5,8–10,14} from a first-order one, with a discontinuity in the long-range chemical order parameter S , to a second-order one, with a smooth transition from $S = 1$ for the perfectly ordered $L1_0$ phase at low temperatures to $S = 0$ for the completely disordered $A1$ phase at high temperatures. In this case, any value of S (i.e., any degree of chemical order) may exist for nanoparticles: we cannot consider that a particle will simply be either “ordered” or “disordered.” A quantitative determination of S for individual nanoparticles will provide deeper insight on the chemical order transition and is thus highly suitable. Having an applicable method for that purpose will allow us to get rid of the averaging effects and the unavoidable inhomogeneous broadening met in the study of entire assemblies of size-distributed particles. In addition, the usual approach for the experimental determination of S , namely, the use of x-ray diffraction, becomes at the same time much more difficult to apply and much less reliable, or even unapplicable when very small particles are considered.

In this Brief Report, we show how high-resolution transmission electron microscopy (HRTEM) may be the most reliable or even the only method offering the possibility of an S quantification for a small (with a diameter less than 4 nm) single CoPt particle. We have studied CoPt nanoparticles synthesized by the low-energy cluster-beam deposition technique

described elsewhere,^{11,15} where CoPt nanoparticles with an $\simeq 3$ nm diameter are produced by laser vaporization and deposited on a substrate (here the thin amorphous carbon film of a commercial TEM grid), under ultrahigh vacuum conditions. Since the as-prepared particles are crystallized in the $A1$ phase, a 2 h 750 K annealing is used to promote chemical ordering.¹¹

There have been a few reports of the chemical order parameter measurement for individual nanoparticles,^{2,16,17} but not for CoPt, always using electron diffraction: the idea was to correlate the intensity of a chemical order (or super-structure) peak, like [001], to the value of S . With a few small particles on a substrate, diffraction with a parallel incident beam is not possible and nanodiffraction or convergent beam electron diffraction is needed. Within such experimental conditions, particles are exposed to a very high fluence, which questions their stability both in orientation and in structure/composition. We have indeed noticed that (see Ref. 18), on one hand, the orientation of a particle observed in nanodiffraction changes on a 100 ms time scale, and on the other hand, with a nanoprobe, the chemical composition of a cluster varies within a few seconds (because of a Co evaporation, the Co/Pt ratio goes from 1 to $\simeq 0.5$ in 40 s). The use of scanning transmission electron microscopy with a high-angle annular dark field (STEM-HAADF) detection may represent the most simple approach in terms of image interpretation: with a Z contrast image, the intensity of an atomic column is almost directly related to its chemical content. However, a narrow probe is needed to reach the atomic contrast, and even if we have succeeded in observing an $L1_0$ contrast on our small CoPt particles, we have observed a very rapid degradation of particles exposed to the electron beam (see Ref. 18).

We have then chosen to use HRTEM because it allows observations without intense illumination, thus preserving the particles' integrity. Even if the observation of so small particles is highly challenging, CoPt clusters are found to be stable (good imaging conditions) for a few seconds. HRTEM dynamical simulations with the multislice method (JEMS software,¹⁹ computational details are given in Ref. 18) have been used to successfully reproduce the observed chemical order contrast: such a contrast is, of course, only visible for correctly oriented particles, but even in such a case, it may not be detected if the objective lens defocus is not in some particular ranges (see Ref. 18). It has also been verified that a contrast with a periodicity corresponding to a [001] spatial frequency (peak in the diffractogram) is the signature

of chemical order and cannot be an artifact appearing in images of chemically disordered particles. Images simulated with perfectly ordered clusters are found to be in good visual agreement with the experimental ones, but we would like to go further.

A first semiquantitative method is illustrated in Fig. 1, where we compare an experimental image to simulations with various chemical order parameters. This allows a visual comparison and provides a range of acceptable S values (here, from 0.7 to 1). Let us remind the reader that to describe the $L1_0$ order, the original fcc lattice is split into two sublattices labeled α and β corresponding to alternating planes in the (001) direction. The long-range order chemical parameter is then defined as $S = (n_\alpha - x)/(1 - f_\alpha)$, where n_α is the probability to have a Co atom on an α site, x the Co concentration, and f_α the fraction of α sites. This definition ensures that $S = 0$ when the atoms are randomly distributed and $S = 1$ for a perfect order (which is only achievable when $x = f_\alpha$). Since S is a global quantity, many different configurations of a cluster correspond to a same value and hence, there is, in fact, no unique HRTEM image corresponding to a given degree of chemical order. From a simulation point of view, we can

randomly generate a single or several chemical configurations by setting the probability to have a Co atom on an α site to $p_\alpha = (S_0 + 1)/2$: this will result in a statistical set of particles²⁰ with $S \simeq S_0$ and $x \simeq 1/2$. This approach has been used for the simulations shown in Fig. 1, where a single configuration has been considered for each S . We can also construct an “average” cluster where each site is occupied at the same time by fractional Co and Pt atoms, with a probability of p_α and $1 - p_\alpha$, respectively (and the symmetrical occupations on β site). This average configuration, where the chemical disorder is homogeneously spread in a particle, should provide a mean image correctly reflecting the one that would be obtained by averaging several randomly generated configurations.

To go further, we need a numerical criterion to find which the S value corresponds to the best agreement between HRTEM observation and simulation. As the degree of chemical order is directly related to the intensity of the sur-structure [001] peak, we have chosen to consider the intensity ratio $R = I_{001}/I_{200}$ (we use [200] as a structure peak since in the experimental image the [002] peak is cut by a dark ring of the microscope contrast transfer function). Note that the intensities are not those of electron diffraction, but those of the corresponding spatial frequency on the HRTEM image: they are obtained from its fast Fourier transform (FFT), which we will call in the following its “diffractogram.” Our method is thus based on the use of HRTEM images, but through an analysis in the reciprocal (Fourier) space. Preliminary steps

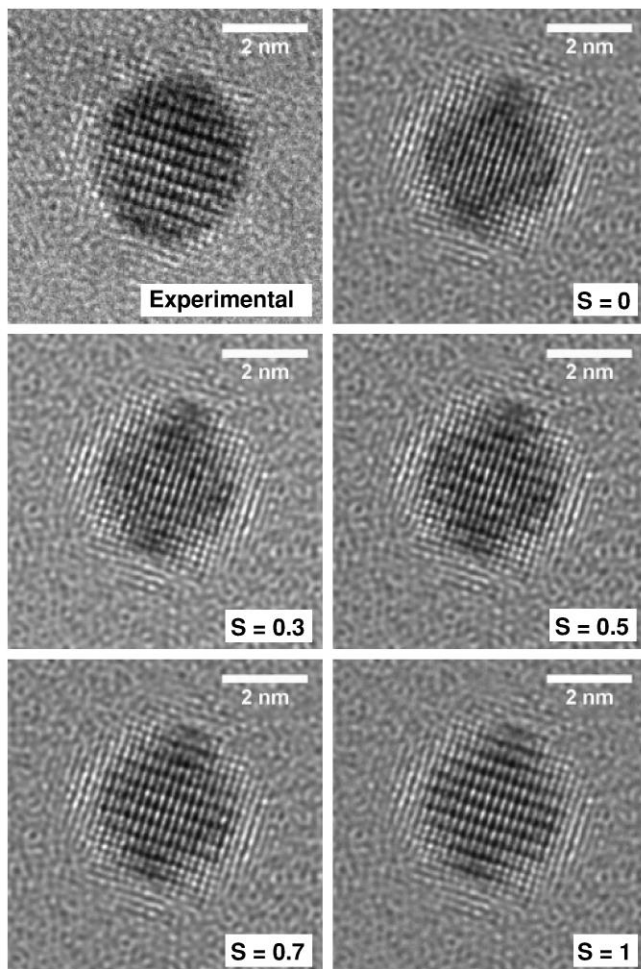


FIG. 1. Comparison between the experimental HRTEM image of a CoPt cluster and simulated images with various values of the chemical order parameter S .

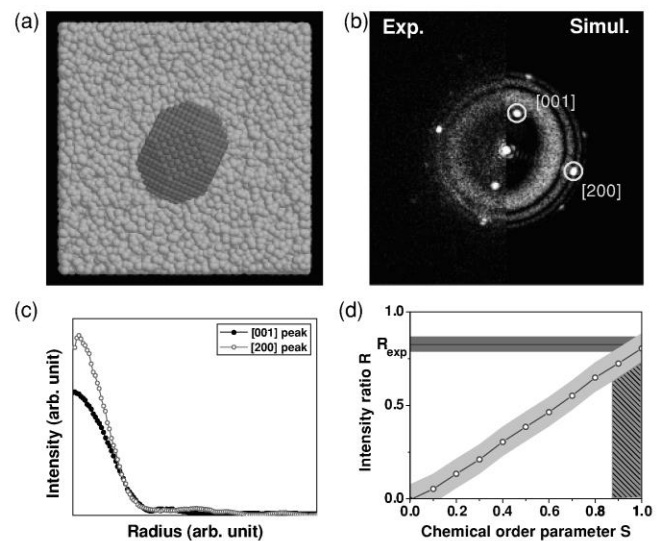


FIG. 2. (Color online) a) Schematic view of the structure used for HRTEM simulations: the truncated octahedral CoPt cluster (here, with a perfect $L1_0$ order) lies on an amorphous carbon film. b) Montage showing the FFT of the experimental HRTEM image (left side) and of a simulated one, with $S = 1$ (right side). The peaks used for the determination of R are indicated. c) Peak profiles determined from the FFT of a simulated HRTEM image (here with $S = 1$): the ratio $R = I_{001}/I_{200}$ is calculated from the integrated intensities. d) Theoretical $R(S)$ curve computed for various degrees of chemical order. The experimental value R_{exp} is indicated and provides an interval of S values (hatched area) which are compatible with the HRTEM observations. The shaded areas correspond to the uncertainties.

are necessary in order to establish a reliable theoretical curve of R as a function of S , which will then be compared to the experimental ratio R_{exp} . These steps are the following: (1) determination of the zone axis from the experimental image; (2) determination of the particle shape (truncated octahedron with additional facets); (3) determination of the microscope parameters (defocus and astigmatism); (4) determination of the lattice tetragonalization; and (5) determination of the tilt angle, with respect to the perfect zone axis orientation. These adjustments are made empirically or with the help of a computer analysis (step 3, for instance), in the direct (steps 2 and 5) or Fourier space (steps 1, 3, and 4). We then compute the value of R from the diffractogram of HRTEM images simulated with different S parameters (see Fig. 2). We use here the “average” configuration approach described above. The peak intensities are determined by the integration of their radial profile [see Fig. 2(c) that displays the one-dimensional profile obtained by the rotational average of the pixel intensities around the peak center position], after a background subtraction.²¹ We find a theoretical $R(S)$ curve which is almost a perfect line.

Of course, we have to put error bars on this line, first because of the statistical spread due to the multiplicity of configurations having the same order parameter S . Interestingly, we have verified with “statistical” calculations on a bulk supercell ($8 \times 8 \times 8$, corresponding to an $\simeq 3.1$ nm thickness) that the mean R value coincides with the value obtained with the average method: this was not trivial, since R is not at all linked in a linear way to the electron-scattering atomic potentials. The standard deviation of R is evaluated to be around 0.04 and is decreasing for high degrees of chemical order (since the number of different arrangements is reducing). In addition, there is a small uncertainty on the precise tilt angle ($\pm 1^\circ$) and defocus value (± 2 nm): we have verified that it has only a

very limited impact on the value of R (see Ref. 18). In the end, we can estimate the uncertainty around the theoretical curve to be $\simeq 0.08$ (upper bound). We also consider a 5% relative uncertainty on the experimental value R_{exp} to account for the various signal processing errors. Finally, as illustrated in Fig. 2, we find that the particle under investigation is almost perfectly ordered: with a confidence interval, we can conclude that $S \in [0.85, 1]$.

The quantification method we propose has been successfully applied to a particle displaying a strong $L1_0$ contrast (and consequently, a large S). Note, however, that for particles with a less pronounced contrast, a certain ambiguity may remain: for instance, a tilted particle with a large S can correspond to the same R as a poorly ordered particle with an “ideal” orientation. To resolve possible ambiguities, a solution might be to use more peak intensities or, if possible, different images of the same particle at different defocus values. Finally, we should also keep in mind that by using a single parameter S to describe the chemical order of a particle, we somehow assume that it is homogeneous: according to theoretical studies, this is not granted as a surface disorder or segregation can exist in such nanosystems.^{8,9,22,23} For the particle we have studied, there was no sign of such effects (which should, in addition, decrease the R value), but they may be extremely subtle and hard to detect using HRTEM.

In conclusion, we have presented and applied a method of $L1_0$ chemical order parameter quantification using HRTEM, which is adapted to the investigation of small individual CoPt and FePt particles, where the “usual” approaches are no more applicable.

The authors gratefully acknowledge O. Boisson, the PLYRA, and the CLYM.

*florent.tournus@univ-lyon1.fr

¹Y. K. Takahashi, T. Koyama, M. Ohnuma, T. Ohkubo, and K. Hono, *J. Appl. Phys.* **95**, 2690 (2004).

²T. Miyazaki, O. Kitakami, S. Okamoto, Y. Shimada, Z. Akase, Y. Murakami, D. Shindo, Y. K. Takahashi, and K. Hono, *Phys. Rev. B* **72**, 144419 (2005).

³S. Fukami and N. Tanaka, *Philos. Mag. Lett.* **84**, 33 (2004).

⁴O. Dmitrieva, B. Rellinghaus, J. Kastner, and G. Dumpich, *J. Cryst. Growth* **303**, 645 (2007).

⁵D. Alloyeau, C. Ricolleau, C. Mottet, T. Oikawa, C. Langlois, Y. Le Bouar, N. Braidy, and A. Loiseau, *Nat. Mater.* **8**, 940 (2009).

⁶R. V. Chepulkii and W. H. Butler, *Phys. Rev. B* **72**, 134205 (2005).

⁷C.-B. Rong, D. Li, V. Nandwana, N. Poudyal, Y. Ding, Z. Wang, H. Zeng, and J. Liu, *Adv. Mater.* **18**, 2984 (2006).

⁸B. Yang, M. Asta, O. N. Mryasov, T. J. Klemmer, and R. W. Chantrell, *Acta Mater.* **54**, 4201 (2006).

⁹M. Müller, P. Erhart, and K. Albe, *Phys. Rev. B* **76**, 155412 (2007).

¹⁰G. Rossi, R. Ferrando, and C. Mottet, *Faraday Discuss.* **138**, 193 (2008).

¹¹F. Tournus, A. Tamion, N. Blanc, A. Hannour, L. Bardotti, B. Prével, P. Ohresser, E. Bonet, T. Epicier, and V. Dupuis, *Phys. Rev. B* **77**, 144411 (2008).

¹²J. B. Staunton, S. Ostanin, S. S. A. Razee, B. Gyroffly, L. Szunyogh, B. Ginatempo, and E. Bruno, *J. Phys.: Condens. Matter* **16**, S5623 (2004).

¹³S. S. A. Razee, J. B. Staunton, B. Ginatempo, F. J. Pinski, and E. Bruno, *Phys. Rev. Lett.* **82**, 5369 (1999).

¹⁴K. Sato, *Nat. Mater.* **8**, 924 (2009).

¹⁵A. Perez *et al.*, *Int. J. Nanotechnol.* **7**, 523 (2010).

¹⁶R. V. Petrova, R. R. Vanfleet, D. Richardson, B. Yao, and K. R. Coffey, *IEEE Trans. Magn.* **41**, 3202 (2005).

¹⁷K. Sato, Y. Hirotsu, H. Mori, Z. Wang, and T. Hirayama, *J. Appl. Phys.* **98**, 024308 (2005).

¹⁸See supplemental material at <http://link.aps.org/supplemental/10.1103/PhysRevB.83.092403> for nanodiffraction, energy dispersive x-ray spectroscopy, and STEM-HAADF on CoPt nanoparticles; $L1_0$ chemical order contrast in simulated HRTEM images; and computational details on HRTEM image simulations and information on the influence of the tilt angle.

¹⁹P. Stadelmann, *Microsc. Microanal.* **9**, 60 (2003).

²⁰ S is the actual chemical order parameter of a particle, while S_0 is the target value used for random generation of a chemical configuration.

²¹The background intensity is removed by subtraction of a rotated diffractogram: the entire FFT is rotated around its center by a few degrees (typically 20°); the rotated image is then subtracted from the original image. The effect is to remove the

amorphous carbon contribution at the peak positions we are interested in.

²²M. E. Gruner, G. Rollmann, P. Entel, and M. Farle, *Phys. Rev. Lett.* **100**, 087203 (2008).

²³R. V. Chepulskaa, W. H. Butler, A. van de Walle, and S. Curtarolo, *Scr. Mater.* **62**, 179 (2010).

Après avoir étudié des assemblées de particules non triées en taille, nous avons mené le même type d'investigation sur des assemblées de CoPt présentant une distribution de taille bien plus fine (dispersion relative de diamètre réduite d'environ un facteur 6, cf. Fig. 18), grâce au générateur d'agrégats équipé d'un déviateur quadrupolaire électrostatique agissant comme un sélecteur de masse. La meilleure résolution en taille a permis de mettre en évidence un effet de dispersion de la constante d'anisotropie magnétique dans ces particules d'alliage [Tournus2010] (cf. Fig. 19), attendu d'après la théorie [Tournus2008b]. En effet, le pic de la courbe ZFC s'est révélé être sensiblement plus large que ce que donnerait le modèle habituel où la distribution d'énergie d'anisotropie est directement liée à la distribution de taille, via la relation $K = K_{\text{eff}}V$ avec une unique constante d'anisotropie pour l'ensemble des nanoparticules.

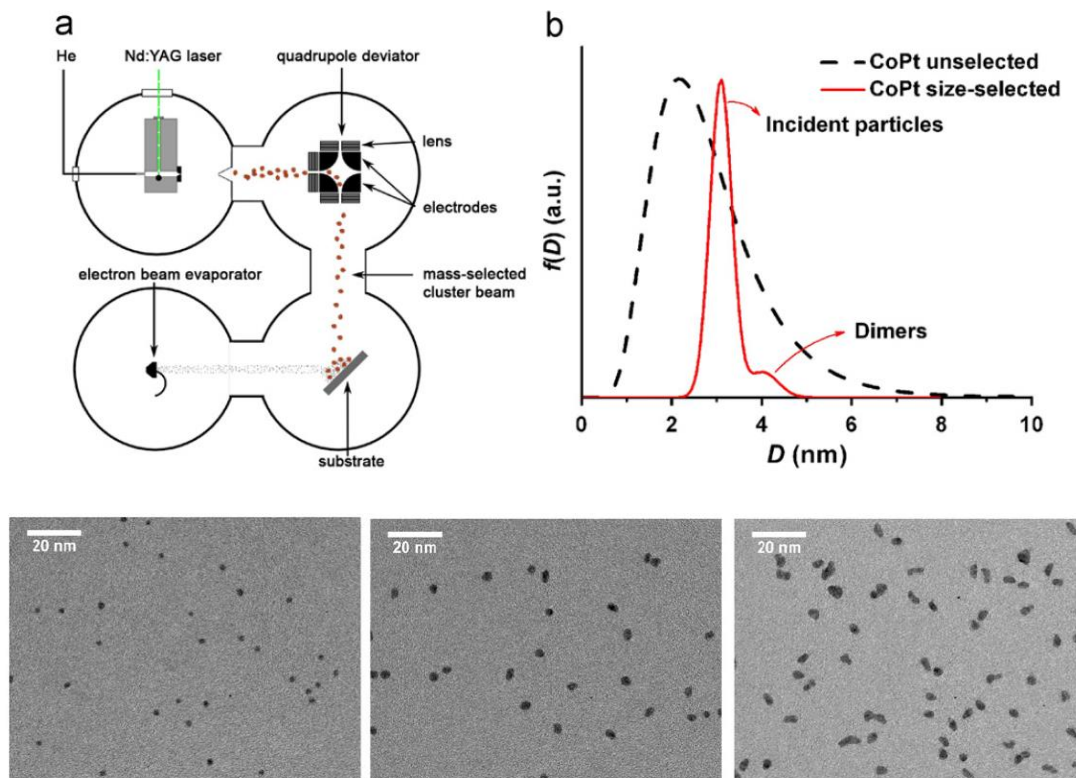


Fig. 18 : En haut, a) schéma de la source d'agrégat du PLYRA équipée d'un déviateur quadrupolaire électrostatique agissant comme un tri en masse (et donc en taille), b) comparaison entre la distribution de taille, déduite d'observations MET, d'agrégats de CoPt produits avec (trait plein) et sans (trait en pointillés) le dispositif de tri en masse. En bas, images MET illustrant la possibilité d'ajuster la taille des particules de CoPt déposées : de gauche à droite, la tension de déviation vaut respectivement 100 V, 300 V, et 500 V, ce qui correspond à un diamètre de 2,0 nm, 3,1 nm et 3,8 nm. Figure tirée de [Tournus2011f].

Les propriétés magnétiques et la structure de particules de différentes tailles (diamètre compris entre 2 nm et 4 nm environ) ont également été étudiées [Dupuis2011, Tournus2011a, Tournus2011f, Dupuis2013, Dupuis2013a, Dupuis2015], en mettant à profit l'ensemble des techniques de mesures et les modélisations correspondantes (ZFC/FC, cycles d'hystérésis, courbes IRM...). Un exemple d'ajustement global est montré Fig. 20, ainsi que des mesures IRM/DCD (cf. Fig. 21) illustrant l'absence d'interactions détectables dans les échantillons considérés (le paramètre δm vaut zéro, comme attendu dans le cas de nano-aimants sans interactions, ce qui permet de relier directement la réponse magnétique globale aux réponses intrinsèques des particules individuelles). On trouve à nouveau que l'anisotropie augmente beaucoup moins que pour le massif.

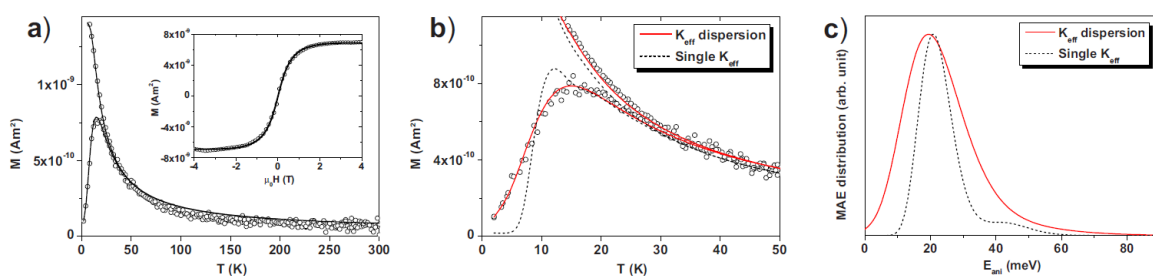


Fig. 19 : a) Ajustement (courbes en trait plein) des mesures magnétiques (ZFC/FC et $m(H)$ à 300 K) expérimentales (points) ; b) comparaison entre des courbes ZFC/FC simulées avec et sans dispersion de constante d'anisotropie K_{eff} ; c) Comparaison entre les distributions d'énergie d'anisotropie avec et sans dispersion de K_{eff} . Figure tirée de [Tournus2010].

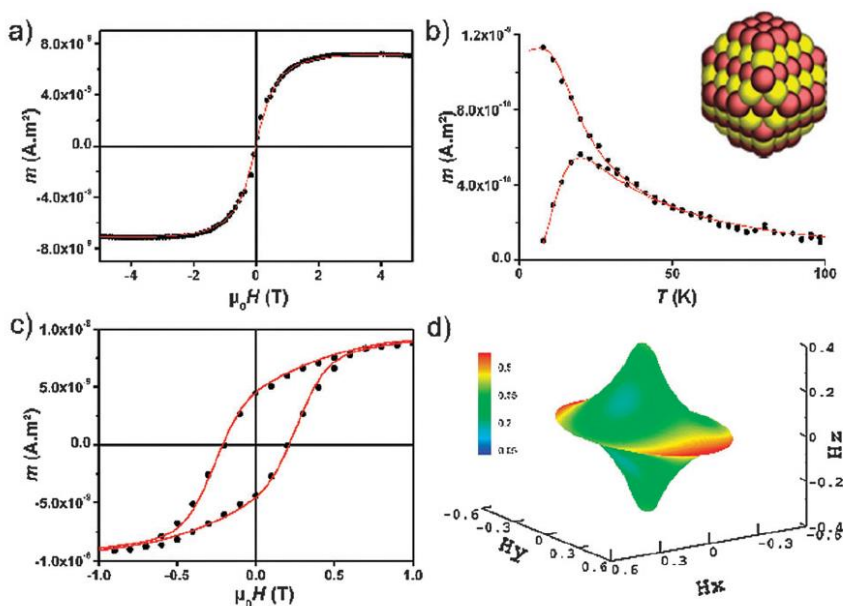
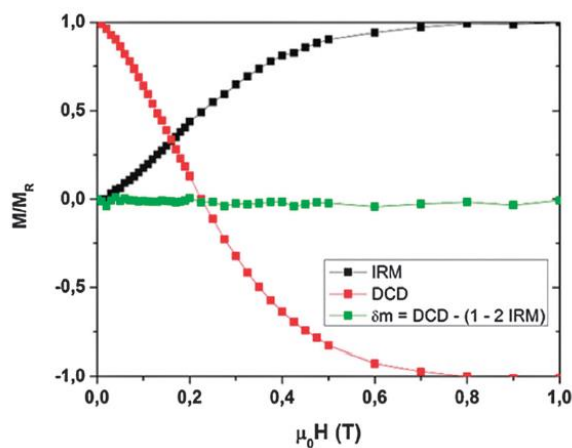


Fig. 20 : Ajustements (courbes en trait plein) des mesures magnétiques expérimentales (points) pour des particules de CoPt d'environ 3,1 nm de diamètre, triées en taille, diluées dans une matrice de carbone amorphe et recuites. a) cycle $m(H)$ à 300 K, b) courbes ZFC/FC, c) cycle $m(H)$ à 2 K, d) asteroïde correspondant au cas moyen, mettant en évidence la contribution bi-axiale à l'anisotropie magnétique. Figure tirée de [Dupuis2015].

Fig. 21 : Courbes IRM/DCD et paramètre δm mesurés à 2 K pour des nanoparticules de CoPt noyées dans une matrice de carbone amorphe et recuites. Le fait que δm reste égal à zéro reflète l'aspect négligeable des interactions magnétiques entre particules. Figure tirée de [Dupuis2015].



En plus de confirmer la mise en ordre chimique des particules, détectée par un changement d'environnement local, des mesures d'EXAFS ont montré que la réduction de taille avait un impact sur les paramètres cristallographiques (rapport c/a apparent) via des effets de relaxation de surface [Blanc2013]. Le rapport de tétragonalisation c/a , déduit des distances Co-Co et Co-Pt (mesures au seuil K du Co), possède une valeur tout à fait inhabituelle, supérieure à 1 ce qui contraste avec le cas du matériau massif (cf. Fig. 22). À l'opposé, le rapport c/a effectif déduit des distances Pt-Co et Pt-Pt vaut 0,92 pour ces mêmes nanoparticules [Dupuis2013a]. Ceci reflète en réalité l'existence de distorsions structurales importantes dans les agrégats (effets de taille finie) qui entraînent une forte disparité entre les distances Co-Co et Pt-Pt (habituellement identiques dans la phase $L1_0$ massive !). Ces résultats expérimentaux sont par ailleurs en accord avec les structures obtenues par simulations ab-initio (DFT) [Blanc2013, Dupuis2013, Dupuis2013a]. Les distances Co-Co se trouvent en effet sensiblement diminuées (avec une large dispersion de valeurs) dans le cas d'une nanoparticule chimiquement ordonnée (cf. Fig. 23).

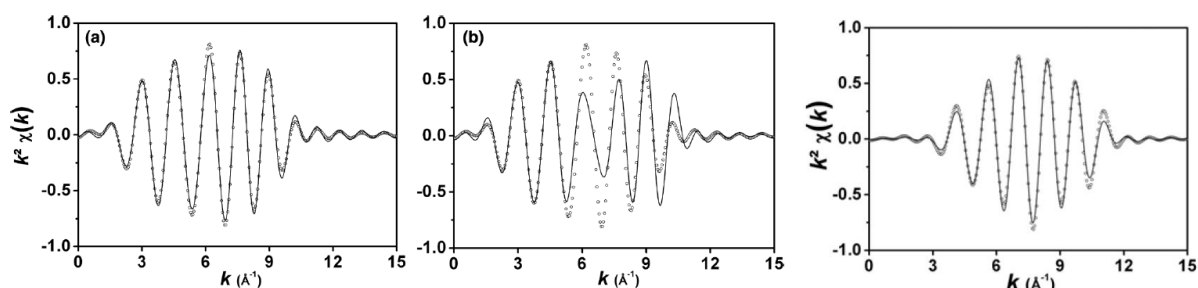


Fig. 22 : Comparaison entre le signal EXAFS expérimental (points, contribution du pic de premiers-voisins uniquement) et les ajustements théoriques (traits pleins), d'une part au seuil K du Co avec un rapport de tétragonalisation $c/a = 1,03$ (à gauche) et $c/a = 0,94$ (au milieu, ce qui correspond à la valeur dans le cas du massif), et d'autre part au seuil K du Pt avec un rapport $c/a = 0,92$. L'échantillon est constitué de nanoparticules de CoPt triées en taille (3.1 nm de diamètre) et recuites. Figure adaptée de [Blanc2013] et [Dupuis2013a].

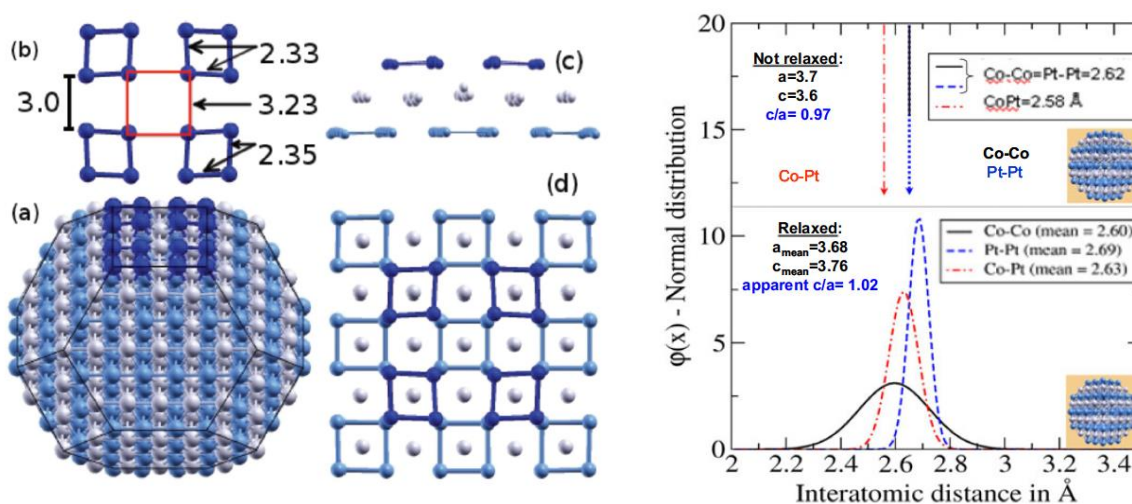


Fig. 23 : À gauche, illustration de la structure relaxée d'une particule de CoPt de 586 atomes (calculs DFT) où l'on observe une forte contraction des distances Co-Co (atomes en bleu), surtout au niveau de la surface. À droite, distribution des distances 1^{er} voisin Co-Co, Co-Pt et Pt-Pt pour un agrégat de CoPt de 201 atomes chimiquement ordonné avant (en haut) et après relaxation (en bas). Figure adaptée de [Blanc2013] et [Dupuis2013a].

Enfin, des études de METHR ont mis en évidence la coexistence (pour des tailles d'environ 3 nm) de particules cristallines et multi-maillées (décaèdres et icosaèdres), ainsi que l'existence de particules présentant plusieurs domaines $L1_0$ dans cette gamme de taille. Ceci peut contribuer (en plus d'effets de relaxation et d'effets électroniques dus à la réduction de taille) à la diminution de l'anisotropie magnétique par rapport à la phase massive. La publication « **Multi- $L1_0$ Domain CoPt and FePt Nanoparticles Revealed by Electron Microscopy** » [Tournus2013b], reproduite ci-dessous, présente ces résultats portant à la fois sur les particules de CoPt et de FePt qui est un système très similaire avec les mêmes problématiques (cf. ci-dessous). Ces observations de METHR démontrent que même des très petites particules peuvent cristalliser dans la phase $L1_0$, et confirment par ailleurs l'existence de décaèdres chimiquement ordonnés, structure « exotique » avec une symétrie d'ordre 5 (peu favorable à une forte anisotropie magnétique !) qui avait été théoriquement prédite.

Multi- $L1_0$ Domain CoPt and FePt Nanoparticles Revealed by Electron Microscopy

F. Tournus,^{1,*} K. Sato,² T. Epicier,³ T.J. Konno,² and V. Dupuis¹

¹*Institut Lumière Matière, UMR5306 Université Lyon 1-CNRS, Université de Lyon, 69622 Villeurbanne cedex, France*

²*Institute for Materials Research, Tohoku University, Sendai 980-8577, Japan*

³*MATEIS, UMR 5510 CNRS and INSA-Lyon, Université de Lyon, F-69621 Villeurbanne, France*

(Received 25 September 2012; published 28 January 2013)

The atomic structure of CoPt and FePt nanoparticles (with a diameter between 2 and 5 nm) has been studied by transmission electron microscopy. The particles have been produced by a laser vaporization cluster source and annealed under vacuum in order to promote chemical ordering. For both alloys, we observe a coexistence of crystalline and multiply twinned particles with decahedral or icosahedral shapes. In addition to particles corresponding to a single $L1_0$ ordered domain, we put into evidence that even small particles can display several $L1_0$ domains. In particular, the chemical order can be preserved across twin boundaries which can give rise to spectacular chemically ordered decahedral particles made of five $L1_0$ domains. The stability of such structures, which had been recently predicted from theoretical simulations, is thus unambiguously experimentally confirmed.

DOI: 10.1103/PhysRevLett.110.055501

PACS numbers: 61.46.Df, 61.66.Dk, 68.37.Og, 75.50.Bb

Although it has recently attracted considerable attention, the structure of bimetallic magnetic nanoparticles such as CoPt or FePt is still debated [1–28]. These nanoalloys are promising for applications, in particular due to the extremely high magnetocrystalline anisotropy (MCA) of the bulk face-centered tetragonal [29] (fct) $L1_0$ phase [30–33] where pure atomic Co (or Fe) and Pt planes are stacked along the [001] direction. At small sizes, these systems appear to be much more complex than single element metallic particles: in addition to the usual existence of peculiar symmetries (icosahedral and decahedral) when the size is reduced [34,35], the various possibilities of chemical ordering offer another degree of freedom. Despite this increased complexity, several theoretical investigations have tackled this question, predicting for nanoparticles smaller than 3 nm the stability (or metastability) of exotic structures displaying at the same time a fivefold symmetry and a chemical order [13–15,23,25]. However, even if the different types of cluster shapes has been experimentally observed [2,6,9,16,25,27,36,37], clear evidence of few nanometers chemically-ordered particles retaining a fivefold symmetry is still missing. Moreover, the question of a preferential surface segregation of one element [13–16,24,38], as well as the possible existence of a threshold particle size for chemical ordering [12,17,22,28,39–42] are still unclear, with sometimes conflicting reported results. Besides, while planar defects (twins and c -domain boundaries) are quite well known [43–45] both in the bulk phase and thin films, their possible occurrence in small CoPt and FePt nanoparticles had not been discussed until very recent observations in FePt particles [28]. An implicit assumption regarding $L1_0$ particles is that they should consist of a single $L1_0$ domain. If it is not the case, the magnetic properties, especially the MCA, should be strongly modified.

In this Letter, we discuss the atomic structure of CoPt and FePt nanoparticles (with a diameter between 2 and 5 nm). For both alloys, we show using transmission electron microscopy (TEM) that crystalline nanocrystals coexist with multiply twinned particles (MTPs) having decahedral or icosahedral symmetries. In addition to particles corresponding to a single $L1_0$ ordered domain, which are met down to a diameter of $D < 2.5$ nm, we put into evidence that even small nanoparticles can display several $L1_0$ domains. In particular, we show that the chemical order can be preserved across twin boundaries which can give rise to spectacular chemically ordered decahedral particles made of five $L1_0$ domains, as theoretically predicted.

CoPt and FePt clusters are synthesized by the mass-selected low-energy cluster-beam deposition technique described elsewhere [46–49]. The nanoparticles are produced by laser vaporization and subsequently size selected using a quadrupolar electrostatic deviator allowing us to adjust the diameter of the deposited clusters (typically between 2 and 5 nm). The particles are then deposited on a substrate (here the thin amorphous carbon film of a commercial TEM grid), under ultrahigh vacuum conditions and capped by amorphous carbon. Since the as-prepared particles are crystallized in the A1 phase, a 2 h annealing at 750 K is used to promote chemical ordering through an enhanced atomic diffusion [17,27]. The samples are then characterized by TEM either in a high resolution mode (HRTEM) or with a high angle annular dark field detector in a scanning TEM mode (STEM-HAADF). In addition to a JEOL 2010F microscope (operating at 200 kV and with a field emission gun), we have used a FEI Titan 80–300 microscope operating at 300 kV with a field emission gun and either a C_s corrector for the objective lens (for HRTEM images with highly

improved spatial resolution [50]) or an aberration corrected probe (for atomic resolution STEM-HAADF images).

As illustrated in Fig. 1, the three types of particle structure (fcc crystal [51], decahedron, icosahedron) can be observed, both for CoPt and FePt [52]. Let us remind the reader that a decahedral cluster is a particular type of MTP made of five fcc domains joined by (111) twins and slightly deformed (it is then a noncrystalline structure). The particle surface consists of both (111) and (100) facets. On the other hand, an icosahedral cluster is made of 20 fcc domains, also joined by (111) twins and stressed, but only displays dense (111) facets. The stability of MTPs at small sizes, instead of truncated octahedral crystalline structures (corresponding to Wulff's equilibrium shape), is due to the gain in surface energy which is then larger than the cost of twins and internal strain. Among the CoPt and FePt particles studied here, we also observe fcc particles with one or a few twins. The relative abundance of each type of structure can hardly be determined in a reliable way, because in many cases the observed HRTEM contrast does not allow us to infer the particle geometry in a straightforward way [53]. Nevertheless, as a general trend, we find

that the proportion of icosahedra is larger for CoPt particles than for FePt particles, which appears to often form decahedra. This must be related to a more favorable twinning in the case of CoPt [14,15,23]. The coexistence of a variety of structures is the result of kinetic trapping phenomena, which favor the formation of MTPs, during the sample preparation (annealing and subsequent cooling down [54] to room temperature). These experimental observations indicate that, in this size range, the energy differences between the different types of clusters are smaller or of the order of the thermal energy. This feature is consistent both with previous experimental studies [2,6,9,16,25], although the present particles are smaller, and with theoretical investigations [13–15,23,25].

Because we are dealing with bimetallic particles, the type of symmetry is not enough to characterize their structure and the question of the chemical order needs to be addressed [52]. Interestingly, both for FePt and CoPt, we observe crystalline particles with a single chemically ordered $L1_0$ domain all along the nanoparticle (see Fig. 2), down to $D = 2.3$ nm (the smallest diameter considered here). Contrary to what is sometimes reported [33,39,41,45] and in agreement with Delalande *et al.* [28], $L1_0$ particles smaller than 3 or 4 nm can exist. In the present case we do not observe any threshold size. Moreover, there is no indication of a preferential surface segregation of one element, contrary to what is often predicted by numerical calculations (especially for CoPt [14,15,55]). A full surface

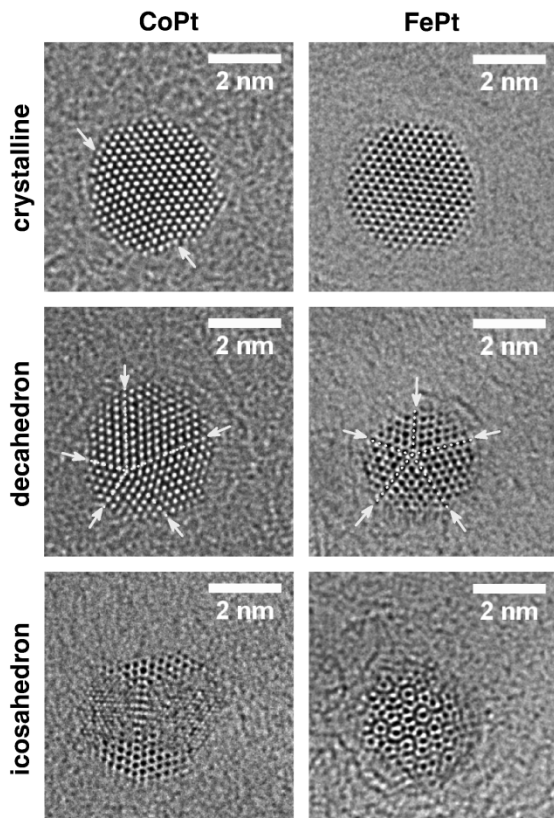


FIG. 1 (color online). C_s -corrected HRTEM images of CoPt (left) and FePt (right) nanoparticles. The three different types of structure are observed. The arrows indicate (111) twins, which are also highlighted by dotted lines in the case of decahedral particles, in order to emphasize the fivefold symmetry.

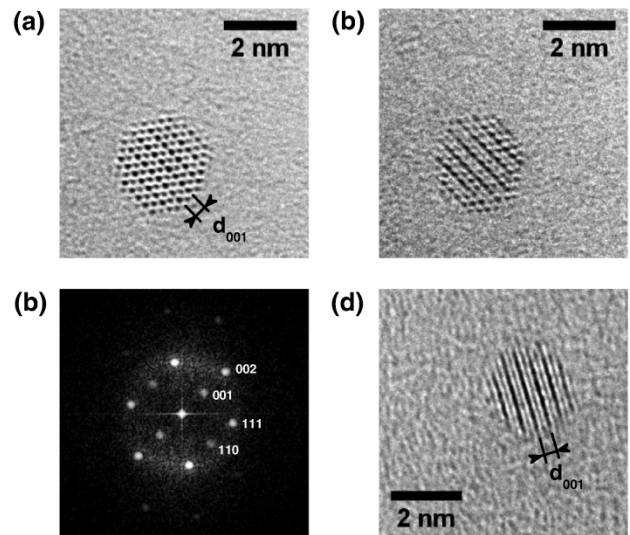


FIG. 2 (color online). C_s -corrected HRTEM images of a FePt cluster [(a) and (b)], corresponding to two different defocus values) and of a CoPt cluster (d). (c) Fast Fourier transform corresponding to image (a), with clear [001] and [110] peaks which are the signature of $L1_0$ order. In (a), the chemical order is evident from the difference in brightness and apparent size between two successive planes of atoms along the [001] direction, which is related to the difference in the scattering factors of Fe and Pt atoms.

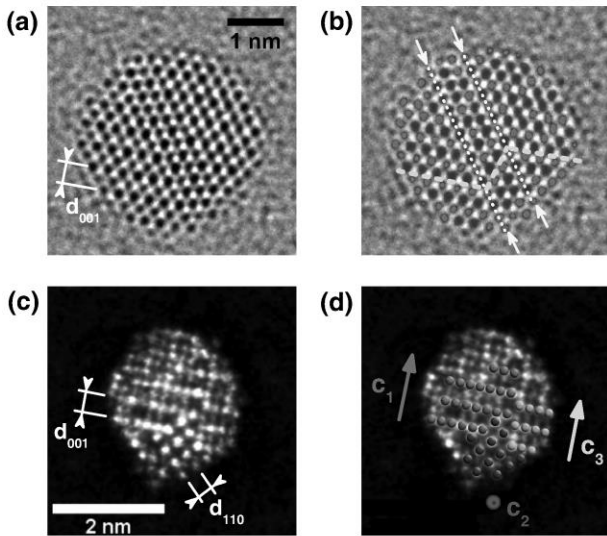


FIG. 3 (color online). (a) C_s -corrected HRTEM image of a CoPt particle displaying a continuous $L1_0$ chemical order over two (111) twins [indicated by arrows in (b)]. As a guide to the eyes, in (b) the atomic columns are colored according to their apparent size in the original image (a): the chemical order follows a “zig-zag” pattern (stressed by the green dashed line). (c) STEM-HAADF image (also called Z-contrast image) of a CoPt particle: the bright dots correspond to Pt-rich atomic columns. Three different $L1_0$ domains can be distinguished, as schematized in (d): the dots represent Pt-rich atomic columns, and are colored (in red, blue or green) according to their domain (intermediate colors correspond to dots common to two domains). The different c axis orientations are also indicated.

segregation would anyway be totally incompatible with the observation of a $L1_0$ order along a particle because for a size of around 2.5 nm, nearly 50% of the atoms are at the surface. The theoretical simulations may significantly overestimate the tendency for one element to segregate [13,14,24,55], or one may imagine that the amorphous carbon surrounding the particles prevents the segregation that would take place in the case of a free particle.

Remarkably, we also observe a chemical order in crystalline particles consisting of several $L1_0$ domains. In some cases, the different c orientations are due to (111) twins [see Figs. 3(a) and 3(b) for CoPt and Figs. 4(a) and 4(b) for FePt] which can preserve a coherent chemical order, as recently reported [28] for small FePt particles. Even more surprisingly, it is also possible to find different $L1_0$ domains in a 2 nm CoPt particle free of twins [Z-contrast image, see Figs. 3(c) and 3(d)]. In this case, one domain has a c axis at 90° with respect to two other domains that are joined by an antiphase boundary (APB). The 90° angle is reminiscent of a (011) c -domain boundary (CDB), which is frequently met in bulk materials and thin films but which was unexpected [45] and had never been reported for such small particles. The two domains with the same c axis direction must be separated by a (010) APB [a “tilted” APB such as a (111), (110) or (011) APB can also be

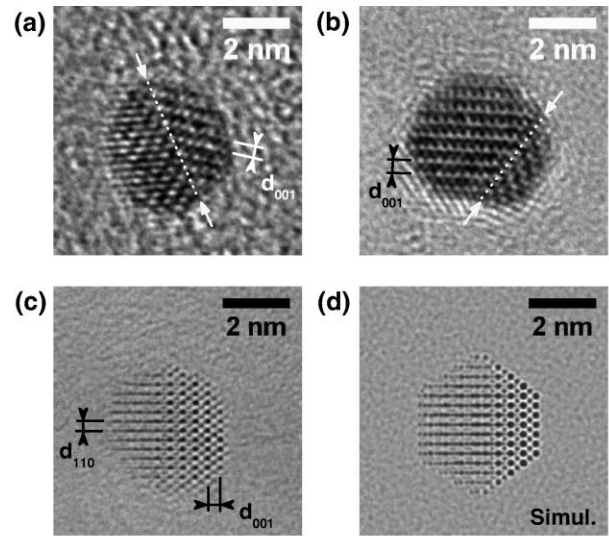


FIG. 4 (color online). (a), (b) HRTEM images of FePt particles with two $L1_0$ domains joined by a (111) twin. (c) C_s -corrected HRTEM image of a FePt particle with a (001) periodicity visible only on one side. This contrast corresponds to a chemically ordered decahedral particle [see Fig. 5(b)] viewed from the side, and is well reproduced by multislice HRTEM simulations (d) [53].

possible] which is also astonishing [40]. Another unusual contrast is often met in CoPt and FePt particles [see Fig. 4(c)], where the $L1_0$ order is clearly visible on one side with a (001) and (110) periodicity which are signatures of the chemical order, while on the other side only the (110) periodicity remains. This means that the chemical order is still present, but with the c axis pointing in another direction. We can also tell that the angle between the distinct domains is not 90° (otherwise we would still observe two families of atomic planes), which dismisses the possibility of a (011) CDB. In fact, what is not trivial and as can be shown with HRTEM simulations [see Fig. 4(d)], this particular contrast corresponds to decahedral particles (see following) indeed made of several $L1_0$ domains sharing the same (110) planes.

Finally, as illustrated in Fig. 5(a), particles showing a striking pentagonal pattern can also be found. They consist of decahedral clusters made of five $L1_0$ domains joined by (111) twins [see Fig. 5(b)]. The c axis of each domain are in the same plane, but are distributed according to a fivefold symmetry. Such a spectacular contrast can only be obtained when a particle is viewed along its fivefold symmetry axis [Fig. 5(b), top view]. Then, the shell-like structure is made self-evident and can manifest itself with different contrasts (see Fig. 6). Multislice image simulations have been performed [53], considering a particle with a perfect chemical order, and are in excellent agreement with the experimental C_s -corrected HRTEM images [Fig. 6(b)]. The “small gray” or “large dark” dots observed for small defocus values (the left side images

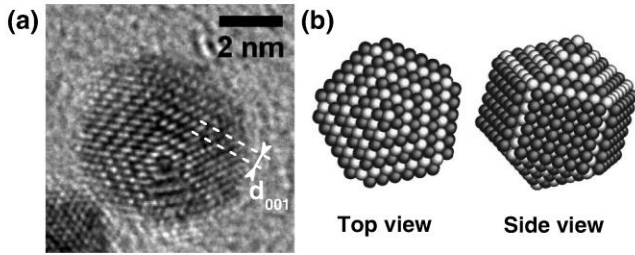


FIG. 5 (color online). (a) HRTEM image of a FePt particle displaying simultaneously a fivefold symmetry and $L1_0$ ordered domains. (b) schematic view of the corresponding chemically ordered decahedral structure, predicted by theoretical calculations.

of Fig. 6), respectively, correspond to Fe and Pt atomic columns. The chemical atomic structure can then be inferred from a HRTEM image and we find that the particle central column can be made as well of Pt as of Fe atoms [see Figs. 6(a) and 6(c)]. Furthermore, no tendency is observed concerning the nature of the outermost atoms [i.e., the (100) facets]: once more, there is no sign of a preferential surface segregation of one element. This

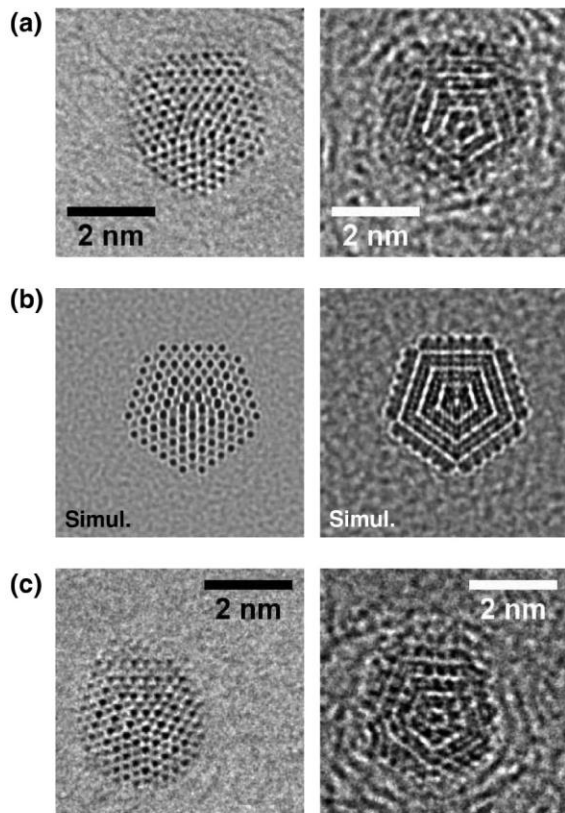


FIG. 6. (a), (c) C_x -corrected experimental HRTEM images of two different chemically ordered decahedral FePt particles, for two defocus values. (b) Multislice image simulation, using the geometry shown in Fig. 5(b) with Fe atoms at the center, to be compared to images (a). Note the reverse contrast of the central atomic column which is made of Fe in (a) and of Pt in (c).

remarkable particle structure is precisely the one predicted by theoretical calculations [13–15,25]. It is frequently met for FePt particles and also exists for CoPt particles, though in this case icosahedral clusters are more often observed. In spite of its predicted stability [14,15], we have not seen any indication of a chemical order in FePt or CoPt icosahedral particles. However, given the complexity of the presumed chemical arrangements for this geometry, extensive HRTEM simulations are needed because it is not evident how such an order could be visible.

Our HRTEM observations experimentally confirm the stability (or at least the metastability) of chemically ordered decahedral particles for a diameter between 2 and 5 nm. Besides, our results also contradict the statement of Andreazza *et al.* [25] that “the noncrystallinity of nanoparticles (Ih or Dh) is a limiting factor to achieve the chemical order.” From a magnetic point of view, it is expected that the MCA of these decahedral particles will be very low, despite that they are exclusively formed of $L1_0$ ordered domains. In the same way, for crystalline particles, twinning and the coexistence of several domains having different c orientations will certainly drastically reduce the MCA as compared to mono- $L1_0$ domain fct particles. This could explain why an assembly of particles can display a quite low MCA [17,56] simultaneously with a local $L1_0$ order (as can be, for instance, inferred from EXAFS [57], or indirectly from the magnetic moments evolution). Additional theoretical calculations are needed to fully apprehend the magnetic properties of these exciting nanoalloy systems.

This work has been supported by GDR-CNRS 3182, COST Action MP0903, the French METSA network, the CLYM [58] and the EMINA project of the French-Japanese Elyt laboratory [59]. The authors acknowledge P. Bayle-Guillemaud and J.-L. Rouvière for STEM-HAADF observations, the PLYRA and N. Blanc for the cluster synthesis, and A. Tamion for his assistance (Fig. 3) and fruitful discussions.

*florent.tournus@univ-lyon1.fr

- [1] Z. R. Dai, S. Sun, and Z. L. Wang, *Nano Lett.* **1**, 443 (2001).
- [2] Z. R. Dai, S. Sun, and Z. L. Wang, *Surf. Sci.* **505**, 325 (2002).
- [3] A. C. C. Yu, M. Mizuno, Y. Sasaki, H. Kondo, and K. Hiraga, *Appl. Phys. Lett.* **81**, 3768 (2002).
- [4] B. Rellinghaus, S. Stappert, M. Acet, and E. F. Wassermann, *J. Magn. Magn. Mater.* **266**, 142 (2003).
- [5] S. Stappert, B. Rellinghaus, M. Acet, and E. F. Wassermann, *J. Cryst. Growth* **252**, 440 (2003).
- [6] B. Rellinghaus, O. Dmitrieva, and S. Stappert, *J. Cryst. Growth* **262**, 612 (2004).
- [7] D. L. Peng, T. Hihara, and K. Sumiyama, *J. Magn. Magn. Mater.* **277**, 201 (2004).
- [8] A. Kovács, K. Sato, G. Sáfrán, P. B. Barna, and Y. Hirotsu, *Philos. Mag.* **84**, 2075 (2004).

- [9] C. Y. Tan, J. S. Chen, B. H. Liu, and G. M. Chow, *J. Cryst. Growth* **293**, 175 (2006).
- [10] O. Dmitrieva, B. Rellinghaus, J. Kastner, and G. Dumpich, *J. Cryst. Growth* **303**, 645 (2007).
- [11] M. Müller and K. Albe, *Acta Mater.* **55**, 6617 (2007).
- [12] M. Müller, P. Erhart, and K. Albe, *Phys. Rev. B* **76**, 155412 (2007).
- [13] G. Rossi, R. Ferrando, and C. Mottet, *Faraday Discuss. Chem. Soc.* **138**, 193 (2008).
- [14] M. E. Gruner, G. Rollmann, P. Entel, and M. Farle, *Phys. Rev. Lett.* **100**, 087203 (2008).
- [15] P. Entel, M. E. Gruner, G. Rollmann, A. Hucht, S. Sahoo, A. T. Zayak, H. C. Herper, and A. Dannenberg, *Philos. Mag.* **88**, 2725 (2008).
- [16] R. M. Wang, O. Dmitrieva, M. Farle, G. Dumpich, H. Q. Ye, H. Poppa, R. Kilaas, and C. Kisielowski, *Phys. Rev. Lett.* **100**, 017205 (2008).
- [17] F. Tournus, A. Tamion, N. Blanc, A. Hannour, L. Bardotti, B. Prével, P. Ohresser, E. Bonet, T. Epicier, and V. Dupuis, *Phys. Rev. B* **77**, 144411 (2008).
- [18] R. Ferrando, J. Jellinek, and R. L. Johnston, *Chem. Rev.* **108**, 845 (2008).
- [19] R. Wang, O. Dmitrieva, M. Farle, G. Dumpich, M. Acet, S. Mejia-Rosales, E. Perez-Tijerina, M. J. Yacaman, and C. Kisielowski, *J. Phys. Chem. C* **113**, 4395 (2009).
- [20] A. Dannenberg, M. E. Gruner, A. Hucht, and P. Entel, *Phys. Rev. B* **80**, 245438 (2009).
- [21] X. Liu and J.-P. Wang, *J. Appl. Phys.* **105**, 07A722 (2009).
- [22] D. Alloyeau, C. Ricolleau, C. Mottet, T. Oikawa, C. Langlois, Y. Le Bouar, N. Braïdy, and A. Loiseau, *Nat. Mater.* **8**, 940 (2009).
- [23] M. E. Gruner, *J. Phys. D* **43**, 474008 (2010).
- [24] R. V. Chepulskii, W. H. Butler, A. van de Walle, and S. Curtarolo, *Scr. Mater.* **62**, 179 (2010).
- [25] P. Andreazza, C. Mottet, C. Andreazza-Vignolle, J. Penuelas, H. C. N. Tolentino, M. De Santis, R. Felici, and N. Bouet, *Phys. Rev. B* **82**, 155453 (2010).
- [26] L. Qin, Y. Zhang, S. Huang, H. Tian, and P. Wang, *Phys. Rev. B* **82**, 075413 (2010).
- [27] N. Blanc, F. Tournus, V. Dupuis, and T. Epicier, *Phys. Rev. B* **83**, 092403 (2011).
- [28] M. Delalande, M. J.-F. Guinel, L. F. Allard, A. Delattre, R. Le Bris, Y. Samson, P. Bayle-Guillemaud, and P. Reiss, *J. Phys. Chem. C* **116**, 6866 (2012).
- [29] Strictly speaking, there is no F symmetry for a tetragonal Bravais lattice. However, fct is used as a shortcut for the F orthorhombic Bravais lattice, that exists, with $a = b \neq c$.
- [30] G. Hadjipanayis and P. Gaunt, *J. Appl. Phys.* **50**, 2358 (1979).
- [31] D. Weller, A. Moser, L. Folks, M. E. Best, W. Lee, M. F. Toney, M. Schwickert, J. U. Thiele, and M. F. Doerner, *IEEE Trans. Magn.* **36**, 10 (2000).
- [32] S. Sun, C. B. Murray, D. Weller, L. Folks, and A. Moser, *Science* **287**, 1989 (2000).
- [33] G. Barcaro, L. Sementa, F. R. Negreiros, R. Ferrando, and A. Fortunelli, *Nano Lett.* **11**, 5542 (2011).
- [34] F. Baletto and R. Ferrando, *Rev. Mod. Phys.* **77**, 371 (2005).
- [35] K. Koga and K. Sugawara, *Surf. Sci.* **529**, 23 (2003).
- [36] J. Penuelas, P. Andreazza, C. Andreazza-Vignolle, H. C. N. Tolentino, M. De Santis, and C. Mottet, *Phys. Rev. Lett.* **100**, 115502 (2008).
- [37] X. Hu, L. Xie, J. Zhu, N. Poudyal, J. P. Liu, and J. Yuan, *J. Appl. Phys.* **105**, 07A723 (2009).
- [38] C. Antoniak, M. Spasova, A. Trunova, K. Fauth, F. Wilhelm, A. Rogalev, J. Minár, H. Ebert, M. Farle, and H. Wende, *J. Phys. Condens. Matter* **21**, 336002 (2009).
- [39] Y. K. Takahashi, T. Koyama, M. Ohnuma, T. Ohkubo, and K. Hono, *J. Appl. Phys.* **95**, 2690 (2004).
- [40] T. Miyazaki, O. Kitakami, S. Okamoto, Y. Shimada, Z. Akase, Y. Murakami, D. Shindo, Y. K. Takahashi, and K. Hono, *Phys. Rev. B* **72**, 144419 (2005).
- [41] C.-b. Rong, D. Li, V. Nandwana, N. Poudyal, Y. Ding, Z. Wang, H. Zeng, and J. Liu, *Adv. Mater.* **18**, 2984 (2006).
- [42] B. Yang, M. Asta, O. N. Mryasov, T. J. Klemmer, and R. W. Chantrell, *Acta Mater.* **54**, 4201 (2006).
- [43] D. E. Laughlin, K. Srinivasan, M. Tanase, and L. Wang, *Scr. Mater.* **53**, 383 (2005).
- [44] M. Kozłowski, R. Kozubski, C. Goyhenex, V. Pierron-Bohnes, M. Rennhofer, and S. Malinov, *Intermetallics* **17**, 907 (2009).
- [45] A. Alam, B. Kraczek, and D. D. Johnson, *Phys. Rev. B* **82**, 024435 (2010).
- [46] R. Alayan, L. Arnaud, A. Bourgey, M. Broyer, E. Cottancin, J. R. Huntzinger, J. Lermé, J. L. Vialle, M. Pellarin, and G. Guiraud, *Rev. Sci. Instrum.* **75**, 2461 (2004).
- [47] D. Tainoff, L. Bardotti, F. Tournus, G. Guiraud, O. Boisron, and P. Mélinon, *J. Phys. Chem. C* **112**, 6842 (2008).
- [48] F. Tournus, N. Blanc, A. Tamion, M. Hillenkamp, and V. Dupuis, *J. Magn. Magn. Mater.* **323**, 1868 (2011).
- [49] F. Tournus, L. Bardotti, and V. Dupuis, *J. Appl. Phys.* **109**, 114309 (2011).
- [50] K. Sato, T. J. Konno, and Y. Hirotsu, *J. Appl. Phys.* **105**, 034308 (2009).
- [51] For a chemically ordered crystal, the structure is fct and not fcc. However, the tetragonalization ratio c/a is very close to 1 so that, regardless of the chemical nature of the atoms (which breaks the cubic symmetry), the unit cell is almost cubic. This is why we may here refer to the fcc structure even if the particles are chemically ordered.
- [52] Note that, even if it is present, the chemical order may not be visible in HRTEM images when a particle is not favorably oriented or if the defocus is not in a suitable range (see, for instance, Ref. [27]).
- [53] See the Supplemental Material at <http://link.aps.org/supplemental/10.1103/PhysRevLett.110.055501> for HRTEM images with nontrivial contrasts, computational details on HRTEM images simulations, and HRTEM images of chemically ordered CoPt decahedra.
- [54] The average cooling rate is of the order of 10 K/min (note that the evolution of the temperature during cooling is nonlinear).
- [55] M. E. Gruner, *J. Phys. Conf. Ser.* **200**, 072039 (2010).
- [56] C. Antoniak, J. Lindner, M. Spasova, D. Sudfeld, M. Acet, M. Farle, K. Fauth, U. Wiedwald, H.-G. Boyen, P. Ziemann *et al.*, *Phys. Rev. Lett.* **97**, 117201 (2006).
- [57] V. Dupuis, N. Blanc, F. Tournus, A. Tamion, J. Tuillon-Combes, L. Bardotti, and O. Boisron, *IEEE Trans. Magn.* **47**, 3358 (2011).
- [58] <http://www.clym.fr>
- [59] <http://www.elyt-lab.com>

B) Nanoparticules de FePt

Nous nous sommes intéressés aux nanoparticules de FePt, qui constituent un système similaire au CoPt, avec les mêmes questions sur la mise en ordre chimique et les propriétés magnétiques [Andreazza2015]. Parallèlement aux études concernant le comportement redox (cf. plus loin) et l'organisation de particules de FePt sur des surfaces (cf. résultats présentés au chapitre 1), nous avons étudié la structure et les propriétés magnétiques intrinsèques d'agrégats de FePt en matrice de carbone. Tout comme pour le CoPt, nous avons montré qu'il était possible d'obtenir par recuit des nanoparticules chimiquement ordonnées dans la phase $L1_0$, même pour des petites particules de 2 nm de diamètre [Tournus2013b]. Nous avons aussi pu mettre en évidence la coexistence de différentes géométries de particules, avec des particules de type octaèdre-tronqué (cristal cfc) et des particules icosaédriques ou décaédriques (multi-mâclées). En particulier la structure décaédrique et chimiquement ordonnée (avec cinq domaines $L1_0$) prédite théoriquement a été observée par microscopie électronique haute résolution (cf. article ci-dessus), ceci dans le cadre d'une collaboration avec l'IMR de l'Université de Tohoku (Japon).

Les propriétés magnétiques (mesures de moments magnétiques par XMCD, cf. Fig. 24) ont également été étudiées [Dupuis2015, Dupuis2015a]. On observe comme pour le CoPt une augmentation du moment de spin et orbital, ainsi qu'une polarisation magnétique importante du Pt (cf. Tableau 2 ci-dessous). En ce qui concerne l'évolution de l'anisotropie magnétique, malgré la forte similitude entre les deux systèmes, le comportement est très différent du CoPt (analyse encore en cours). Des mesures d'EXAFS ont été effectuées (résultats non encore publiés) et indiquent un comportement semblable au CoPt. D'un point de vue magnétique, en vue d'obtenir des particules avec une très forte anisotropie magnétique, le FePt semble plus prometteur que le CoPt. C'est pourquoi, après quelques études sur l'auto-organisation de particules de CoPt sur HOPG (cf. chapitre 1), nous avons ensuite privilégié l'organisation d'agrégats de FePt, sur graphite, puis sur nanotubes de carbone et enfin sur graphène épitaxié sur Ir(111). Ces études, qui donnent d'ores et déjà des résultats très intéressants vont se poursuivre dans les années à venir (cf. chapitre 4).

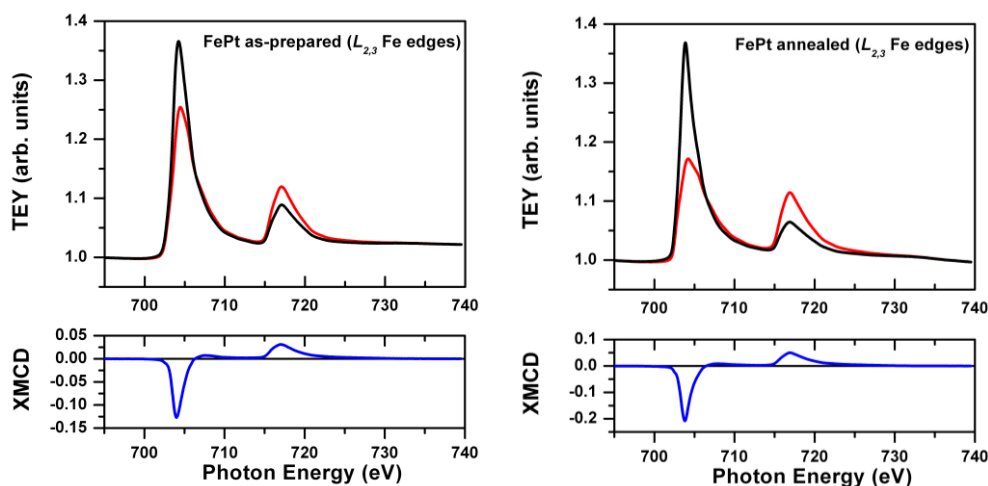


Fig. 24 : Spectres XAS et signal XMCD au seuil L du fer, pour des nanoparticules de FePt sélectionnées en taille (diamètre d'environ 3 nm) et noyées dans une matrice de carbone amorphe, avant et après recuit. Mesures effectuées au synchrotron SLS. Figure tirée de [Dupuis2015a].

Tableau 2 : Moments atomiques de spin (μ_S), orbital (μ_L) et rapport μ_L/μ_S correspondant déterminés d'après des mesures XMCD aux seuils L du Co, du Fe et du Pt pour des particules de CoPt et FePt noyées dans une matrice de carbone. Tableau tiré de [Dupuis2015].

XMCD at various L _{3,2} edges	Co-edge	Fe-edge	Pt-edge
	μ_S (μ_B/at)	μ_S (μ_B/at)	μ_S (μ_B/at)
	μ_L (μ_B/at)	μ_L (μ_B/at)	μ_L (μ_B/at)
	μ_L/μ_S	μ_L/μ_S	μ_L/μ_S
CoPt as-prepared	1.67		0.47
	0.13		0.07
	0.077		0.15
CoPt annealed	1.98		0.52
	0.2		0.1
	0.101		0.192
FePt as-prepared		1.33	—
		0.15	
		0.11	
FePt annealed		2.59	0.57
		0.37	0.07
		0.14	0.13

C) Nanoparticules de FeRh

L'alliage FeRh, chimiquement ordonné dans la phase B2 (structure bcc, de type CsCl) présente une compétition entre un ordre antiferromagnétique (à basse température) et un ordre ferromagnétique (à haute température), se traduisant par l'existence d'une transition méta-magnétique à une température proche de l'ambiante, dans le cas du massif. Cette particularité est attractive pour des applications potentielles dans le domaine de la spintronique et de l'enregistrement magnétique thermiquement assisté. Contrairement aux études précédentes sur ce système (phase massive, films minces ou nanoparticules), nous avons mis en évidence la persistance de l'ordre ferromagnétique jusqu'à très basse température (3 K) pour des nanoparticules de FeRh de 3,3 nm de diamètre, sélectionnées en taille et noyées en matrice de carbone, cristallisées dans la phase chimiquement ordonnée B2 [Hillion2013, Dupuis2015]. Nous avons observé, dans le cadre du travail de thèse d'A. Hillion (co-encadré par V. Dupuis et A. Tamion), des modifications de structure et des propriétés magnétiques lors du recuit des nanoparticules. Tandis qu'après dépôt les particules sont dans une phase fcc chimiquement désordonnée, elles présentent l'ordre chimique de la phase B2 après recuit (cf. Fig. 25, les observations HRTEM ayant fait l'objet d'une collaboration avec l'IMR de l'Université de Tohoku). De plus, les mesures XMCD aux seuils M du Rh et L du Fe (cf. Fig. 25), ont révélé un ordre ferromagnétique pour les particules recuites, jusqu'à une température de 3 K. Les atomes de fer possèdent un fort moment magnétique (3 μ_B), ainsi que les atomes de Rh (1 μ_B). Il est important de noter que dans la phase antiferromagnétique le Rh ne possède pas de moment magnétique. La combinaison des résultats de mesures XMCD et de magnétométrie SQUID permet de caractériser précisément les propriétés magnétiques des particules de FeRh, et montrent que la taille magnétique est identique à la taille géométrique. Autrement dit, il n'y a pas de coexistence entre phase antiferromagnétique et ferromagnétique, mais bien une seule phase pour l'ensemble des particules. D'après des mesures EXAFS au seuil K du Fe [Dupuis2015], l'ordre ferromagnétique pourrait être favorisé par des déformations induites par la petite taille des particules : les distances interatomiques moyennes sont identiques à celles de la phase massive, mais elles présentent une dispersion sensiblement plus grande.

À la suite de la thèse d'A. Hillion, Ghassan Khadra (qui a principalement étudié durant sa thèse les nanoparticules de FeCo, avec l'idée d'avoir à la fois une forte anisotropie et une très grande aimantation) a poursuivi les recherches sur le FeRh, ainsi que plus récemment A. Robert (thèse débutée en oct. 2014). Même si je garde un lien avec cette thématique, je ne fais que l'accompagner, mon activité sur les nanoparticules bimétalliques étant maintenant centrée sur le FePt ou des systèmes mêlant métaux de transition et métaux nobles (comme FeAu, CoAu ou CoAg, cf. chapitre 4).

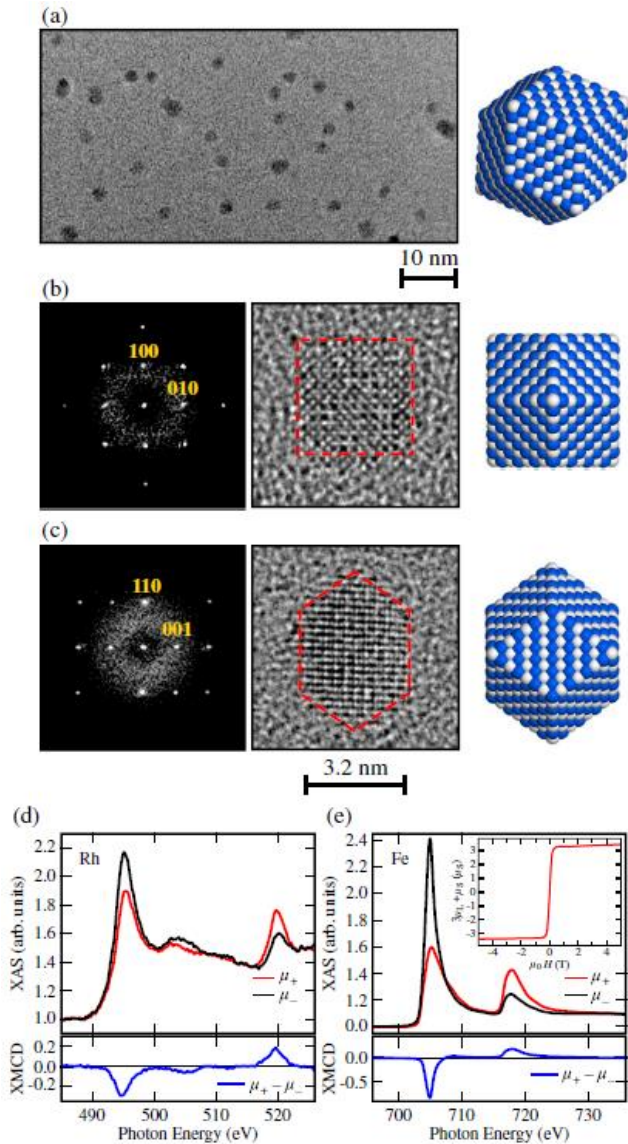


Fig. 25 : Image MET (a) des particules de FeRh (de diamètre 3,3 nm) en matrice de carbone amorphe. Images METHR de nanoparticules de FeRh après recuit, observée selon la direction [001] (b) ou la direction [1-10] (c) : l'ordre chimique correspondant à la phase B2 est clairement visible (présence d'un pic {001} dans la FFT). Spectres XAS et signal XMCD au seuil M du Rh (d) et au seuil L du Fe (e), mesurés à 3 K sous un champ appliqué de 5 T. Figure tirée de [Hillion2013].

D) Spécificités du comportement redox des nanoparticules

Dans le cadre d'une collaboration avec S. Zafeiratos (ICPEES, UMR 7515 CNRS-Université de Strasbourg), nous avons étudié *in situ* le comportement de nanoparticules non protégées, sous atmosphère oxydante et réductrice à haute température (température de l'ordre de 500-600 K). Dans le cas d'agrégats de Co et de CoPt d'environ 3 nm de diamètre, les mesures de photoémission et d'absorption X sur synchrotron ont mis en évidence les spécificités des nanoparticules par rapport aux surfaces des matériaux massifs (oxydation inhabituelle du Co en particulier) [Papaefthimiou2011, Papaefthimiou2011a]. Par exemple, la figure 26 ci-dessous montre que l'oxyde de cobalt n'a pas la même structure dans le cas de nanoparticules de CoPt oxydées que pour le matériau massif : le cobalt reste dans la phase métastable CoO de structure wurtzite, tandis que pour une feuille de CoPt on a du Co₃O₄ (structure spinelle).

Les nanoparticules à base de fer peuvent être utiles en tant que catalyseurs pour différents processus industriels, il est donc important de bien comprendre leur activité et leur stabilité dans un environnement réactif. C'est pourquoi nous avons récemment étudié des nanoparticules bimétalliques

de FePt, FeRh et FeAu préparées par LECBD à l'iLM et triées en taille, par spectroscopie de rayons X (synchrotron BESSY à Berlin) *in situ*, sous atmosphère de O₂ ou H₂ jusqu'à 400°C. Les mesures de photoémission X (XPS) et d'absorption X (XAS) ont montré que l'interaction fer-métal noble affecte la stabilité et la structure de l'oxyde de fer, ainsi que la façon dont les deux constituants de l'alliage se mélangent [Papaefthimiou2014] (cf. Fig. 27 et 28). Ces résultats permettent de clarifier le rôle du métal noble sur les propriétés d'oxydo-réduction des particules bimétalliques à base de fer.

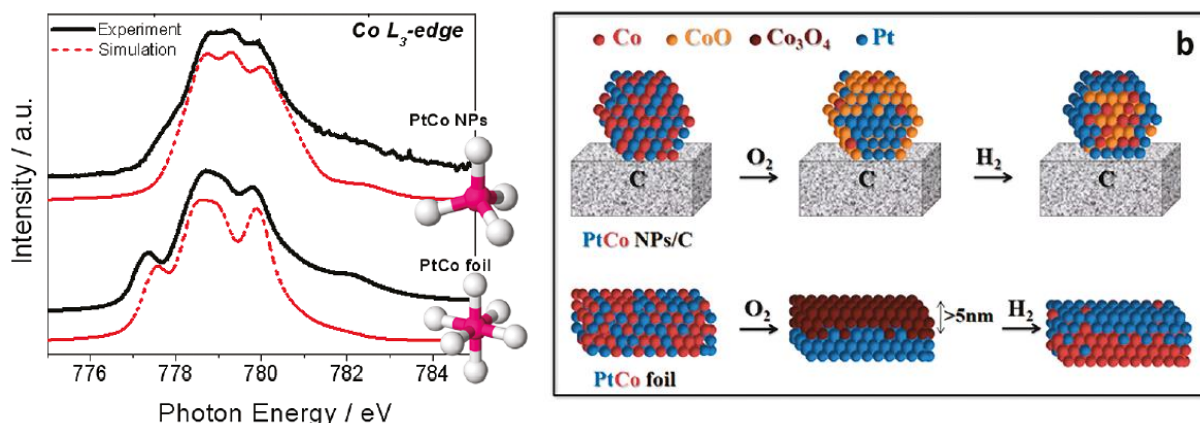
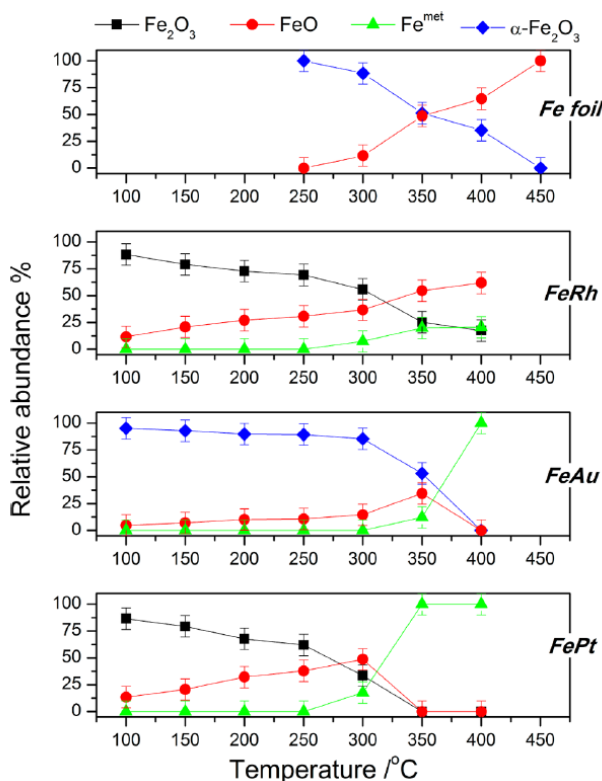


Fig. 26 : À gauche, spectres XAS expérimentaux (courbes en trait plein) et simulés (pointillés) au seuil L₃ de Co pour des nanoparticules de CoPt (en haut) et une feuille de CoPt (en bas). À droite, représentation schématique de la structure atomique et de l'état d'oxydation des nanoparticules de CoPt, comparé au cas d'une feuille de CoPt, en fonction des conditions environnementales (oxydation, puis réduction à chaud). Figure tirée de [Papaefthimiou2011a].

Fig. 27 : Abondances relatives des différents états d'oxydation du Fe, déduites des spectres XAS au seuil L₃ de Fe, pour différentes particules bimétalliques à base de fer, en fonction de la température (sous une atmosphère réductrice de 0,2 mbar de H₂). Pour comparaison, le cas du fer massif est indiqué en haut : on observe des variations significatives de comportement entre les différents systèmes. Figure tirée de [Papaefthimiou2014].



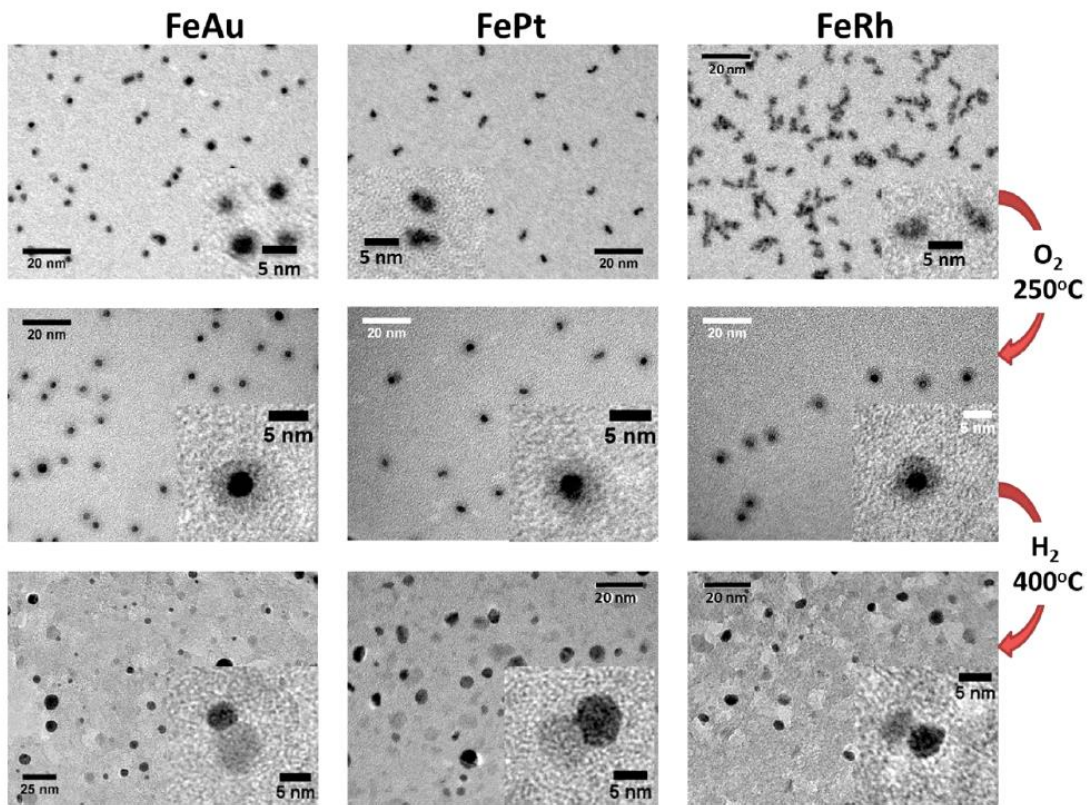


Fig. 28 : Images MET de particules de FeAu, FePt et FeRh (non protégées), après dépôt (en haut), après oxydation sous O_2 à $250^\circ C$ (au milieu) et après réduction sous H_2 à $400^\circ C$ (en bas). Les observations MET sous réalisées ex-situ. Figure tirée de [Papaefthimiou2014].

Chapitre 4 : Études en cours, nouveaux développements et perspectives

1) Nanosystèmes hybrides pour la magnéto-plasmonique

Les plasmons de surface, qu'ils soient localisés (localized surface plasmon resonance : LSPR) ou propagatifs (surface plasmon polariton : SPP), correspondent à un confinement du champ électromagnétique à une échelle inférieure à la longueur d'onde. Ceci résulte en une grande sensibilité à l'environnement proche (pouvant être mise à profit pour des capteurs) et permet par ailleurs d'envisager des dispositifs nano-photoniques innovants. Un point clé pour le développement de la plasmonique est d'être capable de contrôler les propriétés des plasmons à l'aide de paramètres extérieurs (ce qui permettrait alors la réalisation de composants de bases, comme des interrupteurs, modulateurs, coupleurs, multiplexeurs...). Dans ce cadre, l'application d'un champ magnétique est une voie prometteuse, notamment en termes de rapidité. Cependant, le magnétisme et la plasmonique sont habituellement deux phénomènes séparés : au contraire des métaux nobles, les métaux ferromagnétiques ne présentent pas de bonnes propriétés plasmoniques, et réciproquement, un champ magnétique extérieur modifie très peu les propriétés des matériaux utilisés en plasmonique. Il est alors pertinent de combiner ces deux types de matériaux – un métal noble (or, argent) et un métal ferromagnétique (fer, cobalt) – au sein de nano-systèmes bi-métalliques. Cette approche a déjà permis de mettre en évidence des effets magnéto-plasmoniques, c'est-à-dire d'inter-dépendance entre les propriétés magnétiques et plasmoniques [voir G. Armelles et al., *Adv. Optical Mater.* **1**, 10 (2013) pour une revue récente]. Ce couplage est recherché avec principalement deux objectifs : agir sur les propriétés magnéto-optiques à l'aide d'une résonance plasmon, et modifier un plasmon avec un champ magnétique.

L'exaltation des propriétés magnéto-optiques de nanoparticules grâce à la LSPR a déjà été rapportée, ainsi que la possibilité de moduler magnétiquement la propagation d'un plasmon avec des couches minces. Cependant, il reste de nombreuses questions ouvertes et des développements possibles. Notamment, aucun contrôle magnétique de la LSPR n'a encore été démontré et il n'existe pas de travaux sur la modulation d'un SPP en utilisant des nanoparticules magnétiques, alors même que l'utilisation d'assemblées de particules offre des paramètres de contrôle supplémentaires (taille, forme, composition des particules, concentration...) et donne accès à une diversité d'états magnétiques bien plus riche qu'une simple couche uniforme. Il serait par ailleurs pertinent de s'intéresser aux aspects de diffusion/excitation asymétrique de SPP par une particule magnétique, en fonction de son état d'aimantation.

Une collaboration avec Joël Bellessa a récemment démarré sur cette thématique de nanosystèmes hybrides pour la magnéto-plasmonique. Des premières investigations visant à moduler la propagation d'un SPP grâce au champ magnétique (expériences d'interférométrie) ont été menées sur des couches de nanoparticules déposées sur une surface d'argent dans le cadre de stages de master co-encadrés avec J. Bellessa. La mise en place expérimentale s'est avérée délicate et se poursuit actuellement (détection synchrone, avec un système d'aimants permanents afin d'éliminer des artefacts). Parallèlement à ce travail, j'ai commencé à étudier la structure de nanoparticules bimétalliques CoAu en vue de combiner magnétisme et LSPR dans un même nano-objet. Il a ainsi été montré que l'on pouvait obtenir, après recuit pour des particules noyées dans une matrice de carbone amorphe, des structures cœur-coquille Co@Au (cf. Fig. 29).

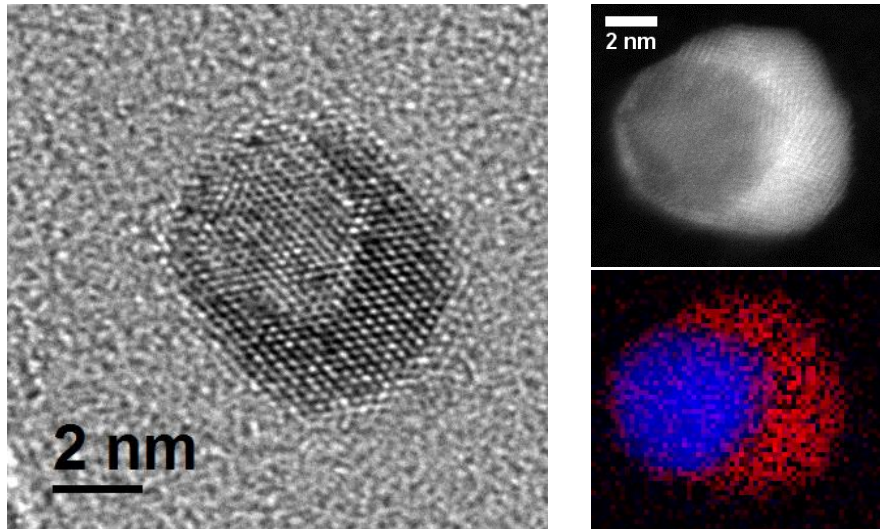


Fig. 29 : À gauche, image MET haute résolution d'une nanoparticule de CoAu après recuit où l'on distingue un cœur décentré de Co entouré d'une coquille d'or. À droite, image STEM-HAADF (en haut) d'une particule de CoAu et cartographie chimique correspondante (en bas) obtenue par STEM-EELS, le Co apparaissant en bleu et l'or en rouge.

C'est dans ce contexte qu'a débutée la thèse d'Ophelliam Loiselet (commencée en octobre 2014), grâce à un financement de la région Rhône-Alpes via l'ARC6 (Technologies de l'Information et de la communication et usages Informatiques Innovants). Ce travail de thèse est effectué en collaboration entre les équipes « Nanostructures magnétiques » et « Matériaux et nanostructures photoniques » de l'ILM et « Nanomagnétisme » du CEA Grenoble. Ce projet propose d'étudier, d'un point de vue essentiellement fondamental, des nano-systèmes mixtes pour la magnéto-plasmonique. L'étude se situe à la croisée de plusieurs disciplines (physique du solide, nanoscience, optique, magnétisme) et porte sur des systèmes modèles avec notamment des particules préparées par voie physique de manière bien contrôlée (taille, composition et concentration ajustable) par LECBD et des échantillons des plots préparés par lithographie au CEA. Enfin, en plus de mesures optiques conventionnelles, des mesures magnéto-optiques seront effectuées.

Durant sa thèse (fin prévue à l'automne 2017), O. Loiselet a principalement étudié des nanoparticules bi-métalliques de Co-Au et Co-Ag diluées dans une matrice diélectrique. Ces nano-systèmes mixtes doivent être caractérisés par des techniques complémentaires permettant de bien cerner les phénomènes physiques en jeu : microscopie électronique en transmission ; spectroscopie de perte d'énergie d'électrons (EELS) ; magnétométrie à SQUID ; magnétométrie et spectroscopie Kerr ; absorption optique ; modélisation... Il est important de noter qu'à cette échelle (particules de taille inférieure à 10 nm), il est possible d'obtenir des phases/matériaux qui n'existent pas habituellement et d'optimiser les interfaces (i.e. le couplage magnéto-plasmonique), pour au final obtenir des propriétés inédites. Les objectifs de ce travail de thèse étaient les suivants :

- Optimiser les effets magnéto-optiques et magnéto-plasmoniques
- Permettre de nouvelles fonctionnalités pour la plasmonique active
- Établir le lien entre les modifications du plasmon et les propriétés des particules
- Maitriser la fabrication de particules bi-métalliques modèles pour la magnéto-plasmonique

Des résultats très intéressants ont d'ores et déjà été obtenus, avec la mise en évidence de nanostructures originales combinant magnétisme et résonance plasmon (cf. Fig. 30 et 31). De nombreuses questions restent ouvertes et cette thématique fera l'objet d'investigations futures (avec notamment la mise en place d'un nouveau dispositif expérimental en collaboration avec l'équipe de Joël Bellessa) qui s'avèreront certainement fructueuses.

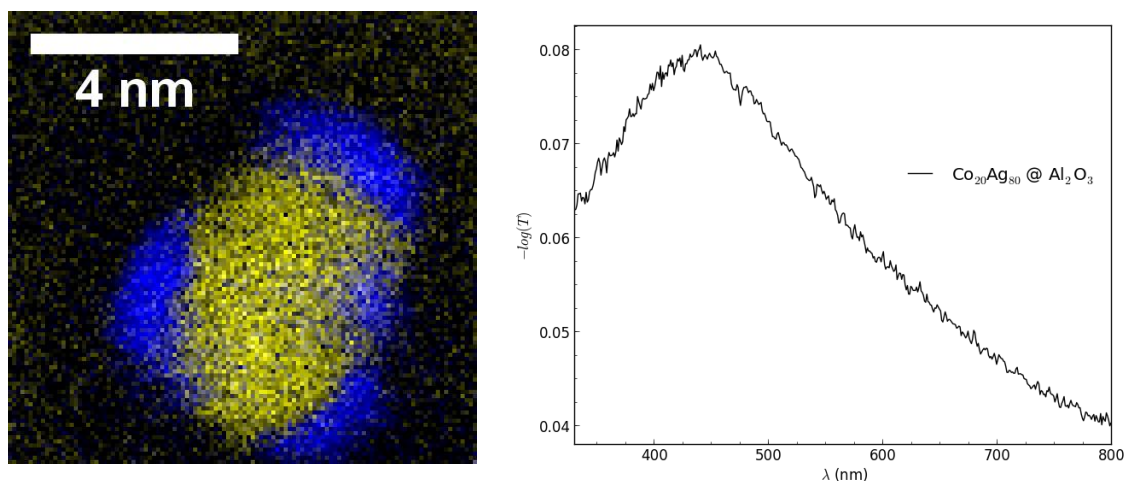


Fig. 30 : À gauche, cartographie chimique (Co en bleu et Ag en jaune) obtenue par STEM-EELS pour une nanoparticule de CoAg non recuite, protégée par une couche de carbone amorphe. À droite, spectre de transmission optique pour une couche de nanoparticules de $Co_{20}Ag_{80}$ non triées en tailles (et non recuites), noyées dans une matrice d'alumine. Le pic situé à environ 450 nm correspond à la résonance plasmon de surface de ces nanoparticules.

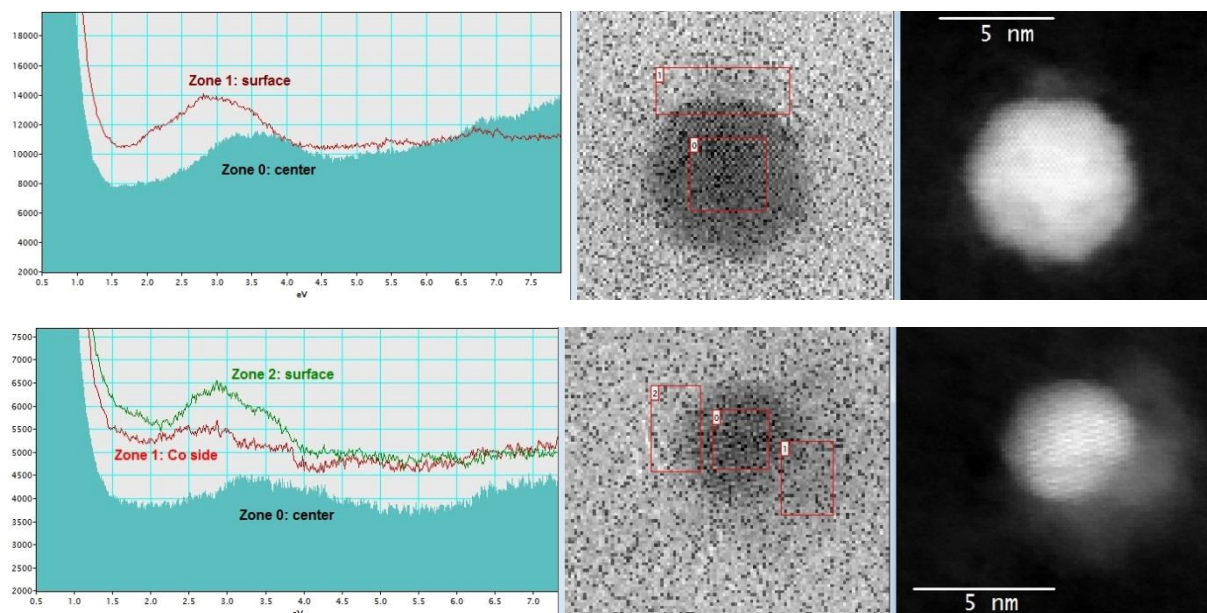


Fig. 31 : Spectroscopie de perte d'énergie (STEM-EELS) sur des particules de CoAg (de différentes compositions) non recuites, protégées par une couche de carbone amorphe : en haut une particule riche en Ag, et en bas une particule avec davantage de Co (zone visible en gris clair sur l'image HAADF). Pour chaque particule, on a tracé (à gauche) les spectres intégrés sur différentes zones, représentées sur le spectre-image (au milieu), qui correspond à l'image HAADF (à droite). La signature d'une résonance de surface est détectable (plasmon, nettement décalé par rapport au pic de volume).

2) Effets d'interfaces et organisation de nanoparticules sur des surfaces

Le dépôt de nanoparticules préformées en phase gazeuse sur des surfaces cristallines, dans des conditions d'ultra-haut vide (UHV), reste un domaine quasiment inexploré jusqu'à présent. Pourtant ceci constitue une approche prometteuse et originale de préparation « bottom-up » de nano-systèmes, complémentaire de la voie habituelle où des atomes sont directement déposés sur le substrat et se regroupent pour faire croître des particules. Le dépôt d'agrégat préformés sur de telles surfaces présente en effet l'avantage de permettre de changer indépendamment la taille des particules et le taux de couverture de la surface, ou encore de déposer des alliages à stœchiométrie contrôlée ce qui s'avère impossible jusqu'à présent par les techniques physiques plus conventionnelles.

Nous avons récemment montré que l'utilisation de gabarit (moiré obtenu avec du graphène épitaxié sur Ir(111)) permettait de piéger sur des sites spécifiques des nanoparticules préformées déposées aléatoirement sur la surface [Linan2015]. Ce comportement inédit a été observé par STM et diffusion des rayons X aux petits angles (GISAXS) pour des agrégats de platine, et très récemment pour des particules d'alliage magnétique FePt (cf. Fig. 32), ce qui est prometteur pour l'obtention de réseaux ultra-denses de nano-aimants. D'une manière générale, ces études sur des agrégats mixtes à vocation magnétique ou catalytique pourraient ainsi permettre d'obtenir des réseaux auto-organisés de nanoparticules de taille sélectionnée et d'orientation et stœchiométrie contrôlée, aux propriétés originales (couplages entre particules, phénomènes de résonance...). Outre la formation de réseaux à pas extrêmement faible et contrôlés sur de grandes surfaces, l'épitaxie des particules sur la surface, permettant d'imposer leur orientation, apparaît très prometteuse dans le domaine du nano-magnétisme.

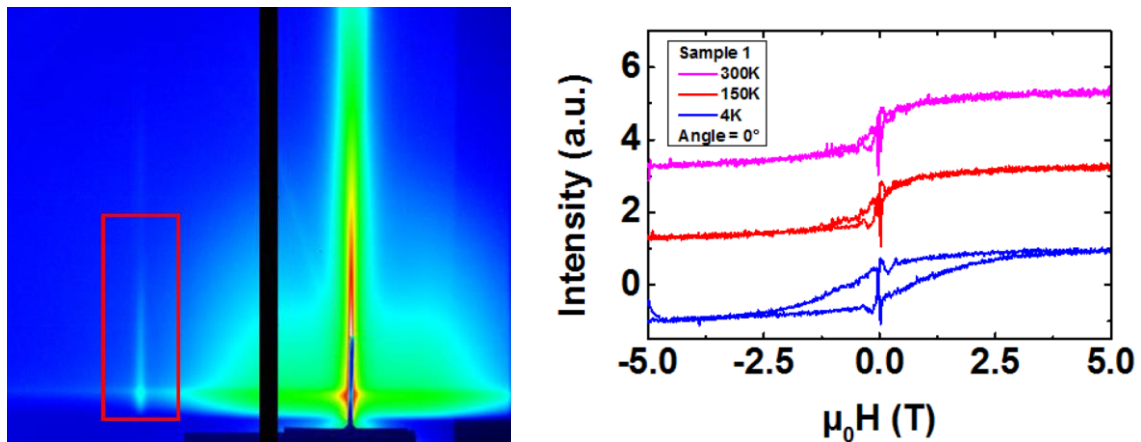


Fig. 32 : À gauche, intensité GISAXS mesurée pour des particules de FePt (diamètre 2,2 nm) déposées à 150°C sur une couche de graphène épitaxiée sur un cristal d'Ir (111) et protégées par du carbone amorphe. La mesure est effectuée selon la direction [100] du moiré et laisse apparaître un pic de corrélation (encadré en rouge) indiquant une disposition cohérente des particules sur la surface, c'est-à-dire une auto-organisation correspondant au réseau de moiré. À droite, cycles d'hystérésis déduits de mesures XMCD (seuil L_3 du Fe, en incidence normale et à différentes températures) pour le même système de nanoparticules après recuit : la très grande coercivité peut être attribuée à la mise en ordre chimique (phase $L1_0$) des particules de FePt. Ces mesures ont été effectuées en 2016 à l'ESRF (ligne BM32) et à SOLEIL (ligne DEIMOS).

Afin de poursuivre ces investigations et de les étendre à d'autres types de surfaces cristallines (par exemple des surfaces vicinales ou reconstruites), le CNRS vient de financer pour l'année 2016 un projet d'équipement qui permettra de disposer d'une chambre de préparation dédiée pour les surfaces cristallines, connectée à la fois au STM et à la chambre de dépôt d'agrégats de la plateforme PLYRA

pour des études *in situ*. Grâce à cet équipement, qui sera installé en cours d'année 2017, il sera possible d'étudier de manière plus exhaustive l'interaction agrégats/surface (diffusion, mouillage, interface) ainsi que l'auto-organisation des particules sur des substrats cristallins. Cet équipement devrait évoluer dans les prochaines années (au gré des financements...), de façon à offrir de nouvelles possibilités en termes de croissances de couches nanométriques (canon et cellule d'évaporation), de préparation et caractérisation des surfaces (bombardement ionique, LEED/Auger).

Une des activités de recherche de l'équipe « Nanostructures magnétiques » consiste ainsi à s'orienter vers un contrôle précis de l'interface nanoparticule/surface permettant d'influer sur les propriétés magnétiques (effets magnéto-élastiques, magnéto-électriques, effets de proximité ferro-supra etc.) et d'obtenir des nano-systèmes originaux. De tels systèmes pourront nous permettre d'élargir nos champs d'investigations sur des phénomènes mettant en jeu l'interaction agrégat-surface, encore mal connue d'un point de vue expérimental mais aussi théorique. Il s'agit en effet de domaines pour lesquels nous étions jusque-là limités à des surfaces « simples » (i.e. ne nécessitant pas de traitement très spécifiques : graphite, nanotubes de carbone...). Citons par exemple : (i) les phénomènes de diffusion, de nucléation et croissance de particules nanométriques (collaboration O. Pierre-Louis, F. Rabilloud (ILM, groupe théorie et modélisation) et F. Calvo (Liphy Grenoble)) ; (ii) les phénomènes de mouillage à l'échelle nanométrique ; (iii) l'étude de l'anisotropie magnétique d'interface. Nous pourrions aussi développer de nouvelles thématiques, notamment en nous appuyant sur des mesures de transport électronique sur des nanoparticules individuelles (blocage de Coulomb et spectroscopie sur des particules magnétiques, fluctuations super-paramagnétiques de particules individuelles, ou effets de confinement dans des particules supraconductrice par exemple). De telles mesures, en microscopie à effet tunnel (STM, et STS à basse température en collaboration avec l'ESPCI) ou par microscopie à électrons balistiques (BEEM, en collaboration avec le LPS), demandent des empilements spécifiques de couches minces (fine barrière isolante, barrière Schottky...). Disposer d'une véritable chambre de préparation des surfaces sous UHV est un atout pour espérer réaliser de tels nano-systèmes. Il est important de noter que le matériel demandé pourra aussi permettre de reprendre la croissance de couches (après un bombardement/recuit de la surface pour la nettoyer) sur des échantillons préalablement synthétisés par d'autres équipes (par exemple pour des empilements complexes comme des jonctions tunnel magnétiques...).

Parmi les sujets en cours et à venir, on peut citer la poursuite des études de l'auto-organisation de nano-aimants sur graphène en allant plus loin dans la caractérisation des propriétés physiques qui en découlent (par exemple propriétés magnétiques sondées par XMCD, cf. Fig. 32) et dans la compréhension des mécanismes. L'étude pourra être étendue à d'autres systèmes 2D présentant des moirés de différentes périodicités et des propriétés structurales et électroniques différentes (par exemple du h-BN). De plus, nous aimerions poursuivre une étude débutée en 2014 sur le dépôt de particules magnétiques (Co et CoPt) sur surface vicinale d'Au(677) présentant des marches atomiques régulières. Une première campagne de mesures de diffraction X et de GISAXS à l'ESRF (cf. Fig. 33) avait alors montré que les particules de CoPt étaient épitaxiées sur l'or, avec un effet étonnant de réorganisation des marches lors d'un recuit (phénomène du type « adsorbate induced faceting », modifiant localement la périodicité des marches). Afin de clarifier ce phénomène, des mesures complémentaires sont nécessaires (effet de la taille des particules, de la densité, de la température de recuit...) et des observations STM *in situ* pourront notamment apporter des informations précieuses.

On peut également mentionner une autre activité émergente dans l'équipe « nanostructures magnétiques », portée par D. Le Roy, où il s'agit de déposer des particules magnétiques sur un substrat ferroélectrique et/ou piézoélectrique (comme par exemple BaTiO₃, cf. Fig. 34), ce qui pourrait

permettre de contrôler leurs propriétés magnétiques à l'aide d'un champ électrique. Sur cette nouvelle thématique, un travail de préparation de surface et d'études préliminaires de dépôt de particules doit être entrepris.

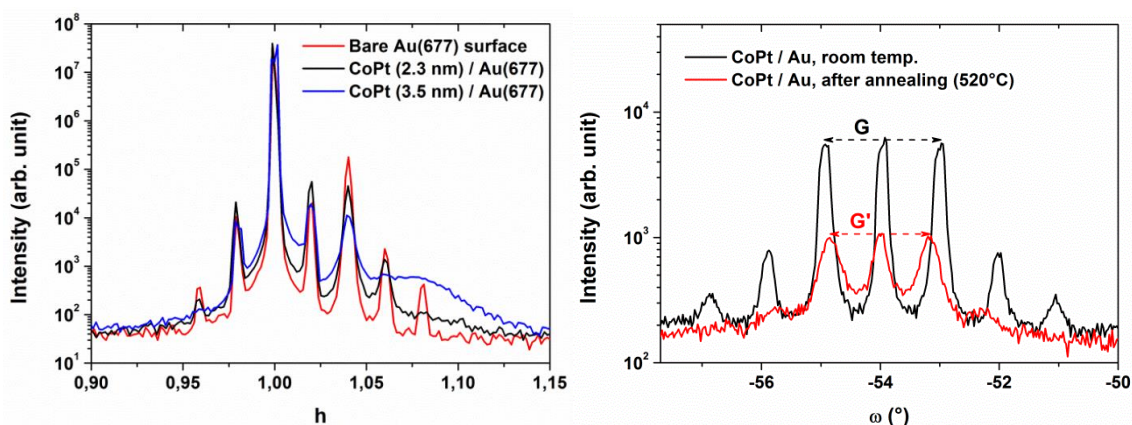


Fig. 33 : À gauche, mesures de diffraction X en incidence rasante (GIXRD), dans la direction $(h00)$, sur un système de nanoparticules de CoPt (de diamètre 2,3 nm ou 3,5 nm) déposées à température ambiante sur une surface vicinale d'Au(677) présentant une reconstruction de surface et des marches atomiques périodiques. À droite, mesures GIXRD, après un dépôt de nanoparticules de CoPt (2,3 nm de diamètre), à différents angles ω autour du pic (100) de l'or, faisant apparaître des pics reflétant la périodicité des marches atomiques sur la surface. Après chauffage à 520°C, on détecte en GIXRD une nette variation (environ 13%) de la périodicité des marches, tandis qu'en GISAXS la période reste la même (rappelons que la période des marches est liée à l'angle de miscut de la surface vicinale) : le phénomène reste à éclaircir...

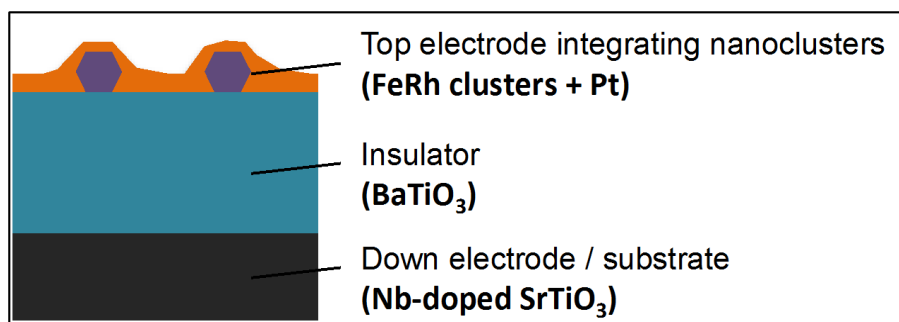


Fig. 34 : Représentation schématique du système que l'on souhaite étudier, visant à contrôler les propriétés magnétiques de particules de FeRh par l'intermédiaire d'une tension électrique appliquée entre l'électrode inférieure (substrat de SrTiO_3 dopé Nb) et l'électrode supérieure (couche de Pt). La qualité de la couche de BaTiO_3 (préparée à l'INL) est primordiale, ainsi que celle de l'interface entre cette couche et les nanoparticules déposées

3) Modélisation de mesures magnétiques, assemblées de nano-aimants

Depuis une dizaine d'année, un gros travail de modélisation de mesures magnétiques sur des assemblées de nano-aimants a été mené (principalement en collaboration avec Alexandre Tamion). La motivation principale derrière cette activité était de déduire, de manière la plus fiable possible, les propriétés intrinsèques des nanoparticules magnétiques à partir de mesures conventionnelles de magnétométrie (comme les courbes de susceptibilité ZFC/FC, cycles d'hystérésis etc.). La confrontation théorie/expérience (en particulier via des procédures efficaces d'ajustement de courbes expérimentales multiples) a ainsi permis de mettre en évidence des effets originaux et spécifiques aux systèmes de nanoparticules (cf. Fig. 35 et 36 par exemple pour des résultats récents sur des

interactions de type « super-ferromagnétique » entre nanoparticules proches). Nous avons voulu raffiner nos modèles de façon à pouvoir considérer des systèmes de plus en plus complexes (par exemple avec une anisotropie biaxiale, une texturation des directions d'anisotropie, des interactions magnétiques...)

Fig. 35 : Mesures magnétiques expérimentales (ZFC/FC (a), courbes IRM/DCD (b), cycles d'hystérésis (c) et courbes Δm (d)) pour des assemblées de nanoparticules de Co dans une matrice d'or, avec différentes concentrations volumiques (de 0,5% à 4%).

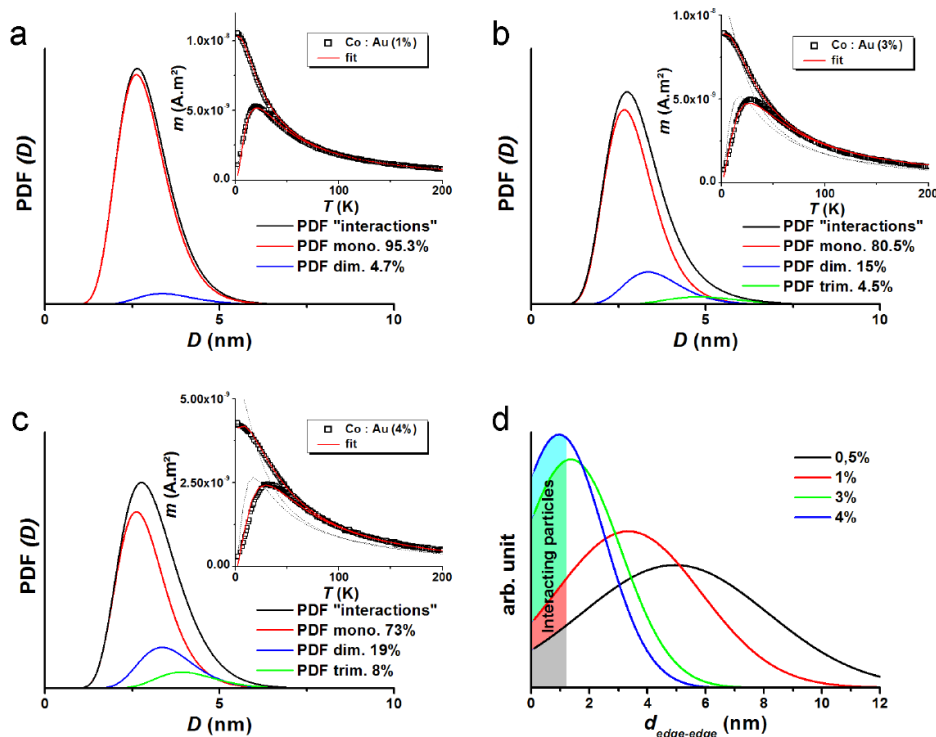
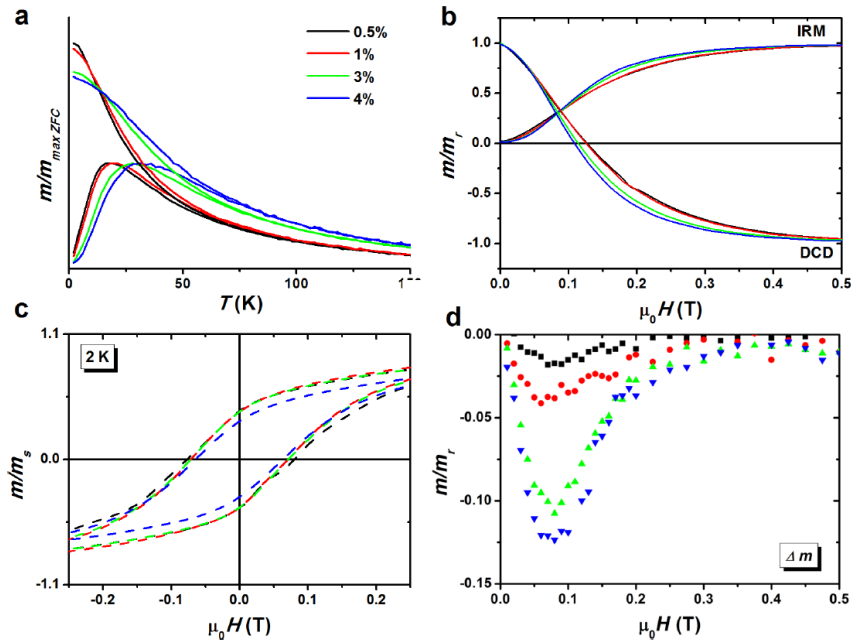


Fig. 36 : Distributions de taille magnétique (en considérant la formation de dimères et trimères magnétiques lorsque les particules sont suffisamment proches) permettant de rendre compte de l'évolution des courbes ZFC/FC avec la concentration de particules (a : 1%, b : 3%, c : 4%), pour des agrégats de Co noyés en matrice d'or. La comparaison simulations/expérience est visible en insert. La figure d) indique la distribution des distances au premier voisin pour les différents cas, ainsi que la zone (distance d'interaction) donnant lieu à la formation de dimères magnétiques.

Récemment, nous avons mis à profit les mesures de moment rémanent selon le protocole IRM et DcD, qui permettent en outre de caractériser les interactions entre nanoparticules magnétiques via le paramètre δm . En particulier, un δm négatif indique un retournement des nanoparticules plus facile en partant d'un échantillon préalablement saturé, et donc un effet déstabilisant des interactions entre particules. Il est alors communément admis d'attribuer ce phénomène aux interactions dipolaires, qui sont alors dites « démagnétisantes ». Pour mieux comprendre l'allure des courbes (position du pic de la courbe δm , lien entre son amplitude et l'intensité des interactions dipolaires...) nous avons cherché à identifier les ingrédients responsables de cet effet et confronter différentes modélisations (champ moyen, premiers voisins...). Ces travaux toujours en cours (cf. Fig. 37) soulèvent de nombreuses questions comme : Dans quelle mesure le champ dipolaire créé par les particules voisines est-il démagnétisant ? Quelle est l'influence de la dispersion de champ dipolaire ressenti par une particule ? Une description de type champ moyen est-elle raisonnable ? Permet-elle d'expliquer l'allure des courbes δm , ou bien la prise en compte des corrélations est-elle nécessaire ? Peut-on avoir des interactions interparticules tout en gardant un δm nul ? Comment l'influence des proches voisins se combine-t-elle aux effets de forme (couche, effet de champ démagnétisant) de l'échantillon ?

Nous cherchons à répondre à ces questions en confrontant des approches analytiques et numériques, de façon à enrichir notre compréhension physique du comportement des assemblées de nanoparticules magnétiques. Les descriptions théoriques seront confrontées par la suite aux observations expérimentales, via des mesures adéquates (champ appliqué selon différentes directions, effets de température sur les courbes δm etc.) sur des systèmes modèles de plots magnétiques ou d'assemblées d'agrégats en matrice.

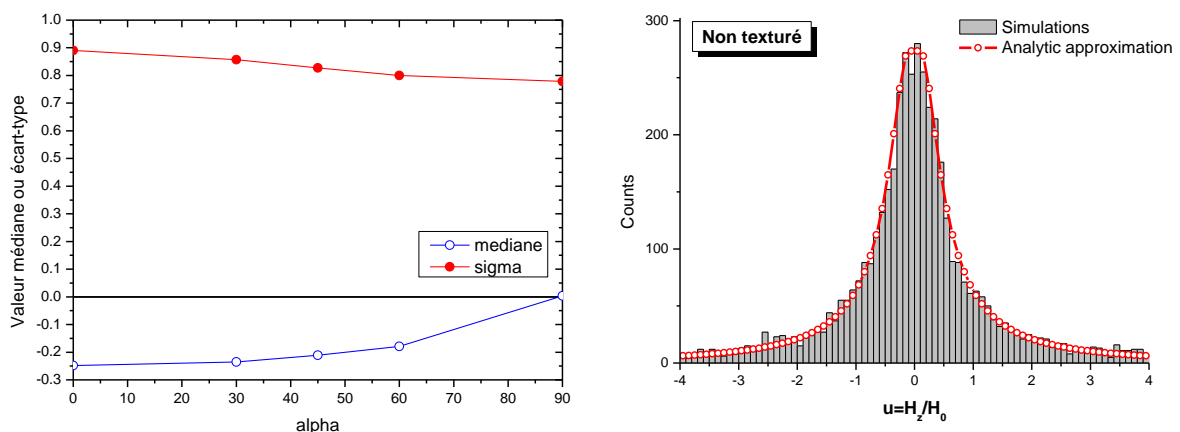


Fig. 37 : À gauche, valeur médiane et écart-type (sigma) de la distribution statistique de champ dipolaire créé par une particule voisine, situé à une distance d de la particule de référence, en fonction de l'angle α reflétant la texturation magnétique (0° correspond au cas saturé, tandis que 90° correspond au cas à rémanence c'est-à-dire le point de départ d'une mesure DCD). Les valeurs sont en unités réduites, c'est-à-dire rapportées au champ dipolaire $H_0 = m/(4\pi d^3)$, où m est le moment magnétique d'une particule. Il est important de noter que dans tous les cas la valeur moyenne de la distribution reste nulle, et on observe que la distribution de champ dipolaire dépend assez peu de l'état magnétique du système. À droite, distribution de champ dipolaire (selon un axe z arbitraire, et en unité réduite) dû au premier voisin, pour un système non texturé, en tenant compte de la distribution statistique des distances au premier voisin (d étant alors la distance moyenne). Les simulations numériques sont en excellent accord avec une approximation analytique simple (reflétant, pour chaque distance une distribution rectangulaire de champ dipolaire).

En plus de cette activité de modélisation sur les interactions dipolaires, on peut citer d'autres travaux prévus, comme la recherche de formules analytiques approchées pour l'évolution de la barrière d'énergie en fonction du champ appliqué dans le cas d'une anisotropie biaxiale, ou la mise au

point de protocoles de mesures complémentaires permettant de caractériser au mieux (c'est-à-dire en lien avec des modèles théoriques fiables) des systèmes de nanoparticules magnétiques.

4) Effets de taille finie dans les nanoparticules supraconductrices et systèmes nano-composites supra-ferro

Les effets de confinement quantique dans les nanoparticules isolées d'éléments supraconducteurs ont été peu étudiés, tandis qu'Anderson a prédit dès 1959 que la supraconductivité n'existait plus en dessous d'une taille critique (typiquement de quelques nanomètres, cf. Tableau 1 ci-dessous tiré de [Bose et al., Rep. Prog. Phys. **77**, 116503 (2014)]) pour laquelle le gap supra est égal à l'espacement entre les niveaux d'énergie électronique de la particule. Alors que de nombreux effets de taille ont été mis en évidence (modification des paramètres critiques, du couplage électron-phonon, de la densité d'états électroniques...), ceux-ci concernent principalement des systèmes supraconducteurs confinés selon une seule direction et des îlots en forte interaction avec un substrat, si bien que les propriétés ne reflètent pas celles d'un nano-système isolé. Ca n'est que très récemment que la validité du critère d'Anderson a été testée pour des particules de Pb (résultats du LPEM, ESPCI à Paris, non encore publiés) obtenus par croissance sur la surface (110) d'InAs. Cette surface permet d'observer le phénomène de blocage de Coulomb, signe du découplage entre le substrat et la particule de Pb, ainsi que des effets de parité reflétant l'existence d'un gap supraconducteur à basse température et au-dessus d'une certaine taille limite.

Table 1. Superconducting parameters for several common elemental superconductors and their reported particle size (PS) dependence. The '0' in the subscript refers to the value in large size limit.

Element	Type	T_{C0} (K)	H_{C0} (T) or H_{C20} (T) ^a	ξ_0 (nm)	λ_L (nm)	T_C/T_{C0} @ PS (nm)	H_{C2}/H_{C20} @ PS (nm)	d_{critical} (nm) Anderson
Al	I	1.14	0.0105	1600	16	3.24 @ \approx 4 nm [2]	\sim 200 @ 4 nm [2]	6.2
Sn	I	3.72	0.0309	230	34	1.6 @ \approx 10 nm [34]	\sim 100 @ 16 nm [4]	4.3
Pb	I	7.19	0.0803	83	37	0.5 @ \approx 4 nm [36]	\sim 110 @ 7.5 nm [40]	3.5
In	I	3.40	0.0293	364	64	1.1 @ \approx 10 nm [7]	\sim 170 @ 36 nm [106]	5.5
Nb	II	9.50	0.1980	38	39	0.5 @ \approx 8 nm [16]	\sim 25 @ 19 nm [41]	6.0

^a The value of critical field quoted is H_{C0} for type I and H_{C20} for type II superconductors.

En collaboration avec H. Aubin du LPEM, nous avons comme projet d'étudier par spectroscopie STS le comportement de nanoparticules préformées déposées sur InAs. L'intérêt de l'approche par dépôt d'agrégats est de ne pas être limité à un type d'îlot, mais d'être versatile en offrant des possibilités variées et inédites (en termes de forme, taille et composition des particules), tout en gardant des systèmes très propres et bien définis compatibles avec des études en physique des surfaces. Il s'agira pour ce travail d'utiliser un système de clivage de substrats d'InAs sous UHV pour obtenir une surface vierge sur laquelle seront ensuite déposés des agrégats (Pb, Sn...). Ceux-ci pourront être étudiés par STM/STS *in situ* (microscope directement connecté à la chambre de dépôt d'agrégats) à température ambiante dans un premier temps, puis à basse température grâce à un système de transfert d'échantillon sous UHV entre Lyon et Paris. Ce travail a débuté fin 2016 en collaboration avec Laurent Bardotti et Pierre Capiod (post-doc).

Par ailleurs, dans l'objectif de mieux comprendre les effets de proximité ferro-supra (pouvant donner lieu à des comportements exotique du type fermion de Majorana), qui se manifestent à l'échelle nanométrique dans des systèmes hybrides, nous pourrions également étudier des

nanoparticules magnétiques déposées sur une surface supraconductrice comme NbSe₂. En plus des effets de confinement étudiés sur des nano-objets individuels, il sera possible de confronter les résultats aux propriétés d'ensemble mesurées (par magnétométrie ou transport électronique) pour des particules noyées dans une matrice (métallique ou magnétique). Le dépôt de nanoparticules en matrice permet d'envisager différents types de systèmes nano-composites ferro-supra : nanoparticules magnétiques en matrice supra, ou réciproquement nanoparticules supra dans une matrice magnétique. Ces systèmes originaux pourront être caractérisés à l'aide de mesures de transport électrique (résistivité, magnéto-résistance) et de magnétométrie (susceptibilité, cycles d'aimantation, cf. Fig. 38). Nous aurons alors accès aux paramètres critiques (température et champ critiques) et nous pourrons étudier les couplages entre magnétisme et supraconductivité dans ces assemblées de particules. Par exemple, on peut s'attendre à une modification des paramètres critiques dans un composite supra contenant des macrospins (où l'on peut changer la configuration magnétique bloquée).

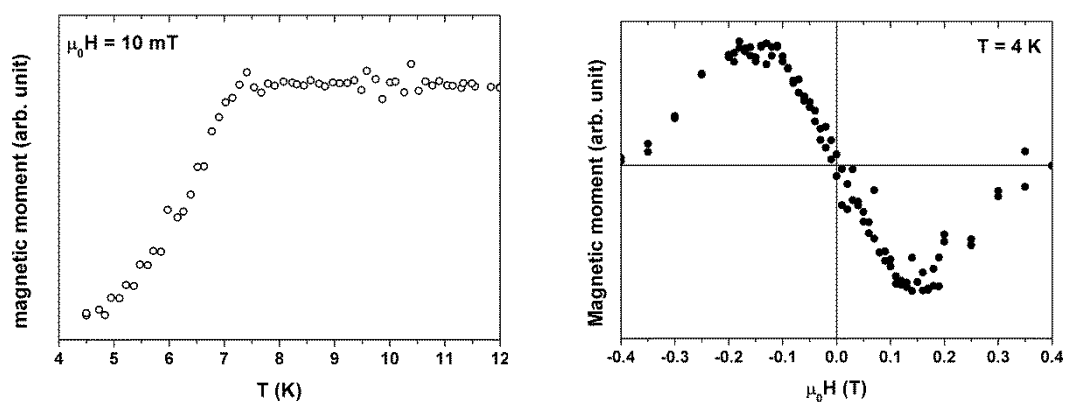
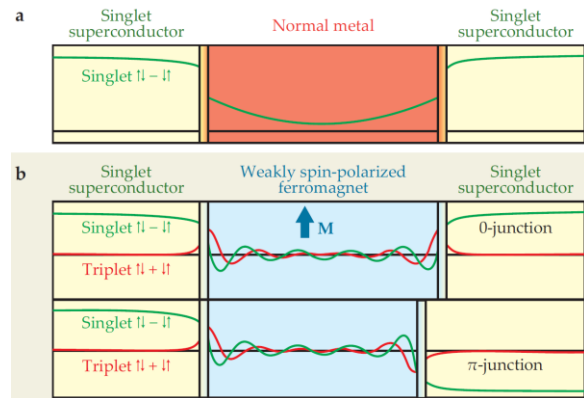


Fig. 38 : Mesures expérimentales de magnétométrie sur une couche d'environ 40 nm d'agrégats de Pb, laissant apparaître la signature de l'état supraconducteur à basse température. À gauche, mesure de susceptibilité $m(T)$ avec un champ appliqué de 10 mT où l'on détecte la transition supra vers 7 K. À droite, cycle d'aimantation $m(H)$ caractéristique de l'état supraconducteur (champ critique et diamagnétisme parfait à bas champ). Ces premiers résultats sur des couches d'agrégats de plomb (non triés, non dilués en matrice) sont encourageants.

Ce type de système devrait en outre permettre d'étudier l'effet d'écrantage de spin prédit théoriquement (dû à un effet de proximité inverse, où le supra modifie les propriétés magnétique du ferro). Il est important de noter que pour nos systèmes mixtes ferro-supra à base de nanoparticules, nous avons une géométrie non planaire originale (les multicouches sont beaucoup étudiées) qui permet d'envisager de nouvelles propriétés. Alors que la réalisation de vanes de spin supraconductrices planaires est difficile, un système granulaire (nano-composite, qui constitue un réseau de jonctions Josephson) pourrait bénéficier des effets de proximité ferro-supra (comme l'apparition de jonctions π , cf. schéma de la Fig. 39) et ainsi présenter des propriétés exotiques (par exemple de magnéto-résistance). Cette thématique est avant tout fondamentale et centrée sur la compréhension et la mise en évidence de mécanismes physiques rencontrés dans les systèmes nano-hybrides ferro/supra.

Fig. 39 : Évolution schématique de l'amplitude de la fonction d'onde de l'état supraconducteur (paires de Cooper) pour une couche de métal normal (en haut) ou de métal ferromagnétique (en bas) intercalée entre deux supraconducteurs. L'apparition d'une jonction π , pour une certaine épaisseur de la couche ferromagnétique, est une manifestation des effets de proximité ferro-supra. Figure tirée de [Eschrig et al., *Phys. Today* **64**, 43 (2011)].



5) Spécificités des nanoparticules bimétalliques, couplage structure-magnétisme

Cette thématique, déjà explorée depuis une dizaine d'année dans le groupe, a montré qu'elle pouvait être très fructueuse avec des résultats originaux obtenus grâce aux études combinées de structure (à l'échelle atomique) et de magnétisme. Le système CoPt a ainsi fait l'objet d'une thèse (Nils Blanc), dont les travaux se sont poursuivis avec l'étude conjointe du FePt. Ces deux systèmes sont très proches mais présentent néanmoins des comportements magnétiques différents, qui restent à creuser dans le cas du FePt (en particulier, contrairement au CoPt, nous avons pu obtenir une très grande anisotropie magnétique dans le cas de nanoparticules de FePt). De même, la compréhension des propriétés magnétiques du FeRh (thèse d'A. Hillion, poursuivie par des études menées dans le cadre de la thèse de G. Khadra et A. Robert), pour lequel la transition métamagnétique n'a pas été observée dans nos petites nanoparticules, mérite des travaux complémentaires. Dans ce système, qui intéresse de nombreuses équipes, structure et magnétisme sont intimement liés, c'est pourquoi de nombreuses questions restent ouvertes (effets du facettage, effets de matrice, effets des distorsions de distances interatomiques...) nécessitant des investigations poussées.

Au-delà des questions portant sur les effets de mise en ordre chimique, de ségrégation ou d'interface, qui seront approfondies pour les systèmes de nanoparticules actuellement considérés (cf. Fig. 40 par exemple pour l'observation d'un ordre chimique inattendu dans des particules de FeAu ou des effets d'interface importants sur le magnétisme de particules de CoAu), il me semble intéressant de se pencher sur les contraintes au sein des particules (déformations, « twinning » ou formation de mâcles) et les effets magnéto-élastiques. Ces derniers, lorsqu'ils mettent en jeu une transition de phase permettent d'obtenir des effets magnéto-caloriques ou un contrôle de transformations structurales à l'aide d'un champ magnétique. De tels effets sont à l'œuvre dans le cas de matériaux ferromagnétiques à mémoire de forme (magnetic shape memory alloys), comme illustré sur la Fig. 41. Peu de travaux ont porté sur des systèmes nanométriques d'alliages magnétiques à mémoire de forme, c'est pourquoi nous pourrions mettre à profit notre savoir-faire (production de nanoparticules bien maîtrisées, caractérisations structurales et magnétiques) pour étudier sous cet angle là des matériaux comme FePd ou NiTi, ou encore des alliages de type Heusler comme Ni-Mn-X (avec X = Ga, Sn, Sb ou In) voire des systèmes plus complexes ou moins courants (Fe ou NiCo à la place de Ni). La présence à l'ILM de chercheurs spécialistes des hautes pressions (équipe (nano)Matériaux pour l'énergie) pourrait aussi donner lieu à de futures collaborations sur de tels systèmes. On peut aussi remarquer que cette thématique peut rejoindre celle présentée plus haut sur les effets d'interface (particules déposées sur

des surfaces), en particulier concernant le domaine de la « straintronics » où la déformation permet d’agir sur les propriétés (magnétiques notamment) d’un nano-objet, via l’utilisation par exemple d’un substrat ou une matrice piézoélectrique.

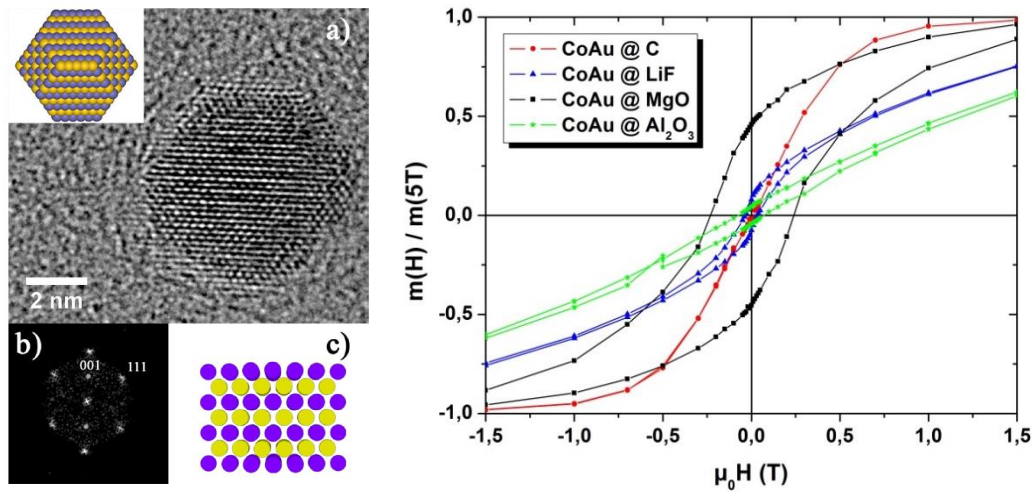


Fig. 40 : À gauche, image METHR d’une particule FeAu recuite présentant la signature d’un ordre chimique $L1_0$ (la FFT correspondante est représentée en b), ainsi que la structure schématique en c). Figure tirée de la thèse d’A. Hillion. À droite, cycles d’hystérésis mesurés à 2 K pour des particules de CoAu non triées en taille noyées dans différentes matrices : alors que les particules incidentes sont les mêmes, les propriétés magnétiques (taille, anisotropie) sont très différentes selon le milieu environnant des nanoparticules, ceci étant très certainement lié à des modifications structurales selon le type de matrice.

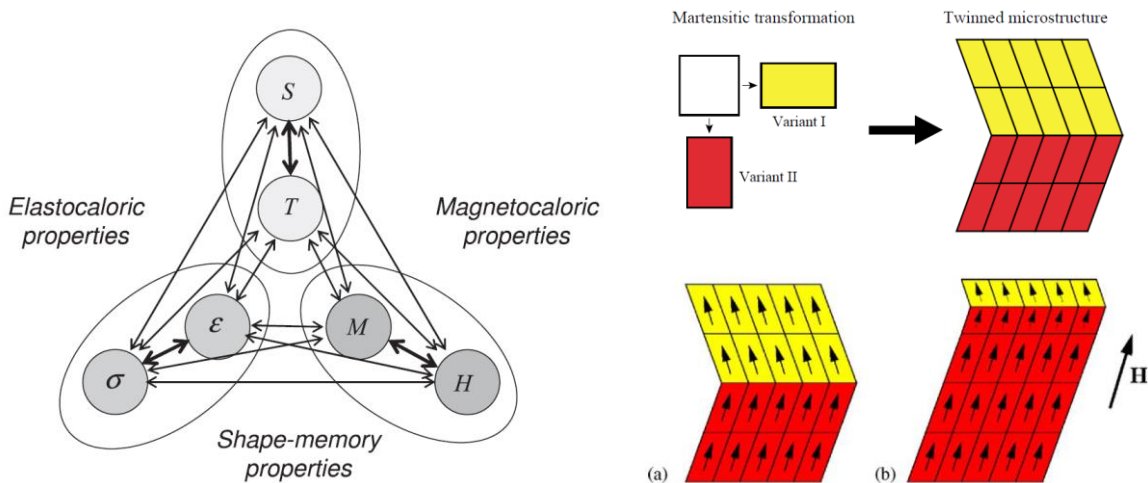


Fig. 41 : À gauche, représentation schématique des liens entre variables thermodynamiques dans le cas des matériaux magnétiques à mémoire de forme. Figure tirée de [Planes et al., *J. Phys.: Cond. Mat.* **21**, 233201 (2009)]. À droite, en haut représentation schématique (en 2D) du lien entre le phénomène de « twinning » et la transformation martensitique rencontrée dans les métaux à mémoire de forme ; en bas, illustration de la redistribution des variants (pour un matériau présentant une aimantation, schématisée ici par les flèches) sous l’effet d’un champ magnétique appliqué (a= sans champ, b=avec champ). Figure tirée de [Enkovaara et al., *Mater. Sci. Engin. A* **378**, 52 (2004)].

6) Nanothermique et magnétisme

Un autre sujet, très prospectif, auquel j'aimerais m'intéresser concerne les aspects thermiques à l'échelle des nanoparticules magnétiques. Il ne s'agit pas ici de s'intéresser à des phénomènes tels que l'hyperthermie (déjà beaucoup étudiée, généralement avec des particules en solution synthétisées par voie chimique) où l'application d'un champ magnétique se traduit par une dissipation d'énergie, mais au contraire d'utiliser le magnétisme comme sonde d'effets nano-thermiques.

D'une manière générale, les propriétés magnétiques de nanoparticules peuvent très fortement dépendre de la température : en effet, le taux de retournement d'un macrospin fait intervenir le ratio $\Delta E/k_B T$ dans une exponentielle, ce qui est d'ailleurs à l'origine du phénomène de superparamagnétisme (ΔE représente la barrière d'énergie à franchir, c'est-à-dire l'énergie d'anisotropie magnétique lorsqu'aucun champ n'est appliqué, mais cette barrière peut être abaissée par application d'un champ). Dans une moindre mesure, la susceptibilité d'une assemblée de nano-aimants dans le régime superparamagnétique varie de manière inversement proportionnelle à la température. Ceci permet d'envisager d'utiliser les caractéristiques magnétiques de nanoparticules comme sonde de température, ce qui me semble être une idée originale. De plus, du fait de leur taille nanométrique, ces sondes pourraient donner une information à l'échelle du nanomètre. Bien sûr, la réalisation de dispositifs mettant en jeu une nanoparticule unique représente un défi (insurmontable ?), mais une approche alternative, s'intéressant à la réponse magnétique d'une assemblée diluée de nanoparticules, peut être fructueuse. Par exemple, on peut tout à fait envisager d'effectuer des mesures de magnétométrie couplées à une illumination laser dans le SQUID. Nous pourrions ainsi être en mesure de détecter indirectement, via l'évolution des propriétés magnétiques des particules, l'élévation de température locale (au niveau des nanoparticules magnétiques) en fonction de différents paramètres (longueur d'onde du laser, durée des pulses, taille des particules, matrice...). Ceci serait particulièrement intéressant dans le cas de systèmes mixtes magnéto-plasmoniques présentant une résonance (d'absorption) autour d'une certaine longueur d'onde dans le visible.

ANNEXE

1) Liste de publications

(par ordre chronologique inverse)

- [**Tournus2016**] “Anisotropy evolution of nanoparticles under annealing: Benefits of isothermal remanent magnetization simulation”, F. Tournus, A. Tamion, A. Hillion, V. Dupuis, J. Magn. Magn. Mater. **419**, 1 (2016).
- [**Dupuis2016**] “Cubic chemically ordered FeRh and FeCo nanomagnets prepared by mass-selected low-energy cluster-beam deposition: a comparative study”, V. Dupuis, A. Robert, A. Hillion, G. Khadra, N. Blanc, D. Le Roy, F. Tournus, C. Albin, O. Boisron, A. Tamion, Beilstein J. Nanotech. **7**, 1850 (2016).
- [**Oyarzun2015**] “Size effects in the magnetic anisotropy of embedded cobalt nanoparticles: from shape to surface”, S. Oyarzun, A. Tamion, F. Tournus, V. Dupuis, M. Hillenkamp, Sci. Rep. **5**, 14749 (2015).
- [**Tournus2015**] “Modelling of isothermal remanence magnetisation curves for an assembly of macrospins”, F. Tournus, J. Magn. Magn. Mater. **375**, 194 (2015).
- [**Khadra2015**] “Anisotropy in FeCo nanoparticles, a first step”, G. Khadra, A. Tamion, F. Tournus, B. Canut, V. Dupuis, Solid State Phenomena **233–234**, 550 (2015).
- [**Andreazza2015**] “Structure and order in cobalt/platinum-type nanoalloys: from thin films to supported clusters”, P. Andreazza, V. Pierron-Bohnes, F. Tournus, C. Andreazza-Vignolle, V. Dupuis, Surf. Sci. Rep. **70**, 188 (2015).
- [**Linass2015**] “Moiré induced organization of size-selected Pt clusters soft landed on epitaxial graphene”, S. Linas, F. Jean, T. Zhou, C. Albin, G. Renaud, L. Bardotti, F. Tournus, Sci. Rep. **5**, 3053 (2015).
- [**Linass2015a**] “Interplay between Raman shift and thermal expansion in graphene: Temperature-dependent measurements and analysis of substrate corrections”, S. Linas, Y. Magnin, B. Poinso, O. Boisron, G. D. Forster, V. Martinez, R. Fulcrand, F. Tournus, V. Dupuis, F. Rabilloud, L. Bardotti, Z. Han, D. Kalita, V. Bouchiat, F. Calvo, Phys. Rev. B **91**, 075426 (2015).
- [**Dupuis2015**] “Intrinsic magnetic properties of bimetallic nanoparticles elaborated by cluster beam deposition”, V. Dupuis, G. Khadra, A. Hillion, A. Tamion, J. Tuaille-Combes, L. Bardotti, F. Tournus, Phys. Chem. Chem. Phys. **17**, 27996–28004 (2015).
- [**Dupuis2015a**] “Magnetic moments in chemically ordered mass-selected CoPt and FePt clusters”, V. Dupuis, G. Khadra, S. Linas, A. Hillion, L. Gragnaniello, A. Tamion, J. Tuaille-Combes, L. Bardotti, F. Tournus, E. Otero, P. Ohresser, A. Rogalev, F. Wilhelm, J. Magn. Magn. Mater. **383**, 73 (2015).
- [**Bardotti2014**] “Self-organisation of size-selected $\text{Co}_x\text{Pt}_{1-x}$ clusters on graphite”, L. Bardotti, F. Tournus, C. Albin, O. Boisron, V. Dupuis, Phys. Chem. Chem. Phys. **16**, 26653 (2014).
- [**Bardotti2014a**] “Behavior of size selected iron-platinum clusters soft landed on carbon nanotubes”, L. Bardotti, F. Tournus, R. Delagrang, J. M. Benoit, O. Pierre-Louis, V. Dupuis, Appl. Surf. Sci. **301**, 564-567 (2014).
- [**Delagrang2014**] “Dimensionality transition in submonolayer growth on carbon nanotubes”, R. Delagrang, F. Tournus, L. Bardotti, J. M. Benoit, O. Pierre-Louis, Phys. Rev. B **89**, 035425 (2014).
- [**Papaefthimiou2014**] “Mixing Patterns and Redox Properties of Iron-Based Alloy Nanoparticles under Oxidation and Reduction Conditions”, V. Papaefthimiou, F. Tournus, A. Hillion, G. Khadra, D. Teschner, A. Knop-Gericke, V. Dupuis, S. Zafeiratos, Chem. Mater. **26**, 1553 (2014).
- [**DeToro2014**] “Ideal superspin glass behaviour in a random-close-packed ensemble of maghemite nanoparticles”, J. A. De Toro, S. S. Lee, R. Mathieu, P. S. Normile, D. Salazar, J. L. Cheong, P. Muñiz, J. M. Riveiro, M. Hillenkamp, A. Tamion, F. Tournus, P. Nordblad, J. Phys.: Conf. Ser. **521**, 012011 (2014).
- [**DeToro2013**] “A nanoparticle replica of the spin-glass state”, J. A. De Toro, S. S. Lee, D. Salazar, J. L. Cheong, P. S. Normile, P. Muñiz, J. M. Riveiro, M. Hillenkamp, F. Tournus, A. Tamion, P. Nordblad, Appl. Phys. Lett. **102**, 183104 (2013).
- [**DeToro2013a**] “Controlled Close-Packing of Ferrimagnetic Nanoparticles: An Assessment of the Role of Interparticle Superexchange Versus Dipolar Interactions”, J. A. De Toro, P. S. Normile, S. S. Lee, D. Salazar, J. L. Cheong, M. Hillenkamp, F. Tournus, A. Tamion, P. Muñiz, J. M. Riveiro, P. Nordblad, J. Phys. Chem. C **117**, 10213 (2013).

- [**Tournus2013**] “Effect of nonlinear superparamagnetic response on susceptibility curves for nanoparticle assemblies”, F. Tournus, A. Hillion, A. Tamion, V. Dupuis, Phys. Rev. B **87**, 174404 (2013).
- [**Tournus2013a**] “Comment on “Nano-particle magnetism with a dispersion of particle sizes” [J. Appl. Phys. 112, 103915 (2012)]”, F. Tournus, A. Tamion, J. Appl. Phys. **114**, 126101 (2013).
- [**Tournus2013b**] “Multi- $L1_0$ domain CoPt and FePt nanoparticles revealed by electron microscopy”, F. Tournus, K. Sato, T. Epicier, T. J. Konno, V. Dupuis, Phys. Rev. Lett. **110**, 055501 (2013).
- [**Blanc2013**] “Element-specific quantitative determination of the local atomic order in CoPt alloy nanoparticles: Experiment and theory”, N. Blanc, L. E. Diaz-Sanchez, A. Y. Ramos, F. Tournus, H. C. N. Tolentino, M. De Santis, O. Proux, A. Tamion, J. Tuaille-Combes, L. Bardotti, O. Boisron, G. M. Pastor, V. Dupuis, Phys. Rev. B **87**, 155412 (2013).
- [**Hillion2013**] “Low temperature ferromagnetism in chemically ordered FeRh nanocrystals”, A. Hillion, A. Cavallin, S. Vlais, A. Tamion, F. Tournus, G. Khadra, J. Dreiser, C. Piamonteze, F. Nolting, S. Rusponi, K. Sato, T. J. Konno, O. Proux, V. Dupuis, H. Brune, Phys. Rev. Lett. **110**, 087207 (2013).
- [**Hillion2013a**] “Advanced magnetic anisotropy determination through isothermal remanent magnetization of nanoparticles”, A. Hillion, A. Tamion, F. Tournus, O. Gaier, E. Bonet, C. Albin, V. Dupuis, Phys. Rev. B **88**, 094419 (2013).
- [**Dupuis2013**] “Specific local relaxation and magnetism in mass-selected CoPt nanoparticles”, V. Dupuis, N. Blanc, L. E. Diaz-Sanchez, A. Hillion, A. Tamion, F. Tournus, G. M. Pastor, Eur. Phys. J. B **86**, 1 (2013).
- [**Dupuis2013a**] “Finite size effects on structure and magnetism in mass-selected CoPt nanoparticles”, V. Dupuis, N. Blanc, L. E. Diaz-Sanchez, A. Hillion, A. Tamion, F. Tournus, G. M. Pastor, A. Rogalev, F. Wilhelm, Eur. Phys. J. D **67**, 25 (2013).
- [**Hillion2012**] “Combined fitting of alternative and direct susceptibility curves of assembled nanostructures”, A. Hillion, M. Pauly, A. Tamion, F. Tournus, M. Hillenkamp, B. P. Pichon, S. Begin-Colin, V. Dupuis, J. Appl. Phys. **112**, 123902 (2012).
- [**Epicier2012**] “Chemical composition dispersion in bi-metallic nanoparticles: semi-automated analysis using HAADF-STEM”, T. Epicier, K. Sato, F. Tournus, T. Konno, J. Nanopart. Res. **14**, 1106 (2012).
- [**Tamion2012**] “Efficient hysteresis loop simulations of nanoparticle assemblies beyond the uniaxial anisotropy”, A. Tamion, E. Bonet, F. Tournus, C. Raufast, A. Hillion, O. Gaier, V. Dupuis, Phys. Rev. B **85**, 134430 (2012).
- [**Tamion2012a**] Response to “Comment on ‘Accurate determination of the magnetic anisotropy in cluster-assembled nanostructures’” [Appl. Phys. Lett. **100**, 136101 (2012)], A. Tamion, M. Hillenkamp, F. Tournus, E. Bonet, V. Dupuis, Appl. Phys. Lett. **100**, 136102 (2012).
- [**Bardotti2012**] “Spontaneous formation of size-selected bimetallic nanoparticle arrays”, L. Bardotti, F. Tournus, M. Pellarin, M. Broyer, P. Mélinon, V. Dupuis, Surf. Sci. **606**, 110 (2012).
- [**Tamion2011**] “Demixing in cobalt clusters embedded in a carbon matrix evidenced by magnetic measurements”, A. Tamion, M. Hillenkamp, A. Hillion, F. Tournus, J. Tuaille-Combes, O. Boisron, S. Zafeiratos, V. Dupuis, J. Appl. Phys. **110**, 063904 (2011).
- [**Papaefthimiou2011**] “Nontrivial Redox Behavior of Nanosized Cobalt: New Insights from Ambient Pressure X-ray Photoelectron and Absorption Spectroscopies”, V. Papaefthimiou, T. Dintzer, V. Dupuis, A. Tamion, F. Tournus, A. Hillion, D. Teschner, M. Havecker, A. Knop-Gericke, R. Schloegl, S. Zafeiratos, ACS Nano **5**, 2182 (2011).
- [**Papaefthimiou2011a**] “When a Metastable Oxide Stabilizes at the Nanoscale: Wurtzite CoO Formation upon Dealloying of PtCo Nanoparticles”, V. Papaefthimiou, T. Dintzer, V. Dupuis, A. Tamion, F. Tournus, D. Teschner, M. Havecker, A. Knop-Gericke, R. Schlögl, S. Zafeiratos, J. Phys. Chem. Lett. **2**, 900 (2011).
- [**Tournus2011**] “Signature of multimers on magnetic susceptibility curves for mass-selected Co particles”, F. Tournus, A. Tamion, N. Blanc, A. Hillion, V. Dupuis, J. Appl. Phys. **109**, 07B502 (2011).
- [**Tournus2011a**] “Coalescence-free $L1_0$ ordering of embedded CoPt nanoparticles”, F. Tournus, N. Blanc, A. Tamion, V. Dupuis, T. Epicier, J. Appl. Phys. **109**, 07B722 (2011).

- [**Tournus2011b**] “Comment on “Determining magnetic nanoparticle size distributions from thermomagnetic measurements” [Appl. Phys. Lett. 96, 222506 (2010)]”, F. Tournus, A. Tamion, Appl. Phys. Lett. **98**, 216102 (2011).
- [**Tournus2011c**] “Size-dependent morphology of CoPt cluster films on graphite: A route to self-organization”, F. Tournus, L. Bardotti, V. Dupuis, J. Appl. Phys. **109**, 114309 (2011).
- [**Tournus2011d**] “Multimer formation for two-dimensional random nanoparticle deposition”, F. Tournus, Phys. Rev. E **84**, 011612 (2011).
- [**Tournus2011e**] “Random nanoparticle deposition: inter-particle distances in 2D, 3D, and multilayer samples”, F. Tournus, J. Nanopart. Res. **13**, 5211 (2011).
- [**Tournus2011f**] “Synthesis and magnetic properties of size-selected CoPt nanoparticles”, F. Tournus, N. Blanc, A. Tamion, M. Hillenkamp, V. Dupuis, J. Magn. Magn. Mater. **323**, 1868 (2011).
- [**Tournus2011g**] “Magnetic susceptibility curves of a nanoparticle assembly, I: Theoretical model and analytical expressions for a single magnetic anisotropy energy”, F. Tournus, E. Bonet, J. Magn. Magn. Mater. **323**, 1109 (2011).
- [**Tournus2011h**] “Magnetic susceptibility curves of a nanoparticle assembly II. Simulation and analysis of ZFC/FC curves in the case of a magnetic anisotropy energy distribution”, F. Tournus, A. Tamion, J. Magn. Magn. Mater. **323**, 1118 (2011).
- [**Blanc2011**] “Measuring the $L1_0$ chemical order parameter of a single CoPt nanoparticle smaller than 4 nm”, N. Blanc, F. Tournus, V. Dupuis, T. Epicier, Phys. Rev. B **83**, 092403 (2011).
- [**Bardotti2011**] “Mass-selected clusters deposited on graphite: Spontaneous organization controlled by cluster surface reaction”, L. Bardotti, F. Tournus, P. Mélinon, M. Pellarin, M. Broyer, Phys. Rev. B **83**, 035425 (2011).
- [**Bardotti2011a**] “Self organisation of Pt and Au clusters deposited on graphite: the role of reactivity”, L. Bardotti, F. Tournus, P. Mélinon, M. Pellarin, M. Broyer, Eur. Phys. J. D **63**, 221 (2011).
- [**Hillion2011**] “Magnetic Interactions Effects on Magnetic Measurements for Nanoparticle Assemblies”, A. Hillion, A. Tamion, F. Tournus, J.-B. Flament, M. Hillenkamp, E. Bonet, V. Dupuis, IEEE Trans. Magn. **47**, 3154 (2011).
- [**Dupuis2011**] “Local Order and Magnetic Properties in Mass-Selected $L1_0$ CoPt Nanoparticles”, V. Dupuis, N. Blanc, F. Tournus, A. Tamion, J. Tuaille-Combes, L. Bardotti, O. Boisron, IEEE Trans. Magn. **47**, 3358 (2011).
- [**Tournus2010**] “Dispersion of magnetic anisotropy in size-selected CoPt clusters”, F. Tournus, N. Blanc, A. Tamion, M. Hillenkamp, V. Dupuis, Phys. Rev. B **81**, 220405(R) (2010).
- [**Perez2010**] “Functional nanostructures from clusters”, A. Perez A., P. Mélinon, V. Dupuis, L. Bardotti, B. Masenelli, F. Tournus, B. Prével, J. Tuaille-Combes, E. Bernstein, A. Tamion, N. Blanc, D. Tainoff, O. Boisron, G. Guiraud, M. Broyer, M. Pellarin, N. Del Fatti, F. Vallée, J.-L. Vialle, C. Bonnet, P. Maioli, Inter. J. Nanotech. **7**, 523 (2010).
- [**Tamion2009**] “Accurate determination of the magnetic anisotropy in cluster-assembled nanostructures”, A. Tamion, M. Hillenkamp, F. Tournus, E. Bonet et V. Dupuis, Appl. Phys. Lett. **95**, 062503 (2009).
- [**Tournus2008**] “Evidence of $L1_0$ chemical order in CoPt nanoclusters: Direct observation and magnetic signature”, F. Tournus, A. Tamion, N. Blanc, A. Hannour, L. Bardotti, B. Prevel, P. Ohresser, E. Bonet, T. Epicier, V. Dupuis, Phys. Rev. B **77**, 144411 (2008).
- [**Tournus2008a**] “XMCD study of CoPt nanoparticles embedded in MgO and amorphous carbon matrices”, F. Tournus, N. Blanc, A. Tamion, P. Ohresser, A. Perez, V. Dupuis, J. Electr. Spectr. and Rel. Phenom. **166**, 84 (2008).
- [**Tournus2008b**] “Magnetic Anisotropy Dispersion in CoPt Nanoparticles: An Evaluation Using the Néel Model”, F. Tournus, S. Rohart, V. Dupuis, IEEE Trans. Magn. **44**, 3201 (2008).
- [**Tainoff2008**] “Self-organization of size-selected bare platinum nanoclusters: Toward ultra-dense catalytic systems”, D. Tainoff, L. Bardotti, F. Tournus, G. Guiraud, O. Boisron, P. Melinon, J. Phys. Chem. C **112**, 6842 (2008).

- [**Moskovkin2007**] “*Model predictions and experimental characterization of Co-Pt alloy clusters*”, P. Moskovkin, S. Pisov, M. Hou, C. Raufast, F. Tournus, L. Favre, V. Dupuis, Euro. Phys. J. D **43**, 27 (2007).
- [**Mélinon2007**] “*Playing with carbon and silicon at the nanoscale*”, P. Mélinon, B. Masenelli, F. Tournus, A. Perez, Nature Materials **6**, 479 (2007).
- [**Tournus2005**] “ *π -stacking interaction between carbon nanotubes and organic molecules*”, F. Tournus, S. Latil, M. I. Heggie, J.-C. Charlier, Phys. Rev. B **72**, 075431 (2005).
- [**Tournus2005a**] “*Comment on “In situ x-ray photoelectron spectroscopic and density-functional studies of Si atoms adsorbed on a C_{60} film” [J. Chem. Phys. **121**, 11351 (2004)]*”, F. Tournus, B. Masenelli, P. Mélinon, J. Le Brusq, A. Perez, J. Chem. Phys. **122**, 237101 (2005).
- [**Tournus2005b**] “*Ab initio study of benzene adsorption on carbon nanotubes*”, F. Tournus, J.-C. Charlier, Phys. Rev. B **71**, 165421 (2005).
- [**Tournus2005b**] “*Mutual orientation of two C_{60} molecules: An ab initio study*”, F. Tournus, J.-C. Charlier, P. Mélinon, J. Chem. Phys. **122**, 094315 (2005).
- [**SanMiguel2005**] “*Synchrotron studies on silicon clathrates: highly stable nanostructured materials*”, A. San Miguel, P. Toulemonde, A. Merlen, B. Masenelli, F. Tournus, T. Kume, S. Le Floch, A. Aouizerat, S. Pascarelli, G. Aquilanti, O. Mathon, T. Le Bihan, J.-P. Itié, S. Yamanaka, Nuclear Instruments and Methods in Physics Research B **238**, 163 (2005).
- [**Tournus2004**] “*Guest displacement in silicon clathrates*”, F. Tournus, B. Masenelli, P. Mélinon, D. Connétable, A. M. Flank, P. Lagarde, C. Cros, M. Pouchard, Phys. Rev. B **69**, 035208 (2004).
- [**Masenelli2004**] “*Nanostructured films from $(C_{60})_nSi_m$ Clusters*”, B. Masenelli, F. Tournus, P. Mélinon, X. Blase, A. Perez, M. Pellarin, M. Broyer, Appl. Surf. Sci. **226**, 226 (2004).
- [**Masenelli2004a**] “*Towards non-van der Waals C_{60} -based materials*”, B. Masenelli, F. Tournus, P. Mélinon, X. Blase, A. Pérez, M. Pellarin, M. Broyer, A. M. Flank, P. Lagarde, Mater. Sci. Eng. A **375-377**, 1285 (2004).
- [**Masenelli2003**] “*Si- C_{60} bond in cluster-based materials*”, B. Masenelli, F. Tournus, P. Mélinon, X. Blase, A. Pérez, M. Pellarin, M. Broyer, A. M. Flank, P. Lagarde, Surf. Sci. **532-535**, 875 (2003).
- [**Pellarin2003**] “*Photodissociation and photoionization of sodium coated C_{60} clusters*”, M. Pellarin, E. Cottancin, J. Lermé, J. L. Vialle, M. Broyer, F. Tournus, B. Masenelli, P. Mélinon, Eur. Phys. J. D **25**, 31 (2003).
- [**Masenelli2002**] “*Ab initio study of C_{60} -silicon clusters*”, B. Masenelli, F. Tournus, P. Mélinon, A. Pérez, X. Blase, J. Chem. Phys. **117**, 10627 (2002).
- [**Pellarin2002**] “*Coating and polymerisation of C_{60} with carbon: A gas phase photodissociation study*”, M. Pellarin, E. Cottancin, J. Lermé, J. L. Vialle, M. Broyer, F. Tournus, B. Masenelli, P. Mélinon, J. Chem. Phys. **117**, 3088 (2002).
- [**Tournus2002**] “*Bridging C_{60} by silicon: Towards non-van der Waals C_{60} -based materials*”, F. Tournus, B. Masenelli, P. Mélinon, X. Blase, A. Perez, M. Pellarin, M. Broyer, A. M. Flank, P. Lagarde, Phys. Rev. B **65**, 165417 (2002).
- [**SanMiguel2002**] “*Pressure stability and low compressibility of intercalated cage-like materials: The case of silicon clathrates*”, A. San Miguel, P. Mélinon, D. Connétable, X. Blase, F. Tournus, E. Reny, S. Yamanaka, J. P. Itié, Phys. Rev. B **65**, 054109 (2002).
- [**Perez2001**] “*Nanostructured Materials from Clusters: Synthesis and Properties*”, A. Pérez, P. Mélinon, V. Dupuis, B. Prével, L. Bardotti, J. Tuaille-Combes, B. Masenelli, M. Treilleux, M. Pellarin, J. Lermé, E. Cottancin, M. Broyer, M. Jamet, M. Négrier, F. Tournus, M. Gaudry, Mater. Trans. **42**, 1460 (2001).

2) Curriculum Vitæ

Florent TOURNUS

Français
Marié, deux enfants
38 ans
Date de naissance : 05/03/1978

Adresse personnelle :
52 av. Félix Faure
69003 Lyon, France
Tél. : 09 52 82 04 88



e-mail: florent.tournus@univ-lyon1.fr

Chargé de Recherche (CR1) CNRS, section 03
Groupe « Nanostructures Magnétiques », Institut Lumière Matière (UMR5306)

Formation universitaire et diplômes :

- 2000-2003 Université Lyon 1 :
Thèse de physique au laboratoire de physique de la matière condensée et nanostructures (LPMCN) :
« Étude du dopage de matériaux covalents cages nanostructurés ».
Soutenue le 08/10/2003 à l'Université Lyon 1.
- Juin 2000 École Normale Supérieure de Lyon – Université Lyon 1 :
Diplôme de Magistère des sciences de la matière, mention assez bien.
- 1999-2000 Université Lyon 1 :
DEA « Matière condensée, surfaces et interfaces », mention très bien, rang : 1^{er}.
- 1998-1999 École Normale Supérieure de Lyon :
Maîtrise de physique.
- 1997-1998 École Normale Supérieure de Lyon :
Licence de physique.
- 1995-1997 Lycée Henri IV, Paris :
Classes préparatoires aux grandes écoles (PCSI et PC*).
- 1994-1995 Lycée Marcel Roby, St Germain en Laye :
Baccalauréat série S, mention très bien.

Emplois :

- 10/2005- CNRS : Chargé de recherche au LPMCN (Université Lyon 1), devenu ILM.
- 11/2004-09/2005 CEA Grenoble : Ingénieur (post-doctorant) au laboratoire nanostructures et magnétisme (DRFMC/SP2M/NM).
- 11/2003-10/2004 Université Catholique de Louvain (Belgique) : Assistant de recherche (post-doctorant) dans l'unité de physico-chimie et de physique des matériaux (PCPM).
- 09/2001-10/2003 Université Lyon 1 : Allocataire moniteur.
- 09/1997-08/2001 École Normale Supérieure de Lyon : Élève normalien (fonctionnaire stagiaire).

Production scientifique :

Plus de 70 publications dans des revues internationales à comité de lecture (plus de 1000 citations, h-index =20).
8 conférences invitées dans des congrès internationaux. Une vingtaine de présentations orales dans des conférences internationales. Co-inventeur d'un brevet déposé.

3) Éléments (actualisés) du dossier de demande d'autorisation d'inscription à l'Habilitation à Diriger des Recherches

ENCADREMENT DE TRAVAUX DE RECHERCHE (maximum 5) :

EFFECTUES:

Nom - Prénom de l'étudiant	Formation (<i>Master, Doctorat, Thèse d'exercice</i>)	Encadrants et % d'encadrement	Date de l'encadrement	Publications (n° de la liste)
BLANC Nils	Doctorat	F. Tournus (70%) T. Epicier (15%) V. Dupuis (15%)	10/2006- 12/2009	
LINAS Sébastien	Post-doc	F. Tournus (50%) L. Bardotti (50%)	01/2013- 06/2014	

EN COURS :

Nom - Prénom de l'étudiant	Formation (<i>Master, Doctorat, Thèse d'exercice</i>)	Encadrants et % d'encadrement	Date de l'encadrement	Publications (n° de la liste)
LOISELET Ophelliam	Doctorat	F. Tournus (50%) J. Bellessa (50%)	10/2014-	
CAPIOD Pierre	Post-Doc	F. Tournus (50%) L. Bardotti (50%)	06/2016- 06/2017	

Commentaire libre :

J'ai également encadré de nombreux stages (licence, master).

PRINCIPALES ACTIVITES D'ENSEIGNEMENT :

DISCIPLINE	ANNEE	NIVEAU	ETABLISSEMENT	HEURES
Physique pour SVT	2007-2008	1 ^{er} cycle	Univ. Lyon 1	12h TD + 14h TP
Microscopie élec.	2009-2010	2 ^e cycle	Univ. Lyon 1	12h TP
Magnétostatique	2010-2011	1 ^{er} cycle	Univ. Lyon 1	12h TD
Électromagnétisme	2011-2012	1 ^{er} cycle	Polytech-Lyon (ISTIL)	20h TD
Électromagnétisme	2012-2013	1 ^{er} cycle	Polytech-Lyon (ISTIL)	10h TD
Électricité	2012-2013	1 ^{er} cycle	IUT Lyon 1	16h TD
Tutorat alternance	2012-2013	2 ^e cycle	Univ. Lyon 1	10h TD
Électricité	2013-2014	1 ^{er} cycle	IUT Lyon 1	16h TD
Mesures physiques	2013-2014	1 ^{er} cycle	IUT Lyon 1	12h TD
Électricité	2014-2015	1 ^{er} cycle	IUT Lyon 1	16h TD

Mesures physiques	2014-2015	1 ^{er} cycle	IUT Lyon 1	12h TD
Traitement de l'info.	2014-2015	1 ^{er} cycle	IUT Lyon 1	12h TD
Mesures physiques	2015-2016	1 ^{er} cycle	IUT Lyon 1	12h TD
Traitement de l'info.	2015-2016	1 ^{er} cycle	IUT Lyon 1	12h TD
Électricité	2015-2016	1 ^{er} cycle	IUT Lyon 1	16h TD
Mesures physiques	2016-2017	1 ^{er} cycle	IUT Lyon 1	12h TD
Traitement de l'info.	2016-2017	1 ^{er} cycle	IUT Lyon 1	12h TD
Électromagnétisme	2016-2017	1 ^{er} cycle	Univ. Lyon 1	24h TD

CONTRATS DE RECHERCHE (3 au maximum) :

2014-2016 : Projet région « ARC 6 – TIC et Usages Informatiques Innovants », intitulé « Nanosystèmes bi-métalliques pour la magnéto-plasmonique », financement d'une bourse de thèse (108 k€).

2011-2014 : Projet ANR « NanoMagnétisme sur Graphène Épitaxié sur Métaux » (ANR-20110-BLAN-1019, responsable J. Coraux), 158 k€ pour partenaire ILM.

2009-2012 : Projet ANR « Étude de la dynamique de retournement de l'aimantation d'agrégats uniques assisté par micro-onde » (ANR-08-NANO-039, responsable E. Bonet), 155 k€ pour partenaire ILM.

DESCRIPTION SUCCINCTE D'AUTRES ACTIVITES :

Participation à différentes actions de formation : formation de microscopie électronique en transmission (INSA Lyon, en 2013 et 2016) « Simulations d'images HRTEM » ; plan action formation « Nanosciences nanotechnologies et société » pour les enseignants du 2nd degré (Univ. Lyon 1 en 2014), « Nanomagnétisme ».

Comité local d'organisation pour EWEG 2013 : 1st European Workshop on Epitaxial Graphene, (Aussois, janv. 2013). Comité scientifique du Colloque Louis Néel 2014 (Autrans, sept. 2014).

Correspondant information/communication du laboratoire (2006-2010) ; membre du conseil de laboratoire (2006-2010) ; responsable des séminaires pour l'axe « nano » de l'ILM ; élu depuis janvier 2015 au Conseil Scientifique de l'Institut de Physique (INP) du CNRS.

Vulgarisation et animations scientifiques : participation à plusieurs éditions de la fête de la science, de la nuit des chercheurs, interventions dans des classes et dans la presse régionale.